University of Alberta

Numerical Study of Free Surface Flow Around Large Obstacles

By

YanMing Zhang ©

A thesis submitted to the
Faculty of Graduate Studies and Research
in partial fulfillment of the requirements
for the degree of Doctor of Philosophy

in

Water Resources Engineering
Department of Civil and Environmental Engineering
University of Alberta

Edmonton, Alberta
Fall, 2003

Your file Votre référence
ISBN: 0-612-88077-X
Our file Notre référence
ISBN: 0-612-88077-X

University of Alberta

Library Release Form

Name of Author: *YanMing Zhang*

Title of Thesis: *Numerical Study of Free Surface Flow around Large Obstacles*

Degree: *Doctor of Philosophy*

Year this Degree Granted: *2003*

Date: May 28, 2003

University of Alberta

Faculty of Graduate Studies and Research

The undersigned certify that they have read, and recommend to the Faculty of Graduate Studies and Research for acceptance, a thesis entitled **Numerical Study of Free Surface Flow around Large Obstacles** submitted by **YanMing Zhang** in partial fulfillment of the requirements for the degree of **Doctor of Philosophy** in **Water Resources Engineering**.

Dr. P. M. Steffler
(Supervisor)

Dr. N. Rajaratnam

Dr. M. R. Loewen

Dr. D. H. Chan

Dr. J. W. Yokota

Dr. B. E. Larock
(External Examiner)

Date: May 27, 2003

ABSTRACT

In this thesis a numerical model was developed to study three-dimensional turbulent flows around large obstacles in an open channel. With this numerical model, a series of numerical tests was carried out, and the properties of turbulent flows around a single obstacle or a cluster of obstacles were investigated. The origin of this study was to study the flow properties around fish habitat structures. Actually, the numerical model can be applied to the study of general turbulent flows under free surfaces.

In the numerical model the three-dimensional Reynolds-averaged Navier-Stokes equations in conjunction with k-ε turbulence model were solved in a free surface fitted coordinate system. First, different forms of governing equations for turbulent flow were investigated, and a concise form of fully transformed governing equations in a general curvilinear coordinate system was derived. In the numerical solution the FAVOR (Fractional Area/Volume Obstacle Representation) technique was extended into the free surface fitted coordinate system. With this feature the problem of complex turbulent flow with a free surface and general shaped obstacles could be solved efficiently. To locate the free surface, a method based on integrating the momentum equation in the vertical direction was developed. After study and tests of several popular difference schemes, a QUICK scheme with UMIST limiter was adopted in this numerical model.

Several test cases were presented to demonstrate the present numerical model. The first test case was to simulate a submerged hydraulic jump. The calculated velocity, free surface profile and turbulence properties of the flow showed a close match with the experimental data. The second test was a submerged hydraulic jump with a baffle sill. The comparison between numerical and experimental data indicated that the current numerical model could catch the general flow structures of the submerged hydraulic jumps. The last two test cases were flows around a single hemisphere or multi-hemispheres attached to a channel bed. The hemispheres were used to represent simple fish habitat structures. The test results proved the reliability of this numerical model to solve complex turbulent flows under free surface.

Using systematic numerical tests with this model the relationship between water depth and the obstacle height, the interaction between obstacles, and the wake area behind different obstacle configurations were investigated. The results of the study provided useful information for the design of fish habitat structures.

Acknowledgements

I would like to thank my supervisor, Dr. P. M. Steffler, for his support and guidance during this research.

I wish to extend my thanks and appreciation to Mr. Chris Katopodis of the Department of Fisheries and Oceans, Government of Canada, for his valuable support and suggestions.

My sincere thinks also go to Dr. N. Rajaratnam, Dr. H. Shamloo, Dr. C. D. Albers, Mr. W. Cui, and Dr. S. Wu for providing relevant information.

I would like to acknowledge the financial support of the University of Alberta through a scholarship and a research assistantship through an operating grant to my supervisor from the Department of Fisheries and Oceans, Government of Canada.

Finally, I would like to thank my dear wife, Beiming, for her patience, love and understanding.

TABLE OF CONTENTS

List of Tables

List of Figures

List of Symbols

H	water depth at downstream of main channel;
W	channel width;
R	height of obstacles;
D	diameter of hemisphere obstacles;
U_0	average velocity of main channel;
F_r	Froude number;
R_e	Reynolds number;
x^i	Cartesian coordinates x, y, z;.
ξ^i	general curvilinear coordinates ξ, η, ζ;
$\vec{e}^i$	contravariant base of general curvilinear coordinates;
$\vec{e}_i$	covariant base of general curvilinear coordinates;
g^{ij}	contravariant metric tensor components;
g_{ij}	covariant metric tensor components;
J	Jacobian of transformation;
g	$=JJ^T$;
p	pressure;
Q	total flow discharge;
U^i	Cartesian velocity, U, V, W or u, v, w;
u^i	contravariant velocity components;
u_i	covariant velocity components;
τ^{ij}	contravariant stress components;
τ_{ij}	covariant stress components;
ε^{ij}	contravariant strain components;
ε_{ij}	covariant strain components;
K	turbulent kinetic energy per unit mass;
ε	turbulent specific dissipation rate;
G_e	generation term in turbulent kinetic energy equation;
μ_l	molecular viscosity;
μ_e	effective viscosity;
ρ	water density.
γ^i	gravity force;

Chapter 1

Introduction

1.1 Introduction

1.1.1 Free Surface Flow around Large Obstacles

Human interference may easily damage the natural environment. One example is the channelization or training of a river to increase its flood capacity, restrict its width, or redirect its course. One of the adverse effects of the channelization is that fish habitat, in the form of velocity and predator refuges is eliminated. One way to relieve the impact is to provide artificial or constructed habitat to replace the natural habitat features, often in the form of obstacles placed in the flow. These obstacles are called fish habitat structures. From a single rock to a complex structure, fish habitat structures vary from design to design. In fish habitat structure design, knowledge of the free surface flow around obstacles is critical.

Flow around and/or over large obstacles in open channel is an important and broad subject in river engineering. Besides the flow around fish habitat structures mentioned above, flows around and over baffle sills, baffle blocks and other energy dissipation structures are also in this category. The common characteristics of the flow around large obstacles in river engineering are high speed turbulent flow, complex boundary conditions, large amplitude free surface waves and strong three-dimensional vortices. Because of these characteristics, the study of the flow around large obstacles is very difficult. Almost all research projects in this area are experimental studies.

In the studies of flow around obstacles, experimental studies have their limitations. In comparison with numerical studies, the high cost and low efficiency of the experimental studies may prevent systematic and extensive experiments, but extensive experiments are often necessary because the geometry of obstacles may be of any shape or of any configuration in an engineering problem. Another concern in experimental studies is the effect of scale. In the problem of free surface flow over obstacles, both gravity and viscosity have important roles in the flow. That requires both Reynolds number similarity and Froude number similarity to be satisfied to avoid distortions. However, in reality only one of them can be satisfied at a time. For modeling large scale, high speed flows in hydraulic engineering, often only Froude number similarity is satisfied.

Considering the limitations of experimental studies, it would be ideal to build a numerical tool to study the complex flow problems. To date, very few numerical studies are found in the area of the free surface flow around large obstacles, because the existence of both a free surface and obstacles makes the problem very difficult. At least one commercial software, Flow-3D (Flow Science Inc.), is known to be able to simulate free surface flow around obstacles. As a general three-dimensional flow solver, it may not be efficient to solve a specific problem. Besides efficiency, a specific model for a particular problem often has more flexibility in extension and manipulation. The major work of this thesis was finished in 1996. At that time the efficiency of a numerical model was even more important than it is today. In addition, to simulate free surface flow around obstacles, specific features such as free surface fitted coordinates combined with the FAVOR technique can solve the problem better than existing general purpose models that work in a Cartesian coordinate system.

1.1.2 Scope of the Study

The objective of this study is to build an efficient numerical model to simulate free surface turbulent flow around and/or over large obstacles. To achieve this goal, the following steps are necessary:

(a) Review current developments of numerical research in fluid flows.
(b) Study and evaluate governing equations for three-dimensional, free surface turbulent flow around and/or over large obstacles.
(c) Test available difference schemes to be used in the numerical model. The schemes should be able to handle strong convection.
(d) Find an efficient and reliable way to locate the free surface profile.
(e) To find a technique to represent general obstacles in the numerical model. There should be no restriction on the shape and number of the obstacles.
(f) To build a grid system that can fit the free surface profile accurately and can be regenerated easily.
(g) To carry out extensive tests to validate the numerical model.

The users of this numerical model will be engineers and biologists, so it must be efficient enough to be able to work in an ordinary personal computer, even though the flow to be solved is one of the most complex turbulent flows.

The secondary purpose of this study is to find general characteristics of the flow around fish habitat structures by using the numerical model in systematic numerical testing. The testing results are used to present recommendations for fish habitat structure designs.

1.2 Experimental Studies of Free Surface Flows around Obstacles

1.2.1 Flow around Fish Habitat Structures

Two early examples of experimental studies of flow around fish habitat structures were found in Katopodis and Rajaratnam's work (Katopodis, 1981; Katopodis and Rajaratnam, 1983). In their experiments the flow past fish habitat structures with different configurations inside a fishway were measured, and the wake areas behind the fish habitat structures were calculated from the measured average velocities. By judging the wake areas to estimate the efficiency of the fish habitat structures, a better design with higher energy dissipation rate was found.

Similar but more detailed work was done by Shamloo (Shamloo, 1996; Shamloo, Rajaratnam and Katopodis, 2001). In Shamloo's thesis, the structure of the flow and the scour pattern around a hemisphere in a simplified fishway were investigated experimentally. The velocity distribution around the hemisphere was measured with a smooth channel bed (no scour) and a mobile channel bed (with scour). Based on the behavior of the free surface, the flow was divided into four regimes according to the ratio of the water depth to the hemisphere height. In each regime he found that the vortex patterns and scour patterns were different. Further study was recommended.

After Shamloo's work, C. D. Albers (1997) made further developments in the experiments of flow around obstacles. In his experiments the flow around a three obstacle cluster was analyzed by flow visualization. The dependence of the flow pattern on the depth of flow and the spacing between obstacles was examined. This was done by examining the separation line on the channel bed near each obstacle and by observing the direction of the bed shear vector over a large area around obstacles.

He found the cluster acted like a single obstacle when the spacing between obstacles was less than 1.1 times of the obstacle diameter.

1.2.2 Flow past Baffle Sills or Baffle Blocks

Submerged hydraulic jumps with or without baffles is a common design element in a hydraulic jump type of stilling basin. There were a considerable number of experiments done on submerged hydraulic jumps without baffles (Long, Steffler and Rajaratnam 1990; Govinda and Rajaratnam, 1989). Very detailed measurements are available in this area. For submerged hydraulic jumps with baffles, N. Rajaratnam and V. Murahari (1971) presented an experimental study of the hydraulic jumps formed by baffle walls or baffle blocks. By dimensional analysis with the integral momentum equation and experimental results, the drag on the baffle wall was analyzed, and a chart for the preliminary design of these stilling basins was created.

S. Wu and N. Rajaratnam (1995) presented another set of experiments on submerged hydraulic jumps with baffle walls. From their experiment results a diagram was developed that was able to predict the condition under which a surface jet would be produced. The characteristics of a deflected jet were also studied. The decay of the maximum velocity in the deflected jet and the surface jet was compared with that of a plain submerged jet.

Some experiments were done in the measurements of the drag on baffle sills. In Tyagi's experiments (Tyagi et al. 1978) the averaged and fluctuating forces on baffle sills were measured. They found these forces were dominated by the sill location and the depth of tail water. In Rajaratnam's experiment (1964) the forces on baffle sills and the forces on baffle blocks were compared. He found an optimum spacing between the baffle blocks when the baffle blocks had a 50% blockage. For this spacing the baffle blocks bear less force.

More detailed information on hydraulic jumps can be found in Rajaratnam (1976) and Hager (1992).

1.2.3 Flow past Obstacles without Free Surface Effect

There are too many examples to be listed about experiments on flow past obstacles without considering free surface. The simplest configuration is flow past a square prism (Vickery, 1966; Lee, 1975; Bearman, 1972; Bearman and Obasaju, 1982). In their experiments, the averaged pressure and fluctuating lift and drag were measured in high Reynolds number flows with $Re>10^5$. More examples are flows past 3-D cubes. Gastro and Robin (1977) measured turbulent flow around a surface-mounted cube in a wind tunnel with $Re=2x10^4\sim10^5$. The cube was arranged to face flow at an angle. To simulate flows around a building in strong wind, Ogava and Oikava (1982) and Gowda et al. (1983) measured the turbulent flows around a cube. Flows past cylinders or wings have been extensively studied and are well understood. No details will be given here.

1.3 Progress of Numerical Simulation

Depending on the dominant characteristics in a flow, different flow modeling strategies can be used. For example, if a flow is dominated only by wind waves and the energy dissipation in the waves is not significant, it can be modeled as potential flow. That will make the problem much simpler. For a complex flow it is also possible to model the flow in two simple phases, for example, a potential flow phase and a viscous flow phase. The two phases can be solved iteratively. After a numerical model is established, a numerical method is to be developed to solve the numerical

model. The numerical method will cover all details such as selection of a grid system, discretization scheme, boundary conditions and turbulence modeling. In the following sections a review of available numerical models and the current development of numerical methods will be presented.

1.3.1 Flow Modeling

1.3.1.1 Potential Flow

The easiest and the most efficient way to solve a flow problem is to model it as a potential flow if the viscous effect in the flow is negligible. There are already mature mathematical theories and computation methods for potential flows. Analytical solutions are also available for certain simple flows. One example is foil theory. The lift force on a two-dimensional foil in high speed flow can be calculated analytically by analogy to the lift force on a rotating cylinder.

Only after the appearance of modern computers did numerical methods for potential flows became a practical engineering tool. An example is the panel method developed a few decades ago. Potential flow is governed by the Laplace equation. The solution of this problem can be obtained by finding a group of fundamental solutions that satisfy the Laplace equation, and the summation of these solutions can be made to satisfy the appropriate boundary conditions. These fundamental solutions may be sources or other higher order singular solutions. Since these fundamental solutions are distributed over the surface of the calculation domain in the form of small panels, this method is called a panel method or the "Hess and Smith Method" (Hess and Smith, 1962). This method is popularly used to calculate the flow around a body without lift. In order to reduce the numerical errors from singularity of the fundamental solutions, the author has tried to use submerged sources instead of surface sources in a potential flow calculation and obtained very good results (Zhang, 1987).

The panel method can also be used in water wave problems (Dawson, 1977). One example is to calculate wave-making resistance of a ship (Chai and Zhang, 1988). The idea of the method is to place panels on the ship hull and also on the free surface near the ship. Since the free surface is a movable boundary, iteration is required to update the position of the free surface. Final results can be found by adjusting the strengths of the sources and the positions of the panels to fit both kinematic and dynamic boundary conditions. After the wave profile is obtained, the pressure distribution can be calculated with the Bernoulli equation, and then the force on the ship can be found. Note that the calculated force is purely from potential flow; the viscous force from friction must be calculated separately. In this way any coupling between gravity and viscosity is neglected.

1.3.1.2 Boundary Layer Theory

Boundary layer theory is one of the most significant contributions to fluid mechanics in the last century (Schlichting, 1979). The essence of boundary layer theory is that it limits the complex viscous flow to the inside of a very thin layer. Outside this thin layer, well-established potential flow theory can be applied. Across the boundary layer, the flow velocity will increase sharply from zero to the exterior velocity. Since the boundary layer is so thin, physical quantities of the flow will have much larger gradients across the boundary layer than parallel to the boundary layer. By comparing the scales of each physical quantity and neglecting lower order ones, the complex governing equations of viscous flow can be simplified to become the boundary layer equations. The first remarkable success of boundary layer theory was the flat plate boundary layer theory that is the foundation of viscous resistance calculations.

The concept of boundary layer theory was proposed by Prandtl in 1904 (H. Schlichting, 1979), but it became relatively useful only after the popularity of

numerical methods. Between the sixties to seventies, viscous flows around smooth surfaces such as wings or ship hulls were solved numerically. At that time the computation time was a major concern, so the numerical solution of viscous flows was based on integral approaches. Viscous flows were characterized by the integration of velocity components across the boundary layer. After integration, the boundary layer equations become a group of ordinary differential equations, which could then be solved easily by numerical methods.

With the increase in computer power, the boundary layer equations could be solved directly by a difference method. The boundary layer equations are a set of partial differential equations that are simplified from the Reynolds-averaged Navier-Stokes equation by dropping the terms of the order less than $\frac{\Delta U}{\Delta y}$, where U is the mainstream velocity and y is the coordinate across the boundary layer. The boundary layer equations are parabolic equations. Therefore, it can not reflect the phenomenon of reversed flows. Usually it is used to determine the flow along a smooth surface without separation.

Another advance in boundary layer theory was called "thick boundary layer theory". In ordinary boundary layer theory the pressure is assumed to be a constant across the boundary layer. If the boundary layer is not thin enough, this assumption is invalid. Generally, the thickness of the boundary layer will increase until the flow separates from attached body. Just before the separation, the boundary thickness will increase quickly. In this region the pressure can not be assumed to be a constant across the boundary layer. To account for the gradient of the pressure across the boundary layer, all terms of the order of $\frac{\Delta p}{\Delta y}$ should be kept in simplifying Reynolds-averaged Navier-Stokes equation. With the thick boundary layer theory, the numerical solution can be extended to the whole boundary layer region just before separation. Zhang's work

(1984) gave an example of the application of thick boundary theory to the solution of flow around an axisymmetric body.

1.3.1.3 Reynolds-Averaged Navier-Stokes Equation

Very soon the thick boundary theory was replaced by the partially parabolic equation method. The reason is that people are not only interested in the flow around a body but also the flow inside the wake of the body. In the wake region the boundary layer theory can not be applied. The partially parabolic equation method also comes from the Reynolds-averaged Navier-Stokes equation by removing the elliptic property in the mainstream direction. The purpose of this simplification is to avoid time consuming iteration from downstream to upstream, because the effect on the flow from the downstream direction is much smaller than from other directions. If there is no reverse flow, this approximation is a good approach. However, for many flows, such as the flows around large obstacles, there will be strong three-dimensional vortices around the obstacles and reverse flow behind the obstacles. When the effect from the downstream direction is strong, the partially parabolic flow assumption can not be applied.

The last choice for the solution of a complex flow is to solve the full Reynolds-averaged Navier-Stokes equation. If turbulence can be modeled properly, this equation could be applied to general flows. In most cases this equation must be used in a curvilinear coordinate system to fit complex boundaries. There are two approaches to convert the governing equations from a Cartesian coordinate system into a curvilinear coordinate system. One is a partial transformation that converts only the coordinates into a curvilinear coordinate system and keeps the velocity components in Cartesian coordinate or other simple orthogonal coordinate system. The purpose of this approach is to make the governing equations simple, because velocity components will not change directions along the curvilinear coordinates.

However, a large deviation between the direction of the velocity components and coordinates may affect numerical accuracy. The second approach is a full transformation that transforms both the coordinate and velocity components into a curvilinear coordinate system. The advantage of this approach is that the velocity components always align with the coordinate axes. With this coordinate transformation, the complex geometry of the real computation domain can be converted into a rectangular domain. As a tradeoff, the curvature of the real boundaries and the direction changes of the velocity components must be counted inside the governing equations. This may make the governing equations too complex to be solved. In addition, if the curvilinear coordinates can not be written analytically, the numerical calculation of the coordinate curvatures and their differentials may be a major source of numerical errors.

To overcome the disadvantage of full transformation of governing equations, the author had derived a concise fully transformed governing equation set that is significantly simpler than the ordinary ones (Zhang, 1988). In the new governing equations, three components of the momentum equation always align with the curvilinear coordinate axes, while in conventional governing equations these component equations are in the directions of the gradient of the coordinate surfaces. The advantage of aligning a momentum equation with a coordinate axis is that no pressure gradients in directions other than this coordinate axis will appear in the momentum equation. As in an orthogonal coordinate system, there will be only one pressure term in each momentum equation. In this thesis, this idea is refined, and the comparisons between conventional fully transformed governing equations, concise fully transformed governing equations and partially transformed governing equations are given.

The Reynolds-averaged Navier-Stokes equation can only give averaged measurements of turbulence properties, that is, the turbulence fluctuations are measured by their correlations. Since these correlations are additional variables to the Navier-Stokes

equation, a turbulence models is required to close the solution procedure. The details of the turbulence model will be discussed in the section of numerical methods.

1.3.1.4 Direct Numerical Simulation

All turbulence models are derived empirically, based on limited measurements. As such, no turbulence model is found to be applicable to all turbulent flows. The results from the turbulence models should also be carefully examined. As an alternative approach, direct simulation for turbulence was developed in recent years.

If the resolution of numerical grids is sufficient, it is possible to resolve major turbulence fluctuations. In such a case, the time-dependent turbulent flow can be solved directly without turbulence modeling. By direct simulation, some findings in turbulent coherent structures such as bursting phenomena (Kline et al., 1967) can be studied numerically. Kim and Moin's (1986) study has successfully explained the busting motions by direct simulation. Many references can be found in the area of direct numerical simulation (Yang and Ferziger, 1993; Michelassi et al., 1993; Tsan-Hsing-Shih and Lumley, 1993; Thomas, 1995; Werner and Wengle, 1989). The barrier to direct simulation is computational power. To simulate small eddies requires a very fine grid. From turbulence theory, if the viscous effect is dominant, the ratio between the characteristic length (L) of the flow and the length scale of the smallest turbulent eddies (l_e) is on the order of $R_e^{3/4}$, where R_e is Reynolds number. To represent the smallest eddies, the mesh size should be less than l_e. Generally the Reynolds number R_e in turbulent flow is above 10^3. For example, if R_e is 10^4 then L/l_e is 10^3. For a three-dimensional flow, the number of cells should equal 10^9. A numerical solution based on this grid size is still beyond today's computer power. That is the reason why direct numerical simulation is not as popular as other approaches.

1.3.1.5 Turbulence Models

As the direct simulation of turbulent flows is not practical, turbulence modeling is necessary to solve the Reynolds-averaged Navier-Stokes equation. The simplest turbulence model is the **Eddy Viscosity Model** (White, 1974). By analogy to laminar flow, it assumes that the shear stress associated with turbulence is also proportional to the strain rate of the fluid. As the laminar diffusion is scaled by viscosity, turbulence mixing process functions like laminar diffusion and it is assumed can also be characterized by a "turbulence viscosity" called "eddy viscosity". The major difference between the two kinds of viscosity is that, in general, laminar viscosity is a constant, while the eddy viscosity varies with the flow. Only in fully developed, isotropic turbulence will the approximation of a constant eddy viscosity in a local region be acceptable.

The most well known turbulence model is Prandtl's **Mixing-Length Model** (White, 1974) that has been popular for more than seventy years. Prandtl assumed that small fluid parcels transport momentum by mixing with each other just like particle collisions in physics. A length-scale called a mixing length was defined. Since the mixing process is the source of the turbulent shear stress, the turbulent viscosity should be proportional to the mixing length and velocity gradient. With considerable accuracy, the mixing-length model can predict the logarithmic distribution of velocity in simple wall-bounded turbulent flows. Because the mixing-length model only reflects the local equilibrium of turbulence, it can not be used in cases where turbulence transport processes are dominant.

In more general turbulent flows the turbulence transport must be considered. Turbulence has different behavior in different regions in a flow. Turbulent eddies are generated in regions with strong shear and destroyed in regions with strong mixing. The process from generation to dissipation of the turbulent eddies is called turbulent transport. To describe the turbulent transport process, some semi-empirical transport

equations were developed. The simplest one is the **One-Equation Model** (Launder and Spalding, 1972) which simulates the transport of turbulent kinetic energy. The turbulent energy is measured by the intensity of velocity fluctuations. It is obvious that only one equation is insufficient to model the turbulence transport because at least two scales, length and times are involved in the transport process. Therefore, the **k-ε Two-Equation Model** (Launder and Spalding, 1972) which commonly characterizes turbulence by turbulence energy per unit mass k and turbulence dissipation rate ε, was developed. From its extensive applications, the k-ε turbulence model has proved to be the most successful turbulence model. Some interesting developments of the **k-ε Two-Equation Model** can be found in (Zijlema et al., 1995; Shin et al., 1994; Yang and Shih, 1993; Speziale and Sarkar, 1987).

For turbulence modeling of surface water flow, a special research was carried out by International Association for Hydraulic Research (ASCE Task Committee, 1988). Among several Two Equation Model, Meller and Yamada (1982) suggested the use of a second-order closure model, in which turbulence diffusivity and viscosity was determined from kinetic energy k and turbulence length scale l. The turbulence transport equations of k and kl were solved.

Other high-order turbulence transport equation models, such as the **Reynolds Stress Model** or **Second Moment Closure** (Launder et al., 1975), are not so popular because to apply these models one needs considerably more computation resources. For example, roughly there may be a 50% increase of computation time with a **Second Moment Closure** in comparison with an **Eddy Viscosity Model** (Lien and Leschziner, 1996). The **Reynolds Stress Model** has a special correction to account for the effects of wall-induced pressure reflections. It may have performed better than other turbulence models in the region near free surfaces. More details about higher-order turbulence models can be found in these references (Lien and Leschziner, 1994b; Leschziner, 1995; Speziale and Gatski, 1994; Sharif and Wong, 1993 also reviewed in the ASCE Task Committee publication).

Large Eddy Simulation (LES) (Deardorff, 1970) is in a different concept in turbulence simulation. The basic idea of **LES** is that if a turbulent eddy is in larger scale than the size of the computational grid, it can be captured by solving the Navier-Stokes equation directly. For these eddies smaller than the grid size, a local eddy viscosity approach can be applied. Theoretically speaking, **LES** should have wider applicability than other turbulence models if the unresolved eddies are small enough. **LES** has limited use because the fine grids required cost too much in terms of computer resources. An review of applying the LES method can be found in Rogallo and Moin (1984).

1.3.2 Numerical Methods

1.3.2.1 Finite Element Method, Finite Volume Method and Finite Difference Method

The finite element method (FEM) and the finite volume method (FVM) are two major numerical methods. FEM discretizes a complex geometry into a group of elements with simple shapes. Since each element can be a different shape, FEM grids are very flexible in conforming to boundary geometry. Although FEM has this advantage, it is difficult to apply it to fluid flow problems. In flow problems, the direction of flow is very important because the effects from upstream nodes are much more significant than those from downstream nodes, so different weights have to be applied to different nodes. As FEM grids are unstructured, i.e., the grids can not be separated by a simple coordinate surface, to apply different weights according to a flow direction that changes with time is not straightforward. In addition, considerable computational time is required to build the element matrices and nodal connectivity in unstructured meshes.

Basically, finite difference method (FDM) is similar to FVM except that the FVM is to discretizes differential equations using an integral point of view while the FDM retains a differential viewpoint. In the FDM, the differential of a physical quantity of a node is approximated by a difference between that node and its neighbor nodes. The choices of these neighbor nodes lead to a variety of difference schemes. The convection of flows can be addressed by placing more weight on the upstream nodes. The weak side of the FDM is that it does not consider physical consistency in the discretization process. As a result, it may produce physically incorrect results in certain cases.

Discretization in the FVM occurs at the level of small cells called finite volumes. Each cell shares common interfaces with its neighbor cells. The method can ensure that the flux that exits from a cell is always equal to the flux entering its neighbor cells. In total, the continuity equation will be satisfied over the whole domain regardless of the number or size of the cells. In the FVM the physical properties of a cell are represented by physical properties of a node inside that cell. The values of these physical properties on a cell surface can be estimated from values of nodes close to this surface. To account the convection effects, different weights and different nodes may be used to estimate the values on the cell surface.

A comparison of FEM and FVM can be found in (K. Nakajima et al., 1994). From the above discussions, FVM is used in the current numerical model.

1.3.2.2 Unstructured Grids, Multi-Grids and Flow around Obstacles

The flexibility of the FEM comes from its use of unstructured grids. Unstructured grids can also be applied in the FVM for flow problems with complex boundaries. The essence of unstructured grids is that the discretized cells are not divided by coordinate surfaces, so they are allowed to change shapes or sites freely. Besides the

advantage of fitting the boundary geometry easily, an unstructured grid can be refined locally. That is a very attractive feature which can improve numerical accuracy when a flow changes dramatically in a local region. On the other hand, unlike cells in structured grids that have a fixed order, a cell in an unstructured grid does not a list of index of its neighbor cells in advance, so the bookkeeping of a list of indices of its neighbor cells is necessary. If a flow has a moving boundary such as a free surface flow, the numbers and shapes of the neighbor cells may continuously change near the moving boundary. That may make local bookkeeping extremely difficult, especially when different weights should be assigned to different neighbor cells according to the flow direction.

An alternative way to increase resolution locally is to use a multi-grid technique. According to its name, grids with different resolutions are used to meet accuracy requirements in different regions. Many examples of unstructured grids (Shahyar, 1992; Quirk, 1994), multi-grids (Farmer and Martinelli, 1994; Hwang and Wu, 1993; Aftosmis, 1994) and obstacle flows with unstructured grids or multi-grids (Gastro and obin, 1977; Vickery, 1966; Gowda et al., 1983; Bearman, 1972; Rizzetta, 1994; Tropea and Gackstatter, 1985; Bai and Fuch, 1994; Ma and Ahamid, 1993) can be found in the references.

Unstructured grids were not used in the current numerical model for the following reasons: All examples in above references are complex flows, but the flows do not have obstacles and free surface at the same time. To calculate the free surface location requires grids to be regenerated repeatedly. That will take considerable computational time, especially for the large grid needed in the calculation of flows around three-dimensional obstacles with the complex geometry of fish habitat structures.

There are a few different methods to model obstacle boundaries. If obstacles have a regular shape, multi-grids may be used. If obstacles have a gradually changing surface contour, it is preferable to use a body fitted coordinate system. For obstacles with

more complex shapes, Sicilian (Flow Science Inc.) developed the FAVOR (Fractional Area/Volume Obstacle Representation) method in a Cartesian coordinate system. In this method the fractions of cell surfaces cut by an obstacle are calculated and only the fluxes passing through the open portions of the cell surface are counted in the calculation. This is an efficient way to treat partially occupied cells.

1.3.2.3 Difference Schemes

a. Centered Difference

The centered difference scheme is one of the most popular difference schemes. It is natural to assume that the value on a cell surface is the average of the values from the two nodes adjacent to that surface. With this assumption the centered difference scheme for a first order differential is equivalent to taking the difference between two nodes at two sides of the node considered. Although only two nodes are used in the centered difference scheme, it has second order accuracy if the mesh is uniformly spaced. As the centered difference scheme is equivalent to taking the arithmetic average without considering the flow direction, it can not treat convection properly. Usually, the centered difference scheme is used in slow-flow problems or used to treat diffusion terms.

b. Upwind Scheme (first order)

To model convection in a flow with more accuracy, more weight should be put on an upstream node. In contrast to a centered difference that assigns the same weight to all nodes, the upwind scheme puts all of the weight on upstream nodes. This implies that the value of an upstream node will carried downstream unchanged in a pure convection process. Since the upwind scheme reflects basic convection properties, it will always produce a stable numerical solution. In contrast to the centered difference

scheme, the upwind difference only has first order accuracy. If a higher order difference scheme such as the centered difference scheme is used together with the first order upwind scheme, the inconsistency will generate a numerical error called numerical diffusion or artificial viscosity. The numerical diffusion acts in a similar way to physical diffusion as it may smear any sharp changes in the solution. The positive side of the artificial viscosity is that it can also increase the stability of numerical solution just like physical viscosity. The evaluation of numerical diffusion from an upwind difference can be found in references such as Taffersall and Mcguirk (1994) and Ramshaw (1991).

c. QUICK Scheme

Trying to find both high accuracy and high stability, Leonard (1979) proposed the QUICK difference scheme. In the QUICK scheme the value on the surface of a control volume is obtained by a parabolic interpolation from two upstream nodes and one downstream node. Then the first order differential in a control volume is approximated by the difference of the values on two opposite surfaces of the control volume. In such a way, the information from at least four nodes is used in the difference scheme that allows the scheme to achieve third order accuracy. Theoretically, the QUICK scheme is also unconditionally stable for numerical solution. However, in the solution of turbulent flows some problems may occur with the QUICK or other high-order upwind schemes in a region involving rapid changes in the solution. In this region overshoots or undershoots may be found in the numerical results. Generally, overshoots may lead to inaccuracy and slow convergence. There has been much research on how to overcome overshoots. Introducing various limiters is the most popular approach (Leer, 1976; Chakravathy and Osher, 1983; Roe, 1985; Leonard, 1988; Lien and Leschziner, 1993). When an abrupt change in a solution is detected, a difference scheme will be switched from high-order difference to a more stable scheme such as a first order upwind scheme.

In general, most limiters are derived from the concept of Total Variation Diminishing (TVD) (Harten, 1983). By the TVD concept a numerical scheme maintaining monotonicity should satisfy the conditions that no new local extrema are created and that the value of an existing local minimum or maximum must be non-decreasing or non-increasing, that is, the Total Variation must not increase. One example is Lien's Upstream Monotonic Interpolation for Scalar Transport (UMIST) limiter (Lien and Leschziner, 1994a). According to the rate of variation of the solution, this limiter switches between QUICK, centered difference, first order upwind difference and second order upwind difference schemes. As opposed to some other limiters that may double the computation time, UMIST is compact and efficient.

Another example of a TVD limiter is the Universal Limiter for Tight Resolution and Accuracy in combination with Simple High Accuracy Resolution Program (ULTRA-SHARP) (Leonard and Mokhtari, 1990). Considering only the steady state, the TVD diagram can be interpreted in terms of a Normalized Variables Diagram (NVD). Using NVD, ULTRA-SHARP is a monotonic implementation of the QUICK scheme. It functions as a switch between QUICK and lower order schemes depending on the variation of the solution. A drawback of this limiter is that it is time consuming because a complex conditional judgement is used to switch between different schemes.

In this thesis, the UMIST limiter is used. By comparing its performance with the QUICK scheme without a limiter, an increase in computer time of less than 20% was observed. The solution procedure is stable.

1.3.2.4 Free Surface Locating

One of the difficulties in the current study is locating the free surface. The major issues to be solved are the representation of the free surface, updating the free surface location and apply the free surface boundary conditions. Some popular methods of treating the free surface boundary will be discussed in this section.

a. Bernoulli Integration

The easiest method for free surface tracking is the Bernoulli integration method. It is based on the assumption that viscous effects can be neglected near the free surface. For potential flow, the energy balance on free surface can be expressed by Bernoulli equation:

$$p + \rho g\zeta + \frac{1}{2}\rho V^2 = \text{constant} \qquad (1.3.2.1)$$

Because the pressure p is constant on the free surface, the elevation ζ of the free surface depends only on the kinetic energy $\rho V^2/2$ and the chosen constant. This approach works well for problem of ocean waves that are assumed to be driven only by gravity after they start. In this case, friction is negligible.

b. Free Surface Height

The Bernoulli equation (1.3.2.1) only reflects the energy or dynamic balance of flow at the free surface. The kinematic boundary condition for the flow on the free surface can be described by the following equation:

$$\frac{\partial H}{\partial t} + u\frac{\partial H}{\partial x} - v + w\frac{\partial H}{\partial z} = 0 \qquad (1.3.2.2)$$

where H is the free surface elevation y = H(t, x, z) and (u, v, w) are the velocity components in (x, y, z) directions.

This is a relatively simple equation with a single variable H. If the amplitude of surface waves is sufficiently small, this boundary condition can be further simplified by applying equation (1.3.2.2) directly on a horizontal water surface.

Equation (1.3.2.2) itself is insufficient to locate the free surface, because both velocity and height of the free surface are unknown. The equation (1.3.2.2) must be solved together with the equation (1.3.2.1) or other additional equations. As a differential equation, equation (1.3.2.2) requires any free surface profile to be continuous.

c. Marker-and-Cell (MAC) Method

A more general free surface tracking method is a Marker-and-Cell (MAC) method (Harlow and Welch, 1965). The idea in this method is to add assumed marker particles to the fluids. By following the marker particles, this algorithm can determine which cells contain fluid and which cells are empty. The free surface can be found by connecting the cells which are partially empty. In this method the cells can be defined by a fixed Eulerian grid.

The method is attractive because it can be applied to a wide range of complicated free surface flows. It is also able to simulate free surface wave breaking. Recently a variety of improvements have been made to increase the accuracy and applicability of the MAC method. In spite of its success, it is difficult to apply this method to three-dimensional flows because considerable computational time is required to accommodate the necessary number of marker particles.

d. Volume-of-Fluid (VOF) Method

The Volume-of-Fluid (VOF) method (Hirt and Nichols, 1981) is based on the concept of a fluid volume fraction. It has similar power as that of the MAC method but it is much simpler. In the VOF method the fluid volume fractions associated with each cell are used as markers in place of the particles used in the MAC method. Unlike the MAC method that requires an average of 16 markers in each cell to insure an accurate tracking of the free surface with large deformations, the VOF method only needs one marker in each cell. This approach is consistent with the resolution of all other flow quantities (velocities, pressure, turbulent energy, etc.). This difference makes the VOF method able to save large amount of computer resources. From the fluid volume fractions the free surface can be located by connecting the cells that are partially full or empty.

In this method the free surface location must be updated by solving a kinematic equation involving the fluid volume fractions.

e. Lagrangian Grid Method

From a physical point of view, the Lagrangian Grid method (Hirt et al., 1970) is the most reasonable approach to tracking a free surface. It defines and tracks free surface by constructing a free surface fitted grid. The grid moves with the fluid interface and tracks the free surface automatically. In addition, the free surface boundary condition can be applied accurately to the free surface that is also a coordinate surface. The limitation of this method is that it cannot track free surfaces that break apart or intersect, because the free surfaces, which are also coordinate surfaces, must be continuous.

1.4 The Approach of Current Numerical Model

The above studies provide guidance building the construction of a numerical model for solving three-dimensional turbulent flow around and/or over large obstacles under a free surface.

In the numerical model developed in this research the three-dimensional Reynolds-averaged Navier-Stokes equation in conjunction with k-ε turbulence model were solved in a free surface fitted coordinate system. In the numerical solution the FAVOR technique was extended into the free surface fitted coordinate system. With this feature the problem of complex turbulent flow with a free surface and general shaped obstacles could be solved efficiently. To locate the free surface, a method based on integrating the momentum equation in the vertical direction was developed. After study and tests of several popular difference schemes, a QUICK scheme with UMIST limiter was adopted in this numerical model.

The details about this numerical model will be given in following Chapters.

Chapter 2

Governing Equations and Coordinate Transformation

2.1 General Concepts

As discussed in the first Chapter, turbulent flow around obstacles with a free surface is a very complex problem. Such a flow problem can only be solved by numerical solution of the Reynolds-averaged Navier-Stokes Equation, LES or by direct numerical simulation, or through extensive experiments. Since the goal of this research is to build an efficient numerical model for engineers, the computational effort should be limited, so solving the Reynolds-averaged Navier-Stokes Equation is the better choice.

To solve these governing equations it is first necessary to choose a coordinate system. For flow with a free surface, it is obvious that a curvilinear coordinate system should be used. A curvilinear coordinate system that fits the flow boundary could improve the accuracy of numerical results and make free surface locating easy.

There are two ways to derive the governing equations in a curvilinear coordinate system. One way is a full transformation, with both velocities and coordinates being transformed into the curvilinear coordinate system. The other way is a partial transformation that, as its name implies, only transforms the original coordinates into curvilinear coordinates and keeps the velocity components in the original orthogonal coordinate components. Generally, the fully transformed equation could produce better results because the velocity components then align with the new coordinate directions. The disadvantage of the fully transformed equations is that the governing

equation will be extremely complex after transformation. This condition occurs because the velocity components also change direction following the coordinates, and this change must be reflected in the governing equations. For a partially transformed equation set, the velocity components only change magnitude but not direction, so the governing equations are simpler. The tradeoff for this simplicity is that the numerical error may increase when the coordinates distort too much.

From the above considerations, a concise set of fully transformed governing equations, which are much simpler than the conventional one, are developed. The original idea of the new transformation is to resolve the momentum equations on the curvilinear coordinate axes themselves rather than on their reciprocal axes as the conventional transformation does. The details about this new transformation are to be discussed in Section 2.4.

In Sections 2.3 and 2.5, the fully transformed governing equation and the partially transformed governing equation will be reviewed. To validate the new concise fully transformed equations, in Section 2.6 all three kinds of governing equations (fully transformed, partially transformed and concise fully transformed) are tested against a numerical bench-mark solution. The conclusion of the test will be used to build the numerical model for free surface flow around and/or over large obstacles.

Tensor analysis will be used to derive the governing equations in a general curvilinear coordinate system. A review of related tensor analysis concepts will be provided in following section.

2.2 Review of the Basic Rules of Tensor Analysis

a. Covariant and Contravariant Bases of Curvilinear Coordinate System

To make the following sections easier to read, some basis tensor rules are refreshed here. For more details of tensor analysis, please refer to a book of tensor analysis (Aris R., 1962).

Tensor analysis is closely related to the mathematics of coordinate transformations. Some definitions of base vector in a curvilinear coordinate are given below. For easy demonstration in plots, the coordinates in this section are assumed to be two dimensional. That means range of tensor indices used here is 1 to 2. As shown in Figure 2.2.1 the base vectors of a general curvilinear coordinate system (ξ^1, ξ^2) are ($\vec{e}_1$, $\vec{e}_2$). These base vectors with **lower indices** are called **covariant** bases. It is very useful to define another set of bases called contravariant bases that are perpendicular to corresponding covariant bases. Contravariant bases are indicated by **upper indices** as ($\vec{e}^1$, $\vec{e}^2$). The relationship these between two bases is

$$\vec{e}^i \vec{e}_j = \delta^i_j$$

$$\delta^i_j = \begin{cases} 1 & i = j \\ 0 & i \neq j \end{cases}$$

Generally, tensor bases are not unit vectors. Only in a Cartesian coordinate system are the covariant and contravariant bases the same. With contravariant bases, it is easy to find a component of a vector. For example, if

$$\vec{U} = u^1 \vec{e}_1 + u^2 \vec{e}_2$$

Then

$$u^1 = \vec{U}\vec{e}^1$$
$$u^2 = \vec{U}\vec{e}^2$$

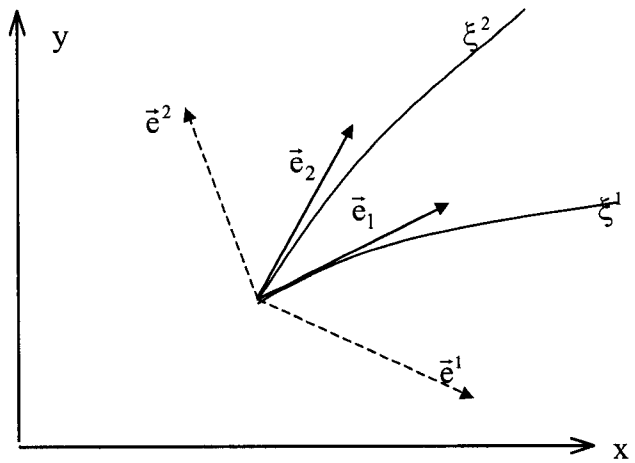

Figure 2.2.1 Covariant and Contravariant Bases

b. Summation Rules

In a coordinate transformation, one finds summations. For example, the chain rule in the coordinate transformation from (x^1, x^2) to (ξ^1, ξ^2) is

$$\frac{\partial f}{\partial x^1} = \frac{\partial f}{\partial \xi^1}\frac{\partial \xi^1}{\partial x^1} + \frac{\partial f}{\partial \xi^2}\frac{\partial \xi^2}{\partial x^1} = \sum_{i=1,2}\frac{\partial f}{\partial \xi^i}\frac{\partial \xi^i}{\partial x^1}$$

With tensor summation rules, the above summation sign can be omitted, such as,

$$\frac{\partial f}{\partial x^1} = \frac{\partial f}{\partial \xi^i}\frac{\partial \xi^i}{\partial x^1}$$

Tensor Summation Rules:

(i) In an expression, if one lower (covariant tensor) index and one upper (contravariant tensor) index are the same, it indicates a summation

For example:

$$a^i b_i = a^1 b_1 + a^2 b_2 + \ldots$$

(ii) If an index is in the denominator of a derivative expression, then an upper index indicates a covariant tensor and a lower index indicates a contravariant tensor.

For example, in

$$\frac{\partial f}{\partial \xi^i}\frac{\partial \xi^i}{\partial x^1} = \frac{\partial f}{\partial \xi^1}\frac{\partial \xi^1}{\partial x^1} + \frac{\partial f}{\partial \xi^2}\frac{\partial \xi^2}{\partial x^1}$$

$\frac{\partial f}{\partial \xi^i}$ is a covariant tensor and $\frac{\partial \xi^i}{\partial x^1}$ is a contravariant tensor. There is a summation in $\frac{\partial f}{\partial \xi^i}\frac{\partial \xi^i}{\partial x^1}$.

c. Tensor equations are invariant with respect to a coordinate transformation

It is easy to think of a tensor as an extension of a vector. A vector is independent of the coordinate system, and so is a tensor. In Figure 2.2.2, in two arbitrary coordinate systems $(\vec{e}_1, \vec{e}_2)$ and $(\vec{e}^1, \vec{e}^2)$, a vector $\vec{M}$ can be written as either

$$\vec{M} = M^1\vec{e}_1 + M^2\vec{e}_2$$

Or

$$\vec{M} = M_1\vec{e}^1 + M_2\vec{e}^2$$

That means that an equation derived in a Cartesian coordinate system can be applied to any coordinate system so long as it is in tensor form.

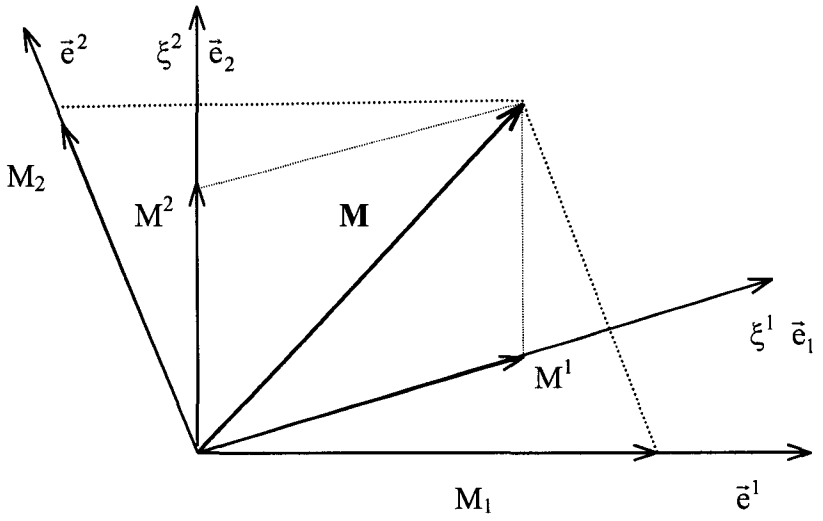

Figure 2.2.2 Vector in Two Coordinate Systems

d. Symmetric and anti-symmetric Tensor

The definition of a symmetric tensor is

$$a^{ij} = a^{ji}$$
$$a_{ij} = a_{ji}$$

For a anti-symmetric tensor

$$a^{ij} = -a^{ji}$$
$$a_{ij} = -a_{ji}$$

It is often useful to construct symmetric and asymmetric tensors as

$$A^{ij} = \frac{(a^{ij} + a^{ji})}{2} \quad \text{symmetry}$$
$$A^{ij} = \frac{(a^{ij} - a^{ji})}{2} \quad \text{anti - symmetry}$$

e. Metric Tensor and Tensor Derivatives

From this section general tensor in a three-dimensional coordinate system is used. The indices of the tensor are in range 1,2,3.

The metric tensor is defined as the product of the coordinate bases:

$$g_{ij} = \vec{e}_i \vec{e}_j$$

$$g^{ij} = \vec{e}^i \vec{e}^j$$

If (x^1, x^2, x^3) are Cartesian coordinates and (ξ^1, ξ^2, ξ^3) are general curvilinear coordinates, then

$$g_{ij} = \frac{\partial x^m}{\partial \xi^i} \frac{\partial x_m}{\partial \xi^j}$$

$$g^{ij} = \frac{\partial \xi^i}{\partial x^m} \frac{\partial \xi^j}{\partial x_m}$$

Another important value of the metric tensor is

$g = |g^{ij}|$ which is the determinant of the g^{ij} matrix.

Without derivation, the derivatives of a first and a second order tensor are given below. Commonly, A tensor derivative is denoted by sign $|_j$

Derivative of a first order tensor:

$$u^i|_k = \frac{\partial u^i}{\partial \xi^k} + u^m \Gamma^i_{mk}$$

$$u_i|_k = \frac{\partial u_i}{\partial \xi^k} - u_m \Gamma^m_{ik}$$

Where

$$\Gamma^i_{jk} = \frac{1}{2} g^{im} \left[\frac{\partial g_{mj}}{\partial \xi^k} + \frac{\partial g_{mk}}{\partial \xi^j} - \frac{\partial g_{jk}}{\partial \xi^m} \right]$$

A special case is the divergence expression:

$$\mathrm{Div}\,\vec{v} = u^i\,|_i$$
$$= \frac{1}{\sqrt{g}}\frac{\partial}{\partial \xi^i}(\sqrt{g}u^i)$$

In this case, expression

$$\Gamma^k_{kj} = \frac{1}{\sqrt{g}}\frac{\partial\sqrt{g}}{\partial \xi^j} \text{ is used.}$$

The derivative of a second order tensor is

$$u^{ij}\,|_k = \frac{\partial u^{ij}}{\partial \xi^k} + u^{im}\Gamma^j_{mk} + u^{mj}\Gamma^i_{mk}$$
$$u_{ij}\,|_k = \frac{\partial u_{ij}}{\partial \xi^k} - u_{im}\Gamma^m_{jk} - u_{mj}\Gamma^m_{ik}$$
$$u^i_j\,|_k = \frac{\partial u^i_j}{\partial \xi^k} - u^i_m\Gamma^m_{jk} + u^m_j\Gamma^i_{mk}$$

f. Conversion between Covariant Tensors and Contravariant Tensors

Using the metric tensor, it is easy to move the tensor index up or down:

$$A^i = \vec{e}^i(A_j\vec{e}^j) = g^{ij}A_j$$
$$A_i = \vec{e}_i(A^j\vec{e}_j) = g_{ij}A^j$$

2.3 Fully Transformed Governing Equations in a General Curvilinear Coordinate System

For the purpose of comparison, first the conventional form of governing equations in a general curvilinear coordinate system is derived. It is straightforward to transform the governing equations of turbulent flow from a Cartesian coordinate system into a general curvilinear coordinate system. Only governing equations of steady flow are shown and used in this thesis. However, it is straightforward to add time dependent terms in following derivations. First, all equations are written in a tensor form, that is, using tensor derivatives $|_j$ to replace $\frac{\partial}{\partial x^j}$:

Equation of Continuity:

$$(\rho u^j)|_j = 0 \qquad (2.3.1)$$

Equations of Momentum:

$$(\rho u^j u^i)|_j = \tau^{ij}|_j - p|^i + \gamma^i \qquad (i=1, 2, 3) \qquad (2.3.2)$$

Equations of K-ε Turbulence Models (here capital K is used for turbulent energy to distinguish if from tensor index k):

$$(\rho u^j K)|_j = (\Gamma_k K|^j)|_j + \rho G_e - \rho\varepsilon \qquad (2.3.3)$$

$$(\rho u^j \varepsilon)|_j = (\Gamma_\varepsilon \varepsilon|^j)|_j + C_1 \rho G_e \frac{\varepsilon}{K} - C_2 \rho \frac{\varepsilon^2}{K} \qquad (2.3.4)$$

Where

u^i: velocity

p: pressure

γ^i : gravity force, product of fluid density and gravity acceleration

τ^{ij} : shear stress defined in equation (2.3.5)

K: turbulent energy per unit mass

ε: turbulence dissipation.

$$\tau^{ij} = \mu_e \varepsilon^{ij} - \frac{2}{3}\delta^{ij}\rho K \tag{2.3.5}$$

$$G_e = \frac{1}{2}\nu_t \varepsilon^{ij}\varepsilon_{ij} \tag{2.3.6}$$

$$\begin{aligned} \varepsilon^{ij} &= u^i\,|^j + u^j\,|^i \\ \varepsilon_{ij} &= u_i\,|_j + u_j\,|_i \end{aligned} \tag{2.3.7}$$

$$\mu_e = \mu_l + \mu_t = \mu_l + C_\mu \rho \frac{K^2}{\varepsilon} \tag{2.3.8}$$

$$\Gamma_k = \frac{\mu_e}{\sigma_k} \qquad \Gamma_\varepsilon = \frac{\mu_e}{\sigma_\varepsilon} \tag{2.3.9}$$

μ_l is coefficient of molecular viscosity. $C_\mu, C_1, C_2, \sigma_k, \sigma_\varepsilon$ are constants (Launder, B. E. and J. L. Spalding, 1972):

C_μ	C_1	C_2	σ_k	σ_ε
0.09	1.43	1.92	1.0	1.3

These constants are empirical data from an internal turbulent flow (Launder and Spalding, 1972). The K-ε turbulent model with these constants has been applied to many different flow situations, mostly in mechanical and aeronautical engineering,

and has been found to work well. For surface water problems these constants will be considered in the next stage of this study.

Using the rules of tensor analysis in section 2.2, the above equations can be transformed into a general curvilinear coordinate system (ξ^1, ξ^2, ξ^3) directly.

Equation of Continuity:

$$\frac{1}{\sqrt{g}}\frac{\partial}{\partial \xi^j}(\sqrt{g}u^j) = 0 \tag{2.3.1a}$$

Equations of Momentum:

$$\begin{aligned}&\frac{1}{\sqrt{g}}\frac{\partial}{\partial \xi^j}(\sqrt{g}(\rho u^j u^i - \tau^{ij})) \\ &= \frac{1}{2}g^{im}\left[\frac{\partial g_{mj}}{\partial \xi^k} + \frac{\partial g_{mk}}{\partial \xi^j} - \frac{\partial g_{jk}}{\partial \xi^m}\right](\tau^{jk} - \rho u^j u^k) - g^{ij}\frac{\partial p}{\partial \xi^j} + \gamma^i\end{aligned} \qquad (i=1,2,3) \tag{2.3.2a}$$

Equations of K-ε Turbulence Models:

$$\frac{1}{\sqrt{g}}\frac{\partial}{\partial \xi^j}(\sqrt{g}\rho u^j K) = \frac{1}{\sqrt{g}}\frac{\partial}{\partial \xi^j}(\sqrt{g}\frac{\mu_e}{\sigma_k}g^{jm}\frac{\partial K}{\partial \xi^m}) + \rho G_e - \rho\varepsilon \tag{2.3.3a}$$

$$\frac{1}{\sqrt{g}}\frac{\partial}{\partial \xi^j}(\sqrt{g}\rho u^j \varepsilon) = \frac{1}{\sqrt{g}}\frac{\partial}{\partial \xi^j}(\sqrt{g}\frac{\mu_e}{\sigma_\varepsilon}g^{jm}\frac{\partial \varepsilon}{\partial \xi^m}) + C_1\rho G_e\frac{\varepsilon}{K} - C_2\rho\frac{\varepsilon^2}{K} \tag{2.3.4a}$$

where

$$\tau^{ij} = \mu_e\varepsilon^{ij} - \frac{2}{3}\delta^{ij}\rho K \tag{2.3.5a}$$

$$G_e = \frac{1}{2}\nu_t\varepsilon^{ij}\varepsilon_{ij} \tag{2.3.6a}$$

$$\varepsilon^{ij} = g^{im}\frac{\partial u^j}{\partial \xi^m} + g^{jm}\frac{\partial u^i}{\partial \xi^m} - \frac{\partial g^{ij}}{\partial \xi^m}u^m$$

$$\varepsilon_{ij} = g_{im}\frac{\partial u^m}{\partial \xi^j} + g_{jm}\frac{\partial u^m}{\partial \xi^i} + \frac{\partial g_{ij}}{\partial \xi^m}u^m \qquad (2.3.7a)$$

The momentum equation (2.3.2a) is very complex in a non-orthogonal coordinate system. A full expansion for this equation will result in 172 terms for each component equation. Quite often this equation must be simplified before solution. Another weak point of this equation is that there are three pressure gradient components in each momentum equation. That makes it difficult to solve the pressure from momentum equations.

To overcome the above problems, a concise form of momentum equation is derived in next section.

2.4 A Concise Form of Fully Transformed Governing Equations

The concept of a concise form of governing equations in a general curvilinear coordinate system was proposed by the author (Zhang, 1988) in the solution of turbulent flow around a ship (Shen, et al., 1988, 1989, 1991; Zhang and Shen, 1990). In this paper, this concept will be refined and an evaluation will be given.

The momentum equation is a vector equation so it can be resolved into components in any three non-parallel directions. Conventionally it is resolved in the direction of reciprocal basis of a coordinate system using the orthogonal condition between reciprocal base vector and coordinate base vector. The following paragraphs will show how to find a simple component equation by resolving the momentum in directions other than the reciprocal basis directions. To make the problem simple,

suppose the momentum equation is resolved in a two-dimensional coordinate system (ξ^1, ξ^2) (as shown in Figure 2.2.2); then the momentum equation can be written as

$$\vec{M} = M^i \vec{e}_i = 0 \tag{2.4.1}$$

where

$$M^i = (\rho u^i u^j)|_j + p|^i - \gamma^i - \tau^{ij}|_j \qquad (i=1,2) \tag{2.4.2}$$

Naturally and conventionally, the component equations can be found by projecting momentum equation to a contravariant basis $(\vec{e}^1, \vec{e}^2)$, which is the reciprocal basis of coordinate $(\vec{e}_1, \vec{e}_2)$, with the relationship $\vec{e}^i \vec{e}_j = \delta^i_j$.

The two component equations are

$$M^1 = \vec{M} \cdot \vec{e}^1 \tag{2.4.3}$$

$$M^2 = \vec{M} \cdot \vec{e}^2 \tag{2.4.4}$$

Let the two component equations equal zero results in the momentum equations:

$$(\rho u^1 u^j)|_j + p|^1 - \gamma^1 - \tau^{1j}|_j = 0 \tag{2.4.5}$$

$$(\rho u^2 u^j)|_j + p|^2 - \gamma^2 - \tau^{2j}|_j = 0 \tag{2.4.6}$$

The expansion of equations (2.4.5) and (2.4.6) will lead to equation (2.3.2a) in Section 2.3.

Theoretically speaking, the momentum equation can be resolved on any two non-parallel axes. The following derivation will show that resolving the momentum equation on the coordinate axes themselves will make significant of difference.

As the momentum equation is a vector, it can also be written in covariant components:

$$\vec{M} = M_i \vec{e}^{\,i} = 0 \tag{2.4.7}$$

$$M_i = (\rho u_i u^j)|_j + p|_i - \gamma_i - \tau_i^j|_j \qquad (i=1,2) \tag{2.4.8}$$

Then two component equations (refer to Figure 2.4.1) are

$$M_1 = \vec{M} \cdot \vec{e}_1 \tag{2.4.9}$$

$$M_2 = \vec{M} \cdot \vec{e}_2 \tag{2.4.10}$$

Then the momentum equations are

$$(\rho u_1 u^j)|_j + p|_1 - \gamma_1 - \tau_1{}^j|_j = 0 \tag{2.4.11}$$

And

$$(\rho u_2 u^j)|_j + p|_2 - \gamma_2 - \tau_2{}^j|_j = 0 \tag{2.4.12}$$

Expansion of equations (2.4.11) and (2.4.12) requires additional knowledge of tensor analysis. Only the final results are given here. The detailed derivations can be found in the Appendix.

The expansion of the momentum equations (2.4.11), (2.4.12) in a general three-dimensional coordinate system is

$$\frac{1}{\sqrt{g}}\frac{\partial}{\partial \xi^j}(\sqrt{g}\rho u^j u_i) = \frac{1}{\sqrt{g}}\frac{\partial}{\partial \xi^j}(\sqrt{g}\tau_i^j) - \frac{1}{2}\frac{\partial g_{jk}}{\partial \xi^i}(\tau^{jk} - \rho u^j u^k) - \frac{\partial p}{\partial \xi^i} + \gamma_i$$

$$(i=1,2,3) \tag{2.4.13}$$

Where

$$\tau_i^j = \mu_e \varepsilon_i^j - \frac{2}{3}\delta_i^j \rho K \tag{2.4.14}$$

$$\varepsilon_i^j = \frac{\partial u^j}{\partial \xi^i} + g^{jm}\frac{\partial u_i}{\partial \xi^m} + u^m g^{pj}\left(\frac{\partial g_{ip}}{\partial \xi^m} - \frac{\partial g_{im}}{\partial \xi^p}\right) \tag{2.4.15}$$

$$G_e = \frac{1}{2}\nu_t \varepsilon_i^j \varepsilon_j^i \tag{2.4.16}$$

It is obvious that equation (2.4.13) is much simpler than equation (2.3.2a). To expand to the same level, there are only 26 terms in equation (2.4.13) in comparison with 172 terms in equation (2.3.2a). Another advantage of equation (2.4.13) is that there is only one pressure term in each component equation. Obtaining the pressure from a known velocity field by integrating the momentum equation will be straightforward. This is also a good feature for a pressure-correction algorithm.

The following is an explanation of how the new resolution can make the governing equation relatively simple and make the pressure solution easy. Rewrite equation (2.4.13) as

$$\begin{aligned}&\frac{\partial}{\partial \xi^j}(\rho u^j u_i) + \frac{\rho u^j u_i}{\sqrt{g}}\frac{\partial}{\partial \xi^j}(\sqrt{g}) \\ &= \frac{1}{\sqrt{g}}\frac{\partial}{\partial \xi^j}(\sqrt{g}\tau_i^j) - \frac{1}{2}\frac{\partial g_{jk}}{\partial \xi^i}(\tau^{jk} - \rho u^j u^k) - \frac{\partial p}{\partial \xi^i} + \gamma_i\end{aligned} \qquad (i=1,2,3) \tag{2.4.17}$$

Then the pressure increase Δp along coordinate ξ^1 can be found by integrating the momentum equation in the ξ^1 direction:

$$-\Delta p = \Delta(\rho u^1 u_1) + \int_{\Delta\xi^1}\left[\sum_{i\neq j}\frac{\partial}{\partial \xi^j}(\rho u^j u_i) + \frac{\rho u^j u_i}{\sqrt{g}}\frac{\partial}{\partial \xi^j}(\sqrt{g}) - \frac{1}{\sqrt{g}}\frac{\partial}{\partial \xi^j}(\sqrt{g}\tau_i^j) + \frac{1}{2}\frac{\partial g_{jk}}{\partial \xi^i}(\tau^{jk} - \rho u^j u^k) - \gamma_i\right] d\xi^1$$

(i=1,2,3) (2.4.18)

As shown in Figure 2.4.1, $\rho u^1 u_1$ is the flux in ξ^1 direction and the pressure difference Δp is the direct driving force for the flux. This occurs because the momentum equation is resolved along the coordinate axis. Usually this simple expression can only be found in an orthogonal curvilinear coordinate system. In an orthogonal curvilinear coordinate system, the covariant bases and contravariant bases are in the same direction, so the resolution of the momentum equation in an orthogonal curvilinear system will always be along the coordinate axes. That is why equation (2.4.18) looks like the momentum equation in an orthogonal coordinate system.

Other researchers have also tried to find a simpler expression for the momentum equation in a general curvilinear coordinate system. For example, He & Salcudean (1994) derived an integrated expression for the momentum equation by applying the divergence theorem in each cell. The resulting equation is similar to equation (2.3.2a) but it appears that some changes of the metric tensor g^{ij} between cells are neglected there.

Since the continuity equation and the K-ε turbulence model equations are not vector equations, the expansion of them in general curvilinear coordinate system will not depend on the method of resolution.

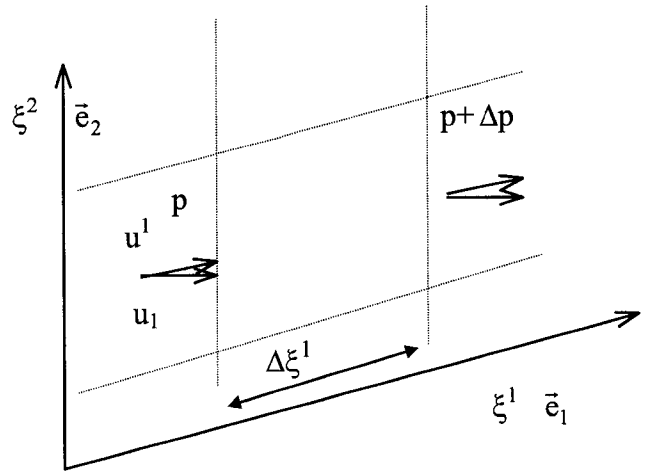

Figure 2.4.1 Pressure and Flux

2.5 Partially Transformed Governing Equations in a General Curvilinear Coordinate System

Partially transformed governing equations are still very popular just because they are simple. If the coordinates do not distort too much from orthogonality, the partially transformed governing equations may be the best choice. In this section the partially transformed governing equations will be derived.

Let x^i, U^i be coordinates and velocity components in a Cartesian coordinate system, and let ξ^i, u^i be their counterparts in a general curvilinear coordinate system. Then the transform from Cartesian coordinates to curvilinear coordinates is as shown below.

First some symbols are defined:

$$\sqrt{g} = \begin{vmatrix} \frac{\partial x}{\partial \xi} & \frac{\partial y}{\partial \xi} & \frac{\partial z}{\partial \xi} \\ \frac{\partial x}{\partial \eta} & \frac{\partial y}{\partial \eta} & \frac{\partial z}{\partial \eta} \\ \frac{\partial x}{\partial \zeta} & \frac{\partial y}{\partial \zeta} & \frac{\partial z}{\partial \zeta} \end{vmatrix} \tag{2.5.1}$$

$$\beta^{j}{}_{i} = \frac{\partial \xi^{j}}{\partial x^{i}} \tag{2.5.2}$$

$$\beta^{ji} = \frac{\partial \xi^{j}}{\partial x_{i}} \tag{2.5.3}$$

It is obvious $\beta^{ji} = \beta^{j}{}_{i}$, because $x^{i}=x_{i}$ in the Cartesian coordinate system.

And it is easy to prove that

$$\frac{\partial(\sqrt{g}\beta^{j}{}_{i})}{\partial \xi^{j}} = 0 \tag{2.5.4}$$

Since

$$\nabla^{2} x^{i} = 0,$$

Then from tensor analysis, one finds

$$\nabla^2 x^i = \frac{1}{\sqrt{g}}\frac{\partial}{\partial \xi^j}(\sqrt{g} g^{jm}\frac{\partial x^i}{\partial \xi^m})$$
$$= \frac{1}{\sqrt{g}}\frac{\partial}{\partial \xi^j}(\sqrt{g}\frac{\partial \xi^j}{\partial x^n}\frac{\partial \xi^m}{\partial x_n}\frac{\partial x^i}{\partial \xi^m})$$
$$= \frac{1}{\sqrt{g}}\frac{\partial}{\partial \xi^j}(\sqrt{g}\frac{\partial \xi^j}{\partial x^n}\delta^{in})$$
$$= \frac{1}{\sqrt{g}}\frac{\partial}{\partial \xi^j}(\sqrt{g}\frac{\partial \xi^j}{\partial x^i})$$
$$= \frac{1}{\sqrt{g}}\frac{\partial}{\partial \xi^j}(\sqrt{g}\beta^j{}_i)$$
$$= 0$$

By applying equations (2.5.2) and (2.5.3), the transformations from Cartesian coordinates to curvilinear coordinates are

$$\frac{\partial f}{\partial x^i} = \beta^j{}_i \frac{\partial f}{\partial \xi^j} = \frac{1}{\sqrt{g}}\frac{\partial}{\partial \xi^j}(\sqrt{g}\beta^j{}_i f) \tag{2.5.5}$$

$$\frac{\partial f}{\partial x_i} = \beta^{ji} \frac{\partial f}{\partial \xi^j} = \frac{1}{\sqrt{g}}\frac{\partial}{\partial \xi^j}(\sqrt{g}\beta^{ji} f) \tag{2.5.6}$$

The relationship between the covariant tensor velocity and the Cartesian velocity is

$$u^i = \beta^i{}_j U^j \tag{2.5.7}$$

With these expressions the governing equation can be converted to the curvilinear coordinate system easily.

In the Cartesian coordinate system, the continuity equation is

$$\frac{\partial(\rho U^j)}{\partial x^j} = 0 \tag{2.5.8}$$

In a curvilinear coordinate system

$$\frac{1}{\sqrt{g}}\frac{\partial}{\partial \xi^j}(\sqrt{g}\rho\beta_i^j U^i) = 0 \tag{2.5.9}$$

Or

$$\frac{1}{\sqrt{g}}\frac{\partial}{\partial \xi^j}(\sqrt{g}\rho u^j) = 0$$

In which u^j is a velocity component in curvilinear coordinate system.

The momentum equation in Cartesian coordinates is

$$\frac{\partial}{\partial x^j}(\rho U^j U^i) = \frac{\partial p}{\partial x_i} + \frac{\partial \tau^{ij}}{\partial x^j} + \gamma^i \tag{2.5.10}$$

To transform each term into the curvilinear coordinate system, one find the following:

$$\begin{aligned}
&\frac{\partial}{\partial x^j}(\rho U^j U^i) \\
&= \frac{1}{\sqrt{g}}\frac{\partial}{\partial \xi^m}(\sqrt{g}\beta_j^m \rho U^j U^i) \\
&= \frac{1}{\sqrt{g}}\frac{\partial}{\partial \xi^j}(\sqrt{g}\rho u^j U^i)
\end{aligned} \tag{2.5.11}$$

$$\frac{\partial p}{\partial x_i} = \beta^{ji}\frac{\partial p}{\partial \xi^j} \tag{2.5.12}$$

$$\tau^{ij} = \mu_e \varepsilon^{ij} - \frac{2}{3}\delta^{ij}\rho K \tag{2.5.13}$$

$$\begin{aligned} \varepsilon^{ij} &= \frac{\partial U^i}{\partial x_j} + \frac{\partial U^j}{\partial x_i} \\ &= \beta^{mj}\frac{\partial U^i}{\partial \xi^m} + \beta^{mi}\frac{\partial U^j}{\partial \xi^m} \end{aligned} \tag{2.5.14}$$

Substituting equations (2.5.13) and (2.5.14) into the shear stress term results in

$$\frac{\partial \tau^{ij}}{\partial x^j} = \frac{1}{\sqrt{g}}\frac{\partial}{\partial \xi^k}\left[\sqrt{g}\beta^k{}_j\mu_e\left(\beta^{mj}\frac{\partial U^i}{\partial \xi^m} + \beta^{mi}\frac{\partial U^j}{\partial \xi^m}\right) - \frac{2}{3}\sqrt{g}\beta^k{}_j\delta^{ij}\rho K\right] \tag{2.5.15}$$

By using the metric tensor $g^{km} = \beta^k{}_j\beta^{mj}$, equation (2.5.15) can also be written as

$$\frac{\partial \tau^{ij}}{\partial x^j} = \frac{1}{\sqrt{g}}\frac{\partial}{\partial \xi^k}\left[\sqrt{g}\mu_e\left(g^{km}\frac{\partial U^i}{\partial \xi^m} + \beta^k{}_j\beta^{mi}\frac{\partial U^j}{\partial \xi^m}\right) - \frac{2}{3}\sqrt{g}\beta^{ki}\rho K\right] \tag{2.5.16}$$

The final momentum equations are then

$$\begin{aligned} &\frac{1}{\sqrt{g}}\frac{\partial}{\partial \xi^j}(\sqrt{g}\rho u^j U^i) \\ &= \frac{1}{\sqrt{g}}\frac{\partial}{\partial \xi^j}\left[\sqrt{g}\mu_e\left(g^{jm}\frac{\partial U^i}{\partial \xi^m} + \beta^j{}_k\beta^{mi}\frac{\partial U^k}{\partial \xi^m}\right) - \frac{2}{3}\sqrt{g}\beta^{ji}\rho K\right] - \beta^{ji}\frac{\partial p}{\partial \xi^j} + \gamma^i \end{aligned} \tag{2.5.17}$$

This equation is much simpler than the momentum equation in Section 2.3, because the velocity components will not change direction.

The K-ε turbulence model equations should be of the same form as the fully transformed equations (2.3.3a), (2.3.4a), because they are scalar equations.

$$\frac{1}{\sqrt{g}}\frac{\partial}{\partial \xi^j}(\sqrt{g}\Gamma_k u^j K) = \frac{1}{\sqrt{g}}\frac{\partial}{\partial \xi^j}(\sqrt{g}\Gamma_k\, g^{jm}\frac{\partial K}{\partial \xi^m}) + \rho G_e - \rho\varepsilon \qquad (2.5.18)$$

$$\frac{1}{\sqrt{g}}\frac{\partial}{\partial \xi^j}(\sqrt{g}\Gamma_\varepsilon u^j \varepsilon) = \frac{1}{\sqrt{g}}\frac{\partial}{\partial \xi^j}(\sqrt{g}\Gamma_\varepsilon\, g^{jm}\frac{\partial \varepsilon}{\partial \xi^m}) + C_1\rho G_e\frac{\varepsilon}{K} - C_2\rho\frac{\varepsilon}{K^2} \qquad (2.5.19)$$

2.6 Comparison of Three Kinds of Governing Equations

2.6.1 Benchmark Tests

There have been very few studies about different forms of the governing equations and their possible effects on numerical results. In a paper by Sotiropoulos et al. (1994) the difference between fully transformed and partially transformed governing equations was mentioned, but no detailed study and comparison were made. In the present study, the solution of a benchmark flow problem is used to demonstrate the difference between the three kinds of governing equations discussed in the previous sections. This benchmark solution was proposed by Demirdzic, Lilek and Peric (1992). It is a skewed-driven cavity flow problem. As shown in Figure 2.6.1, the domain of the flow is a parallelogram. On all boundaries except the top boundary, the velocities are zero. On the top boundary, the velocity is parallel to x-axis with a unit magnitude. Two sets of results are available with angle α equal to 30 degrees and 45 degrees. The flow Reynolds number varies from 100 to 1000. The "exact results" given in this reference are also numerical results obtained by a finite volume method with a very fine grid (Demirdzic and Peric, 1990). This benchmark result has also been tested by other researchers (Oosterlee et al., 1993).

The test calculation was made in a non-orthogonal coordinate system (ξ, η) shown in Figure 2.6.2.

The transformation to this coordinate system is

$$\begin{cases} x = a\xi & a = \cos\beta \\ y = b\xi + \eta & b = \sin\beta \end{cases} \tag{2.6.1}$$

In this coordinate system

$$\begin{bmatrix} x_\xi & x_\eta \\ y_\xi & y_\eta \end{bmatrix} = \begin{bmatrix} a & 0 \\ b & 1 \end{bmatrix}$$

$$\begin{bmatrix} \beta^1{}_1 & \beta^1{}_2 \\ \beta^2{}_1 & \beta^2{}_2 \end{bmatrix} = \begin{bmatrix} \xi_x & \xi_y \\ \eta_x & \eta_y \end{bmatrix} = \begin{bmatrix} 1/a & 0 \\ -b/a & 1 \end{bmatrix}$$

$$\sqrt{g} = \begin{vmatrix} x_\xi & x_\eta \\ y_\xi & y_\eta \end{vmatrix} = a$$

$$\begin{bmatrix} g_{11} & g_{12} \\ g_{21} & g_{22} \end{bmatrix} = \begin{bmatrix} 1 & b \\ b & 1 \end{bmatrix}$$

$$\begin{bmatrix} g^{11} & g^{12} \\ g^{21} & g^{22} \end{bmatrix} = \frac{1}{a^2} \begin{bmatrix} 1 & -b \\ -b & 1 \end{bmatrix}$$

Let velocities (U, V) be Cartesian coordinate components, and let velocity components u^i, u_i be the contravariant and covariant components, respectively. The relationships between the velocity components are:

$$\begin{cases} u_1 = u^1 + bu^2 \\ u_2 = bu^1 + u^2 \end{cases} \tag{2.6.2}$$

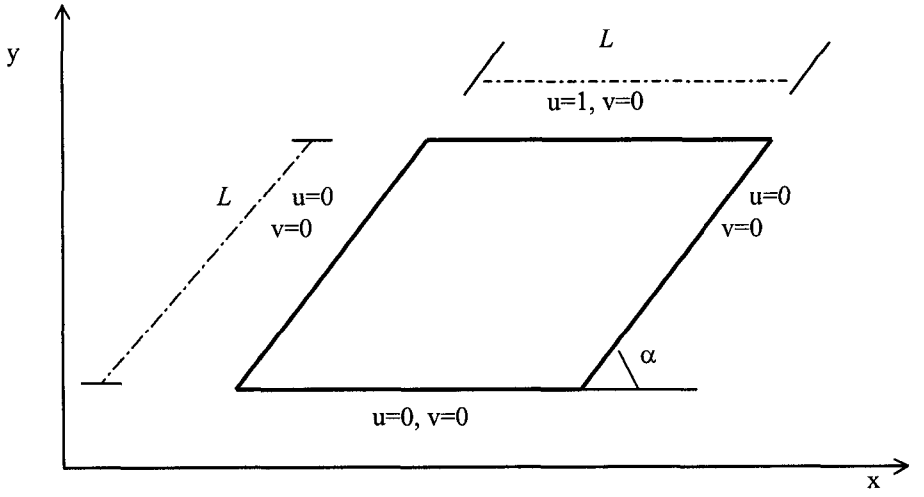

Figure 2.6.1 Skewed Driven Cavity Flow

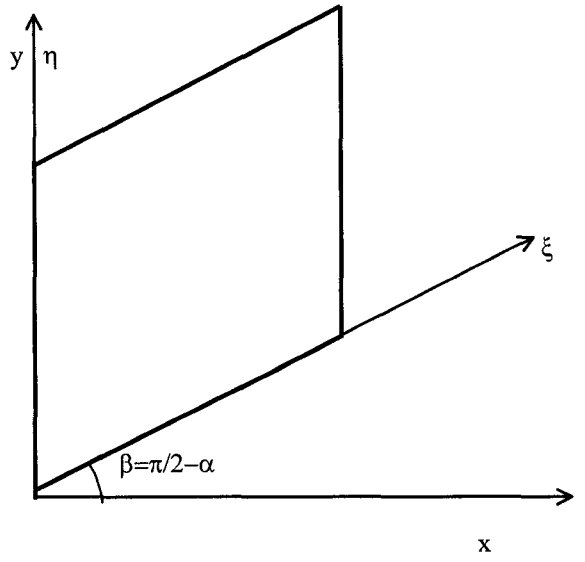

Figure 2.6.2 Non-Orthogonal Coordinate System (ξ, η)

$$\begin{cases} u^1 = \dfrac{U}{a} \\ u^2 = V - \dfrac{b}{a}U \end{cases} \tag{2.6.3}$$

$$\begin{cases} u_1 = aU + bV \\ u_2 = V \end{cases} \tag{2.6.4}$$

The expressions for the force of gravity in the different coordinate systems are

Cartesian:

$$\begin{cases} F^1 = 0 \\ F^2 = -\gamma \end{cases} \tag{2.6.5}$$

Contravariant:

$$\begin{cases} f^1 = 0 \\ f^2 = -\gamma \end{cases} \tag{2.6.6}$$

Covariant:

$$\begin{cases} f_1 = g_{11}f^1 + g_{12}f^2 = -b\gamma \\ f_2 = g_{21}f^1 + g_{22}f^2 = -\gamma \end{cases} \tag{2.6.7}$$

With these expressions the three kinds of governing equations in this coordinate system can be derived. The benchmark flow is laminar flow. The governing equations thus include only continuity and momentum equations.

A. Conventional governing equation

Continuity equation

$$\frac{\partial}{\partial \xi}(\rho u^1) + \frac{\partial}{\partial \eta}(\rho u^2) = 0 \tag{2.6.8}$$

Momentum equations

$$\frac{\partial}{\partial \xi}(\rho u^1 u^1) + \frac{\partial}{\partial \eta}(\rho u^2 u^1)$$
$$= \frac{\mu}{a^2}\left(\frac{\partial^2 u^1}{\partial \xi^2} - 2b\frac{\partial^2 u^1}{\partial \xi \partial \eta} + \frac{\partial^2 u^1}{\partial \eta^2}\right) + f^1 - \frac{1}{a^2}\frac{\partial p}{\partial \xi} + \frac{b}{a^2}\frac{\partial p}{\partial \eta} \tag{2.6.9}$$

$$\frac{\partial}{\partial \xi}(\rho u^1 u^2) + \frac{\partial}{\partial \eta}(\rho u^2 u^2)$$
$$= \frac{\mu}{a^2}\left(\frac{\partial^2 u^2}{\partial \xi^2} - 2b\frac{\partial^2 u^2}{\partial \xi \partial \eta} + \frac{\partial^2 u^2}{\partial \eta^2}\right) + f^2 - \frac{1}{a^2}\frac{\partial p}{\partial \eta} + \frac{b}{a^2}\frac{\partial p}{\partial \xi} \tag{2.6.10}$$

B. Concise form of governing equation

Continuity equation

$$\frac{\partial}{\partial \xi}(\rho u^1) + \frac{\partial}{\partial \eta}(\rho u^2) = 0 \tag{2.6.11}$$

Momentum equations

$$\frac{\partial}{\partial \xi}(\rho u^1 u_1) + \frac{\partial}{\partial \eta}(\rho u^2 u_1)$$
$$= \frac{\mu}{a^2}\left(\frac{\partial^2 u_1}{\partial \xi^2} - 2b\frac{\partial^2 u_1}{\partial \xi \partial \eta} + \frac{\partial^2 u_1}{\partial \eta^2}\right) + f_1 - \frac{\partial p}{\partial \xi} \tag{2.6.12}$$

$$\frac{\partial}{\partial\xi}(\rho u^1 u_2)+\frac{\partial}{\partial\eta}(\rho u^2 u_2)$$
$$=\frac{\mu}{a^2}\left(\frac{\partial^2 u_2}{\partial\xi^2}-2b\frac{\partial^2 u_2}{\partial\xi\partial\eta}+\frac{\partial^2 u_2}{\partial\eta^2}\right)+f_2-\frac{\partial p}{\partial\eta} \tag{2.6.13}$$

C. Partially transformed governing equations

Continuity equation

$$\frac{\partial}{\partial\xi}(\rho U)+\frac{\partial}{\partial\eta}[\rho(aV-bU)]=0 \tag{2.6.14}$$

Momentum equations

$$\frac{\partial}{\partial\xi}(\rho UU)+\frac{\partial}{\partial\eta}[\rho(aV-bU)U]$$
$$=\frac{\mu}{a}\left(\frac{\partial^2 U}{\partial\xi^2}-2b\frac{\partial^2 U}{\partial\xi\partial\eta}+\frac{\partial^2 U}{\partial\eta^2}\right)+F_1-\frac{\partial p}{\partial\xi}+b\frac{\partial p}{\partial\eta} \tag{2.6.15}$$

$$\frac{\partial}{\partial\xi}(\rho UV)+\frac{\partial}{\partial\eta}[\rho(aV-bU)V]$$
$$=\frac{\mu}{a}\left(\frac{\partial^2 V}{\partial\xi^2}-2b\frac{\partial^2 V}{\partial\xi\partial\eta}+\frac{\partial^2 V}{\partial\eta^2}\right)+F_2-a\frac{\partial p}{\partial\eta} \tag{2.6.16}$$

Because this coordinate system is not a curvilinear coordinate system, there is no obvious indication which governing equation is simpler, but the difference in pressure term is shown. In the concise governing equation, only one pressure gradient term exists in each momentum equation.

2.6.2 Comparison of Results and Conclusions

First the three different governing equations described in section (2.6.1) are solved with the same resolution on a 92*92 grid. The three kinds of governing equations, the conventional fully transformed equations, the concise form of the fully transformed equations and partially transformed equations are referred to as equations A, equations B and equations C respectively hereafter. From numerical tests, the deviation in numerical results caused by the non-alignment of a velocity component with the coordinate axis or by the different pressure solution procedures can be found.

Figures 2.6.3, 2.6.4 show the velocities u, v along two centerlines $\eta = \frac{1}{2}L$ and $\xi = \frac{1}{2}L$. The solid line is a calculated result from equations A, while points are reference data from Demirdzic et al., (1992). It shows that the results fit very well. Figures 2.6.5 to 2.6.8 give similar comparisons between results calculated by equations B and C and benchmark data.

Although the three governing equations give very similar results at this resolution, careful study shows that equations A give the best results. Equations B show a slight deviation in the region near = 0.85. The transformation between contravariant velocities and covariant velocities may be one reason for this deviation. Because staggered grids are used in the calculation, the contravariant velocities must be calculated from the average of the covariant velocities of four neighboring nodes. When the resolution increases to 128*128, as shown in Figures 2.6.9 and 2.6.10, this deviation disappears.

Figures 2.6.7 and 2.6.8 show that equations C give less accurate results than do equations A or B, especially for velocity component v. The error may come from the pressure solution procedure and velocity transformation. This error can also be

partially removed by increasing the resolution. Figures 2.6.11 and 2.6.12 show a better agreement between the calculated velocities from equations C and the reference data when the grid sizes increases to 128*128.

Equations C have another limitation. In the second test case when α equals 30 degrees, and then the angle between velocity U and coordinate ξ is 60 degrees, the equations C can not produce a converged solution, while equations A or B still work well. Figures 2.6.13 to 2.6.16 show the results calculated by equations A and B when α equals 30 degrees with a 128*128 grid. These calculated results fit the reference data very well.

These results demonstrate the advantage of equations B. So long as the errors from the transformation between contravariant velocities and covariant velocities are removed by applying a reasonably fine grid or a non-staggered grid, equations B can produce the same good results as equations A.

Equations C can produce fairly good results, if the grid is not excessively distorted. The balance between computational effort and computation accuracy should be adjusted according to practical requirements.

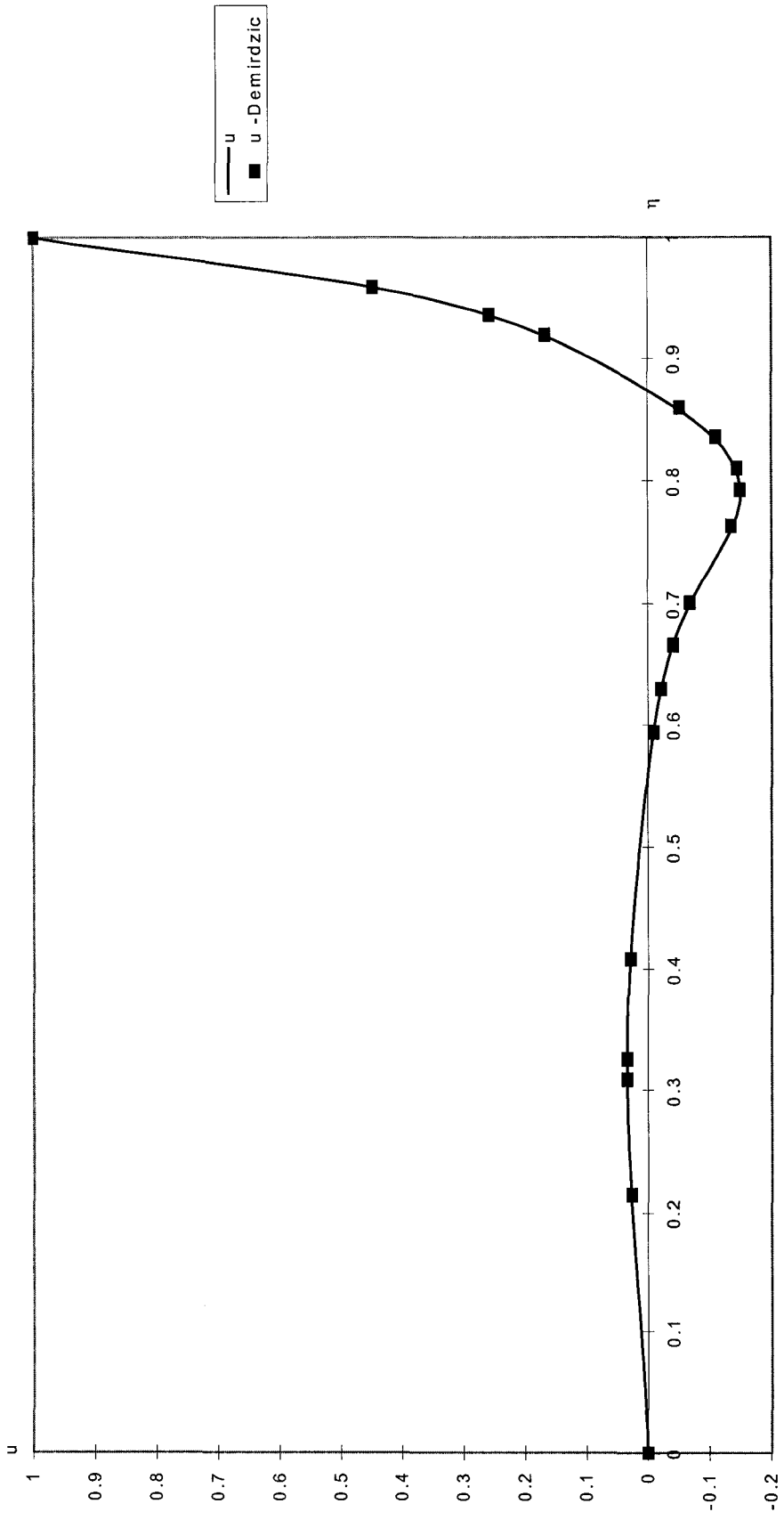

Figure 2.6.3 Velocity Component u, Calculated by Fully Transformed Equations, 92*92 Grid

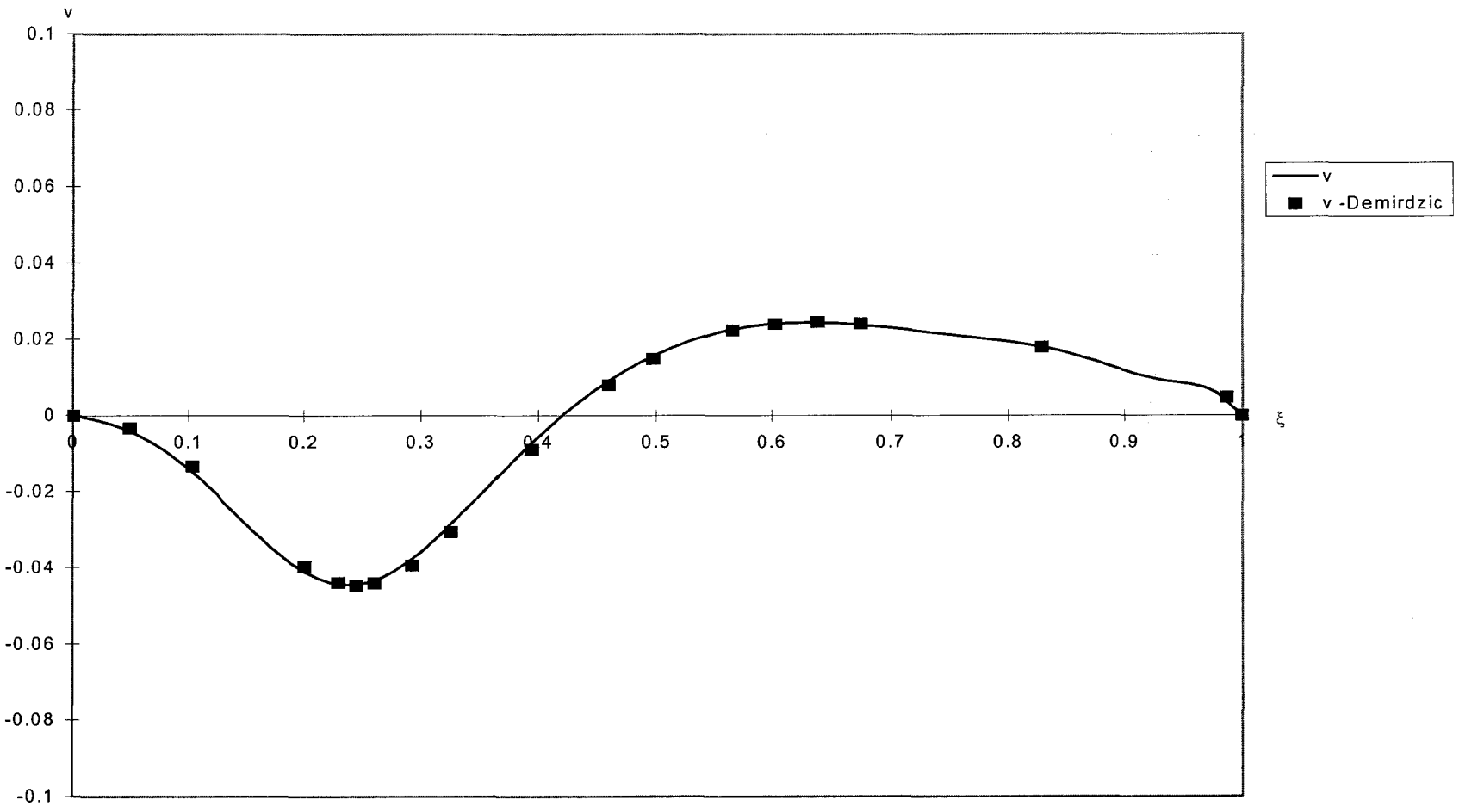

Figure 2.6.4 Velocity Component v, Calculated by Fully Transformed Equations, 92*92 Grid

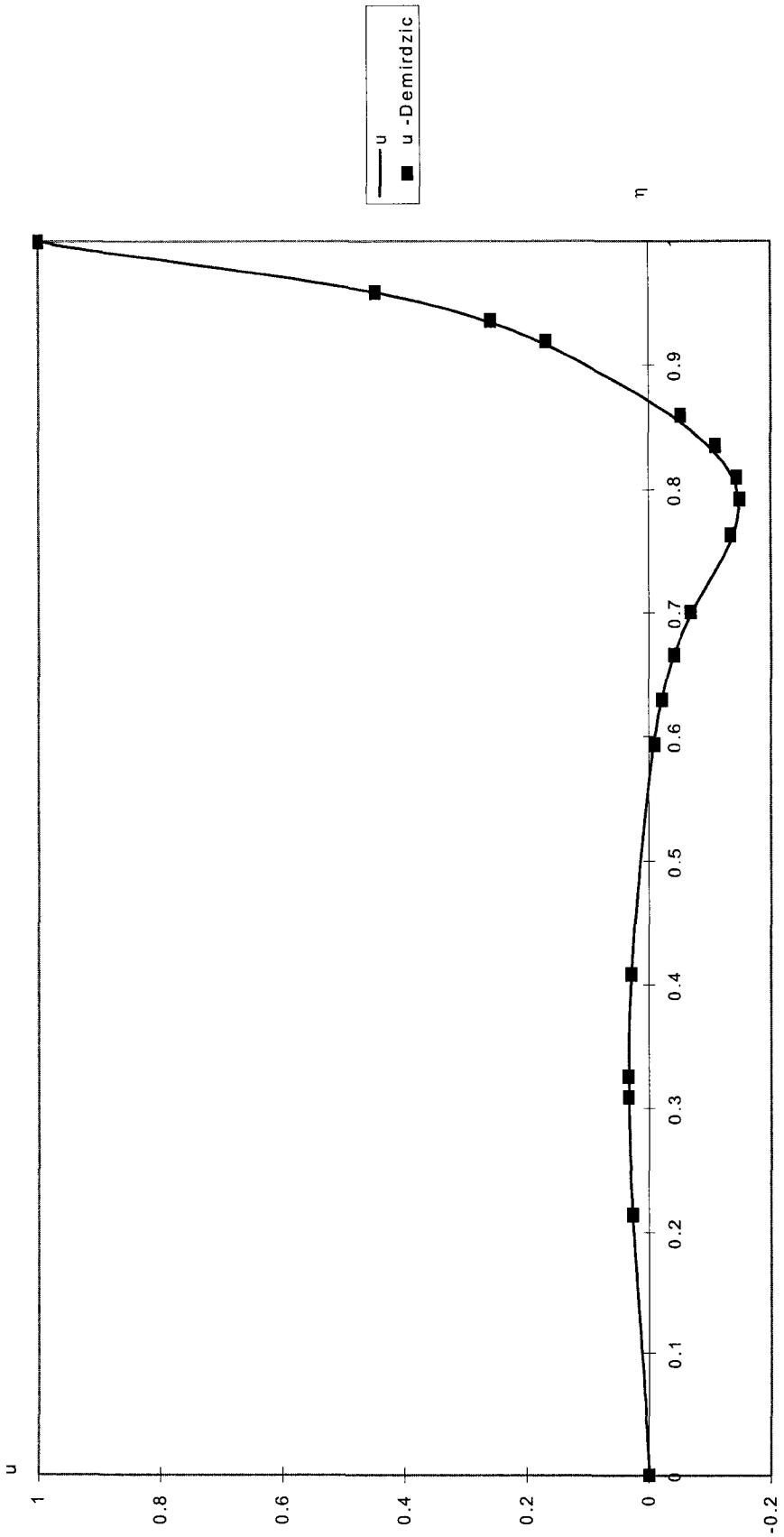

Figure 2.6.5 Velocity Component u, Calculated by Concise Fully Transformed Equations, 92*92 Grid

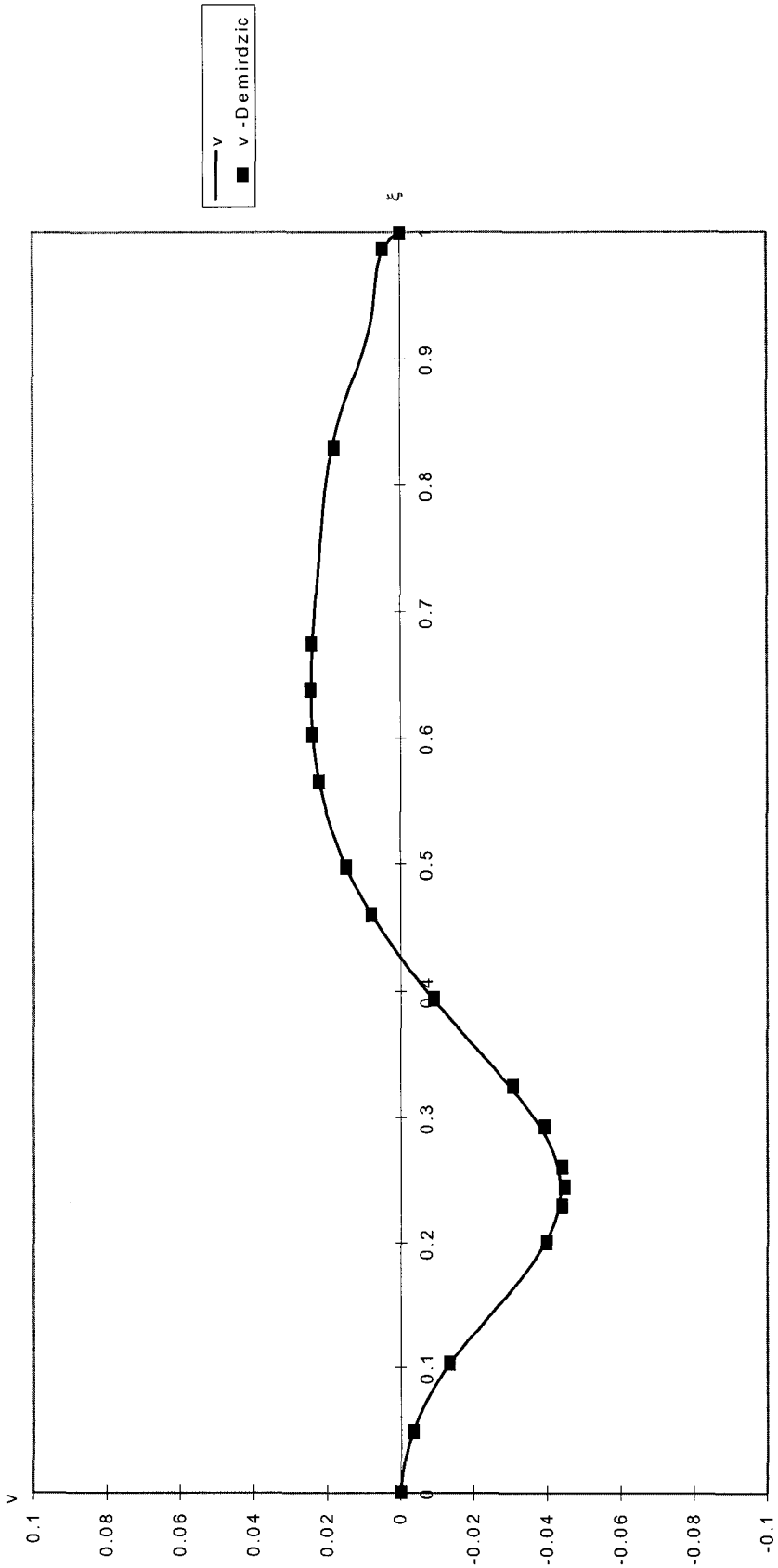

Figure 2.6.6 Velocity Component v, Calculated by Concise Fully Transformed Equations, 92*92 Grid

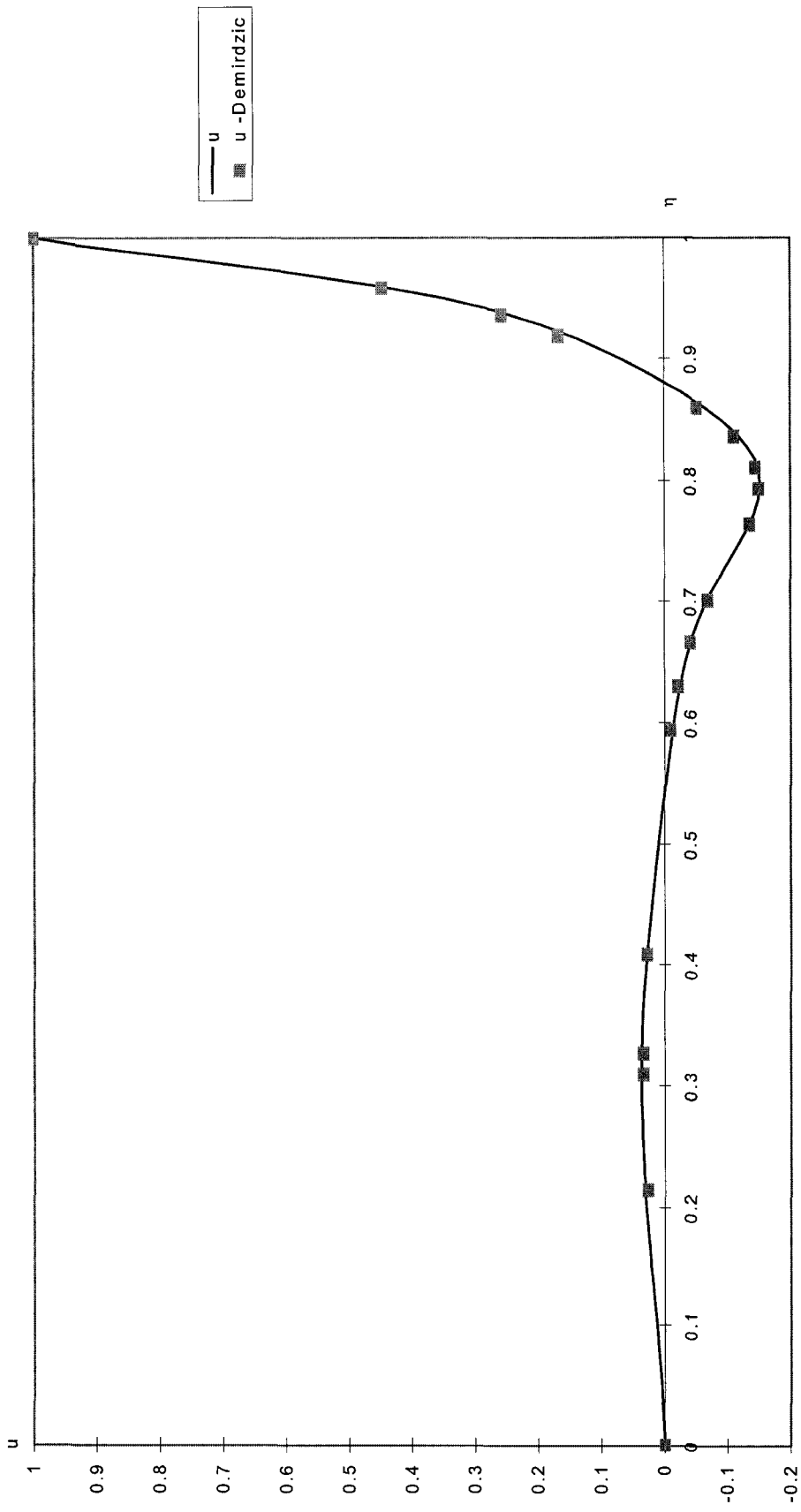

Figure 2.6.7 Velocity Component u, Calculated by Partially Transformed Equations, 92*92 Grid

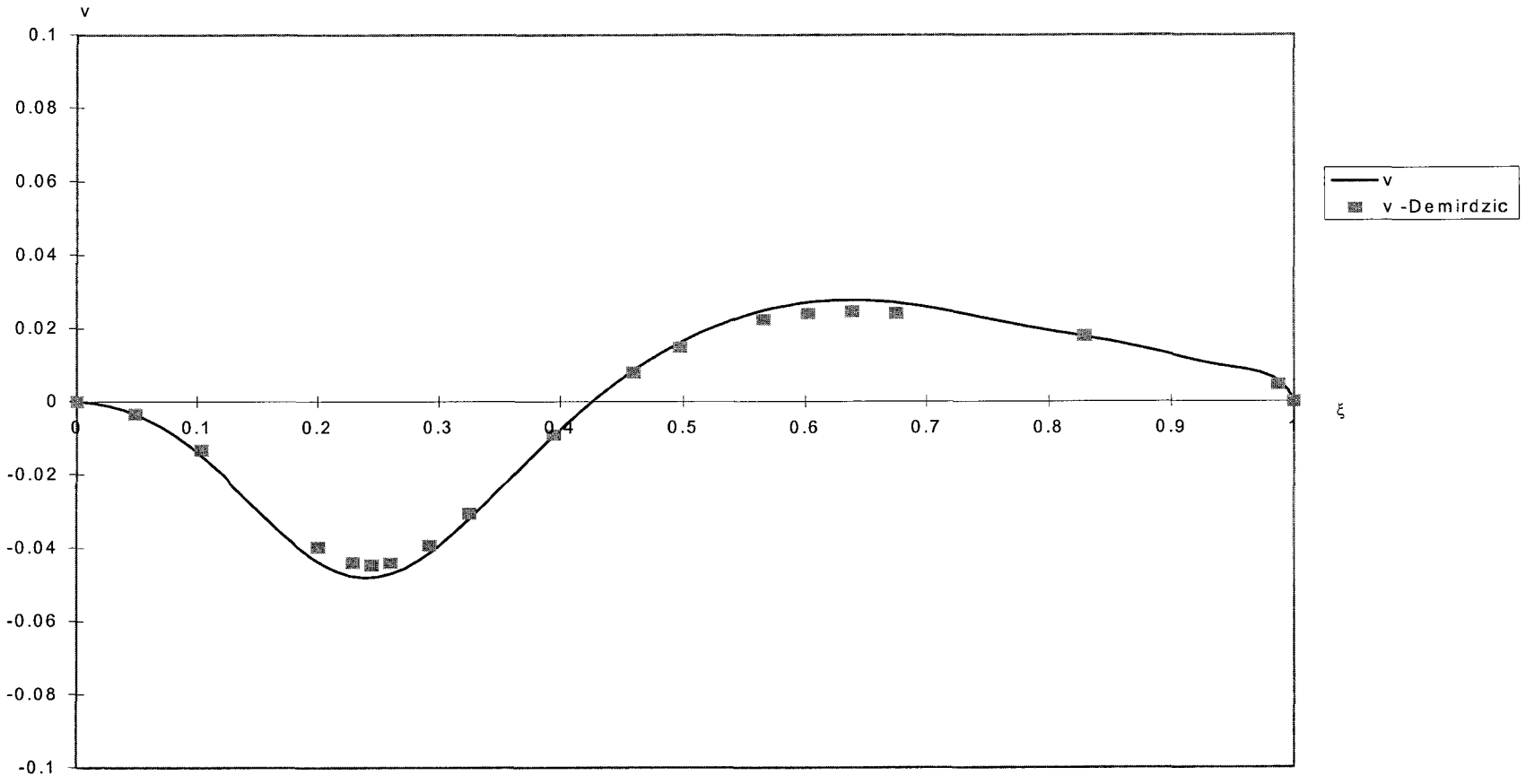

Figure 2.6.8 Velocity Component v, Calculated by Partially Transformed Equations, 92*92 Grid

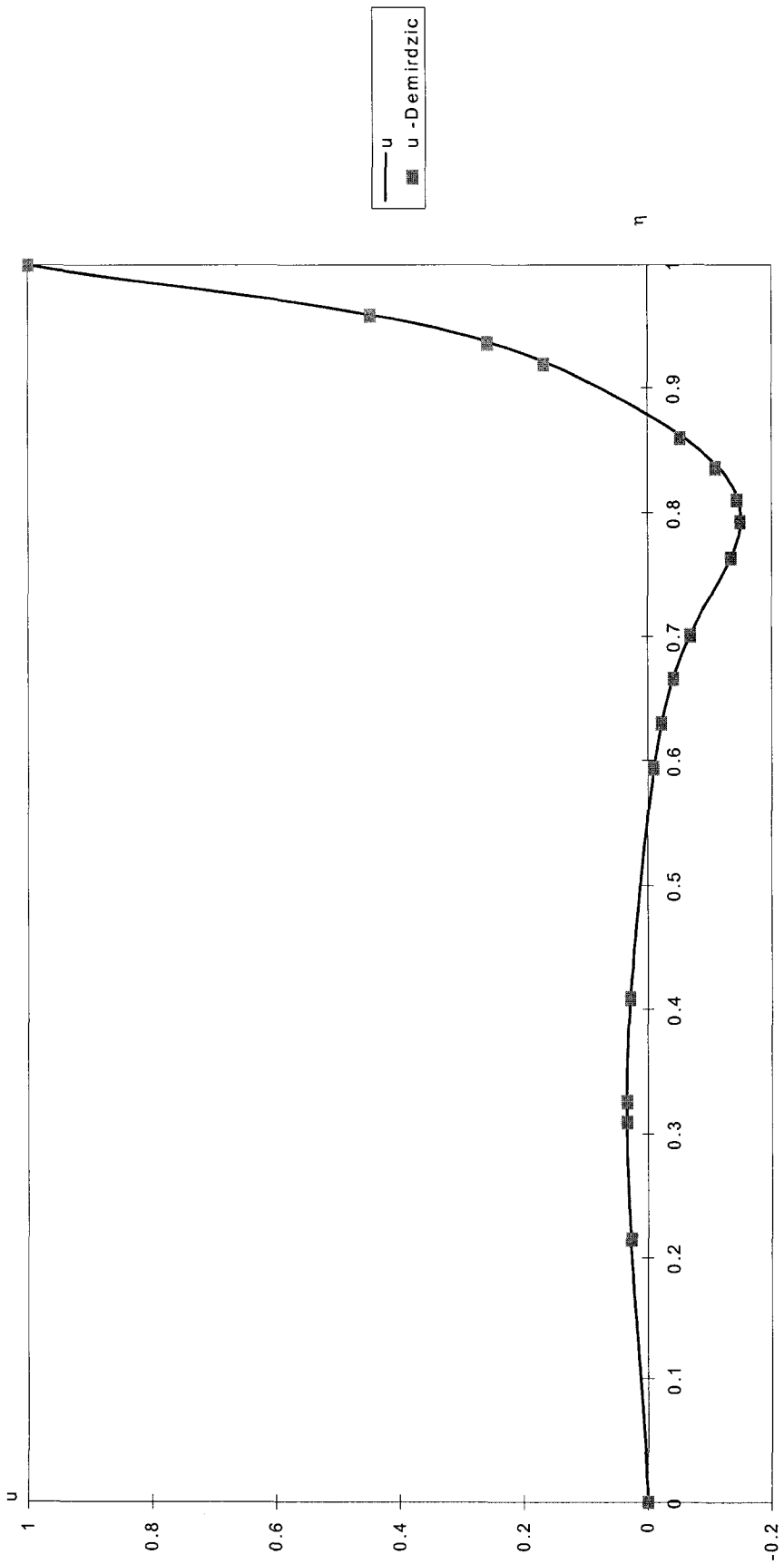

Figure 2.6.9 Velocity Component u, Calculated by Concise Fully Transformed Equations, 128*128 Grid

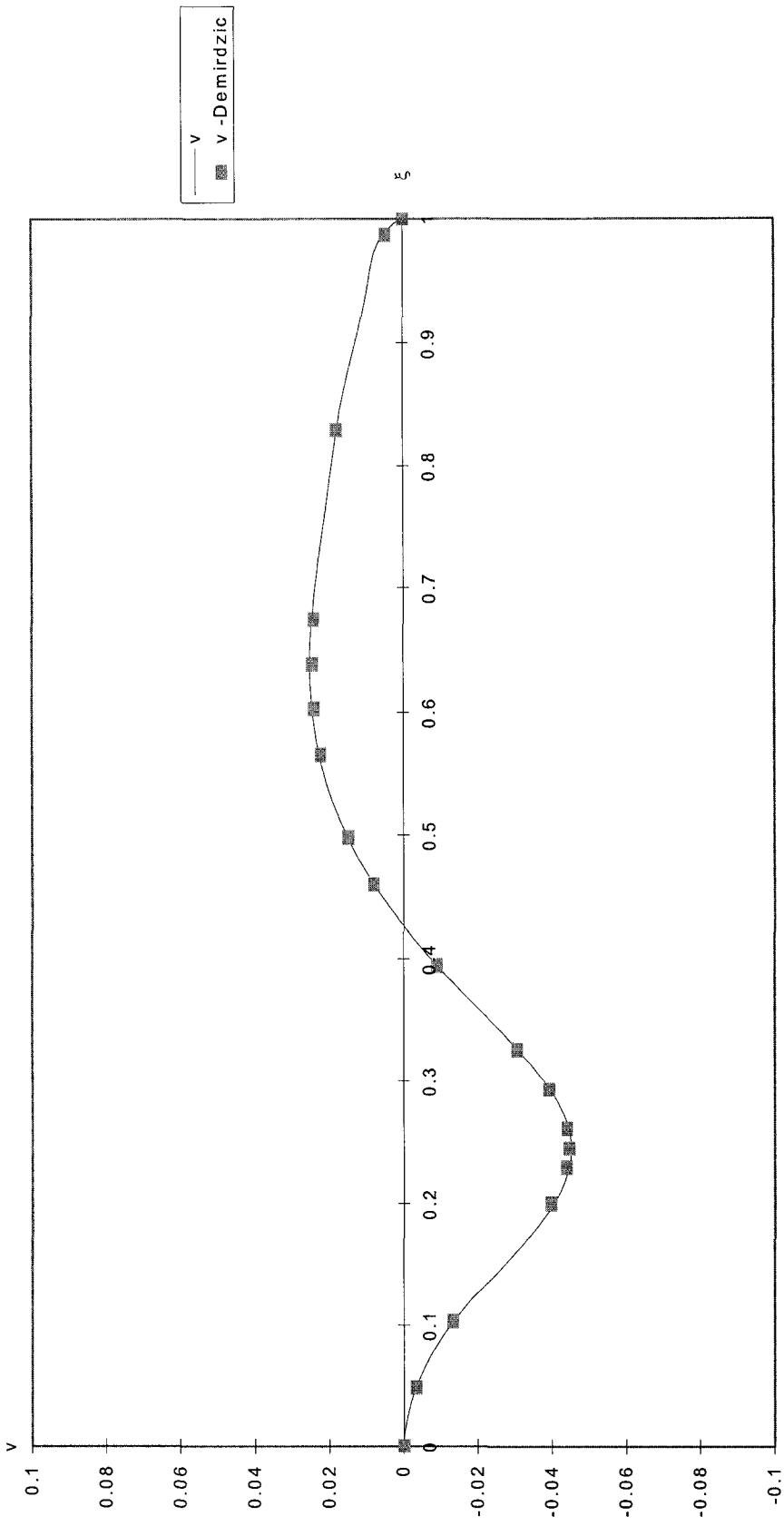

Figure 2.6.10 Velocity Component v, Calculated by Concise Fully Transformed Equations, 128*128 Grid

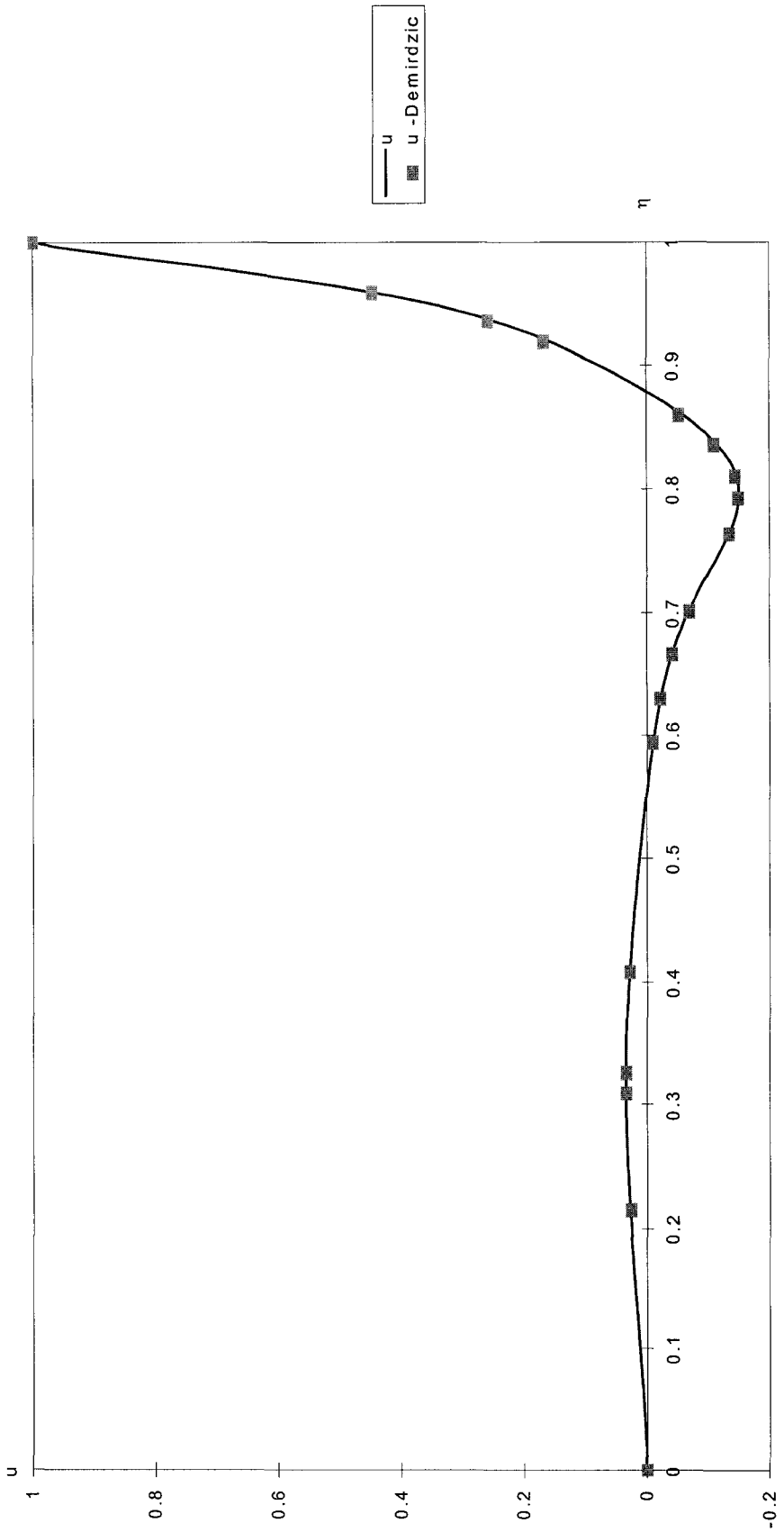

Figure 2.6.11 Velocity Component u, Calculated by Partially Transformed Equations, 128*128 Grid

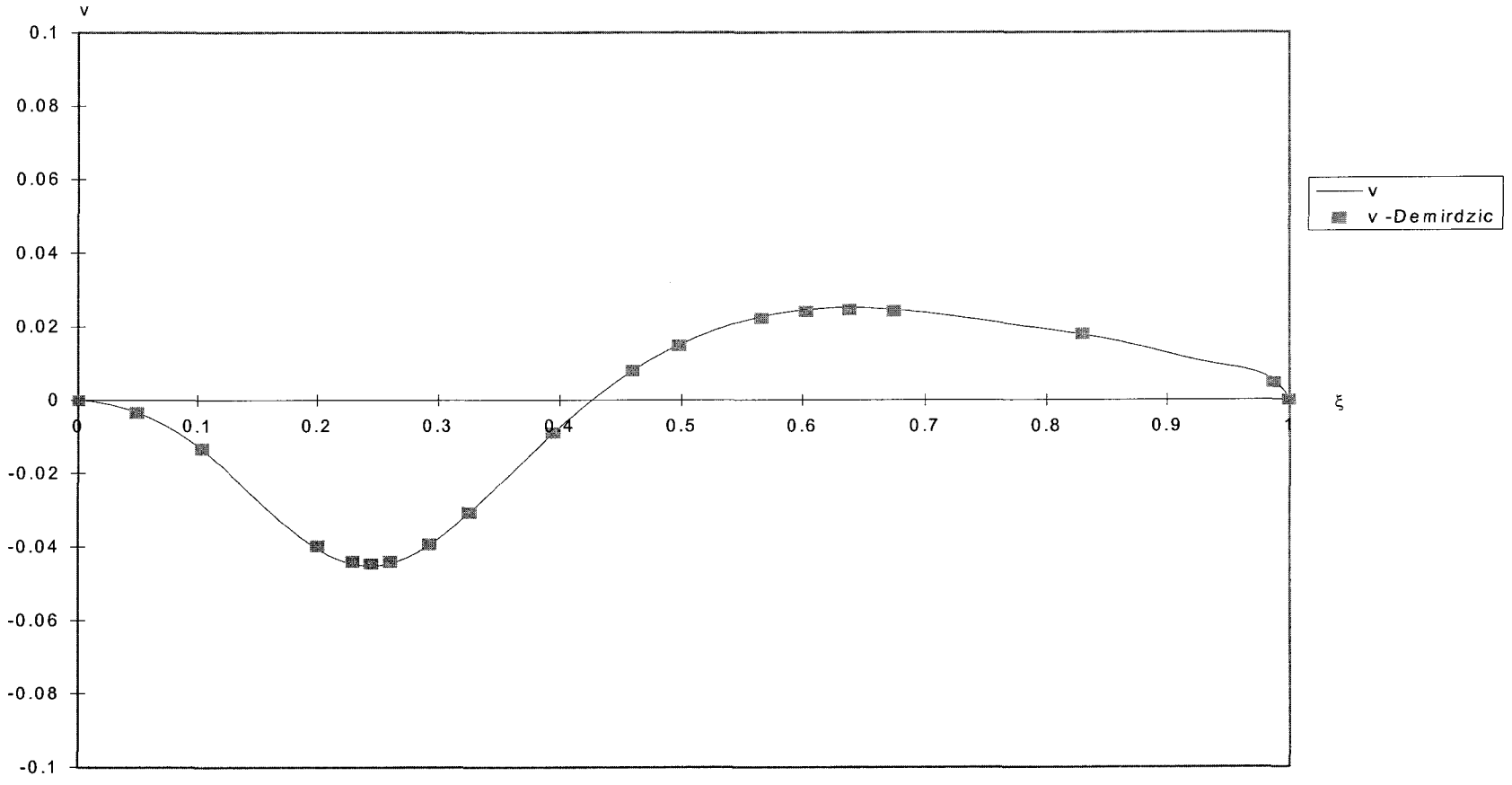

Figure 2.6.12 Velocity Component v, Calculated by Partially Transformed Equations, 128*128 Grid

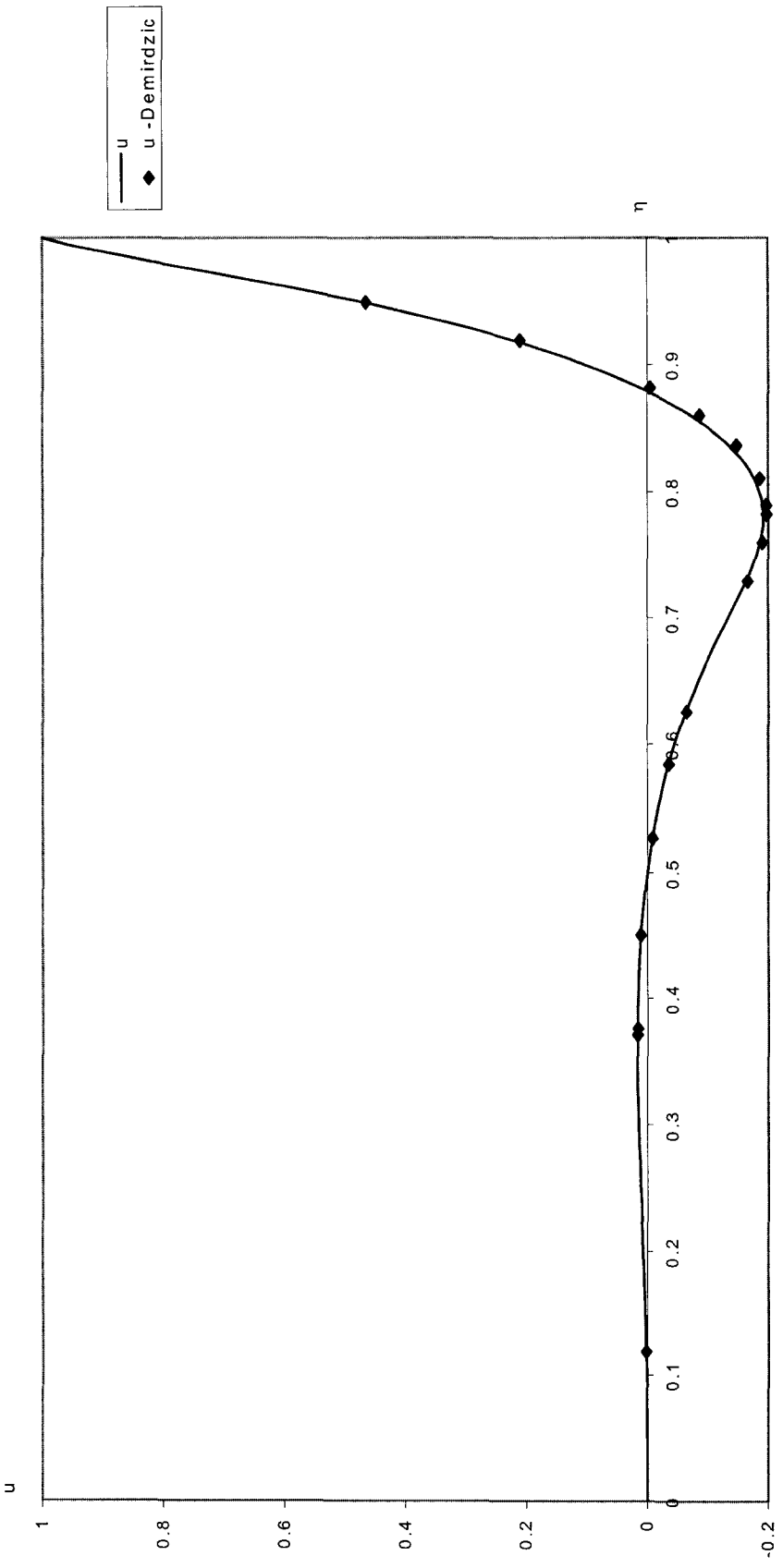

Figure 2.6.13 Velocity u, Calculated by Fully Transformed Equations, 128*128 Grid, $\alpha=30^0$

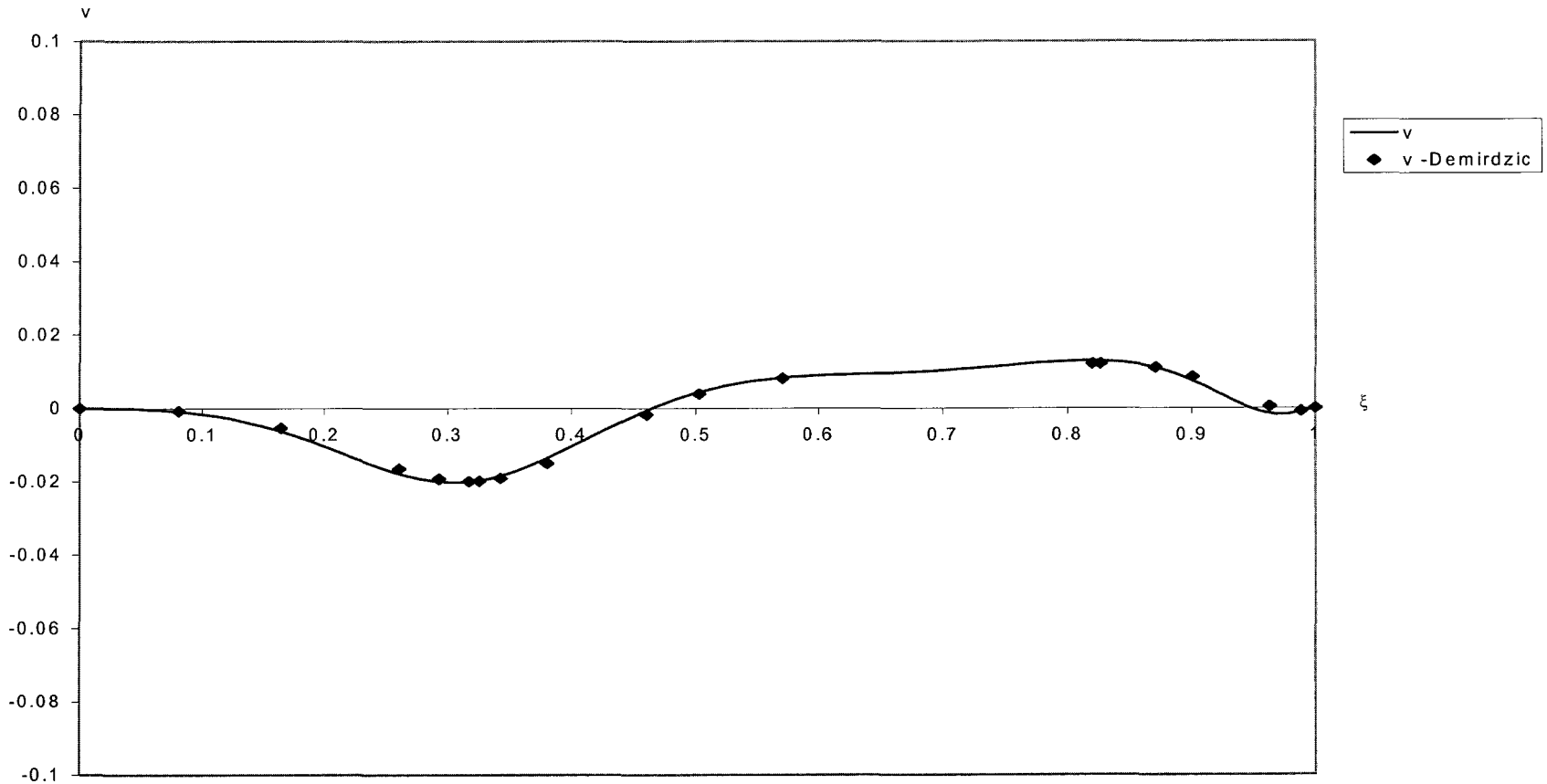

Figure 2.6.14 Velocity v, Calculated by Fully Transformed Equations, 128*128 Grid, $\alpha=30^{o}$

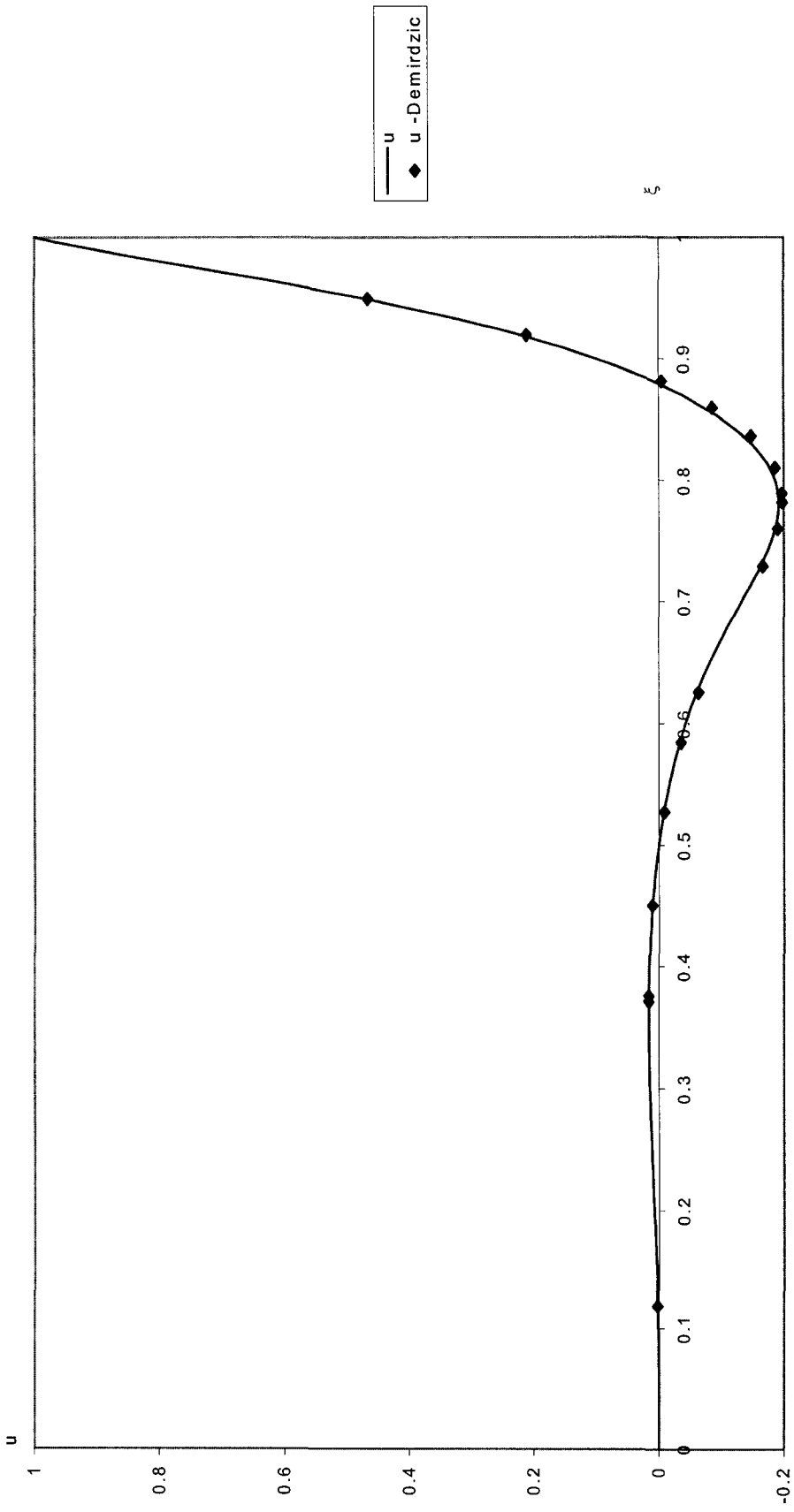

Figure 2.6.15 Velocity u, Calculated by Concise Fully Transformed Equations, 128*128 Grid, $\alpha=30^{\circ}$

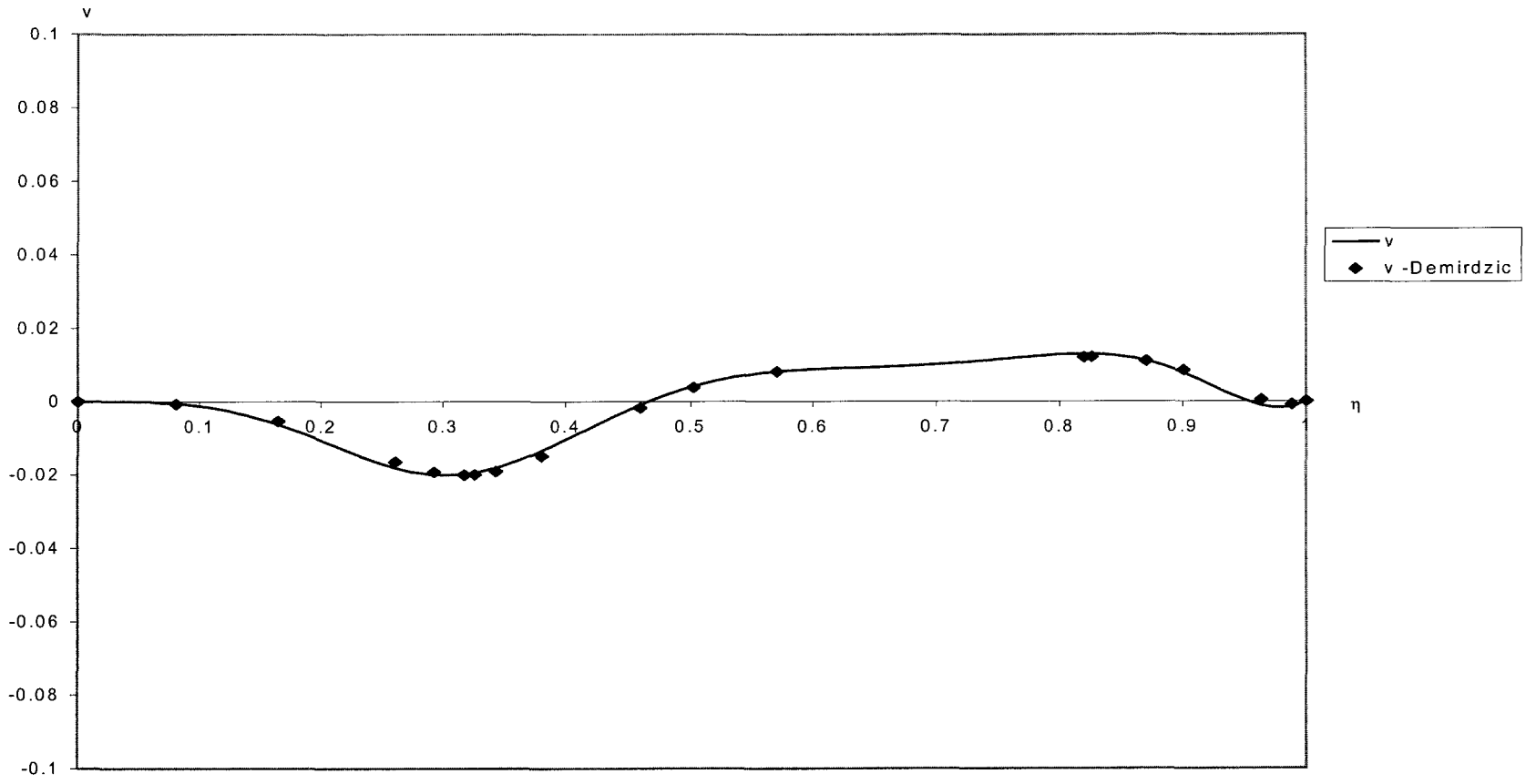

Figure 2.6.16 Velocity v, Calculated by Concise Fully Transformed Equations, 128*128 Grid, $\alpha=30^{o}$

Chapter 3

Numerical Procedures

Free surface flow around large obstacles is a difficult subject with unique properties. A special numerical model should be built to handle this problem efficiently. Detailed derivations and numerical tests should be conducted before the numerical model is built. In this chapter, the coordinate system, numerical difference schemes, the numerical discretization method, the pressure solution procedure, the free surface tracking and obstacle modeling will be studied.

3.1 Difference Schemes

Simulation of the convection in a fluid flow is a challenging problem, because a delicate balance between accuracy and stability must be established. This may be done by choosing a proper difference scheme. For example, a centered difference is second order accurate but may cause instability. A first order upwind scheme has the advantage of unconditional stability. However, it is only first order accurate and may cause numerical diffusion.

A few years ago the Power Law difference scheme (Patankar, 1980) was the most popular scheme because it could always produce smooth and stable results. The Power Law difference scheme is a scheme that switches dynamically within the envelope of upwind, exponential and centered difference schemes according to the flow direction and the ratio between convection and diffusion. When convection is dominant, it reduces to a first order upwind difference. When diffusion is dominant, it reduces to a centered difference. In between, it approximates an exponential difference scheme. More recently it was found that the Power Law scheme might

smear sharp changes in a numerical result and has low accuracy (Leonard and Mokhtari, 1990).

To improve the accuracy of upwind difference schemes, Leonold proposed a QUICK (Quadratic Upwind Interpolation for Convective Kinematics) scheme (Leonard, 1979). In the QUICK scheme, at least four nodes, biased toward the upwind direction, are used in the difference. With four nodes, a scheme with third-order accuracy can be constructed, and the upwinding bias will ensure unconditional stability. The only problem for this scheme is the possibility of oscillations or overshooting when the Reynolds number is high. To fix this problem, a number of limiters have been developed, such as SHARP (Leonard, 1988), SMART (Gaskell and Lau, 1988) and UMIST (Lien and Leschziner, 1994a). These limiters are used to find an application range in which QUICK will not cause oscillations. Outside this range other lower order difference schemes such as a simple upwind scheme are applied.

Usually the QUICK scheme is used on a uniform grid. When computation capacity is limited, a non-uniform grid may be necessary. In the next section a QUICK scheme with a UMIST (Upstream Monotonic Interpolation for Scalar Transport) limiter on a non-uniform grid is derived.

3.1.1 QUICK Difference Scheme with UMIST Limiter in Non-uniform Grids

The difference between various difference schemes is how the value at the surface of a control volume is interpolated. Referring to Figure 3.1.1, a QUICK scheme can be derived in the following way.

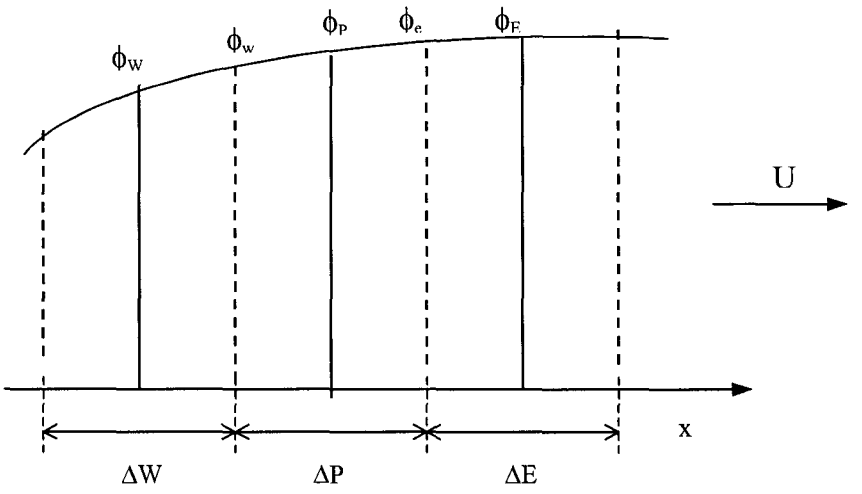

Figure 3.1.1 QUICK Difference Scheme

(i) Suppose the velocity U>0 then the value of ϕ at node e can be written as

$$\bar{\phi}_e^+ = \bar{\phi}_p + \frac{f(r_e^+)}{2}(1-\bar{\phi}_p) \tag{3.1.1}$$

Where sign "+" denotes the velocity is positive, and

$$\bar{\phi}_e^+ = \frac{\phi_e - \phi_W}{\phi_E - \phi_W} \qquad \bar{\phi}_P = \frac{\phi_P - \phi_W}{\phi_E - \phi_W} \tag{3.1.2}$$

$$r_e^+ = \frac{\phi_P - \phi_W}{\phi_E - \phi_P} \tag{3.1.3}$$

To find an appropriate expression for $f(r_e^+)$, a parabolic interpolation is used, such as $\bar{\phi} = a\xi + b\xi^2$, where ξ is the local coordinate:

$$\xi = \frac{x - x_W}{x_E - x_W} \tag{3.1.4}$$

It is easy to find that

$$a = \frac{\bar{\phi}_P \xi_E^2 - \xi_P^2}{\xi_P \xi_E (\xi_E - \xi_P)} = a_1 \bar{\phi}_P + a_2 \tag{3.1.5}$$

$$b = \frac{\bar{\phi}_P \xi_E - \xi_P}{\xi_P \xi_E (\xi_E - \xi_P)} = b_1 \bar{\phi}_P + b_2 \tag{3.1.6}$$

To apply this interpolation in equation (3.1.1), $f(r_e^+)$ can be obtained as

$$f(r_e^+) = 2[(a_1\xi_e + b_1\xi_e^2 + a_2\xi_e + b_2\xi_e^2 - 1)r_e^+ + (a_2\xi_e + b_2\xi_e^2)] \tag{3.1.7}$$

After rearrangement, one obtains

$$f(r_e^+) = 2[\alpha_e r_e^+ + \beta_e] \tag{3.1.8}$$

Where

$$\alpha_e = \frac{\Delta P \Delta E}{(\Delta W + \Delta P)(\Delta W + 2\Delta P + \Delta E)}$$

$$\beta_e = \frac{(\Delta W + 2\Delta P)\Delta P}{(\Delta E + \Delta P)(\Delta W + 2\Delta P + \Delta E)}$$

In a uniform grid, this equation can be simplified to

$$f(r_e^+) = 2\left[\frac{1}{8} r_e^+ + \frac{3}{8}\right] \tag{3.1.9}$$

In another popular grid, the logarithmic grid, equation (3.1.8) becomes

$$f(r_e^+) = 2\left[\frac{q^3 r_e^+ + 1 + 2q}{(1+q)^3}\right] \qquad (3.1.10)$$

Where $q = \Delta x_{i+1} / \Delta x_i$, usually a constant.

(ii) Similarly, when $U < 0$, the value at node w is then

$$\bar{\phi}_w^- = \bar{\phi}_p + \frac{f(r_w^-)}{2}(1 - \bar{\phi}_p) \qquad (3.1.11)$$

Where

$$\bar{\phi}_w^- = \frac{\phi_w - \phi_E}{\phi_W - \phi_E} \qquad \bar{\phi}_P = \frac{\phi_P - \phi_E}{\phi_W - \phi_E} \qquad (3.1.12)$$

$$r_w^- = \frac{\phi_P - \phi_E}{\phi_W - \phi_P} \qquad (3.1.13)$$

$$f(r_w^-) = 2[\alpha_w r_w^- + \beta_w] \qquad (3.1.14)$$

Where

$$\alpha_w = \frac{\Delta P \Delta W}{(\Delta E + \Delta P)(\Delta W + 2\Delta P + \Delta E)}$$

$$\beta_w = \frac{(\Delta E + 2\Delta P)\Delta P}{(\Delta W + \Delta P)(\Delta W + 2\Delta P + \Delta E)}$$

(iii) UMIST limiter

Now QUICK is the most popular high-order difference scheme because it has third-order accuracy and unconditional stability. The shortcoming of this scheme is that

there may be oscillations in the solution when the cell Peclet number ($P = \frac{\rho u \Delta x}{\Gamma}$) is higher than two. Following the concept of Total Variation Diminishing (TVD) (Harten, 1983; Sweby, 1984) schemes, F. S. Lien and M. A. Leschziner (1994a) formulated a compact, QUICK-based limiter called the Upstream Monotonic Interpolation for Scalar Transport (UMIST) scheme. The expression for UMIST can be written

$$f(r) = \max[0,\ \min(2r, \beta + \alpha r, \underbrace{\alpha + \beta r}_{\text{QUICK}}, 2)] \qquad (3.1.15)$$

For a uniform grid, α=0.75 and β=0.25. General expressions for α and β can be found in equations (3.1.16) and (3.1.17).

With this limiter the monotonicity of the solution can be assured. Actually the equation (3.1.15) was derived for a uniform grid. To extend it to a non-uniform grid is only an approximation.

From the above derivation, in a non-uniform grid for positive velocity,

$$\alpha = \frac{2\Delta P(\Delta W + 2\Delta P)}{(\Delta E + \Delta P)(\Delta W + 2\Delta P + \Delta E)} \qquad (3.1.16)$$

and

$$\beta = \frac{2\Delta P \Delta E}{(\Delta W + \Delta P)(\Delta W + 2\Delta P + \Delta E)} \qquad (3.1.17)$$

For logarithmic grids

$$\begin{cases} \alpha = \dfrac{2(1+2q)}{(1+q)^3} \\ \beta = \dfrac{2q^3}{(1+q)^3} \end{cases} \tag{3.1.18}$$

3.1.2 Power Law Difference Scheme

For the purpose of comparison, the Power Law difference scheme is

$$\phi_e = \phi_P + \frac{1 - A(P_e)}{P_e}(\phi_W - \phi_P) \tag{3.1.19}$$

where

$$A(P_e) = MAX[0,\ (1 - |P_e|/10)^5] \tag{3.1.20}$$

The Peclet number $P_e = \dfrac{\rho u_e \Delta x}{\Gamma_e}$ is a ratio of convection and diffusion terms.

3.2 Discretization of Governing Equations

The governing equation was discretized for the control volume shown in Figure 3.2.1.

It is a common practice to write all governing equations in general form

$$\frac{\partial \phi}{\partial t} = \frac{\partial}{\partial \xi}(-\rho u \phi + \Gamma_\xi \frac{\partial \phi}{\partial \xi}) + \frac{\partial}{\partial \eta}(-\rho v \phi + \Gamma_\eta \frac{\partial \phi}{\partial \eta}) + \frac{\partial}{\partial \zeta}(-\rho w \phi + \Gamma_\zeta \frac{\partial \phi}{\partial \zeta}) + S_\phi \tag{3.2.1}$$

where ϕ may be u, v, w, p, K or ε.

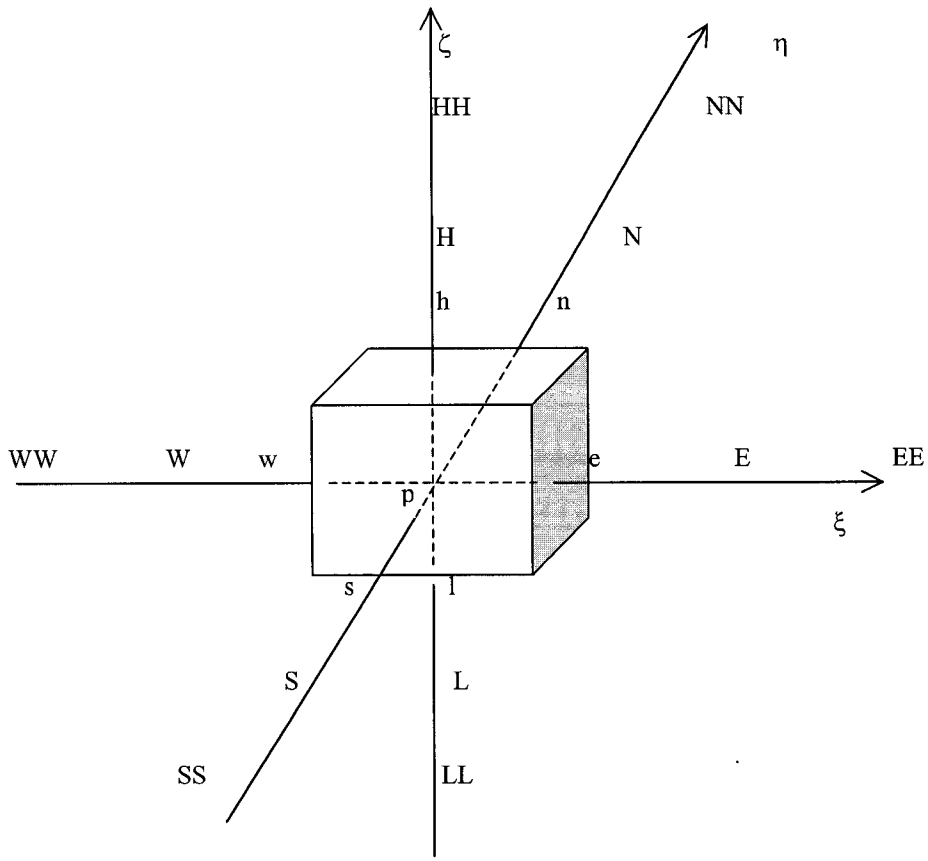

Figure 3.2.1 Control Volume and Nodes

Discretizing this equation in the cell shown in Figure 3.2.1, one obtains

$$
\begin{aligned}
(\phi_P - \phi_P^0)C_T = {} & C_w^+\phi_w^+ + C_w^-\phi_w^- - C_e^+\phi_e^+ - C_e^-\phi_e^- \\
& -(\phi_P - \phi_W)D_w + (\phi_E - \phi_P)D_e \\
& + C_s^+\phi_s^+ + C_s^-\phi_s^- - C_n^+\phi_n^+ - C_n^-\phi_n^- \\
& -(\phi_P - \phi_S)D_s + (\phi_N - \phi_P)D_n \\
& + C_l^+\phi_l^+ + C_l^-\phi_l^- - C_h^+\phi_h^+ - C_h^-\phi_h^- \\
& -(\phi_p - \phi_L)D_l + (\phi_H - \phi_P)D_h \\
& + S_U + S_p\phi_P
\end{aligned}
\tag{3.2.2}
$$

where the subscript P denotes a node in the center of the cell; ϕ_P^0 is the value of ϕ_P at the previous time step. In addition,

$$
C_T = \frac{\rho\Delta\xi\Delta\eta\Delta\zeta}{\Delta t} \tag{3.2.3}
$$

$$
\begin{cases}
C_e^+ = \dfrac{1}{2}(C_e + |C_e|) \\
C_e^- = \dfrac{1}{2}(C_e - |C_e|)
\end{cases}
\tag{3.2.4}
$$

$$
C_e = (\rho u A)_e \tag{3.2.5}
$$

$$
A_e = \Delta\eta\Delta\zeta \tag{3.2.6}
$$

$$
D_e = \frac{\Gamma_{\xi e}A_e}{\xi_E - \xi_P} \tag{3.2.7}
$$

$$
S_\phi = S_U + S_P\phi_P \tag{3.2.8}
$$

S_ϕ is the source term that includes the rest of the governing equation. It can be expressed artificially as a linear function in the form of equation (3.2.8).

When the difference schemes (3.1.1) and (3.1.11) are substituted into equation (3.2.2), the result is

$$
\begin{aligned}
(\phi_P-\phi_P^0)C_T = {} & C_w^+[\phi_W+\frac{f(r_w^+)}{2}(\phi_P-\phi_W)]+C_w^-[\phi_P+\frac{f(r_w^-)}{2}(\phi_W-\phi_P)] \\
& -C_e^+[\phi_P+\frac{f(r_e^+)}{2}(\phi_E-\phi_P)]-C_e^-[\phi_E+\frac{f(r_e^-)}{2}(\phi_P-\phi_E)] \\
& -(\phi_P-\phi_W)D_w+(\phi_E-\phi_P)D_e \\
& +C_s^+[\phi_S+\frac{f(r_s^+)}{2}(\phi_P-\phi_S)]+C_s^-[\phi_P+\frac{f(r_s^-)}{2}(\phi_S-\phi_P)] \\
& -C_n^+[\phi_P+\frac{f(r_n^+)}{2}(\phi_N-\phi_P)]-C_n^-[\phi_N+\frac{f(r_n^-)}{2}(\phi_P-\phi_N)] \\
& -(\phi_p-\phi_S)D_s+(\phi_N-\phi_P)D_n \\
& +C_l^+[\phi_L+\frac{f(r_l^+)}{2}(\phi_P-\phi_L)]+C_l^-[\phi_P+\frac{f(r_l^-)}{2}(\phi_L-\phi_P)] \\
& -C_h^+[\phi_P+\frac{f(r_h^+)}{2}(\phi_H-\phi_P)]-C_h^-[\phi_H+\frac{f(r_h^-)}{2}(\phi_P-\phi_H)] \\
& -(\phi_p-\phi_L)D_l+(\phi_H-\phi_P)D_h \\
& +S_U+S_p\phi_P
\end{aligned}
\qquad (3.2.9)
$$

By rearranging terms, equation (3.2.9) can be separated into two parts: one is the expression for the upwind difference, and the other one represents the QUICK supplementary modification.

$$
\left.
\begin{aligned}
(\phi_P-\phi_P^0)C_T = {} & C_w^+\phi_W+C_w^-\phi_P-(\phi_p-\phi_W)D_w \\
& -C_e^+\phi_P-C_e^-\phi_E+(\phi_E-\phi_P)D_e \\
& +C_s^+\phi_S+C_s^-\phi_P-(\phi_p-\phi_S)D_s \\
& -C_n^+\phi_P-C_n^-\phi_N+(\phi_N-\phi_P)D_n \\
& +C_l^+\phi_L+C_l^-\phi_P-(\phi_p-\phi_L)D_l \\
& -C_h^+\phi_P-C_h^-\phi_H+(\phi_H-\phi_P)D_h \\
& +S_U+S_p\phi_P
\end{aligned}
\right\} \text{Upwind}
$$

$$+\frac{1}{2}[(C_w^+ f(r_w^+) - C_w^- f(r_w^-))(\phi_P - \phi_W) + (C_e^+ f(r_e^+) - C_e^- f(r_e^-))(\phi_P - \phi_E)$$
$$+ (C_s^+ f(r_s^+) - C_s^- f(r_s^-))(\phi_P - \phi_S) + (C_n^+ f(r_n^+) - C_n^- f(r_n^-))(\phi_P - \phi_N)$$
$$+ (C_l^+ f(r_l^+) - C_l^- f(r_l^-))(\phi_P - \phi_L) + (C_h^+ f(r_h^+) - C_h^- f(r_h^-))(\phi_P - \phi_H)] \Big\} \text{ QUICK}$$

(3.2.10)

where

$$r_e^+ = \frac{\phi_P - \phi_W}{\phi_E - \phi_P} \qquad r_e^- = \frac{\phi_E - \phi_{EE}}{\phi_P - \phi_E}$$

$$r_w^+ = \frac{\phi_W - \phi_{WW}}{\phi_P - \phi_W} \qquad r_w^- = \frac{\phi_P - \phi_E}{\phi_W - \phi_P}$$

$$r_n^+ = \frac{\phi_P - \phi_S}{\phi_N - \phi_P} \qquad r_n^- = \frac{\phi_N - \phi_{NN}}{\phi_P - \phi_N}$$

$$r_s^+ = \frac{\phi_S - \phi_{SS}}{\phi_P - \phi_S} \qquad r_s^= = \frac{\phi_P - \phi_N}{\phi_S - \phi_P}$$

$$r_h^+ = \frac{\phi_P - \phi_L}{\phi_H - \phi_P} \qquad r_h^- = \frac{\phi_H - \phi_{HH}}{\phi_P - \phi_H}$$

$$r_l^+ = \frac{\phi_L - \phi_{LL}}{\phi_P - \phi_L} \qquad r_l^- = \frac{\phi_P - \phi_H}{\phi_L - \phi_P}$$

The continuity equation can be discretized as

$$C_e^+ - C_w^- + C_n^+ - C_s^- + C_h^+ - C_l^- = C_w^+ - C_e^- + C_s^+ - C_n^- + C_l^+ - C_h^- \quad (3.2.11)$$

Equation (3.2.10) can be simplified, after substitution of equation (3.2.11) to obtain

$$
\left.\begin{aligned}
0 = {} & (D_w + C_w^+)\phi_W + (D_e - C_e^-)\phi_E \\
& + (D_s + C_s^+)\phi_S + (D_n - C_n^-)\phi_N \\
& + (D_l + C_l^+)\phi_L + (D_h - C_h^-)\phi_H \\
& - (D_w + D_e + D_s + D_n + D_l + D_h \\
& + C_w^+ - C_e^- + C_s^+ - C_n^- + C_l^+ - C_h^- + C_T - S_p)\phi_P \\
& + S_U + \phi_P^0 C_T
\end{aligned}\right\} \text{Upwind}
$$

$$
\left.\begin{aligned}
& + \frac{1}{2}\{[(C_w^+ f(r_w^+) - C_w^- f(r_w^-)](\phi_P - \phi_W) + [C_e^+ f(r_e^+) - C_e^- f(r_e^-)](\phi_P - \phi_E) \\
& + [C_s^+ f(r_s^+) - C_s^- f(r_s^-)](\phi_P - \phi_S) + [C_n^+ f(r_n^+) - C_n^- f(r_n^-)](\phi_P - \phi_N) \\
& + [C_l^+ f(r_l^+) - C_l^- f(r_l^-)](\phi_P - \phi_L) + [C_h^+ f(r_h^+) - C_h^- f(r_h^-)](\phi_P - \phi_H)\}
\end{aligned}\right\} \text{QUICK}
$$

(3.2.12)

After rearranging terms in the equation, the final result is

$$
\begin{aligned}
& A_W\phi_W + A_E\phi_E + A_S\phi_S + A_N\phi_N + A_L\phi_L + A_H\phi_H \\
& = (A_W + A_E + A_S + A_N + A_L + A_H - S_p + C_T)\phi_P + S_U + C_T\phi_P^0
\end{aligned}
\qquad (3.2.13)
$$

It is easy to find that a stable solution can be established if all coefficients are positive and

$$-S_p + C_T \geq 0$$

The coefficients in equation (3.2.13) are

$$
\begin{aligned}
A_W &= D_w + C_w^+ - \frac{1}{2}[C_w^+ f(r_w^+) - C_w^- f(r_w^-)] \\
A_E &= D_e - C_e^- - \frac{1}{2}[C_e^+ f(r_e^+) - C_e^- f(r_e^-)] \\
A_S &= D_s + C_s^+ - \frac{1}{2}[C_s^+ f(r_s^+) - C_s^- f(r_s^-)] \\
A_N &= D_n - C_n^- - \frac{1}{2}[C_n^+ f(r_n^+) - C_n^- f(r_n^-)]
\end{aligned}
\qquad (3.2.14)
$$

$$A_L = D_l + C_l^+ - \frac{1}{2}[C_l^+ f(r_l^+) - C_l^- f(r_l^-)]$$
$$A_H = D_h - C_h^- - \frac{1}{2}[C_h^+ f(r_h^+) - C_h^- f(r_h^-)]$$

For comparison, the coefficients of the discretized equation according to the Power Law difference scheme are also given below:

$$\begin{aligned} A_W &= D_w A(P_w) + C_w^+ \\ A_E &= D_e A(P_e) - C_e^- \\ A_S &= D_s A(P_s) + C_s^+ \\ A_N &= D_n A(P_n) - C_n^- \\ A_L &= D_l A(P_l) + C_l^+ \\ A_H &= D_h A(P_h) - C_h^- \end{aligned} \qquad (3.2.15)$$

where

$$A(P_e) = MAX[0,\ (1-|P_e|/10)^5] \qquad (3.2.16)$$

and Peclet number

$$P_e = \frac{C_e}{D_e} \qquad (3.2.17)$$

3.3 Evaluation of Difference Schemes

To evaluate the accuracy of various difference schemes, a test case was run twice using the QUICK-UMIST scheme and the Power Law scheme. The test case is the same problem in Chapter 2 with a 45° angle between coordinate axes. The results are plotted in Figures 3.3.1 and 3.3.2. In the figures the solid line represents the calculated velocity by QUICK-UMIST scheme, while the points are benchmark data. The velocity calculated by the Power-Law scheme is plotted as a dashed line. It is obvious the QUICK-UMIST scheme is more accurate. Of course, the QUICK-UMIST scheme needs more computational time, but the increase in computer time is limited. In this comparison, a 92*92 grid is used.

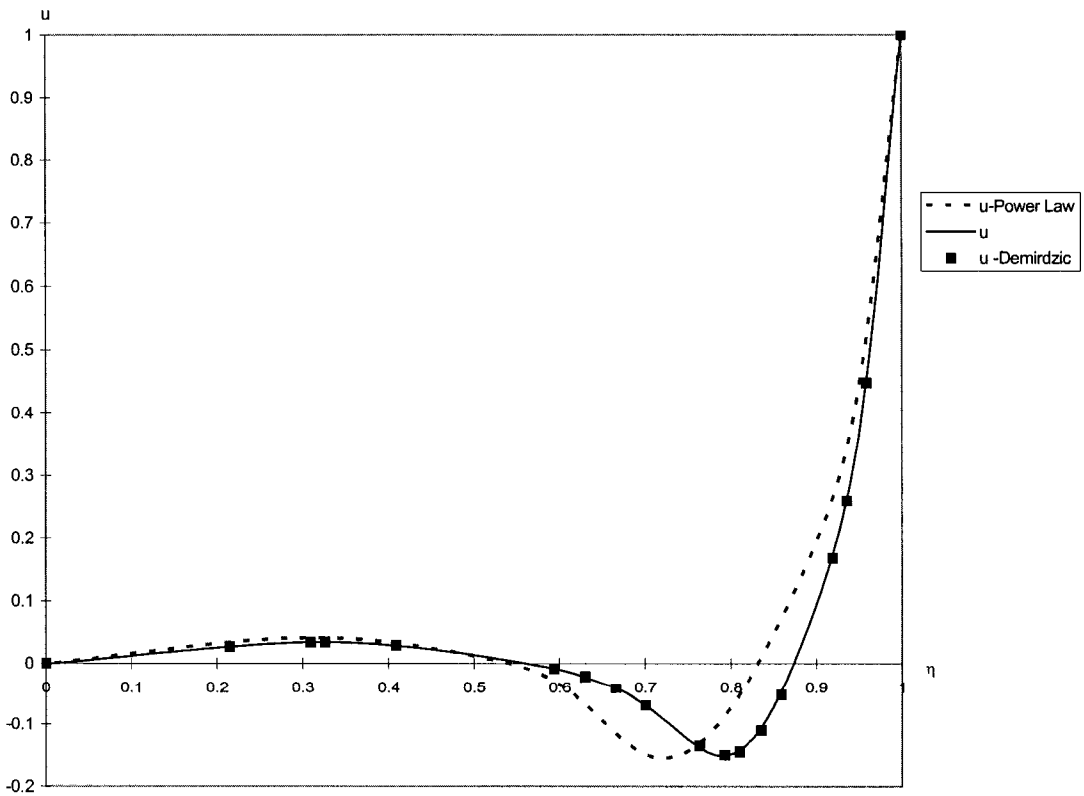

Figure 3.3.1 Calculated Velocity u by two Difference Schemes

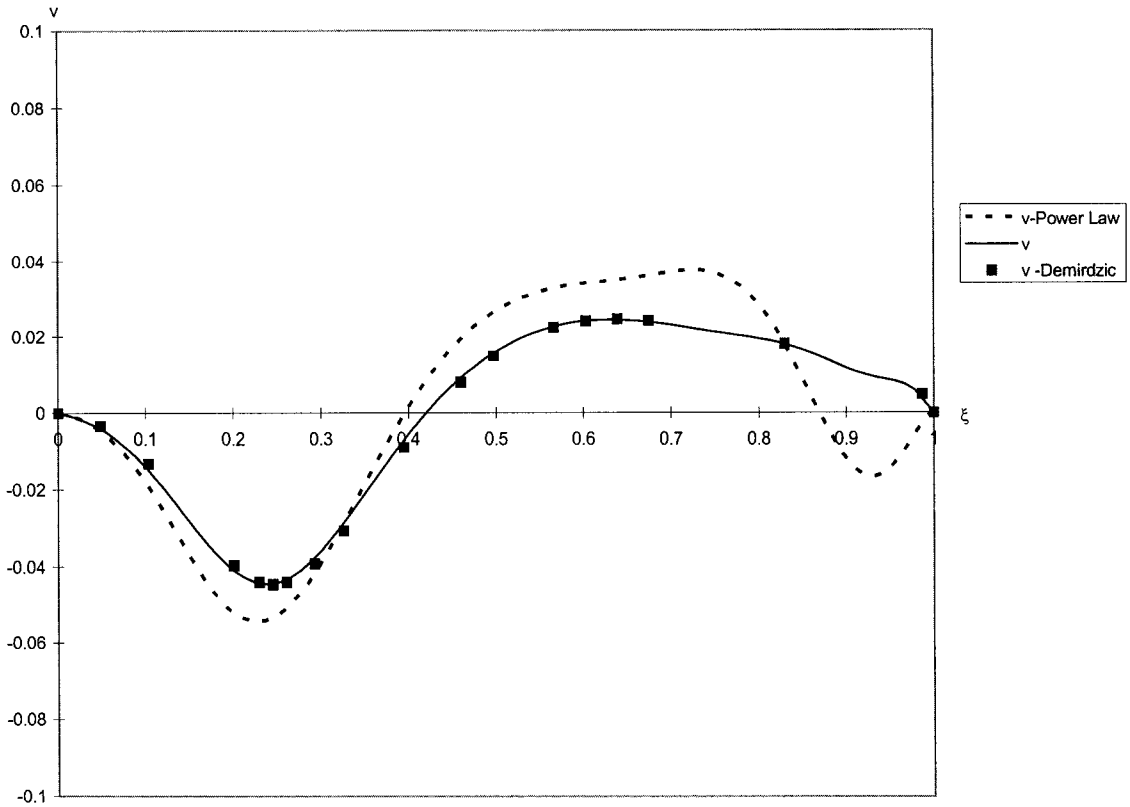

Figure 3.3.2 Calculated Velocity v by two Difference Schemes

3.4 Pressure Correction Procedures

There is no single pressure equation, from which the value of the pressure can be found directly. A common approach for the pressure solution is to derive a pressure Poisson equation by combining the momentum equations and continuity equation together. SIMPLE-like (Semi-Implicit Method for Pressure Linked Equations) algorithms are a good example (Patankar S. V., 1980). They solve a pressure correction equation, which is in fact a discretized pressure Poisson equation, to obtain s solution for the pressure. Currently SIMPLE-like algorithms are the most popular pressure solution algorithms.

Another pressure solution algorithm is the pseudo-compressible algorithm. In this algorithm fluid is always assumed to be compressible, so the pressure can be found from the density solution that is governed by the continuity equation. Since this algorithm will not be used in the present study, no further discussion will be given.

Considering the importance of solution procedure for the pressure, the derivation and application of the SIMPLE and SIMPLER algorithms for different sets of governing equations will be discussed in detail.

3.4.1 Comparison of Pressure Correction Procedures for Different Sets of Governing Equations: SIMPLE Algorithm

3.4.1.1 Continuity and Momentum Equations

For the three sets of governing equations in Chapter 2, the continuity equation will be always the same.

Equation of Continuity

$$\frac{\partial}{\partial \xi^j}(\sqrt{g}u^j) = 0 \qquad (3.4.1)$$

Where u^j is a contravariant component of the velocity.

For the concise governing equations

$u^j = g^{jk}u_k$.

For the partially transformed governing equations

$$u^j = \frac{\partial \xi^j}{\partial x^k} U^k .$$

The momentum equations are given below

A. Conventional Momentum Equation:

$$\frac{\partial}{\partial \xi^j}(\sqrt{g}\rho u^j u^i) = \frac{\partial}{\partial \xi^j}(\sqrt{g}\mu_e g^{jm}\frac{\partial u^i}{\partial \xi^m}) + S_{\phi a}u^i + S_a - \sqrt{g}\, g^{im}\frac{\partial p}{\partial \xi^m} \qquad (i=1,2,3)$$

(j=m only for the first term in the right side of the equation) (3.4.2)

$$S_a = \frac{\sqrt{g}}{2} g^{im}\left[\frac{\partial g_{mj}}{\partial \xi^k} + \frac{\partial g_{mk}}{\partial \xi^j} - \frac{\partial g_{jk}}{\partial \xi^m}\right](\tau^{jk} - \rho u^j u^k)$$
$$+ \frac{\partial}{\partial \xi^j}[\sqrt{g}(\tau^{ij} - \mu_e g^{jm}\frac{\partial u^i}{\partial \xi^m})] + \sqrt{g}\gamma^i - S_{\phi a}u^i \qquad (3.4.3)$$
(j=m only)

B. Concise Momentum Equation:

$$\frac{\partial}{\partial \xi^j}(\sqrt{g}\rho u^j u_i) = \frac{\partial}{\partial \xi^j}(\sqrt{g}\mu_e g^{jm}\frac{\partial u_i}{\partial \xi^m}) + S_{\phi b}u_i + S_b - \sqrt{g}\frac{\partial p}{\partial \xi^i} \qquad (i=1,2,3) \quad (3.4.4)$$

(j=m only for the first term in the right side of the equation)

$$S_b = \frac{\sqrt{g}}{2}\frac{\partial g_{jk}}{\partial \xi^i}(\rho u^j u^k - \tau^{jk}) + \frac{\partial}{\partial \xi^j}[\sqrt{g}(\tau_i^j - \mu_e g^{jm}\frac{\partial u_i}{\partial \xi^m})] + \sqrt{g}\gamma_i - S_{\phi b}u_i \qquad (3.4.5)$$
(j=m only)

C. Partially Transformed Momentum Equation:

$$\frac{\partial}{\partial \xi^j}(\sqrt{g}\rho u^j U^i) = \frac{\partial}{\partial \xi^j}(\mu_e \sqrt{g} g^{jm} \frac{\partial U^i}{\partial \xi^m}) + S_{\phi c} U^i + S_c - \sqrt{g}\beta^{ji} \frac{\partial p}{\partial \xi^j} \qquad (3.4.6)$$

(j=m only for the first term in the right side of the equation)

$$S_c = \frac{\partial}{\partial \xi^j}\left[\mu_e \sqrt{g}\left(\underset{(j=m\ only)}{g^{jm} \frac{\partial U^i}{\partial \xi^m}} + \beta^j{}_k \beta^{mi} \frac{\partial U^k}{\partial \xi^m}\right) - \frac{2}{3}\sqrt{g}\beta^{ji}\rho K\right] - S_{\phi c} U^i + \sqrt{g}\gamma^i \qquad (3.4.7)$$

Here $S_{\phi a}$, $S_{\phi b}$, $S_{\phi c}$ are coefficients of the linear term in the momentum equations. Most of the time it is assigned an artificial value to control the convergence and stability in the solution.

The differences between equation (3.4.2), (3.4.4) and (3.4.6) are found in $S_{\phi a}$, $S_{\phi b}$, $S_{\phi c}$, S_a, S_b, S_c and the pressure terms. If one lets $S_{\phi a}$, $S_{\phi b}$, $S_{\phi c}$ be the same in these equations (It is common to let $S_{\phi a} = S_{\phi b} = S_{\phi c} = 0$), then the coefficients in the discrete equations derived from equations (3.4.2), (3.4.4) and (3.4.6) should also be the same.

Equations (3.4.2), (3.4.4) and (3.4.6) can be written as

$$A_P^{(i)} u^i = A^i_j u^j + V S_a - V\sqrt{g}\, g^{im} \frac{\partial p}{\partial \xi^m} \qquad (i=1,2,3) \qquad (3.4.2a)$$

$$A_P^{(i)} u_i = A^j_i u_j + V S_b - V\sqrt{g} \frac{\partial p}{\partial \xi^i} \qquad (i=1,2,3) \qquad (3.4.4a)$$

$$A_P^{(i)} U^i = A^i_j U^j + V S_c - V\sqrt{g}\beta^{mi} \frac{\partial p}{\partial \xi^m} \qquad (i=1,2,3) \qquad (3.4.6a)$$

where

$A^i_j = A^j_i$ are coefficients of the discretized equations.

$V = \delta\xi\delta\eta\delta\zeta$ is the volume of a cell. A superscript $^{(i)}$ indicates the (i) direction. It is not a tensor index.

A subscript *p* denotes a node at the center of a cell. These equations are summed over *j*, the number of neighbor nodes, and over *m*, the number of dimensions.

3.4.1.2 Pressure Correction for the Conventional Governing Equations

First, the velocity and pressure are split into a primary part and a correction:

$$u^i = u^{*i} + u^{'i}$$
$$p = p^* + p' \qquad (i=1,2,3) \qquad (3.4.8)$$

The primary part is usually the result from the most recent past iteration. After inserting equation (3.4.8) into equation (3.4.2a), then equation (3.4.2a) can also be split into two equations:

$$u^{*i} = \frac{A^i_j u^{*j}}{A^{(i)}_p} + \frac{VS_a}{A^{(i)}_p} - \frac{V\sqrt{g}\, g^{im} \frac{\partial p^*}{\partial \xi^m}}{A^{(i)}_p} \qquad (i=1,2,3) \qquad (3.4.9)$$

$$u^{'i} = \frac{A^i_j u^{'j}}{A^{(i)}_p} - \frac{V\sqrt{g}\, g^{im} \frac{\partial p'}{\partial \xi^m}}{A^{(i)}_p} \qquad (i=1,2,3) \qquad (3.4.10)$$

With these equations, the velocity can be related to the pressure by

$$u^i = u^{*i} + \bar{u}^{'i} - B^{im} \frac{\partial p'}{\partial \xi^m} \qquad (i=1,2,3) \qquad (3.4.11)$$

where

$$\bar{u}^{'i} = \frac{A^i_j u^{'j}}{A^{(i)}_p}$$

and

$$B^{im} = \frac{V\sqrt{g}\, g^{im}}{A^{(i)}_p}$$

The next step is to discretize the continuity equation for a finite volume (refer to Figure 3.2.1):

$$\delta(A_i u^i) = 0 \tag{3.4.12}$$

The operator $\delta(f_i)$ is defined as

$$\delta(f_i) = f_e - f_w + f_n - f_s + f_h - f_l \tag{3.4.13}$$

and $A_i = \frac{V\sqrt{g}}{\delta\xi^i}$ is the area of a surface normal to the i-th direction of the finite volume .

If one replaces u^i using equation (3.4.11), then

$$\delta(A_i u^i) = \delta(A_i u^{*i}) + \delta(A_i \bar{u}^{'i}) - \delta(A_i B^{im} \frac{\partial p'}{\partial \xi^m}) = 0 \tag{3.4.14}$$

This is the pressure correction equation that is sought:

$$\delta(A_i B^{im} \frac{\partial p'}{\partial \xi^m}) = \delta(A_i u^{*i}) + \delta(A_i \bar{u}^{'i}) \tag{3.4.15}$$

Expansion of this equation over a control volume will lead to

$$(A_1B^{1m}\frac{\partial p'}{\partial \xi^m})_e-(A_1B^{1m}\frac{\partial p'}{\partial \xi^m})_w+(A_2B^{2m}\frac{\partial p'}{\partial \xi^m})_n-(A_2B^{2m}\frac{\partial p'}{\partial \xi^m})_s+$$
$$(A_3B^{3m}\frac{\partial p'}{\partial \xi^m})_t-(A_3B^{3m}\frac{\partial p'}{\partial \xi^m})_b=\delta(A_i u^{*i})+\delta(A_i \bar{u}^{i}) \qquad (3.4.16)$$

Further expansion of the first term gives

$$(A_1B^{1m}\frac{\partial p'}{\partial \xi^m})_e=(A_1B^{11}\frac{\partial p'}{\partial \xi}+A_1B^{12}\frac{\partial p'}{\partial \eta}+A_1B^{13}\frac{\partial p'}{\partial \zeta})_e$$
$$=(A_1\frac{B^{11}}{\delta\xi})_e(p'_E-p'_P)+(A_1\frac{B^{12}}{\delta\eta})_e(p'_{Ne}-p'_{Se})+(A_1\frac{B^{13}}{\delta\zeta})_e(p'_{Te}-p'_{Be}) \qquad (3.4.17)$$

In a common finite volume method it is assumed that the pressure at a center node is dependent only on the pressure at the six closest neighboring nodes, i. e.

$$p_P=f(p_E,p_W,p_N,p_S,p_H,p_L)$$

Following this assumption, an approximation must be introduced.

$$(A_1B^{1m}\frac{\partial p'}{\partial \xi^m})_e\approx(A_1\frac{B^{11}}{\delta\xi})_e(p'_E-p'_P) \qquad (3.4.18)$$

That means the pressure gradients in directions other than 1-th direction are omitted.

Similarly

$$(A_1B^{1m}\frac{\partial p'}{\partial \xi^m})_w\approx(A_1\frac{B^{11}}{\delta\xi})_w(p'_P-p'_W) \qquad (3.4.19)$$

$$(A_2B^{2m}\frac{\partial p'}{\partial \xi^m})_n\approx(A_2\frac{B^{22}}{\delta\eta})_n(p'_N-p'_P) \qquad (3.4.20)$$

$$(A_2 B^{2m} \frac{\partial p'}{\partial \xi^m})_s \approx (A_2 \frac{B^{22}}{\delta \eta})_s (p'_P - p'_S) \tag{3.4.21}$$

$$(A_3 B^{3m} \frac{\partial p'}{\partial \xi^m})_t \approx (A_3 \frac{B^{33}}{\delta \zeta})_t (p'_H - p'_P) \tag{3.4.22}$$

$$(A_3 B^{3m} \frac{\partial p'}{\partial \xi^m})_b \approx (A_3 \frac{B^{33}}{\delta \zeta})_b (p'_P - p'_L) \tag{3.4.23}$$

The final discretized pressure correction equation is

$$A_P p'_p = \sum A_{nb} p'_{nb} - \delta(A_i u^{*i}) - \delta(A_i \bar{u}^{'i}) \tag{3.4.24}$$

where the subscript *nb=E,W,N,S,H,L* demotes neighbor nodes, and the coefficients are

$$A_E = (A_1 \frac{B^{11}}{\delta \xi})_e = (A_1 A_1 \frac{g^{11}}{A_P^{(1)}})_e \tag{3.4.25}$$

$$A_W = (A_1 \frac{B^{11}}{\delta \xi})_w = (A_1 A_1 \frac{g^{11}}{A_P^{(1)}})_w$$

$$A_N = (A_2 \frac{B^{22}}{\delta \eta})_n = (A_2 A_2 \frac{g^{22}}{A_P^{(2)}})_n$$

$$A_S = (A_2 \frac{B^{22}}{\delta \eta})_s = (A_2 A_2 \frac{g^{22}}{A_P^{(2)}})_s$$

$$A_T = (A_3 \frac{B^{33}}{\delta \zeta})_h = (A_3 A_3 \frac{g^{33}}{A_P^{(3)}})_h$$

$$A_B = (A_3 \frac{B^{33}}{\delta \zeta})_l = (A_3 A_3 \frac{g^{33}}{A_P^{(3)}})_l$$

with

$$A_P = A_E + A_W + A_N + A_S + A_H + A_L \tag{3.4.26}$$

For the SIMPLE algorithm, the last term in equation (3.4.24) can be dropped, because it will approach zero when convergence is achieved, leaving

$$A_P p'_p = \sum A_{nb} p'_{nb} - \delta(A_i u^{*i}) \qquad (3.4.27)$$

If the physical components of velocity $\bar{u}^i = u^i h_i$ are used, the expressions for equations (3.4.25) to (3.4.27) will remain the same, so long as $\bar{A}_i = A_i / h_i$, and $\bar{A}_P^{(i)} = A_P^{(i)} / h_i$ are used to replace A_i, $A_P^{(i)}$.

After p' is determined by solving equation (3.4.24), the velocity can be updated by

$$u^i = u^{*i} - \frac{V\sqrt{g}\, g^{im}}{A_p^{(i)}} \frac{\partial p'}{\partial \xi^m} \approx u^{*i} - \frac{V\sqrt{g}\, g^{ii}}{A_p^{(i)}} \frac{\partial p'}{\partial \xi^i} \qquad (3.4.28)$$

An approximation must be used here because the pressure difference is only available in the i-th direction.

3.4.1.3 Pressure Correction for the Concise Governing Equations

Similar to the above section, let

$$u_i = u_i^* + u_i' \qquad (i=1,2,3) \qquad (3.4.29)$$
$$p = p^* + p'$$

Splitting equation (3.4.4a) results in

$$u_i^* = \frac{A_i^j u_j^*}{A_p^{(i)}} + \frac{VS_a}{A_p^{(i)}} - \frac{V\sqrt{g}\,\frac{\partial p^*}{\partial \xi^i}}{A_p^{(i)}} \qquad (i=1,2,3) \qquad (3.4.30)$$

$$u_i^{'} = \frac{A_i^j u_j^{'}}{A_p^{(i)}} - \frac{V\sqrt{g}\,\frac{\partial p^{'}}{\partial \xi^i}}{A_p^{(i)}} \qquad (i=1,2,3 \qquad (3.4.31)$$

The velocity can be written as

$$u_i = u_i^* + \bar{u}_i^{'} - B_{(i)}\frac{\partial p^{'}}{\partial \xi^i} \qquad (i=1,2,3) \qquad (3.4.32)$$

where

$$\bar{u}_i^{'} = \frac{A_i^j u_j^{'}}{A_p^{(i)}} \qquad (3.4.33)$$

and

$$B_{(i)} = \frac{V\sqrt{g}}{A_p^{(i)}} \qquad (3.4.34)$$

Now discretize the continuity equation in the same way as before

$$\delta(A_i u^i) = 0 \qquad (3.4.35)$$

Since $u^i = g^{im}u_m$, one finds

$$\begin{aligned}
&\delta(A_i u^i) = \delta(A_i g^{im} u_m) \\
&= \delta(A_i g^{im} u_m^*) + \delta(A_i g^{im}\bar{u}_m^{'}) - \delta(A_i g^{im} B_{(i)}\frac{\partial p^{'}}{\partial \xi^m}) \\
&= \delta(A_i u^{*i}) + \delta(A_i \bar{u}^{'i}) - \delta(A_i B^{im}\frac{\partial p^{'}}{\partial \xi^m}) \\
&= 0
\end{aligned} \qquad (3.4.36)$$

Equation (3.4.36) is exactly the same as equation (3.4.14). That means the pressure correction equation is the same in these two cases. The only difference is the velocity correction equation.

In this case, the velocity correction is

$$u_i = u_i^* - \frac{V\sqrt{g}}{A_p^{(i)}}\frac{\partial p'}{\partial \xi^i} \qquad (3.4.37)$$

As opposed to equation (3.4.28), there is no approximation in equation (3.4.37). That is a good feature to accelerate convergence.

3.4.1.4 Pressure Correction for the Partially Transformed Governing Equations

Let

$$U^i = U^{*i} + U^{'i}$$
$$p = p^* + p' \qquad (i=1,2,3) \qquad (3.4.38)$$

Then equation (3.4.6a) can be written as

$$U^{*i} = \frac{A_j^i U^{*j}}{A_p^{(i)}} + \frac{VS_c}{A_p^{(i)}} - \frac{V\sqrt{g}\,\beta^{ij}\frac{\partial p^*}{\partial \xi^j}}{A_p^{(i)}} \qquad (i=1,2,3) \qquad (3.4.39)$$

$$U^{'i} = \frac{A_j^i U^{'j}}{A_p^{(i)}} - \frac{V\sqrt{g}\,\beta^{ij}\frac{\partial p'}{\partial \xi^j}}{A_p^{(i)}} \qquad (i=1,2,3) \qquad (3.4.40)$$

and

$$U^i = U^{*i} + \overline{U}^{'i} - C^{ij}\frac{\partial p'}{\partial \xi^j} \qquad (i=1,2,3) \qquad (3.4.41)$$

where

$$\overline{U}^{'i} = \frac{A^i_j U^{'j}}{A^{(i)}_p} \qquad (i=1,2,3) \qquad (3.4.42)$$

and

$$C^{ij} = \frac{V\sqrt{g}\beta^{ij}}{A^{(i)}_p} \qquad (i=1,2,3) \qquad (3.4.43)$$

Now discretize the continuity equation by using the relationship $u^i = \beta^i_j U^j$:

$$\begin{aligned}\delta(A_i u^i) &= \delta(A_i \beta^i_j U^j) \\ &= \delta(A_i \beta^i_j U^{*j}) + \delta(A_i \beta^i_j \overline{U}^{'j}) - \delta(A_i \beta^i_j C^{jm} \frac{\partial p'}{\partial \xi^m}) = 0\end{aligned} \qquad (3.4.44)$$

Finally, the pressure correction equation is

$$\delta(A_i \beta^i_j C^{jm} \frac{\partial p'}{\partial \xi^m}) = \delta(A_i \beta^i_j U^{*j}) + \delta(A_i \beta^i_j \overline{U}^{'j}) \qquad (3.4.45)$$

Since $\beta^i_j \beta^{jm} = g^{im}$, equation (3.4.45) can be written as

$$\delta(A_i \sqrt{g} \frac{g^{ij}}{A^{(i)}_p} \frac{\partial p'}{\partial \xi^j}) = \delta(A_i u^{*i}) + \delta(A_i \overline{u}^{'i}) \qquad (3.4.46)$$

This equation is the same as equation (3.4.14).

Here velocity correction equation is different from that for conventional or concise governing equations.

$$U^i = U^{*i} - \frac{V\sqrt{g}\beta^{ij}}{A^{(i)}_p} \frac{\partial p'}{\partial \xi^j} \qquad (3.4.47)$$

As in the conventional equation, it can be approximated as

$$U^i = U^{*i} - \frac{V\sqrt{g}\,\beta^{ii}}{A_p^{(i)}}\frac{\partial p'}{\partial \xi^i} \qquad (3.4.48)$$

3.4.1.5 Conclusions

For the SIMPLE algorithm the pressure solution procedure for the three kinds of governing equations is always the same. The only difference is the velocity correction. Except for the concise governing equation, the other two sets of governing equations require an approximation in the velocity correction equation.

In the following section, it will be shown that there is a major difference between the concise governing equation and the conventional governing equation if the SIMPLER algorithm is used.

3.4.2. Pressure Correction by the SIMPLER Algorithm

The SIMPLER algorithm is a revision of the SIMPLE algorithm. In the SIMPLE algorithm pressure is obtained by means of a pressure correction p', while in the SIMPLER algorithm pressure can be found directly from pressure equation.

A. Conventional Momentum Equation

From equation (3.4.2a) the velocity can be written as

$$u^i = \hat{u}^i - B^{ij}\frac{\partial p}{\partial \xi^i} \qquad (i=1,2,3) \qquad (3.4.49)$$

where

$$\hat{u}^i = \frac{A^i_j u^j + VS_a}{A_P^{(i)}} \tag{3.4.50}$$

and

$$B^{ij} = g^{ij}\frac{V\sqrt{g}}{A_P^{(i)}} \tag{3.4.51}$$

From the continuity equation, it can be found that

$$\delta(A_i u^i) = \delta(A_i \hat{u}^i - A_i B^{ij}\frac{\partial p}{\partial \xi^j}) = 0 \tag{3.4.52}$$

or

$$\delta(A_i B^{ij}\frac{\partial p}{\partial \xi^j})_{i=j} = \delta(A_i \hat{u}^i - A_i B^{ij}\frac{\partial p}{\partial \xi^j})_{i\neq j} \tag{3.4.53}$$

This is the pressure correction equation for the SIMPLER algorithm.

The discretization of equation (3.4.53) results in

$$\begin{aligned}
&\left[A_1A_1\frac{g^{11}}{A_P^{(1)}}\right]_e(p_E - p_P) - \left[A_1A_1\frac{g^{11}}{A_P^{(1)}}\right]_w(p_P - p_W) + \\
&\left[A_2A_2\frac{g^{22}}{A_P^{(2)}}\right]_n(p_N - p_P) - \left[A_2A_2\frac{g^{22}}{A_P^{(2)}}\right]_s(p_P - p_S) + \\
&\left[A_3A_3\frac{g^{33}}{A_P^{(3)}}\right]_h(p_H - p_P) - \left[A_3A_3\frac{g^{33}}{A_P^{(3)}}\right]_l(p_P - p_L) \\
&= (A_1\bar{u}^1)_e - (A_1\bar{u}^1)_w + (A_2\bar{u}^2)_n - (A_2\bar{u}^2)_s \\
&+ (A_3\bar{u}^3)_h - (A_3\bar{u}^3)_l \\
&- \left[A_1A_2\frac{g^{12}}{A_P^{(1)}}\right]_e(p_{Ne} - p_{Se}) - \left[A_1A_3\frac{g^{13}}{A_P^{(1)}}\right]_e(p_{Te} - p_{Be}) \\
&+ \left[A_1A_2\frac{g^{12}}{A_P^{(1)}}\right]_w(p_{Nw} - p_{Sw}) + \left[A_1A_3\frac{g^{13}}{A_P^{(1)}}\right]_w(p_{Tw} - p_{Bw})
\end{aligned} \tag{3.4.54}$$

$$
\begin{aligned}
&-\left[A_2A_1\frac{g^{21}}{A_P^{(2)}}\right]_n(p_{En}-p_{Wn})-\left[A_2A_3\frac{g^{23}}{A_P^{(2)}}\right]_n(p_{Tn}-p_{Bn})\\
&+\left[A_2A_1\frac{g^{21}}{A_P^{(2)}}\right]_s(p_{Es}-p_{Ws})+\left[A_2A_3\frac{g^{23}}{A_P^{(2)}}\right]_s(p_{Ts}-p_{Bs})\\
&-\left[A_3A_1\frac{g^{31}}{A_P^{(3)}}\right]_h(p_{Eh}-p_{Wh})-\left[A_3A_2\frac{g^{32}}{A_P^{(3)}}\right]_l(p_{Nh}-p_{ht})\\
&+\left[A_3A_1\frac{g^{31}}{A_P^{(3)}}\right]_h(p_{El}-p_{Wl})+\left[A_3A_2\frac{g^{32}}{A_P^{(3)}}\right]_l(p_{Nl}-p_{Sl})
\end{aligned}
$$

In this case the pressures on the right side of the equation must be determined iteratively, because they are unknown.

The following section will show for the concise momentum equation that the pressure can be obtained directly from a known velocity distribution. No iteration is required.

B. Concise Momentum Equation

From equation (3.4.4.a), the velocity can be written as

$$u_i = \hat{u}_i - B_{(i)}\frac{\partial p}{\partial \xi^i} \qquad (i=1,2,3) \qquad (3.4.55)$$

where

$$\hat{u}_i = \frac{A_i^j u_j + VS_a}{A_P^{(i)}} \qquad (3.4.56)$$

and

$$B_{(i)} = \frac{V\sqrt{g}}{A_P^{(i)}} \qquad (3.4.57)$$

If one rewrites the discretized continuity equation

$$\delta(A_i u^i) = 0 \tag{3.4.58}$$

as

$$\delta(A_i g^{ii} u_i) = \delta(A_i g^{ii} u_i - A_i u^i) \tag{3.4.59}$$

then the substitute equation (3.4.55) into the equation (3.4.59) will lead to a pressure correction equation:

$$\delta(A_i g^{ii} B_{(i)} \frac{\partial p}{\partial \xi^i}) = \delta(A_i g^{ii} \hat{u}_i) + \delta(A_i u^i - A_i g^{ii} u_i) \tag{3.4.60}$$

Expanding this equation results in

$$\begin{aligned}
&(A_1 \frac{A_1 g^{11}}{A_P^{(1)}})_e (p_E - p_P) - (A_1 \frac{A_1 g^{11}}{A_P^{(1)}})_w (p_P - p_W) + \\
&(A_2 \frac{A_2 g^{22}}{A_P^{(2)}})_n (p_N - p_P) - (A_2 \frac{A_2 g^{22}}{A_P^{(2)}})_s (p_P - p_S) + \\
&(A_3 \frac{A_3 g^{33}}{A_P^{(3)}})_h (p_H - p_P) - (A_3 \frac{A_3 g^{33}}{A_P^{(3)}})_l (p_P - p_L) \\
&= (A_1 g^{11} \hat{u}_1 + A_1 g^{12} u_2 + A_1 g^{13} u_3)_e - (A_1 g^{11} \hat{u}_1 + A_1 g^{12} u_2 + A_1 g^{13} u_3)_w \\
&+ (A_2 g^{21} u_1 + A_2 g^{22} \hat{u}_2 + A_2 g^{23} u_3)_n - (A_2 g^{21} u_1 + A_2 g^{22} \hat{u}_2 + A_2 g^{23} u_3)_s \\
&+ (A_3 g^{31} u_1 + A_3 g^{32} u_2 + A_3 g^{33} \hat{u}_3)_h - (A_3 g^{31} u_1 + A_3 g^{32} u_2 + A_3 g^{33} \hat{u}_3)_l
\end{aligned} \tag{3.4.61}$$

Since the pressure does not appear on the right hand side of equation (3.4.61), it can be determined directly without iteration. When $\hat{u}_i$ approaches u_i, the right side of the equation approaches zero.

C. Conclusions

In conclusion, the derivation above shows that the pressure correction procedures are similar for the two sets of governing equations with the SIMPLER scheme. The

advantage of the concise governing equation is that it is able to find the correct pressure distribution from a correct velocity distribution in one step. No iterations are required as for the conventional governing equations.

It is easy to prove for the partially transformed governing equations that the pressure solution procedure by the SIMPLER scheme is actually the same as in the conventional governing equations, using the same procedures in this section. No details will be provided here.

3.5 Construction of Curvilinear Coordinate System

To simulate free surface flow, no doubt a coordinate system that follows the free surface is a good choice because the free surface boundary condition can be easily applied on a coordinate surface. To calculate the flow around obstacles, many modelers prefer to use a body-fitted coordinate system. But that may not be a good choice in the present work. The reason is that large obstacles in streams, including fish habitat structures, may have very strange shapes. The body-fitted coordinates may change sharply along the surface of the obstacles, which may damage numerical results. In addition, the existence of the free surface means that the coordinates must be regenerated repeatedly following the free surface. The cost to regenerate body-fitted coordinates repeatedly around a complex geometry may be too large to be practical. From these considerations, a special curvilinear coordinate system (ξ, η, ζ) is chosen (refer to Figure 3.5.1) for the current numerical method.

$$\begin{cases} x = \xi \\ y = y_b(\xi,\zeta) + \int_0^{\eta} h_2(\xi,\eta,\zeta)d\eta \\ z = \zeta \end{cases} \qquad (3.5.1)$$

The position of the free-surface y_f is adjusted by the function $h(\xi, \eta, \zeta)$, while η_f is a constant.

$$y_f(\xi,\zeta) = y_b(\xi,\zeta) + \int_0^{\eta_f} h_2(\xi,\eta,\zeta)d\eta \qquad (3.5.2)$$

The function $y_b(\xi,\zeta)$ is the profile of the channel bed. It may be a constant, assuming a flat rigid bed.

The advantage of this coordinate system is its simplicity and efficiency. There is only one variable $h(\xi, \eta, \zeta)$ to control whole grid system and this grid can be regenerated rapidly.

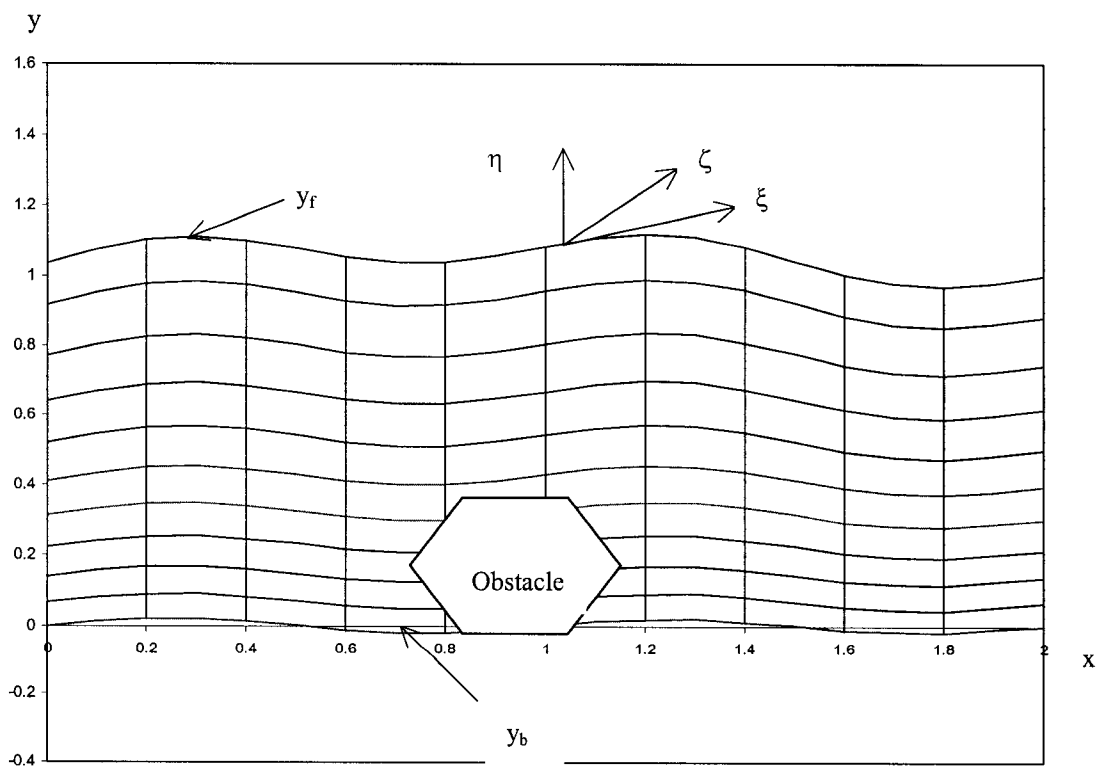

Figure 3.5.1 Free Surface Fitted Coordinate System

The coordinate transformation to a Cartesian coordinate can be completed by employing the following equations:

$$\begin{bmatrix} x_\xi & y_\xi & z_\xi \\ x_\eta & y_\eta & z_\eta \\ x_\zeta & y_\zeta & z_\zeta \end{bmatrix} = \begin{bmatrix} 1 & \int_0^\eta \frac{\partial h}{\partial \xi} d\eta + \frac{\partial y_b}{\partial \xi} & 0 \\ 0 & h & 0 \\ 0 & \int_0^\eta \frac{\partial h}{\partial \zeta} d\eta + \frac{\partial y_b}{\partial \zeta} & 1 \end{bmatrix} \tag{3.5.3}$$

$$\begin{bmatrix} \xi_x & \eta_x & \zeta_x \\ \xi_y & \eta_y & \zeta_y \\ \xi_z & \eta_z & \zeta_z \end{bmatrix} = \begin{bmatrix} 1 & -\frac{y_\xi}{y_\eta} & 0 \\ 0 & \frac{1}{y_\eta} & 0 \\ 0 & -\frac{y_\zeta}{y_\eta} & 1 \end{bmatrix} \tag{3.5.4}$$

By tensor analysis, the metric tensor can be found by

$$g_{ij} = \frac{\partial x^m}{\partial \xi^i} \frac{\partial x_m}{\partial \xi^j} = \begin{bmatrix} 1+y_\xi y_\xi & y_\xi y_\eta & y_\xi y_\zeta \\ y_\xi y_\eta & y_\eta y_\eta & y_\eta y_\zeta \\ y_\xi y_\zeta & y_\zeta y_\eta & 1+y_\zeta y_\zeta \end{bmatrix} \tag{3.5.5}$$

$$g^{ij} = \frac{\partial \xi^i}{\partial x^m} \frac{\partial \xi^j}{\partial x_m} = \begin{bmatrix} 1 & \eta_x & 0 \\ \eta_x & \eta_x^2+\eta_y^2+\eta_z^2 & \eta_z \\ 0 & \eta_z & 1 \end{bmatrix} \tag{3.5.6}$$

and

$$\sqrt{g} = \begin{vmatrix} x_\xi & y_\xi & z_\xi \\ x_\eta & y_\eta & z_\eta \\ x_\zeta & y_\zeta & z_\zeta \end{vmatrix} = y_\eta = h \tag{3.5.7}$$

For the partially transformed governing equations,

$$\beta^{j}_{i} = \frac{\partial \xi^{j}}{\partial x^{i}} = \begin{bmatrix} \xi_x & \eta_x & \zeta_z \\ \xi_y & \eta_y & \zeta_y \\ \xi_z & \eta_z & \zeta_z \end{bmatrix} = \frac{1}{y_\eta} \begin{bmatrix} y_\eta & -y_\xi & 0 \\ 0 & 1 & 0 \\ 0 & -y_\zeta & y_\eta \end{bmatrix} \tag{3.5.8}$$

The metric coefficients are

$$\begin{aligned} h_1 &= \sqrt{g_{11}} = \sqrt{1 + y_\xi y_\xi} \\ h_2 &= \sqrt{g_{22}} = y_\eta \\ h_3 &= \sqrt{g_{33}} = y_\zeta \end{aligned} \tag{3.5.9}$$

Using this coordinate transformation, the moving boundary was converted into a new variable $h_2(\xi,\eta,\zeta)$ The solution domain in the curvilinear coordinate system is a rectangular domain: $0 \le \xi \le \xi_L, 0 \le \eta \le \eta_f, 0 \le \zeta \le \xi_W$, in which ξ_L , η_f , ζ_W are constants.

3.6 Free Surface Locating

One major factor making the present problem difficult is the unknown free surface. To represent the unknown free surface boundary, a variable $h_2(\xi,\eta,\zeta)$ must to be introduced. This variable is coupled with the other flow variables and must be determined iteratively.

In this thesis, the free surface is determined by integrating the concise momentum equation in the vertical direction to find the point at which the pressure is equal to atmosphere pressure.

The concise momentum equation in the η direction is

$$\frac{1}{\sqrt{g}}\frac{\partial}{\partial \xi^j}(\sqrt{g}\rho u^j u_2) = \frac{1}{\sqrt{g}}\frac{\partial}{\partial \xi^j}(\sqrt{g}\tau_2^j) - \frac{1}{2}\frac{\partial g_{jk}}{\partial \xi^2}(\tau^{jk} - \rho u^j u^k) - \frac{\partial p}{\partial \xi^2} + \gamma_2 \qquad (3.6.2)$$

Expanding and rearranging equation (3.6.2)

$$\frac{\partial p}{\partial \eta} = \gamma_2 - \frac{\partial}{\partial \eta}(\rho u^2 u_2) + \frac{\partial \tau_2^2}{\partial \eta} + R \qquad (3.6.3)$$

where

$$\begin{aligned} R = & -\rho u^1 \frac{\partial u_2}{\partial \xi} + u_2 \frac{\partial}{\partial \eta}(\rho u^2) - \rho u^3 \frac{\partial u_2}{\partial \zeta} \\ & + \frac{\partial \tau_2^1}{\partial \xi} + \frac{\partial \tau_2^3}{\partial \zeta} + \frac{\tau_2^1}{\sqrt{g}}\frac{\partial \sqrt{g}}{\partial \xi} + \frac{\tau_2^2}{\sqrt{g}}\frac{\partial \sqrt{g}}{\partial \eta} + \frac{\tau_2^3}{\sqrt{g}}\frac{\partial \sqrt{g}}{\partial \zeta} \\ & - \frac{1}{2}\frac{\partial g_{11}}{\partial \eta}(\tau^{11} - \rho u^1 u^1) - \frac{1}{2}\frac{\partial g_{22}}{\partial \eta}(\tau^{22} - \rho u^2 u^2) - \frac{1}{2}\frac{\partial g_{33}}{\partial \eta}(\tau^{33} - \rho u^3 u^3) \\ & - \frac{\partial g_{12}}{\partial \eta}(\tau^{12} - \rho u^1 u^2) - \frac{\partial g_{23}}{\partial \eta}(\tau^{23} - \rho u^2 u^3) - \frac{\partial g_{13}}{\partial \eta}(\tau^{13} - \rho u^1 u^3) \end{aligned}$$

The next step is to integrate equation (3.6.3) over a cell just below the free surface (refer to Figure 3.6.1).

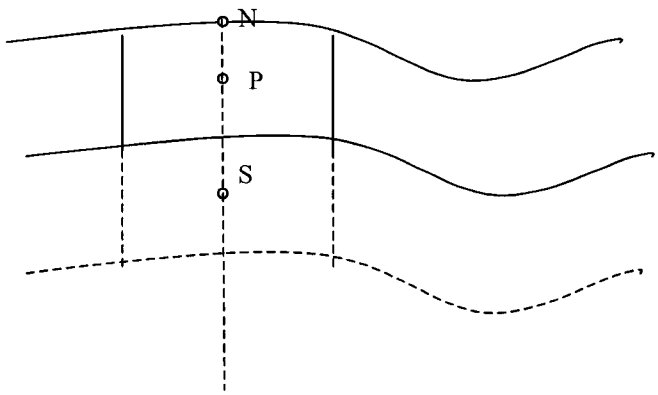

Figure 3.6.1 Integration under Free Surface

Assuming $R \approx R(\xi, \zeta)$ along line [N, P, S], the integration of equation (3.6.3) becomes

$$p_N - p_P = (\gamma_2 + R)(\eta_N - \eta_P) - (\rho u^2 u_2)_N + (\rho u^2 u_2)_P + (\tau_2^2)_N - (\tau_2^2)_P \qquad (3.6.4)$$

and

$$p_P - p_S = (\gamma_2 + R)(\eta_P - \eta_S) - (\rho u^2 u_2)_P + (\rho u^2 u_2)_S + (\tau_2^2)_P - (\tau_2^2)_S \qquad (3.6.5)$$

By combining equations (3.6.4) and (3.6.5), the time consuming-calculation of term R can be avoided.

$$(\eta_N - \eta_P) = (\eta_P - \eta_S)\frac{p_N - p_P + (\rho u^2 u_2)_N - (\rho u^2 u_2)_P - (\tau_2^2)_N - (\tau_2^2)_P}{p_P - p_S + (\rho u^2 u_2)_P - (\rho u^2 u_2)_S - (\tau_2^2)_P - (\tau_2^2)_S} \qquad (3.6.6)$$

Equation (3.6.6) indicates the pressure variation in the η direction is nearly linear but the slope of this linear distribution is not necessary γ_2.

If p_N is set to be zero, then a new $(\eta_N)_{new}$ can be estimated from equation (3.6.6).

With $(\eta_N)_{new}$, the grid system in equation (3.5.1) can be updated to make it fit the free surface. A new measurement coefficient $(h_2)_{new}$ can be calculated by

$$h_2(\xi,\eta,\varsigma)_{new} = h_2(\xi,\eta,\varsigma)\frac{\int_0^{(\eta_N)_{new}} h_2(\xi,\eta,\varsigma)d\eta}{\int_0^{\eta_N} h_2(\xi,\eta,\varsigma)d\eta} \tag{3.6.7}$$

The updated free surface can be found from

$$y(\xi,\varsigma) = \int_0^{\eta_N} h_2(\xi,\eta,\varsigma)_{new}\, d\eta \tag{3.6.8}$$

As the changes of velocity u^2, u_2 and shear stress τ_2^2 in the region near the free surface are smaller than the change in pressure, equation (3.6.6) can be further simplified to become

$$(\eta_N - \eta_P) = (\eta_P - \eta_S)\frac{p_N - p_P}{p_P - p_S} \tag{3.6.9}$$

When Cartesian velocity components are used, the velocities in equation (3.6.6) can be found by

$$\begin{aligned} u^2 &= \eta_x U + \eta_y V + \eta_z W \\ u_2 &= x_\eta U + y_\eta V + z_\eta W \end{aligned} \tag{3.6.10}$$

The expression for the shear stress is

$$\tau_2^2 = \mu_e \varepsilon_2^2 - \frac{2}{3}\rho K \tag{3.6.11}$$

using

$$\varepsilon_2^2 = \frac{\partial u^2}{\partial \xi^2} + g^{2m}\frac{\partial u_2}{\partial \xi^m} + u^m g^{p2}\left(\frac{\partial g_{2p}}{\partial \xi^m} - \frac{\partial g_{2m}}{\partial \xi^p}\right) \tag{3.6.12}$$

With the current free surface locating and grid updating method, the grid moves together with the free surface in the iteration in the same way as that in a Lagrangian grid method (Hirt et al., 1970) would, but the current method is much simpler. In comparison with Marker-and-Cell (MAC) method (Harlow and Welch, 1965) or Volume-of-Fluid (VOF) methods (Hirt and Nichols, 1981), the current free surface method can significantly save computer memory and reduce CPU time, because only the height of the surface must be stored and the height can be updated by a simple algebraic operation. In entire solution process, the computational effort to regenerate the grid is barely noticeable.

3.7 Representation of Obstacles

In the current numerical model the obstacles in the flow are allowed to have any shape, orientation and position. This variety requires a general method to model these obstacles. In this thesis, a marked cell method is used to represent obstacles, and FAVOR technique is used to represent boundary cells. By this method the cells inside the body of each obstacle are marked and assigned a very large viscosity coefficient. One difficulty in current study is that the grid changes when free surface is updated, so the marked cells may enter or leave the obstacle boundary when grid changes. Therefore, after free surface position is updated, the cells must to be marked again.

Since a grid can only change shape in vertical direction, a simple approach can be used to mark cells. Instead of marking three-dimensional cells one by one, only the positions of the upper and lower boundaries of the obstacles need be recorded or marked. As shown in Figure 3.7.1, the boundaries $[x_1, x_2]$, $[Z_1(x), Z_2(x)]$ and $[Y_1(x,z), Y_2(x,z)]$ are used to identify the cells inside the obstacles.

The marked cell method can be applied to obstacles of any shape. Since coordinates do not need to fit the possibly complex geometry of an obstacle, a simple coordinate system can be used. When the shape of the obstacle changes, a grid need not be regenerated. The tradeoff of this flexibility is that the boundary of an obstacle can cut through a cell.

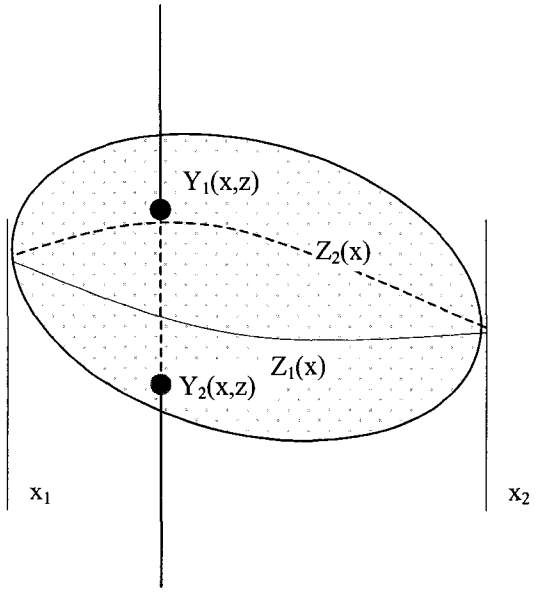

Figure 3.7.1 Marking Obstacles

To deal with these fractional cells on the boundary of the obstacles, the idea of the FAVOR technique (Flow Science, Inc.), an important feature in the commercial software *Flow-3D*, was adopted in the current study. By this technique, the portion of cell surfaces and the portion of volume blocked by obstacles in a fractional cell are calculated. To calculate the flux across a control surface, only the flux that crosses an actual open area is used.

Usually, the FAVOR technique is associated with rectangular grids. One disadvantage of rectangular grids is that they can not be refined locally. In this thesis, the FAVOR technique was extended to the current free surface fitted grid. This grid system is as simple as a rectangular grid system, but it can fit the free surface.

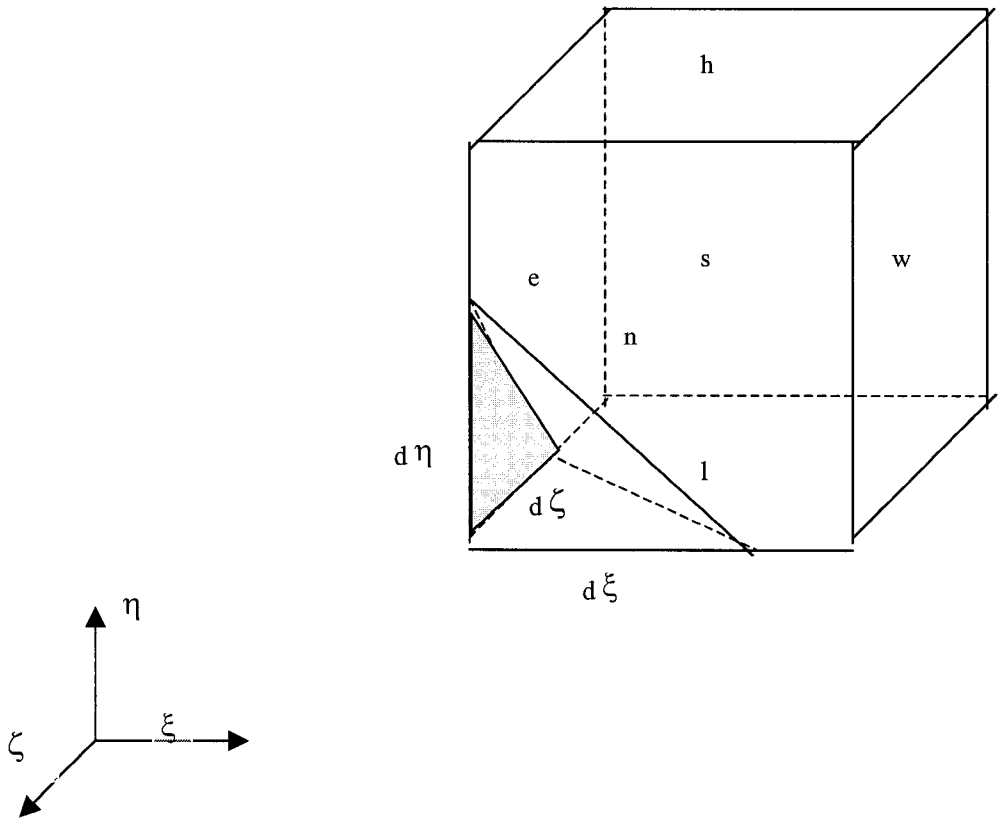

Figure 3.7.2 Ratio of Opening

An example is presented to demonstrate how to apply FAVOR idea.

For a continuity equation with source

$$\frac{1}{\sqrt{g}}\frac{\partial}{\partial \xi^j}(\sqrt{g}u^j) = S$$

it can be discretized as (refer to Figure 3.7.2)

$$(F_\xi \sqrt{g}\Delta\eta\Delta\zeta u)_e - (F_\xi \sqrt{g}\Delta\eta\Delta\zeta u)_w + (F_\eta \sqrt{g}\Delta\xi\Delta\zeta v)_n - (F_\eta \sqrt{g}\Delta\xi\Delta\zeta v)_s$$
$$(F_\varsigma \sqrt{g}\Delta\xi\Delta\eta w)_h - (F_\varsigma \sqrt{g}\Delta\xi\Delta\eta w)_l = F_v \sqrt{g}\Delta\xi\Delta\eta\Delta\zeta S$$

where

F_ξ, F_η, F_ζ	ratio of opening area to total area of a surface of a cell
Fv	ratio of opening volume to total volume of a cell

These opening ratios have to be calculated case by case. In this example, for surface e in Figure 3.7.2,

$$F_\xi = 1 - \frac{1}{2}\frac{d\eta d\zeta (h_2 h_3)_{bc}}{\Delta\eta\Delta\zeta (h_2 h_3)_c}$$

where $()_{bc}$ means at center of blocked area and $()_c$ means at center of the cell surface.

If there is no blockage, all ratios of opening are equal to 1.

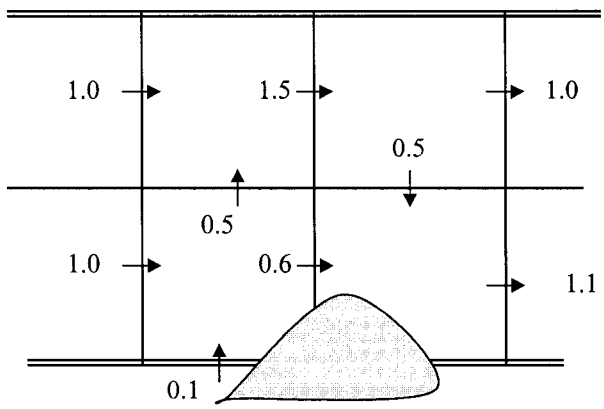

Figure 3.7.3 Mass Conservation

Figure 3.7.3 is used to show that FAVOR will not affect the mass conservation property of the Finite Volume Method. Since two neighbor cells always share the same area, velocity and blockage rate on that interface, the flux leaves a cell always equals the flux entering its neighbor cell. If the mass conservation is satisfied in each cell, then the mass conservation will be satisfied in whole domain of the solution.

In this model the FAVOR was only applied to convection terms but not to pressure gradient terms to avoid the difficulty to calculate pressure on the obstacle surface. On

those nodes inside the obstacles, velocity, turbulent energy and turbulent dissipation rate will be zeroes because large viscosity was assigned to these nodes. For an obstacle with irregular surface, how to apply wall function or evaluate turbulent stress on the obstacle surface need further study.

As mentioned in Chapter 2, an unstructured grid can be used to model boundaries of complex geometry, but it is very difficult to generate and update an unstructured grid. In an unstructured grid, a list of indices of all neighbor cells must be stored. If the boundary of the flow changes, the members in the list may also change. This is the reason for developing this free surface fitted, FAVOR enabled grid system.

It should be pointed out that obstacles could be treated by FAVOR itself. The purpose of combining FAVOR with the marked-cell method is to keep the option that FAVOR can be employed or not employed depending on obstacle shape.

3.8 Summary

In this chapter, a combination of the QUICK difference scheme with the UMIST limiter on a non-uniform grid was developed, and proved to be notably better than the Power Law difference scheme in numerical accuracy. A simple and practical curvilinear coordinate system is constructed. This coordinate can fit a free surface smoothly, and it is easy to regenerate. An efficient free surface locating and grid updating method was developed to allow a quick regeneration of the grid. By extending FAVOR to the free surface fitted coordinate system, obstacles having an arbitrary shape in the flow can be modeled. Also, detailed pressure correction procedures in three curvilinear coordinate systems were derived and assessed. The studies in this chapter establish a foundation for an efficient and flexible numerical model to determine complex free surface flows around large obstacles.

Chapter 4

Simulation of Free Surface Flow around Large Obstacles

4.1 Numerical Model to Simulate Free Surface Flow around Obstacles

4.1.1 Basic Concepts

Based on the studies in Chapter 2 and 3, a numerical model was developed to calculate free surface flow over and around large obstacles. At this first stage of the study the partially transformed governing equations are used. This approach is reasonable because little distortion is anticipated if one only requires the coordinate system to fit the free surface but not the surface of obstacles. Although the concise fully transformed governing equations have several advantages, they are still more complex for three-dimensional turbulent flow than are the partially transformed governing equations. In a subsequent study, after the numerical model is proven to work properly, the concise fully transformed governing equations will be developed and applied.

The K-ε turbulence model is used in the present numerical model. In comparison with other high-order turbulent models, it requires less computational effort. Generally, within the same computational capability, to improve numerical results by refining grid is more efficient than adopting a higher-order turbulence model.

In the current numerical model the governing equations are solved by a SIMPLE-like approach (Patankar, 1980) on finite volume grids. This is one of the most popular and reliable approach to solve fluid flow and heat transfer problems. The QUICK difference scheme can produce third order accuracy, but the oscillations associated with the scheme may cause the numerical results to deteriorate. So a UMIST limiter is applied to the QUICK scheme in unequally spaced grids. The numerical testing in Chapter 3 shows that this approach works very well.

To locate the position of free surface, a Lagrangian grid is the best choice if an efficient way to generate boundary fitted grids can be found. Efficiency of grid generation is very important because the grids must be regenerated each time after the free surface location is updated. Actually, the major reason that makes a Lagrangian grid less popular is the difficulty of generating a curvilinear coordinate grid if the boundary geometry is complex. To generate a coordinate system to fit the boundary of an obstacle such as a natural rock is almost impossible. Even if this kind of coordinate system could be generated, it may be too distorted to maintain reasonable numerical accuracy.

The solution to model a free surface flow with large obstacles in this numerical model is to combine a free surface fitted coordinate system with the FAVOR technique. The key point is to separate obstacle coordinate fitting from free surface coordinate fitting. If grids are only required to fit the free surface, they can be generated by a simple scheme such as equation (4.1.1), which is an analytical transformation and can be used to regenerate a grid easily. In this grid system, the free surface locating can be done by simply extending or shrinking the coordinate in the vertical direction. A second advantage to separate obstacle fitting from free surface fitting is that any restrictions on obstacle geometry are removed. Without obstacle fitting, part of the grid will be occupied by the obstacles. The FAVOR technique was used to include the effect of partially open cell surfaces.

In following paragraphs, a detailed formulation of this numerical model will be given.

The curvilinear coordinate system (ξ, η, ζ) in the model has already been defined in Chapter 3:

$$\begin{cases} x = \xi \\ y = y_b(\xi,\zeta) + \int_0^{\eta} h_2(\xi,\eta,\zeta)d\eta \\ z = \zeta \end{cases} \tag{4.1.1}$$

In this coordinate system the turbulent flow can be solved from the following governing equations.

Continuity Equation

$$\frac{\partial(\sqrt{g}u^1)}{\partial\xi} + \frac{\partial(\sqrt{g}u^2)}{\partial\eta} + \frac{\partial(\sqrt{g}u^3)}{\partial\zeta} = 0 \tag{4.1.2}$$

where $\sqrt{g} = y_\eta = h_2$ and h_2 is metric coefficient in the η direction.

The contravariant velocity components in the curvilinear coordinate system are u^1, u^2, u^3 :

$$\begin{cases} u^1 = U \\ u^2 = \eta_x U + \eta_y V + \eta_z W \\ u^3 = W \end{cases} \tag{4.1.3}$$

And (U, V, W) are the Cartesian components of the velocity.

Momentum Equation

$$\frac{\partial}{\partial \xi^j}(\sqrt{g}\rho u^j U^i) = \frac{\partial}{\partial \xi^j}(\mu_e \sqrt{g} g^{jm} \frac{\partial U^i}{\partial \xi^m})_{j=m} + S_\phi U^i + S_c - \sqrt{g}\beta^{mi} \frac{\partial p}{\partial \xi^m}_{i=m} \quad (i=1,2,3) \qquad (4.1.4)$$

$$S_c = \frac{\partial}{\partial \xi^j}\left[\mu_e \sqrt{g}\left(g^{jm} \frac{\partial U^i}{\partial \xi^m}_{j\neq m} + \beta^j{}_k \beta^{mi} \frac{\partial U^k}{\partial \xi^m}\right) - \frac{2}{3}\sqrt{g}\beta^{ji}\rho K\right] - S_\phi U^i - \sqrt{g}\,\beta^{mi} \frac{\partial p}{\partial \xi^m}_{i\neq m} + \sqrt{g}\gamma^i$$

Where γ^i is the gravity vector, defined as $[\gamma^1, \gamma^2, \gamma^3] = [0, -\rho g, 0]$.

To simplify the problem, S_ϕ can be set to zero.

From equation (3.5.8) the coefficients β^{ij} can be calculated by

$$\begin{bmatrix} \beta^1{}_1 & \beta^1{}_2 & \beta^1{}_3 \\ \beta^2{}_1 & \beta^2{}_2 & \beta^2{}_3 \\ \beta^3{}_1 & \beta^3{}_2 & \beta^3{}_3 \end{bmatrix} = \begin{bmatrix} \beta^{11} & \beta^{12} & \beta^{13} \\ \beta^{21} & \beta^{22} & \beta^{23} \\ \beta^{31} & \beta^{32} & \beta^{33} \end{bmatrix} = \begin{bmatrix} 1 & 0 & 0 \\ \frac{-y_\xi}{h} & \frac{1}{h} & \frac{-y_\zeta}{h} \\ 0 & 0 & 1 \end{bmatrix} \qquad (4.1.5)$$

With a given free surface elevation and a distribution of $h_2(\xi, \eta, \zeta)$ the geometric tensors can be calculated from

$$\begin{bmatrix} g^{11} & g^{12} & g^{13} \\ g^{21} & g^{22} & g^{23} \\ g^{31} & g^{32} & g^{33} \end{bmatrix} = \begin{bmatrix} 1 & \frac{-y_\xi}{h} & 0 \\ \frac{-y_\xi}{h} & \frac{(y_\xi)^2 + 1 + (y_\zeta)^2}{h^2} & \frac{-y_\zeta}{h} \\ 0 & \frac{-y_\zeta}{h} & 1 \end{bmatrix} \qquad (4.1.6)$$

The expanded momentum equations in the three coordinate directions are the followings:

U-Equation

$$\frac{\partial}{\partial\xi}(\rho hu^1U)+\frac{\partial}{\partial\eta}(\rho hu^2U)+\frac{\partial}{\partial\zeta}(\rho hu^3U)$$
$$=\frac{\partial}{\partial\xi}(\mu_e h\frac{\partial U}{\partial\xi})+\frac{\partial}{\partial\eta}(\mu_e(\frac{(y_\xi)^2+1+(y_\zeta)^2}{h})\frac{\partial U}{\partial\eta})+\frac{\partial}{\partial\zeta}(\mu_e h\frac{\partial U}{\partial\zeta})-h\frac{\partial p}{\partial\xi}+S_U$$

(4.1.7)

$$S_U=-\frac{\partial}{\partial\xi}(\mu_e y_\xi\frac{\partial U}{\partial\eta})-\frac{\partial}{\partial\eta}(\mu_e y_\xi\frac{\partial U}{\partial\xi})-\frac{\partial}{\partial\eta}(\mu_e y_\zeta\frac{\partial U}{\partial\zeta})-\frac{\partial}{\partial\zeta}(\mu_e h y_\zeta\frac{\partial U}{\partial\eta})$$
$$+\frac{\partial}{\partial\xi}[\mu_e(h\frac{\partial U}{\partial\xi}-y_\xi\frac{\partial U}{\partial\eta})]+\frac{\partial}{\partial\eta}[-\mu_e\frac{y_\xi}{h}(h\frac{\partial U}{\partial\xi}-y_\xi\frac{\partial U}{\partial\eta})]$$
$$+\frac{\partial}{\partial\eta}[\frac{\mu_e}{h}(h\frac{\partial V}{\partial\xi}-y_\xi\frac{\partial V}{\partial\eta})]$$
$$+\frac{\partial}{\partial\eta}[-\mu_e\frac{y_\zeta}{h}(h\frac{\partial W}{\partial\xi}-y_\xi\frac{\partial W}{\partial\eta})]+\frac{\partial}{\partial\zeta}[\mu_e(h\frac{\partial W}{\partial\xi}-y_\xi\frac{\partial W}{\partial\eta})]$$
$$-\frac{2}{3}\rho[h\frac{\partial K}{\partial\xi}-y_\xi\frac{\partial K}{\partial\eta}]+y_\xi\frac{\partial p}{\partial\eta}$$

Following equations can be used to map this equation to discretized equations (3.2.1) and (3.2.8).

$$\phi=hU$$
$$\Gamma_\xi=\mu_e h$$
$$\Gamma_\eta=\mu_e(\frac{(y_\xi)^2+1+(y_\zeta)^2}{h})$$
$$\Gamma_\zeta=\mu_e h$$
$$S_\phi=-h\frac{\partial p}{\partial\xi}+S_U$$

V-Equation

$$\frac{\partial}{\partial\xi}(\rho hu^1V)+\frac{\partial}{\partial\eta}(\rho hu^2V)+\frac{\partial}{\partial\zeta}(\rho hu^3V)$$
$$=\frac{\partial}{\partial\xi}(\mu_e h\frac{\partial V}{\partial\xi})+\frac{\partial}{\partial\eta}(\mu_e(\frac{(y_\xi)^2+1+(y_\zeta)^2}{h})\frac{\partial V}{\partial\eta})+\frac{\partial}{\partial\zeta}(\mu_e h\frac{\partial V}{\partial\zeta})-\frac{\partial p}{\partial\eta}+S_V \quad (4.1.8)$$

$$S_V=-\frac{\partial}{\partial\xi}(\mu_e y_\xi\frac{\partial V}{\partial\eta})-\frac{\partial}{\partial\eta}(\mu_e y_\xi\frac{\partial V}{\partial\xi})-\frac{\partial}{\partial\eta}(\mu_e y_\zeta\frac{\partial V}{\partial\zeta})-\frac{\partial}{\partial\zeta}(\mu_e y_\zeta\frac{\partial V}{\partial\eta})$$
$$+\frac{\partial}{\partial\xi}(\mu_e\frac{\partial U}{\partial\eta})+\frac{\partial}{\partial\eta}[\frac{\mu_e}{h}(-y_\xi\frac{\partial U}{\partial\eta}+\frac{\partial V}{\partial\eta}-y_\zeta\frac{\partial W}{\partial\eta})+\frac{\partial}{\partial\zeta}(\mu_e\frac{\partial W}{\partial\eta})]-\frac{2}{3}\rho\frac{\partial K}{\partial\eta}+h\gamma^2$$

Following equations can be used to map this equation to discretized equations (3.2.1) and (3.2.8).

$$\phi=hV$$
$$\Gamma_\xi=\mu_e h$$
$$\Gamma_\eta=\mu_e(\frac{(y_\xi)^2+1+(y_\zeta)^2}{h})$$
$$\Gamma_\zeta=\mu_e h$$
$$S_\phi=-h\frac{\partial p}{\partial\eta}+S_V$$

W-Equation

$$\frac{\partial}{\partial\xi}(\rho hu^1W)+\frac{\partial}{\partial\eta}(\rho hu^2W)+\frac{\partial}{\partial\zeta}(\rho hu^3W)$$
$$=\frac{\partial}{\partial\xi}(\mu_e h\frac{\partial W}{\partial\xi})+\frac{\partial}{\partial\eta}(\mu_e h(\frac{(y_\xi)^2+1+(y_\zeta)^2}{h})\frac{\partial W}{\partial\eta})+\frac{\partial}{\partial\zeta}(\mu_e h\frac{\partial W}{\partial\zeta})-h\frac{\partial p}{\partial\zeta}+S_W \quad (4.1.9)$$

$$S_W = -\frac{\partial}{\partial\xi}(\mu_e y_\xi \frac{\partial W}{\partial\eta}) - \frac{\partial}{\partial\eta}(\mu_e y_\xi \frac{\partial W}{\partial\xi}) - \frac{\partial}{\partial\eta}(\mu_e y_\zeta \frac{\partial W}{\partial\zeta}) - \frac{\partial}{\partial\zeta}(\mu_e y_\zeta \frac{\partial W}{\partial\eta})$$
$$+ \frac{\partial}{\partial\xi}[\mu_e(h\frac{\partial U}{\partial\zeta} - y_\zeta \frac{\partial U}{\partial\eta})] + \frac{\partial}{\partial\eta}[-\mu_e \frac{y_\xi}{h}(h\frac{\partial U}{\partial\zeta} - y_\zeta \frac{\partial U}{\partial\eta}))]$$
$$+ \frac{\partial}{\partial\eta}[\frac{\mu_e}{h}(h\frac{\partial V}{\partial\zeta} - y_\zeta \frac{\partial V}{\partial\eta})]$$
$$+ \frac{\partial}{\partial\eta}[-\mu_e \frac{y_\zeta}{h}(h\frac{\partial W}{\partial\zeta} - y_\zeta \frac{\partial W}{\partial\eta})] + \frac{\partial}{\partial\zeta}[\mu_e(h\frac{\partial W}{\partial\zeta} - y_\zeta \frac{\partial W}{\partial\eta})]$$
$$-\frac{2}{3}\rho[h\frac{\partial K}{\partial\zeta} - y_\zeta \frac{\partial K}{\partial\eta}] + y_\zeta \frac{\partial p}{\partial\eta}$$

Following equations can be used to map this equation to discretized equations (3.2.1) and (3.2.8).

$$\phi = hW$$
$$\Gamma_\xi = \mu_e h$$
$$\Gamma_\eta = \mu_e(\frac{(y_\xi)^2 + 1 + (y_\zeta)^2}{h})$$
$$\Gamma_\zeta = \mu_e h$$
$$S_\phi = -h\frac{\partial p}{\partial\zeta} + S_W$$

K-Turbulence Model Equation

$$\frac{\partial}{\partial\xi}(h\rho u^1 K)\frac{\partial}{\partial\eta}(h\rho u^2 K)\frac{\partial}{\partial\zeta}(h\rho u^3 K)$$
$$= \frac{\partial}{\partial\xi}(\Gamma_k h\frac{\partial K}{\partial\xi}) + \frac{\partial}{\partial\eta}(\Gamma_k(\frac{(y_\xi)^2 + 1 + (y_\zeta)^2}{h})\frac{\partial K}{\partial\eta}) + \frac{\partial}{\partial\zeta}(\Gamma_k h\frac{\partial K}{\partial\zeta}) + S_K \qquad (4.1.10)$$

In this equation

$$S_K = -\frac{\partial}{\partial\xi}[\Gamma_k y_\xi \frac{\partial K}{\partial\eta}] - \frac{\partial}{\partial\eta}[\Gamma_k(y_\xi \frac{\partial K}{\partial\xi} + y_\zeta \frac{\partial K}{\partial\zeta})]$$
$$-\frac{\partial}{\partial\zeta}[\Gamma_k y_\zeta \frac{\partial K}{\partial\eta}] + \rho\sqrt{g}(G_e - \varepsilon)$$

Following equations can be used to map this equation to discretized equations (3.2.1) and (3.2.8).

$$\phi = hK$$
$$\Gamma_\xi = \Gamma_k h$$
$$\Gamma_\eta = \Gamma_k \left(\frac{(y_\xi)^2 + 1 + (y_\zeta)^2}{h}\right)$$
$$\Gamma_\zeta = \Gamma_k h$$
$$S_\phi = S_K$$

ε-Turbulence Model Equation

$$\frac{\partial}{\partial\xi}(h\rho u^1\varepsilon) + \frac{\partial}{\partial\xi^j}(h\rho u^2\varepsilon) + \frac{\partial}{\partial\xi^j}(h\rho u^3\varepsilon)$$
$$= \frac{\partial}{\partial\xi}(\Gamma_\varepsilon h\frac{\partial\varepsilon}{\partial\xi}) + \frac{\partial}{\partial\eta}(\Gamma_\varepsilon(\frac{(y_\xi)^2 + 1 + (y_\zeta)^2}{h})\frac{\partial\varepsilon}{\partial\eta}) + \frac{\partial}{\partial\zeta}(\Gamma_\varepsilon h\frac{\partial\varepsilon}{\partial\zeta}) + S_\varepsilon \qquad (4.1.11)$$

In these equation

$$S_\varepsilon = -\frac{\partial}{\partial\xi}[\Gamma_\varepsilon y_\xi\frac{\partial\varepsilon}{\partial\eta}] - \frac{\partial}{\partial\eta}[\Gamma_\varepsilon(y_\xi\frac{\partial\varepsilon}{\partial\xi} + y_\zeta\frac{\partial\varepsilon}{\partial\zeta})]$$
$$-\frac{\partial}{\partial\zeta}[\Gamma_\varepsilon y_\zeta\frac{\partial\varepsilon}{\partial\eta}] + h\rho(C_1G_e\frac{\varepsilon}{K} - C_2\frac{\varepsilon}{K^2})$$

Following equations can be used to map this equation to discretized equations (3.2.1) and (3.2.8).

$$\phi = h\varepsilon$$
$$\Gamma_\xi = \Gamma_\varepsilon h$$
$$\Gamma_\eta = \Gamma_\varepsilon \left(\frac{(y_\xi)^2 + 1 + (y_\zeta)^2}{h}\right)$$
$$\Gamma_\zeta = \Gamma_\varepsilon h$$
$$S_\phi = S_\varepsilon$$

The shear stress can be calculated by

$$\tau^{ij} = \mu_e \varepsilon^{ij} - \frac{2}{3}\delta^{ij}\rho K \tag{4.1.12}$$

In which

$$\varepsilon^{ij} = \beta^{mj}\frac{\partial U^i}{\partial \xi^m} + \beta^{mi}\frac{\partial U^j}{\partial \xi^m} \tag{4.1.13}$$

The components of equation (4.1.13) are

$$\begin{aligned}
\varepsilon^{11} &= 2\left(\frac{\partial U}{\partial \xi} - \frac{y_\xi}{h}\frac{\partial U}{\partial \eta}\right) \\
\varepsilon^{22} &= 2\left(\frac{1}{h}\frac{\partial V}{\partial \eta}\right) \\
\varepsilon^{33} &= 2\left(\frac{\partial W}{\partial \zeta} - \frac{y_\zeta}{h}\frac{\partial W}{\partial \eta}\right) \\
\varepsilon^{12} &= \varepsilon^{21} = \frac{1}{h}\frac{\partial U}{\partial \eta} + \frac{\partial V}{\partial \xi} - \frac{y_\xi}{h}\frac{\partial V}{\partial \eta} \\
\varepsilon^{23} &= \varepsilon^{32} = \frac{1}{h}\frac{\partial W}{\partial \eta} + \frac{\partial V}{\partial \zeta} - \frac{y_\zeta}{h}\frac{\partial V}{\partial \eta} \\
\varepsilon^{31} &= \varepsilon^{13} = \frac{\partial W}{\partial \xi} - \frac{y_\xi}{h}\frac{\partial W}{\partial \eta} + \frac{\partial U}{\partial \zeta} - \frac{y_\zeta}{h}\frac{\partial U}{\partial \eta}
\end{aligned} \tag{4.1.14}$$

The terms in $S_U, S_V, S_W, S_K, S_\varepsilon$ can be discretized by center difference scheme. With these geometric tensor components specified, the velocity, pressure and turbulence characteristics K, ε can be determined from equations (4.1.2) and (4.1.7) to (4.1.11).

Solution Procedures

1. Assume hydrostatic pressure
2. Solve momentum equations to obtain U, V and W
3. Solve the pressure correction equation to obtain p′

4. Modify pressure and velocity by p′
5. Solve turbulence model to obtain K and ε
6. Check for convergence?
7. Go back to step 2

4.1.2 Boundary Conditions

In this section the application of boundary conditions for the solution will be discussed by using an example of turbulent flow in an open channel with straight walls. The basic coordinates x, y, z point in the downstream, vertical and transverse directions, respectively.

a. Upstream Boundary

The inlet velocity U is assumed to have a $\frac{1}{n}$ power law distribution and V, W are assumed to be zero.

$$U = \frac{Q}{\int_A (\frac{2y_n z_n}{HB})^{\frac{1}{n}} dA} (\frac{2y_n z_n}{HB})^{\frac{1}{n}} \quad (4.1.15)$$

$$V = 0 \quad (4.1.16)$$

$$W = 0 \quad (4.1.17)$$

Where y_n, z_n are distances measured from the bed and side walls. The water depth is H and the width of the channel is B. n=7 is a constant which is normally used for fully-developed turbulence along a smooth boundary, and Q is the total volume flow rate.

It is not easy to determine the appropriate values of the turbulent energy K and turbulence dissipation rate ε along the upstream boundary. An assumption was used

that the disturbance of turbulent energy and dissipation rate at the upstream boundary are not so important, so long as the region of interest is far enough from the upstream boundary. With this assumption, a simple boundary condition expressing the local equilibrium of turbulence is applied (White, 1974).

At the upstream boundary the turbulent kinetic energy per unit mass is assumed to be a constant that can be calculated from local equilibrium conditions as

$$K = \frac{u_\tau^2}{C_\mu^{1/2}} \tag{4.1.18}$$

where u_τ is the shear velocity that must be estimated from experimental data or otherwise specified. The other constant is $C_\mu = 0.09$.

The turbulence dissipation rate ε is assumed to be

$$\varepsilon = \frac{u_\tau^3}{\chi y_n} \tag{4.1.19}$$

where

$$\chi y_n = \min(0.4 y_n,\ 0.09H)$$

b. Downstream Boundary

At the downstream boundary the gradients of all of the variables in the mainstream direction are assumed to be zero. This assumes the downstream boundary is far enough from the obstacles that flow changes in a steady rate in mainstream direction.

$$\frac{\partial U}{\partial \xi} = \frac{\partial V}{\partial \xi} = \frac{\partial W}{\partial \xi} = \frac{\partial K}{\partial \xi} = \frac{\partial \varepsilon}{\partial \xi} = \frac{\partial p}{\partial \xi} = 0 \tag{4.1.20}$$

c. Free Surface Boundary

On the free surface, the component of velocity normal to the surface should be zero. The normal vector $\vec{n}$ on the free surface η = constant is

$$\vec{n} = \frac{\vec{\nabla}\eta}{\left|\vec{\nabla}\eta\right|} = \frac{\vec{e}^2}{\left|\vec{e}^2\right|}$$

Thus the velocity boundary condition on free surface is

$$v_n = \vec{v}\cdot\vec{n} = \frac{u^2}{\left|\vec{e}^2\right|} = 0$$

or

$$u^2 = -y_\xi U + V - y_\varsigma W = 0 \qquad (4.1.21)$$

In which u^2 is the contravariant component of the velocity.

For velocity components U and V, it is assumed

$$\frac{\partial U}{\partial \eta} = \frac{\partial V}{\partial \eta} = 0 \qquad (4.1.22)$$

On the free surface the turbulent energy and dissipation rate are assumed to be zero. The pressure is chosen to be the atmospheric pressure. Symmetric boundary condition for turbulence on free surface was tested. It appears the symmetric boundary condition will under estimate free surface waves. This assumption may be overly simplified. The more detailed turbulence boundary condition such as (W. Rodi, 1980) should be studied.

$$p = p_a \qquad (4.1.23)$$

$$K = 0 \qquad (4.1.24)$$

$$\varepsilon = 0 \qquad (4.1.25)$$

d. Wall Boundaries

On solid walls all required values of variables are zero.

Since the K-ε turbulence model can not be applied in a near-wall region, a simple wall function method is used to determine the turbulent viscosity.

The log law velocity distribution near a smooth wall is

$$\frac{U}{\mu_\tau} = \frac{1}{\kappa}\ln(Ey^+) \tag{4.1.26}$$

with $\kappa = 0.4$ and $E = 9.0$.

From local equilibrium conditions in the near-wall region,

$$\mu_\tau^2 = \frac{\tau_w}{\rho} = \sqrt{C_\mu K} \tag{4.1.27}$$

Then

$$y^+ = \frac{yu_\tau}{\mu_l} = \frac{y(C_\mu K)^{\frac{1}{4}}}{\mu_l} \tag{4.1.28}$$

Suppose on the first node away from the wall that the velocity is U_2 and the distance between that node and the wall is Δy. Then the shear stress can be approximated as

$$\tau_w = \rho u_\tau^2 = \mu_e \frac{U_2}{\Delta y} \tag{4.1.29}$$

To apply equation (4.1.27) to U_2,

$$\mu_e \frac{U_2}{\Delta y} = \mu_e \frac{\mu_\tau}{\Delta y \kappa} \ln(Ey_2^+) = \rho \mu_\tau^2 \tag{4.1.30}$$

or

$$\mu_e \frac{1}{\mu_l \kappa} \ln(Ey_2^+) = \frac{\rho \mu_\tau \Delta y}{\mu_l} = y_2^+ \tag{4.1.31}$$

Finally,

$$\mu_e = \frac{y_2^+ \mu_l \kappa}{\ln(Ey_2^+)} \tag{4.1.32}$$

This equation can only be applied in the near wall-region and above the viscous sub-layer. In summary, the effective viscosity coefficient is given by

$$\mu_e = \mu_l \qquad (y^+ \le 11.6) \tag{4.1.33}$$

$$\mu_e = \frac{y_2^+ \mu_l \kappa}{\ln(Ey_2^+)} \qquad (11.6 < y^+ < 120) \tag{4.1.34}$$

$$\mu_e = \mu_l + \rho C_\mu \frac{K^2}{\varepsilon} \qquad (120 \le y^+) \tag{4.1.35}$$

where μ_l is the laminar viscosity.

After numerical grid is generated, it is necessary to check the y^+ value for the first cell and to adjust the grid size near the wall if necessary to ensures that at least one row of cells are in the region where log-law is applicable.

4.2 Application to Hydraulic Jump

4.2.1 Submerged Hydraulic Jump

To verify the applicability of the current numerical model, this model was first used to reproduce an experiment about flow in a submerged hydraulic jump. In this experiment detailed measurements of velocity and turbulence characteristics are provided.

This experiment was carried out in the T. Blench Hydraulic Laboratory at the University of Alberta by D. Long, P. M. Steffler and N. Rajaratnam (1990), and related numerical results are also available (Long, Steffler and Rajaratnam, 1991). As shown in Figure 4.2.1, the submerged jump was located just downstream from a vertical gate in a horizontal rectangular channel that was 0.467m wide, 0.515m deep and 0.75m long with two glass walls and an aluminum bed. The heights were y_1=0.015 m and y_2=0.206 m. The flow velocity was controlled by the sluice gate and was set to 3.14 m/s at the plane of the gate. The corresponding Froude number in terms of inlet velocity and y_1 was 8.19. The velocity and turbulence measurements were collected by a Laser Doppler Anemometer (LDA) system. The LDA is more accurate than common probes, and it can measure detailed turbulence fluctuations. (Steffler, Rajaratnam and Peterson, 1985)

Since the channel is very wide in comparison with the water depth, the flow can be assumed to be two-dimensional, so long as measurements are not taken near the walls. This assumption is also verified by a numerical test in this section. A 50*40 resolution in the x*y Plane is used. A sample plot of a grid is shown in Figure 4.2.2.

Using the current numerical model with the boundary conditions specified in Section 4.1.2, the Reynolds-averaged velocity, pressure, turbulent energy and turbulence dissipation were calculated. In Figure 4.2.3, the horizontal velocity distribution is plotted and it shows very good agreement with the measured data. For this kind of

flow the development of velocity is controlled by wall friction, the turbulent viscosity and the free surface location. The comparison results indicate that the wall function, the turbulence model and the free surface locating technique in this numerical model are good approaches for a simple channel flow.

In Figure 4.2.4 the free surface profile is plotted. Very good agreement between the calculation and the measured data is observed, except for a small deviation near the entry gate. This deviation is tolerable because there are some factors in the real flow that were not considered in the numerical model. One example is air entrainment that may not be a critical factor for the overall submerged hydraulic jump flow but it may affect the local free surface profile.

Although there are no experimental data available for comparison of calculated and measured pressure distributions, the calculated pressure is plotted in Figure 4.2.5. An abrupt change in pressure was found near the lip of the gate. This change shows the effect of dynamic pressure in a high-speed flow.

This experiment provided detailed turbulence data. Figures 4.2.6 to 4.2.8 show the distribution of turbulence intensities $\sqrt{\overline{u'u'}}$, $\sqrt{\overline{u'v'}}$ and $\sqrt{\overline{v'v'}}$ from measurement and from numerical calculations. The result shows that the current numerical model can capture all of the important turbulence characteristics. The quantities of $\sqrt{\overline{u'u'}}$, $\sqrt{\overline{u'v'}}$ and $\sqrt{\overline{v'v'}}$ are also called turbulence shear stresses per unit mass and can be calculated from equation (4.1.12). For most turbulent flows, the shear stress values are primarily influenced by turbulent mixing. Information about shear stress is very important in study of channel bed scour, bed settlement transportation and stability of hydraulic structures. It is a very attractive feature when a numerical model can produce reliable shear stress information.

To verify the two-dimensional assumption, the numerical model was used to simulate the same flow problem with a three-dimensional model. Figure 4.2.9A shows flow

patterns from the 3-D model at sections of z = 0.05B, 0.25B and 0.45B, where B is the channel width and the flow pattern from 2-D model. It shows that at z = 0.25B and z = 0.45B, flow patterns from the 3-D model are very similar to the 2-D flow pattern. That means the 2-D assumption is applicable to a range approximately the middle 50% of channel width. Figure 4.2.9B presents the comparison of the free surfaces from the 2-D and 3-D calculations. The conclusion is that, except for a region close to channel side walls, the two-dimensional assumption is a good approximation.

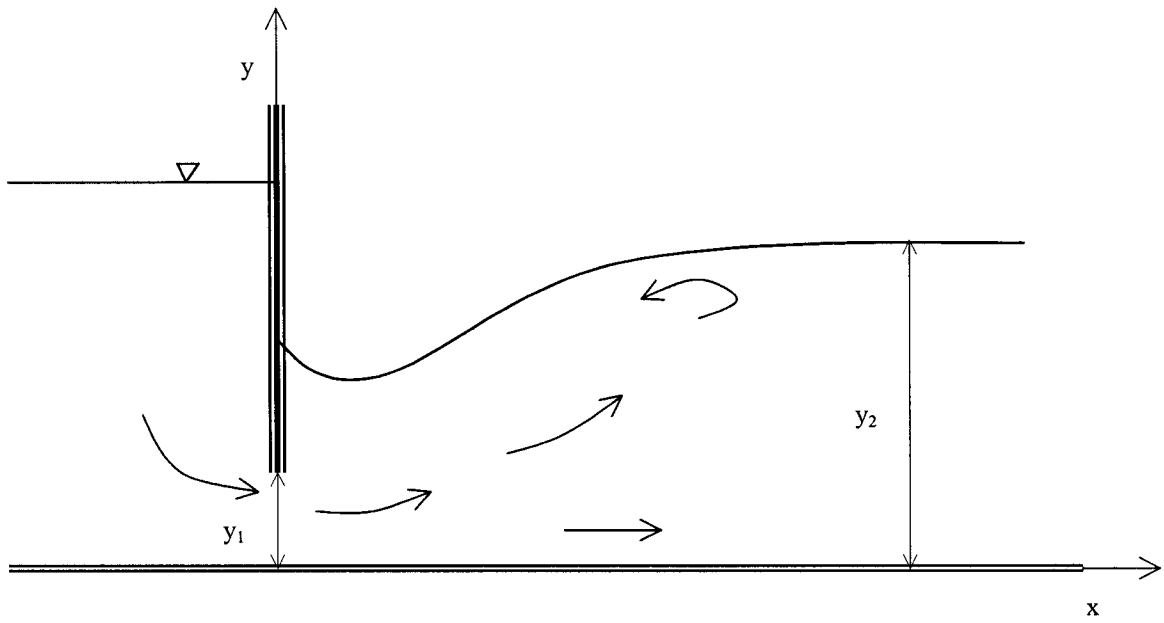

Figure 4.2.1 Submerged Hydraulic Jump

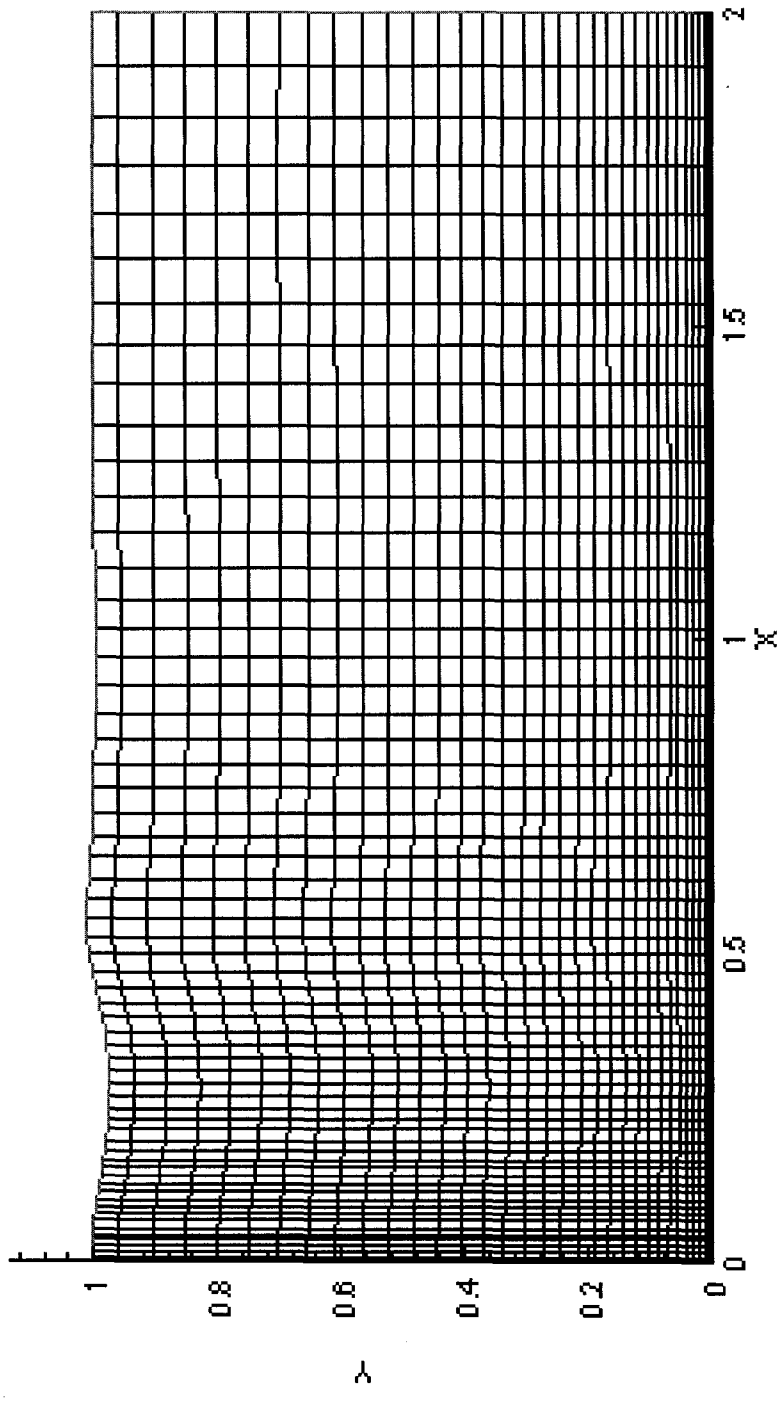

Figure 4.2.2 Grid for Numerical Solution

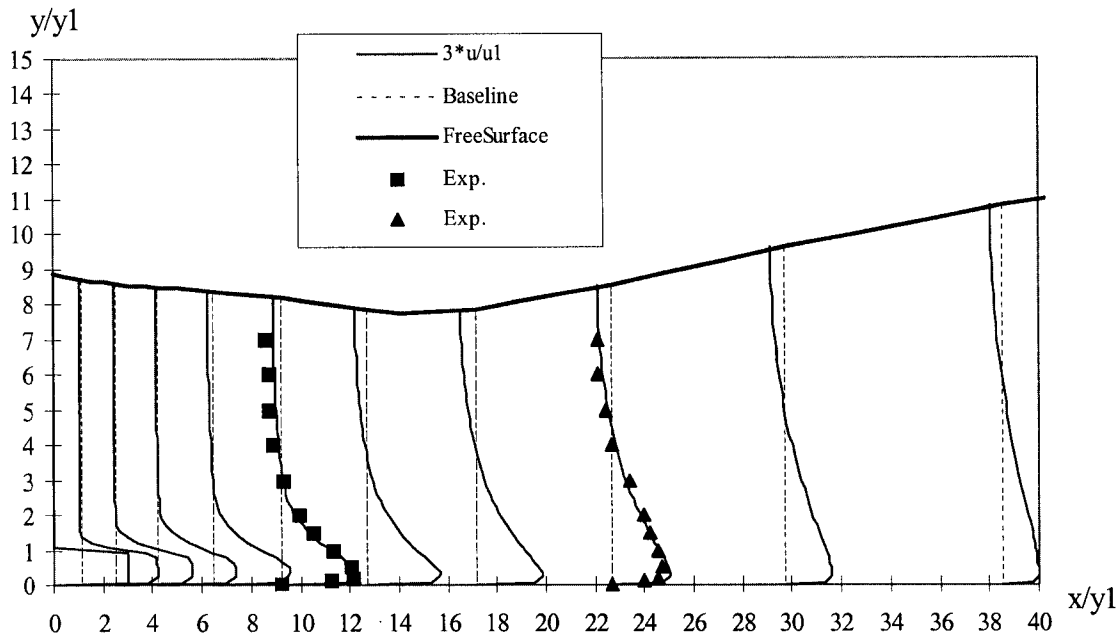

Figure 4.2.3 Velocity u/u_1; Scale 3:1

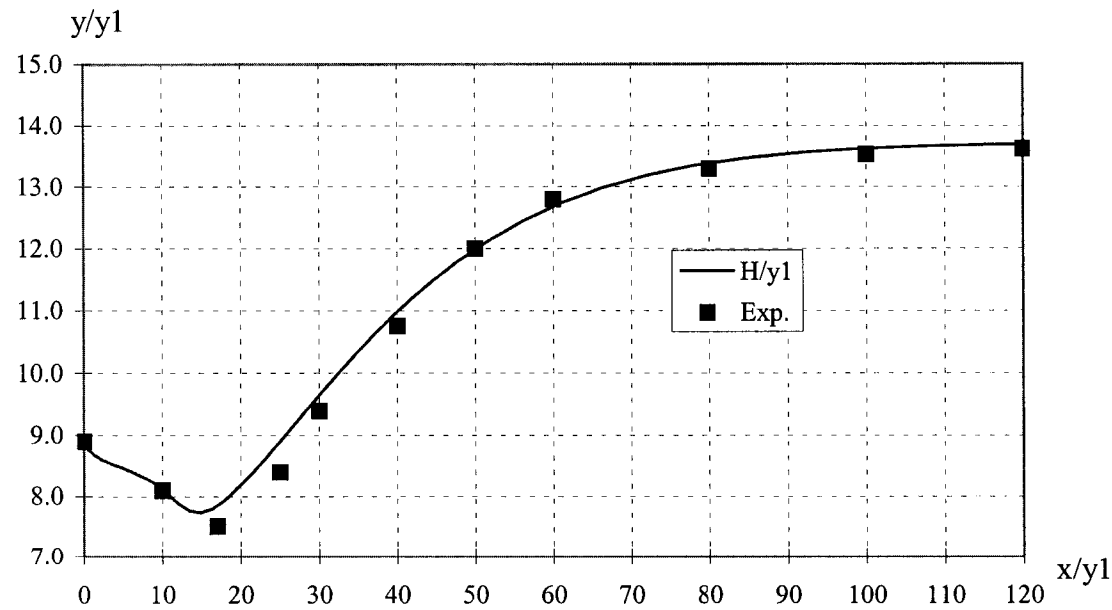

Figure 4.2.4 Free Surface

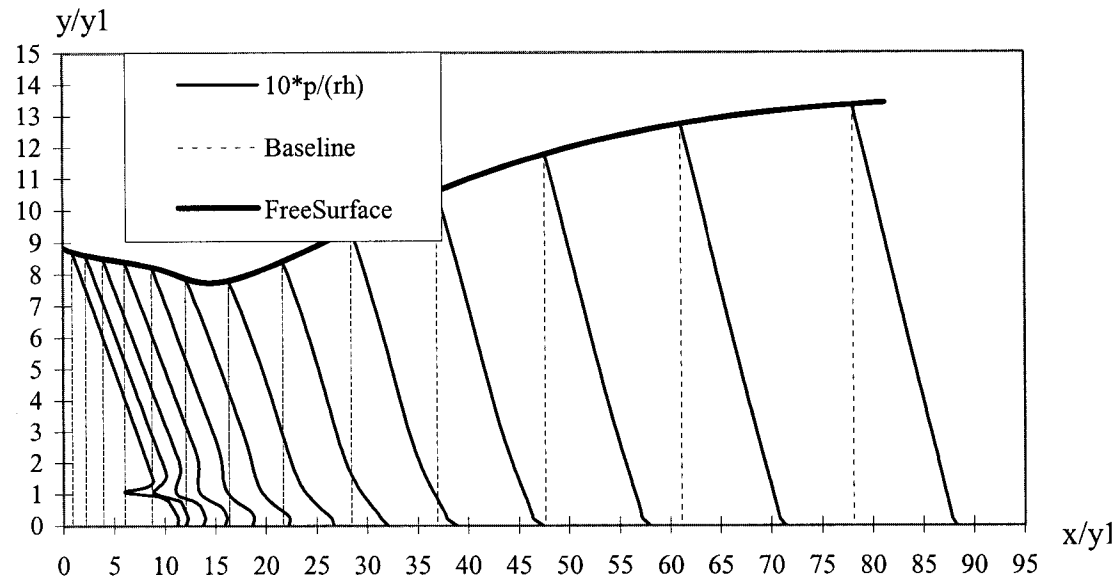

Figure 4.2.5 Calculated Pressure Distribution; Scale 1:10

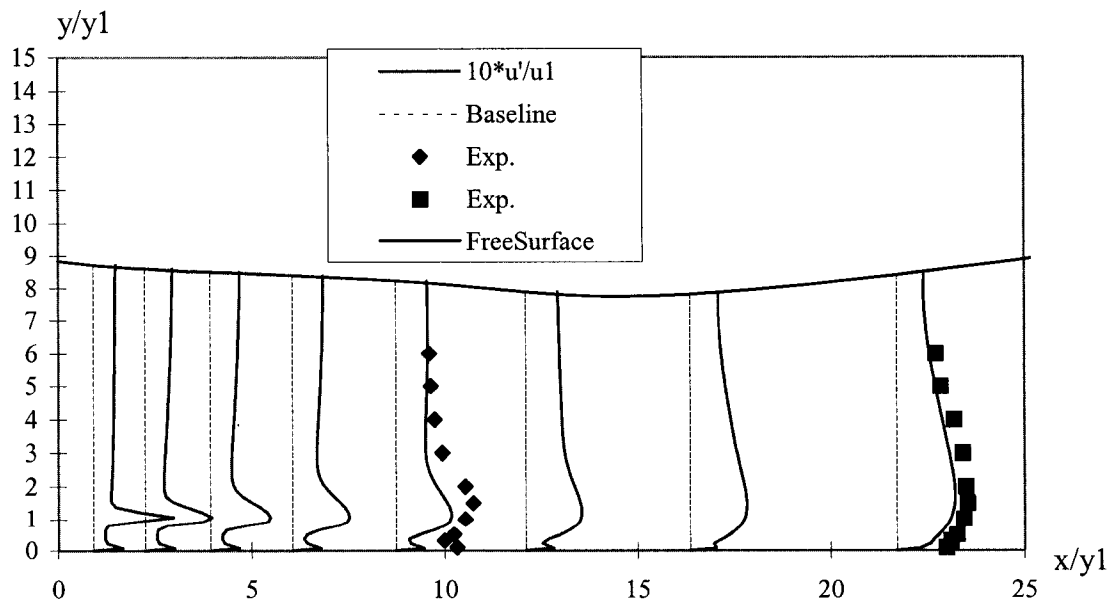

Figure 4.2.6 Turbulence Intensity $\sqrt{\overline{u'u'}}/u_1$; Scale 1:10

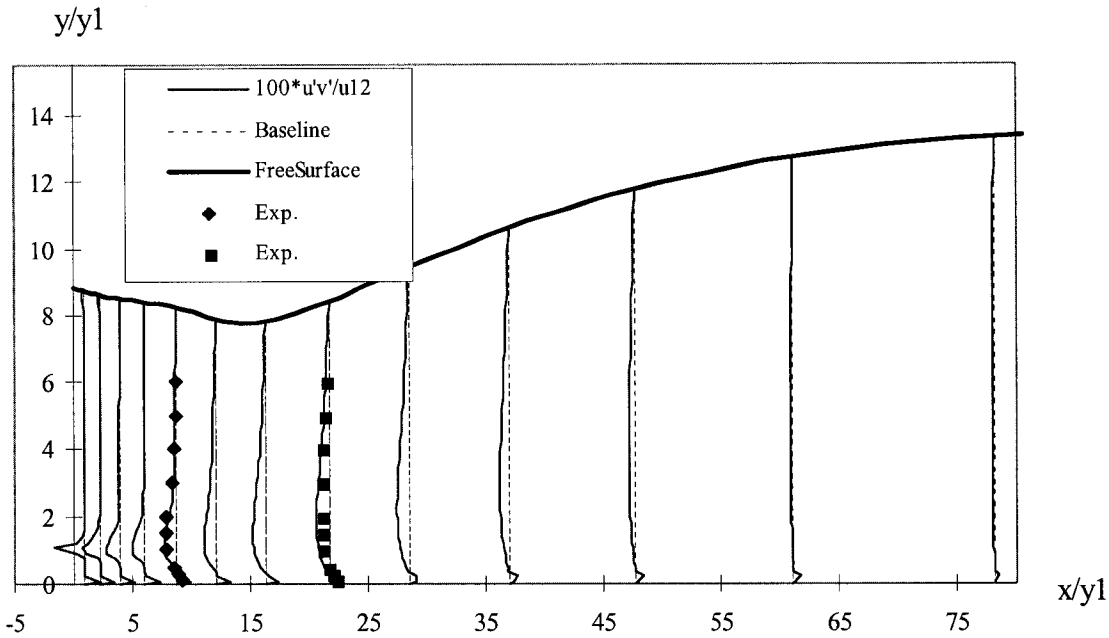

Figure 4.2.7 Turbulence Intensity $\sqrt{\overline{u'v'}}/u_1$; Scale 1:100

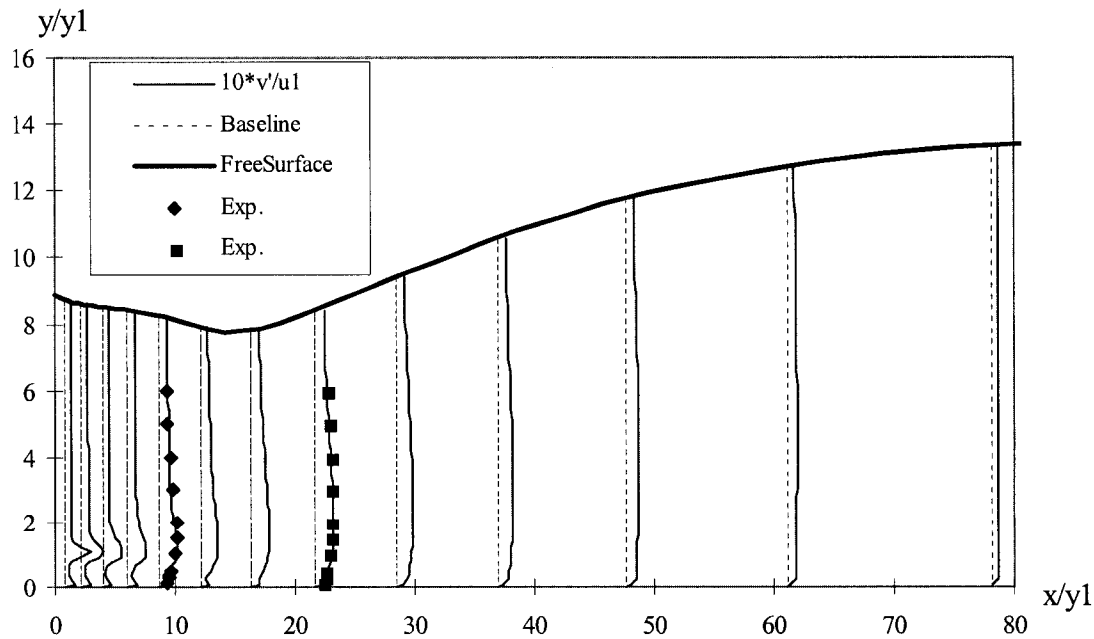

Figure 4.2.8 Turbulence Intensity $\sqrt{\overline{v'v'}}/u_1$; Scale 1:10

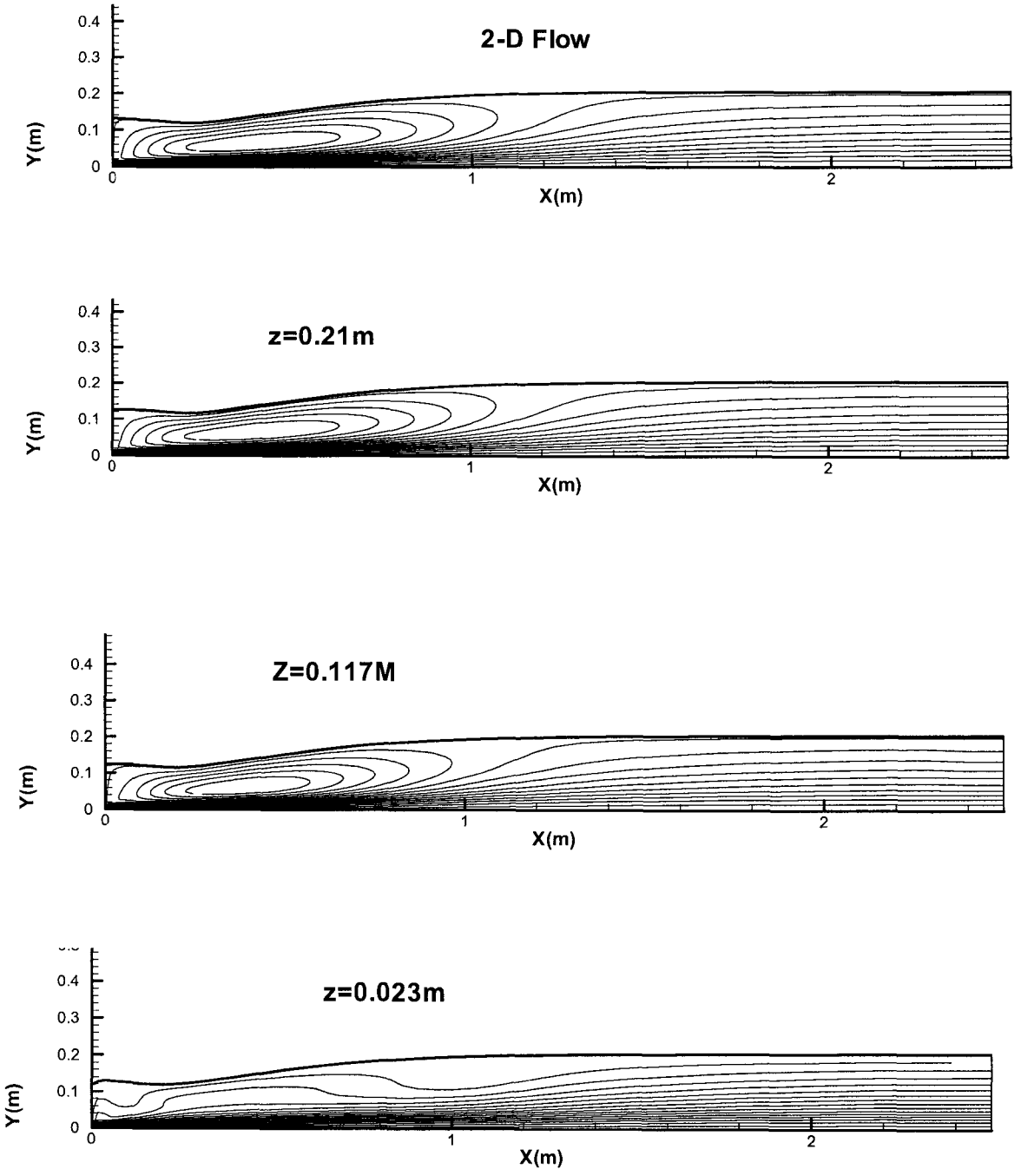

Figure 4.2.9A u-v Streamlines at z/B=0.45, 0.25 and 0.05 and 2-D streamline

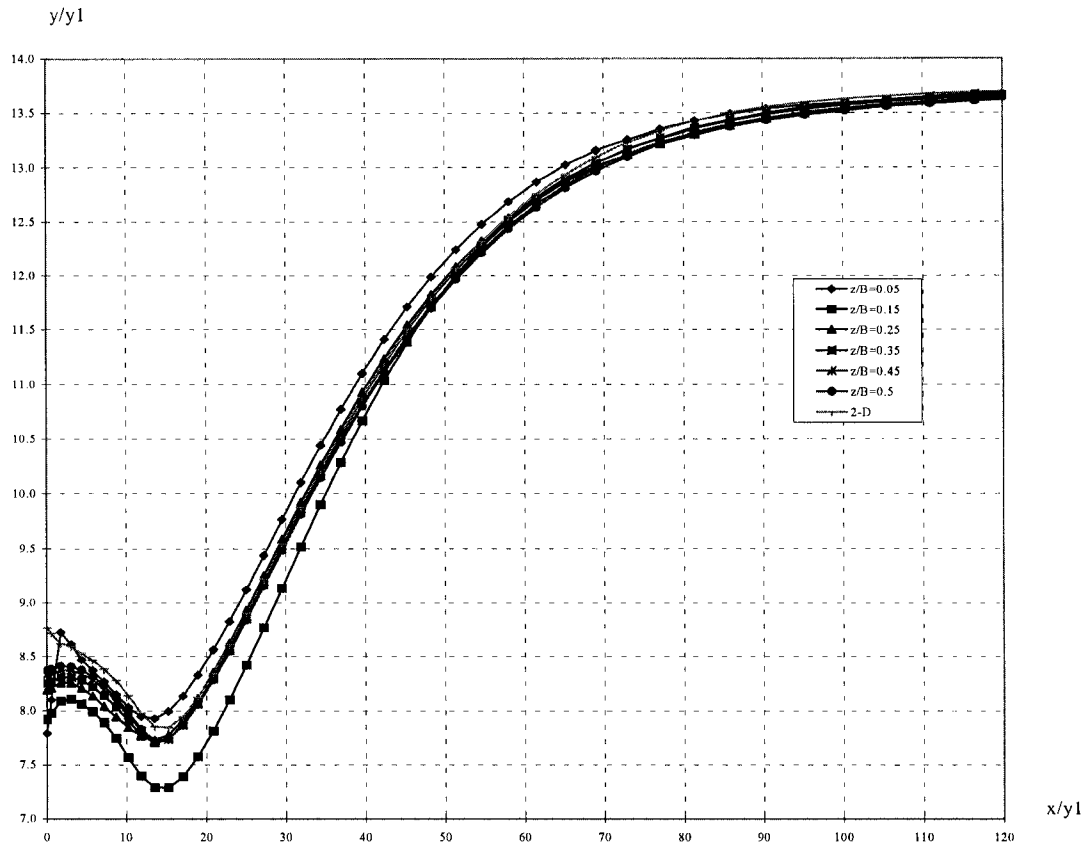

Figure 4.2.9B Comparison of 2-D and 3-D Free Surfaces

4.2.2 Submerged Hydraulic Jump with a Baffle Wall

The second test case for the current numerical model is to simulate a submerged hydraulic jump with a baffle wall. The experimental results of this flow are from Wu and Rajaratnam (1995). In this section, part of Wu's experiment is repeated in a numerical simulation, and a comparison between the experimental and calculated results is given.

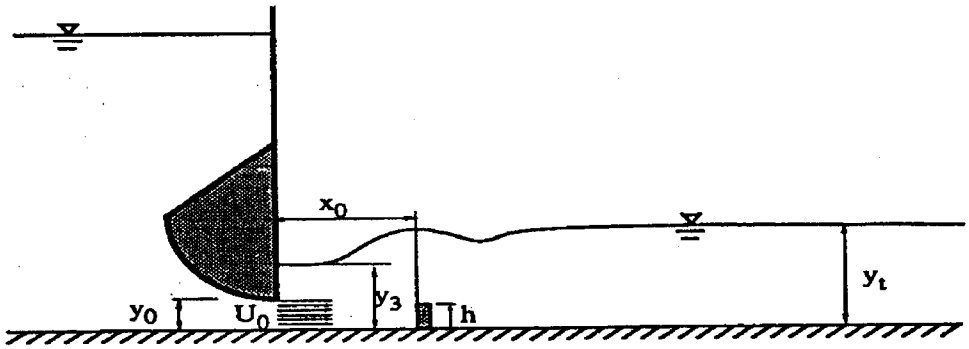

Figure 4.2.10 Submerged Flow with Baffles
(adapted from Wu and Rajaratnam, 1995)

The experiments were performed in a flume, 7.6 m long, 0.455 m wide and 0.6m deep, with an aluminum bed and glass side walls. The experiment was arranged as is shown in Figure 4.2.10. A series of measurements was made with different sets of x_0, y_0, y_t, h and U_0. In each experiment an averaged velocity u was measured with a pitch probe or a Prandtl tube. Two typical experiments, one is a reattached wall jet and the other is a deflected surface jet, were chosen from Wu's experiments for numerical tests. The parameters in these two experiments are shown in Table 4.2.1.

In Wu's experiments, it was found that the flow patterns could differ, depending on the initial condition, even through the experimental parameters were unchanged. In experiment 5 the flow was initially a reattached wall jet with a larger y_t and it maintained this state when y_t was reduced to 440 mm. Contrarily, in experiment 6 the flow was initially a deflected surface jet with a smaller initial y_t, and it remained a deflected surface jet when y_t was increased to 440 mm. In both cases the flow patterns are unstable. Some external disturbance may cause the flow to change state from one to the other. Furthermore, Wu found there were a lower limit and an upper limit for the baffle height. Below the lower limit, the flow was definitely a reattached wall jet, regardless of the initial condition. Above the upper limit the flow was a deflected surface jet. The baffle heights in experiments 5 and 6 were in-between the lower and upper limits.

Table 4.2.1 Details of Experiments for a Submerged Jump with a Baffle Wall

Expe. No.	y_0 (mm)	F_0	y_t (mm)	S	x_0 (mm)	h (mm)	x_0/y_t	h/y_t	Flow State	Remarks
5	10	5.48	440	5.08	400	11.6 (8)*	0.909	0.026	RWJ*	Bistable
6	10	5.48	440	5.08	400	11.6	0.909	0.026	DSJ*	Bistable

RWJ*: Reattached wall jet

DSJ*: Deflected surface jet

* In the corresponding calculation h=8 mm is used.

For numerical calculations a 62*40 non-uniform grid in (x, y) plane similar to Figure 4.2.2, is used. The boundary conditions are these used for the submerged jump without baffles. The baffle was represented by a column of cells with an extra large viscosity coefficient.

First the bi-stable property of the flow is investigated. By increasing the baffle height gradually from 5mm to 11.6mm, it was found the flow will change state from reattached wall jet to a deflected surface jet when the baffle height is greater than 8 mm. Unlike the finding in the experiment, no transient zone was found in the numerical simulation. It is easy to understand this difference. Because a numerical model is mathematical abstraction of the real world phenomena, uncounted disturbances or uncertainties in the real world are absent in the numerical model. It is these disturbances or uncertainties that make the flow unstable.

Except for the bi-stable behavior the numerical results match reasonably well with the experimental data. To keep the flow as a reattached wall jet in the numerical simulation, a baffle height of 8 mm was used, as opposed to 11.6mm in experiment 5.

Figure 4.2.11 shows the streamlines measured in experiments 5 and 6. A deflected surface jet and an attached wall jet are shown. Figure 4.2.12 shows the streamlines from the numerical results. The comparison indicates a close match between experimental and calculated results for the deflected surface jet. There is some difference in the streamlines of the reattached jump because different bump heights were used.

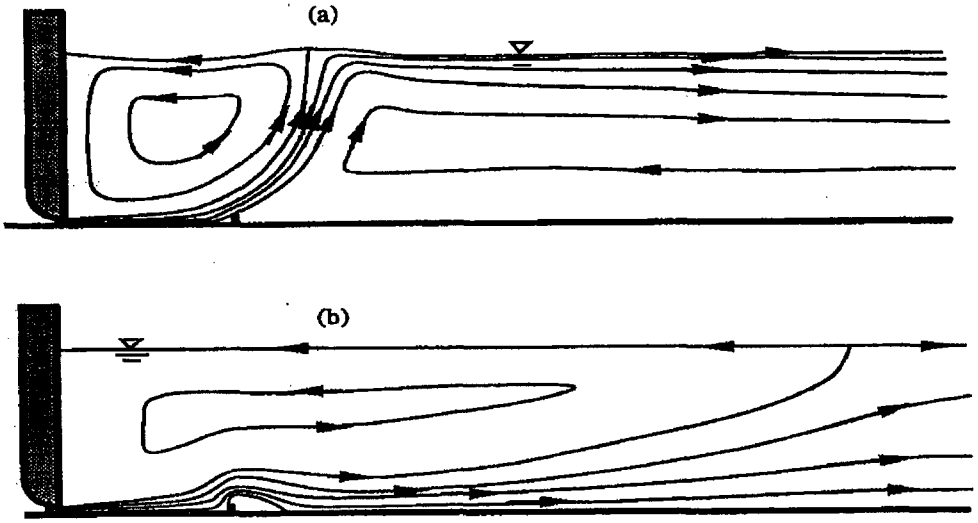

Figure 4.2.11 Flow Regimes of Submerged Flow with Baffles:
(a) Deflected Surface Jet; (b) Reattached Wall Jet
(Adapted from Wu and Rajaratnam, 1995)

Figure 4.2.13 shows velocity field from Wu's experiment, while Figure 4.2.14 presents corresponding results from the numerical simulation. The comparison between experimental data and numerical results indicates the numerical method can produce a good prediction of the flow.

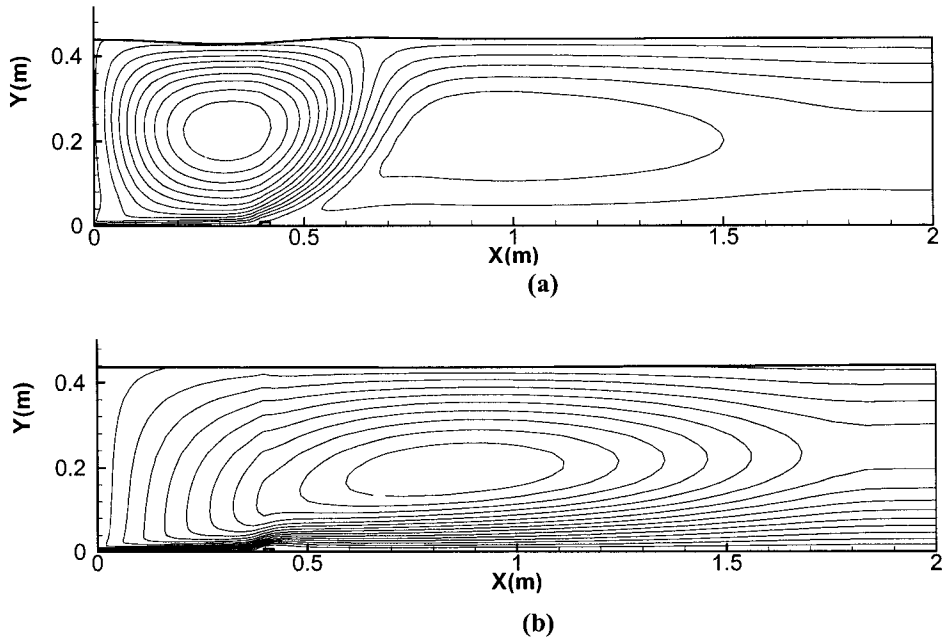

Figure 4.2.12 Calculated Streamlines for Submerged Jump with a Baffle Wall: (a) Deflected Surface Jet; (b) Reattached Wall Jet

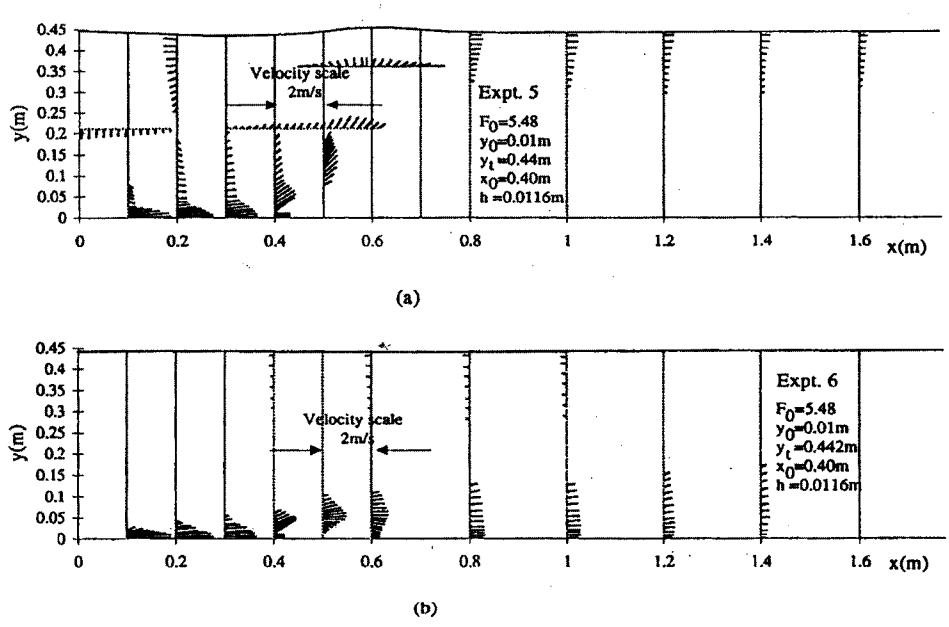

Figure 4.2.13 Typical Velocity Fields: (a) Deflected Surface Jet; (b) Reattached Wall Jet (Adapted from Wu and Rajaratnam, (1995))

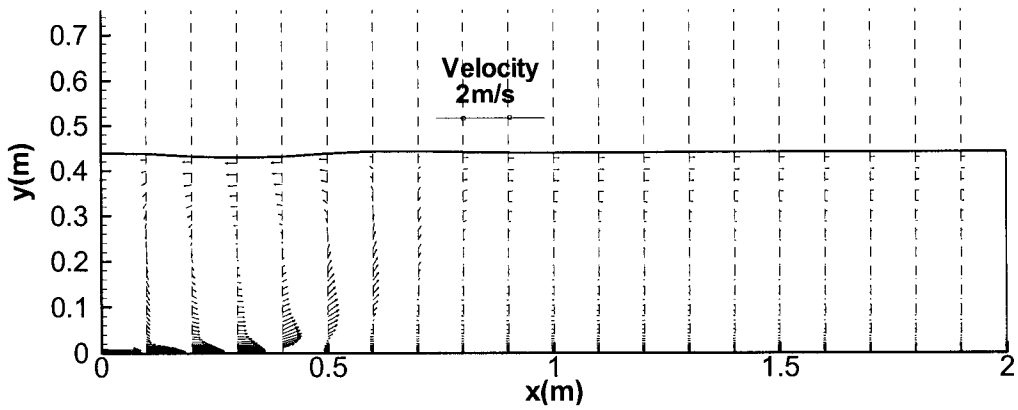

(a)

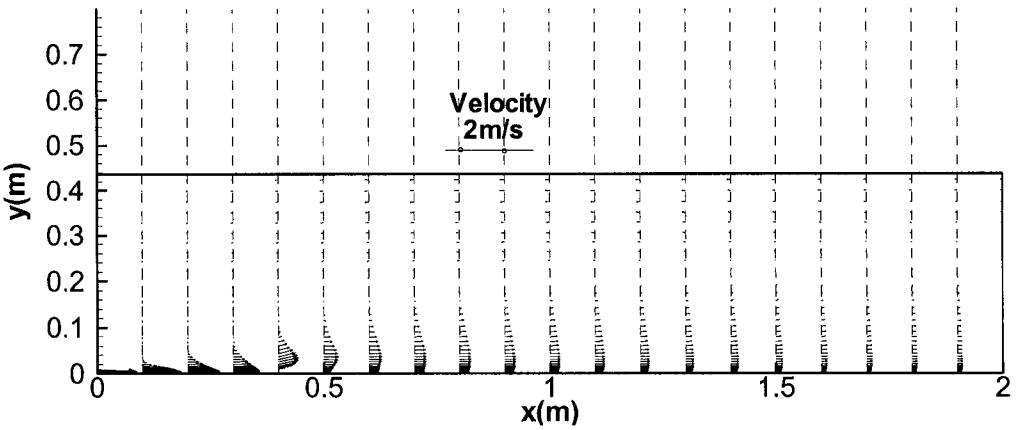

(b)

Figure 4.2.14 Calculated Velocity Fields: (a) Deflected Surface Jet; (b) Reattached Wall Jet

The distribution of the longitudinal forward velocity component u, just before the baffle in a dimensionless form, is plotted in Figures 4.2.15 and 4.2.16, where y is the distance from the bed; here u_m is the velocity that is the maximum value of u, and b is the value of y where $u = u_m/2$ and $\partial u/\partial y<0$. The dots in the figures are measured values, and the solid line is from calculated results. The figures show numerical model performance well.

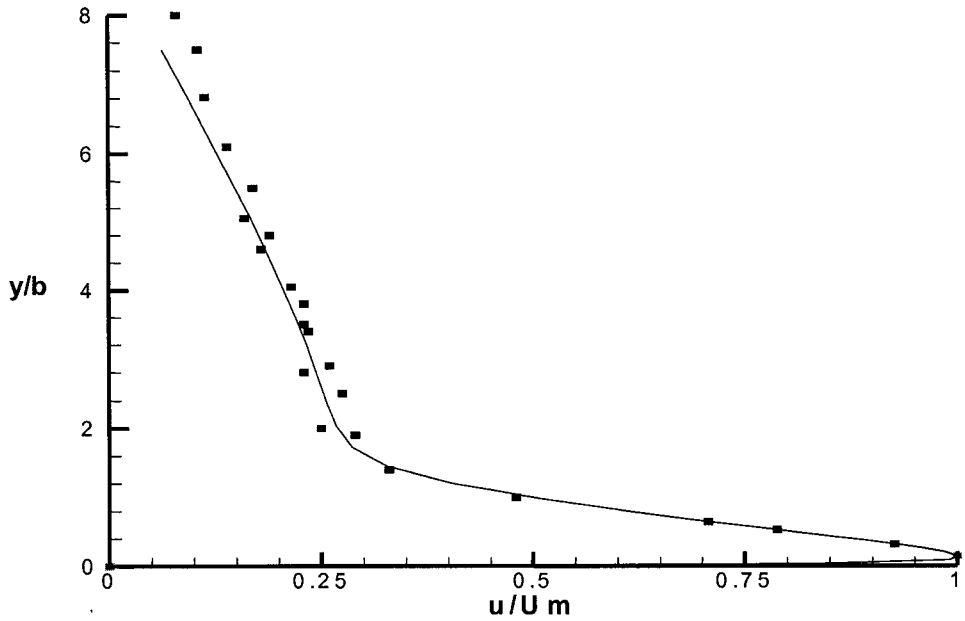

Figure 4.2.15 Velocity Distribution Upstream of the Baffle for Experiment 5

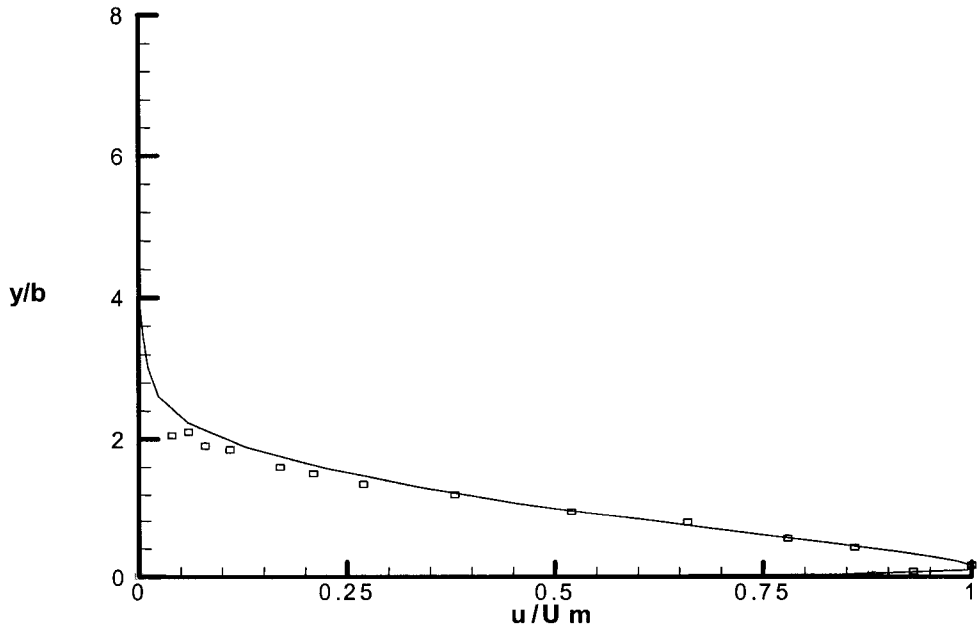

Figure 4.2.16. Velocity Distribution Upstream of the Baffle for Experiment 6

The above comparisons demonstrate that the current numerical model can simulate baffled submerged jet flows properly. The advantage of the numerical model is its efficiency. For this two-dimensional problem it only takes a few minutes for a complete run on a PC of 1 GHz speed. And the numerical model can provide much more information than the experiment does.

4.3 Free Surface Flow around a Hemisphere

4.3.1 Flow Domain Layout

This test case is a 3-D flow around a hemisphere in an open channel. The experiments were carried out in a flume in the T. Blench Hydraulic Laboratory at the University of Alberta, Edmonton, by Shamloo and Rajaratnam (1996, 2001). The flume was 18m long, 1.22m wide and 0.65m high. The bed of the flume was non-erodible, made of smooth aluminum, and the side walls were made of plexiglass. By adjusting the slope and tailgate of the flume, different flow velocities and water depths could be achieved. The velocity and shear stress were measured by yaw and pitch probes, and the water free surface location was measured by a point gauge. The obstacle was a 0.13 m diameter Styrofoam hemisphere glued on the flume bed.

In their experiments the effect of the free surface on the flow for different relative depths (H/d: ratio between water depth and diameter of the hemisphere) and Froude numbers F_r defined by averaged mainstream velocity and water depth was investigated. From the experimental results it was found that the flow can be divided into four regimes. In the first regime the relative depth is between 4.12 and 4.26, and the Froude number range from 0.128 to 0.272. The flow in this regime is deeply submerged sub-critical flow. The interaction between the free surface, and

hemisphere is negligible. In regime 2 the free surface is near the hemisphere with H/d between 1.89 to 1.46, and Froude number is in the range from 0.34 to 0.56. In this case notable free surface waves were generated near the hemisphere, and significant oscillations downstream in the wake were observed. When the relative depth was decreased further to about 1.2 and F_r is between 0.29 and 0.48, the flow is in regime 3. In this regime the strength of the vertex near the hemisphere is not so strong as that in regime 2, and the small layer of fluid over the hemisphere leads to a weak separation. In contrast with regime 2, the free surface waves became sharp and strong with short length. Regime 4 is significantly different from the other regimes. In this regime the water surface is lower than the top of the hemisphere. The downwash flow over the body disappears, and the wake approaches two-dimensional flow with the appearance of a Karman vortex street.

It will be shown late in this Chapter that the above observations will be verified by numerical simulation. The computation domain for numerical simulation is a section of the flume shown in Figures 4.3.1 and 4.3.2. Only the z direction the Figure 4.3.1 is in scale. The length of the computational domain is 1.54 m, which is about 12 times the obstacle dimension. The boundary conditions for the calculation have been given in Section 4.1.2.

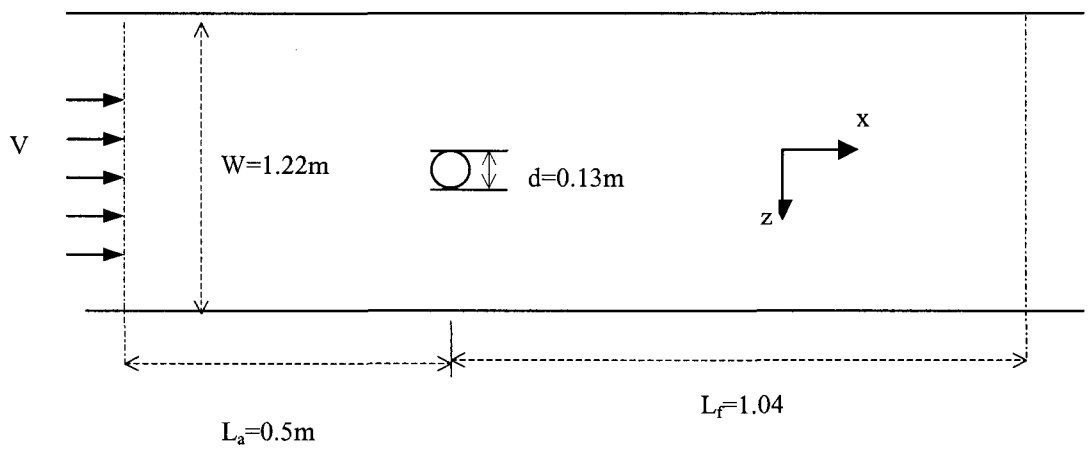

Figure 4.3.1 Top View of the Computational Domain

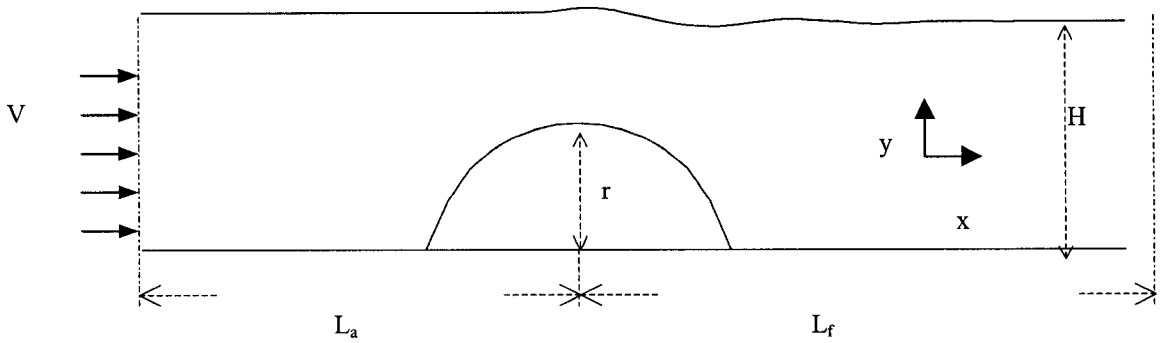

Figure 4.3.2 Side View of the Computational Domain

4.3.2 Comparisons with Experimental Data

Most test runs were conducted on a PC with 32 MB RAM and 233 MHz CPU. It may take about one day to make a complete run, depending on the convergence criterion. The size of the mesh is 59*18*47 in the (ζ,η,ξ) directions, respectively. This resolution is not fine enough for a complicated flow. Nevertheless, it is good enough to validate the numerical model. Three testing runs with parameters as shown in Table 4.3.1 are presented.

Table 4.3.1 Specifications of Three Test Cases

CASES	Water Depth H (m)	Flux $Q(m^3/s)$	Velocity U_0(m/s)	Froude No. Fr	Reynolds No. Re	Computation Domain x(m)*y(m)*z(m)
A	0.120	0.054	0.369	0.340	$4.8*10^4$	1.54*0.120*1.22
B	0.072	0.030	0.342	0.407	$4.4*10^4$	1.54*0.072*1.22
C	0.042	0.008	0.156	0.243	$2.0*10^4$	1.54*0.042*1.22

The hemispherical obstacle was placed on the center of the channel bed, one half meter downstream from the inlet plane. The Reynolds number characterized by the average velocity and diameter of the obstacle is in the range between 20,000 and 48,000 which indicates the flow is fully turbulent.

Case A: H = 0.12 m

In this case, the water depth is about two times the obstacle height. The obstacle will generate a notable wave on water surface. In turn, the shape of the free surface will affect the velocity and pressure distributions around the obstacle.

Figures 4.3.3 and 4.3.4 present the comparison between the calculated and measured velocity at centerline plane of the channel. The solid lines depict the calculated results and the symbols indicate the measured data at different channel locations. Only the portion of the channel that is within twice the obstacle dimension in x direction is shown. The velocity is plotted on a 1:10 scale. The horizontal velocity u shows a reasonably good agreement with the experimental data except inside the wake. The experimental velocity is larger than the calculated velocity on the top of the obstacles. It appears the larger velocity on the top of the obstacle in the experiment delays boundary layer separation and carries more kinetic energy into the wake. As a result, the measured velocity recovers faster than calculated velocity does. Looking at the velocity profile immediately above the obstacle, the measured velocity profile is more like a potential flow profile. However, the calculated velocity profile can not bend so abruptly to match the sharp velocity gradient near the obstacle surface. To reduce this difference, the turbulent model and wall function should be studied and comparisons with more experimental data are also necessary.

Figure 4.3.4 presents the comparisons of vertical component of the velocity. The measured velocity profile and calculated velocity profile appear similar but with notable differences. In this figure the velocity is plotted at a 1:2 scale. The maximum vertical velocity difference is about 0.06m/s. One reason for this difference may be

the wall function. As mentioned before, if the measured flow separates later, the flow will plunge down more into the wake than the computational flow.

Figure 4.3.5 shows that the calculated free surface profile basically matches the measured surface profile in front and on top of the hemispheres. Above the wake region, the experimental data show stronger free surface waves than the computed solution does. Further study is necessary for the details of free surface waves. Figure 4.3.5 is not in scale in the vertical direction to exaggerate the difference between measured and calculated data. In the plot the vertical coordinate is normalized by R, the radius of the obstacle.

The velocity profiles at the water level y = D/4 above the channel bed are calculated and compared with the measured data, as shown in Figures 4.3.6 and 4.3.7, where D is the diameter of the obstacle. Two profiles of the components u/U_0 and w/U_0 at stations x = 0.695m and x = 0.76m are plotted. U_0 is average velocity calculated by flux divided by the channel cross-section. The comparison also indicates that the calculated velocity recovers more slowly than the measured velocity does. There is also a difference between measured and calculated w/U_0. Note that the measured w/U_0 is not zero at the channel centerline. If the measured w/U_0 is shafted to zero at the channel centerline in Figure 4.3.7, the difference decreases. The comparison shows the numerical model can produce velocity profiles similar to the experimental data, but refinements to improve accuracy are necessary. That will be the work of the next stage of this research.

Shamloo found in his measurements a separation line in front of the obstacle and a re-circulation region behind the obstacle. In Figures 4.3.8 calculated streamlines in centerline plane are plotted. It clearly shows a small re-circulation region in front of the obstacle and a large re-circulation region behind the obstacle.

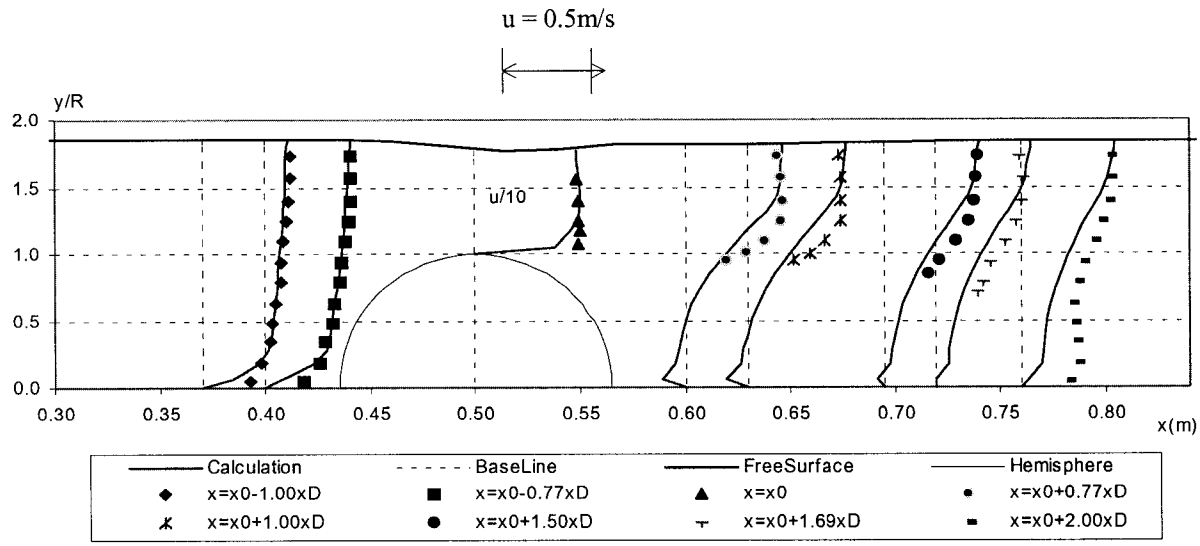

Figure 4.3.3 Horizontal Velocity at Centerline Plane of the Channel; Scale 1:10

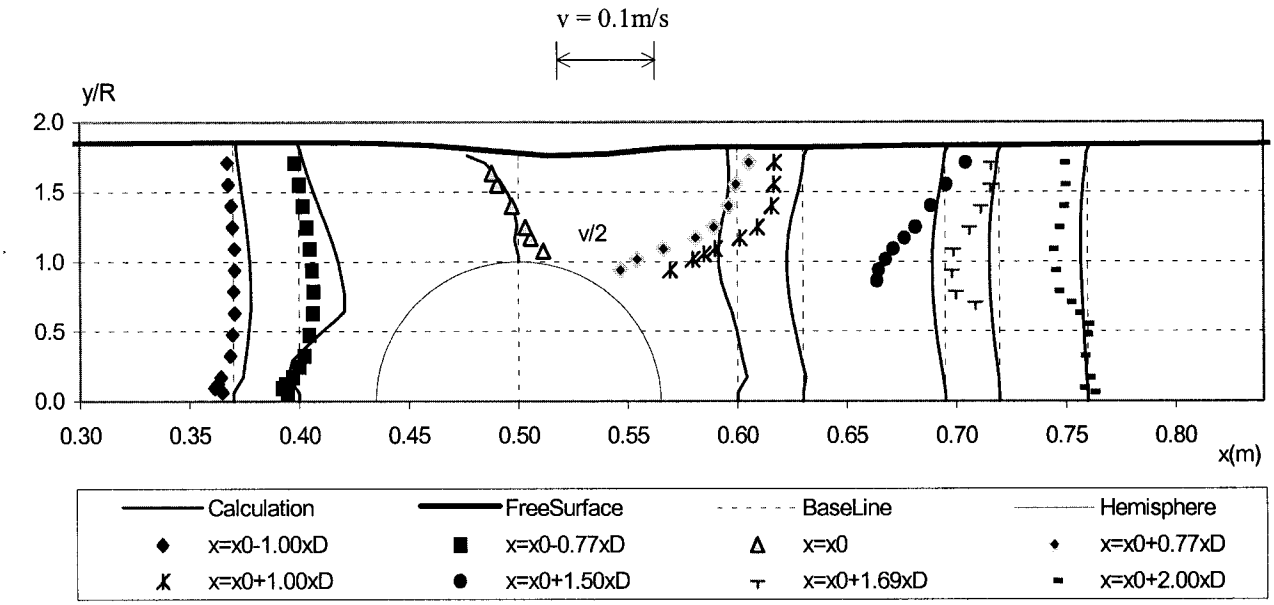

Figure 4.3.4 Vertical Velocity at Centerline Plane of the Channel; Scale 1:2

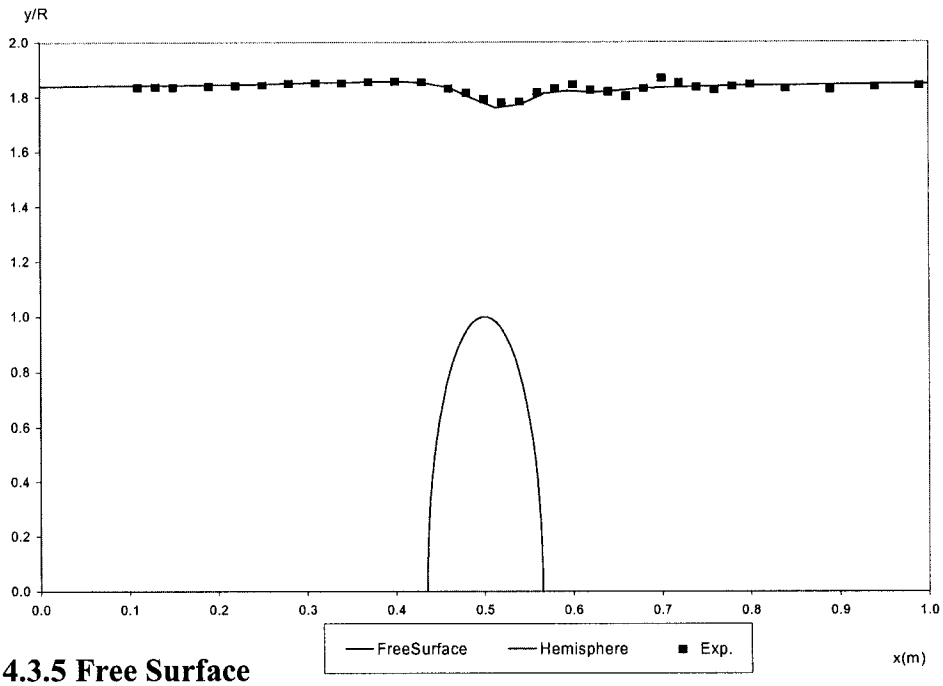

Figure 4.3.5 Free Surface

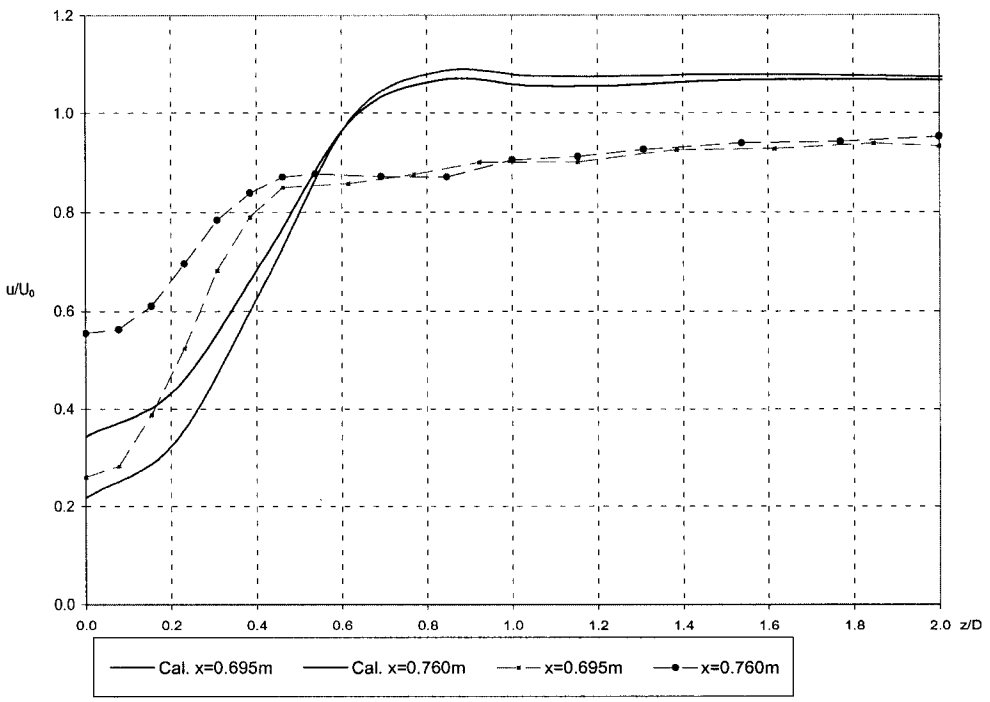

Figure 4.3.6 Lateral Profiles of U/U_0

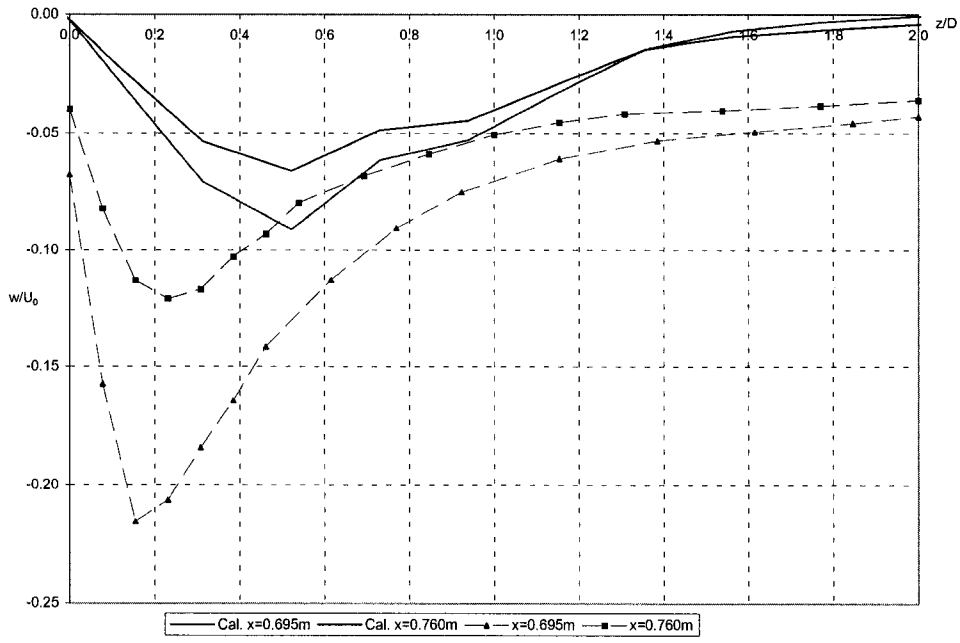

Figure 4.3.7 Lateral Profiles of W/U_0

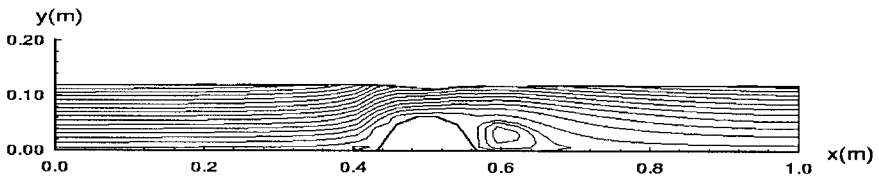

Figure 4.3.8 Streamlines in Centerline Plane

Case B: H = 0.072 m

In this case the water surface lies just above the top of the obstacle. As a result, the obstacle can make more significant waves than it does in **case A**.

Figures 4.3.9 and 4.3.10 show the calculated and measured velocities. The horizontal velocity U matches well the measured data in front of the obstacle, but there are differences in the wake of the obstacle. At a cross section 3D downstream from the hemisphere, the measured velocity u recovers up to 75% of the average velocity, but the calculated velocity is still in the wake of the obstacle. It seems that the actual flow has stronger mixing than does the calculated flow. In a high Reynolds number region the mixing process is dominated by turbulence, so more studies are needed for turbulence modeling. In addition, the real flow in the experiments tended to separate later than the flow in the numerical model. More energy was carried into the wake in the experiments and that would enable measured velocity field to recover sooner. In Figure 4.3.10 some differences are found between the measured and calculated vertical velocity field v. It is strange that the measured v is negative in the entire domain regardless of the free surface having significant slopes in both directions. The measurements of vertical velocity V in **Case C** also show a similar tendency.

The comparison between the calculated and measured free surface elevations is plotted in Figure 4.3.11. Some discrepancies are anticipated because the measured data are results from a time average of an unsteady real flow. The oscillation in the wake because of the vortex shedding is not encountered in the numerical model.

Case C: H = 0.042 m

In this case the top of the obstacle is above the water surface. The flow is something like the flow around a cylinder attached to the channel bed. Because there is no thin

layer of fluid over the top of the obstacle as was **Case B**, no significant surface waves will be generated.

Like the flow in **Case B**, the calculated flow has a larger wake region than does the measured flow. In comparison with the horizontal velocity distribution the vertical velocity is of negligible magnitude, and the water surface is almost flat. Detailed data on the calculated and measured velocities and free surface profiles are presented in Figures 4.3.12 to 4.3.14.

From theses comparisons, it seems that there is room for improvement in the turbulence modeling and in particular the use of the wall function for a complex three-dimensional flow. In section 4.2 it was shown that the current turbulence model and wall function work well for a two-dimensional flow. The author also tried to increase grid size in vertical direction, from 18 to 28, but no significant improvements were found. Further testing seems necessary. On the other hand, to make an improvement for a three-dimensional flow, more comparisons with more detailed experimental data are necessary.

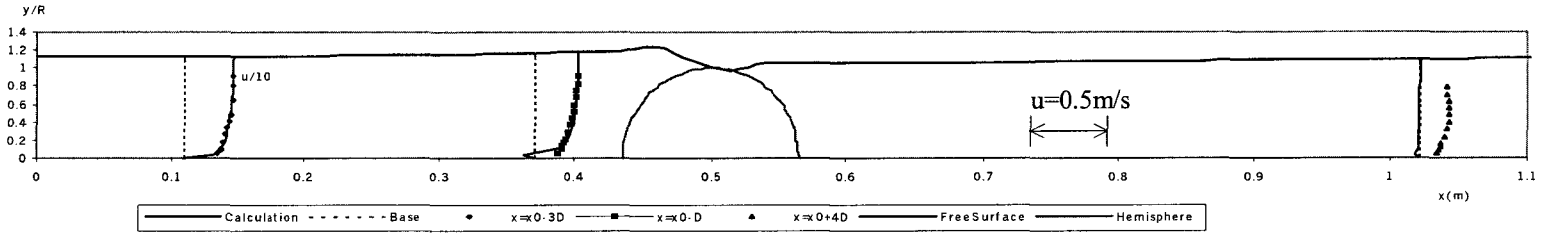

Figure 4.3.9 Horizontal Velocity Distribution: H = 0.072 m

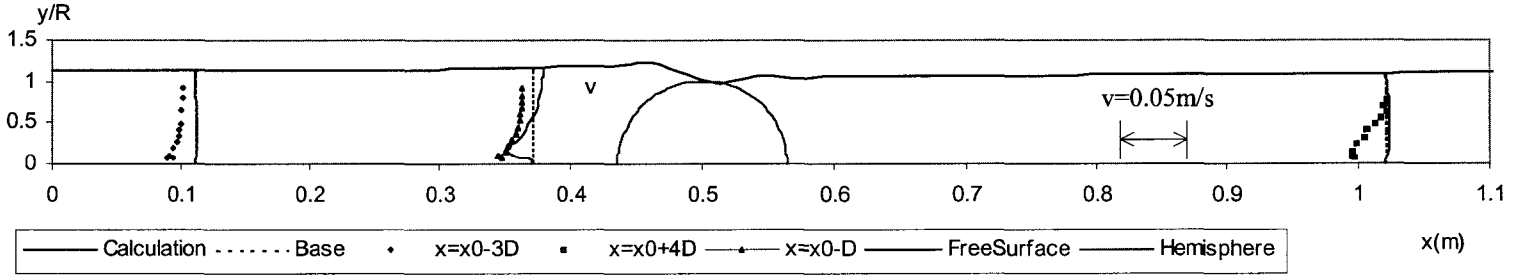

Figure 4.3.10 Vertical Velocity Distribution: H = 0.072 m

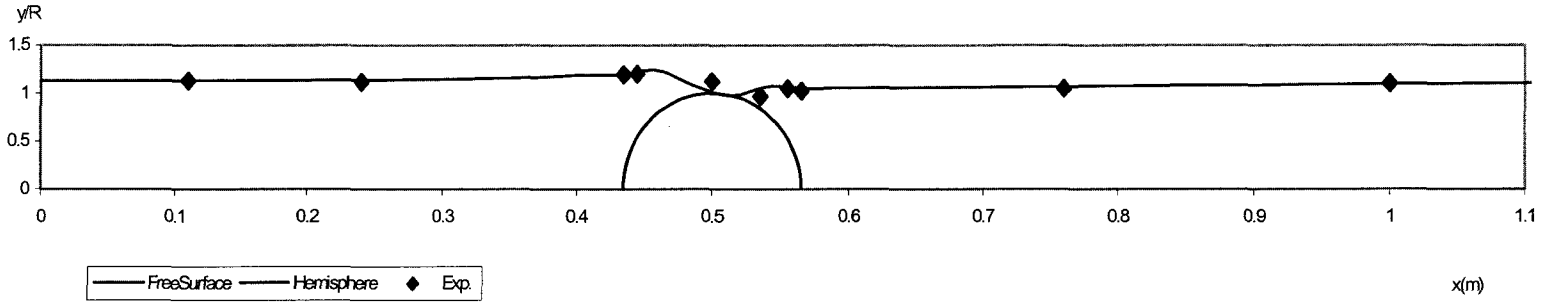

Figure 4.3.11 Free Surface: H = 0.072 m

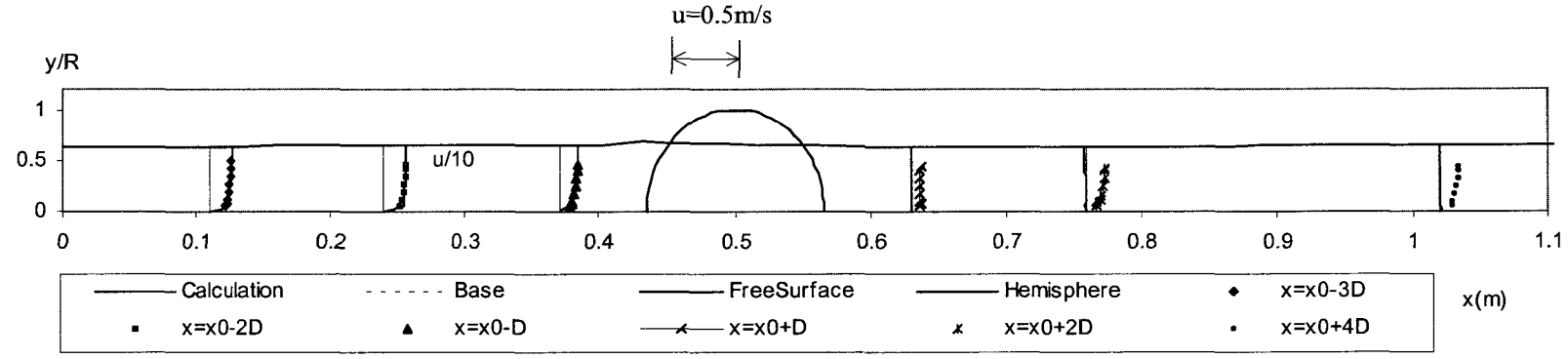

Figure 4.3.12 Horizontal Velocity Distribution: H = 0.042 m

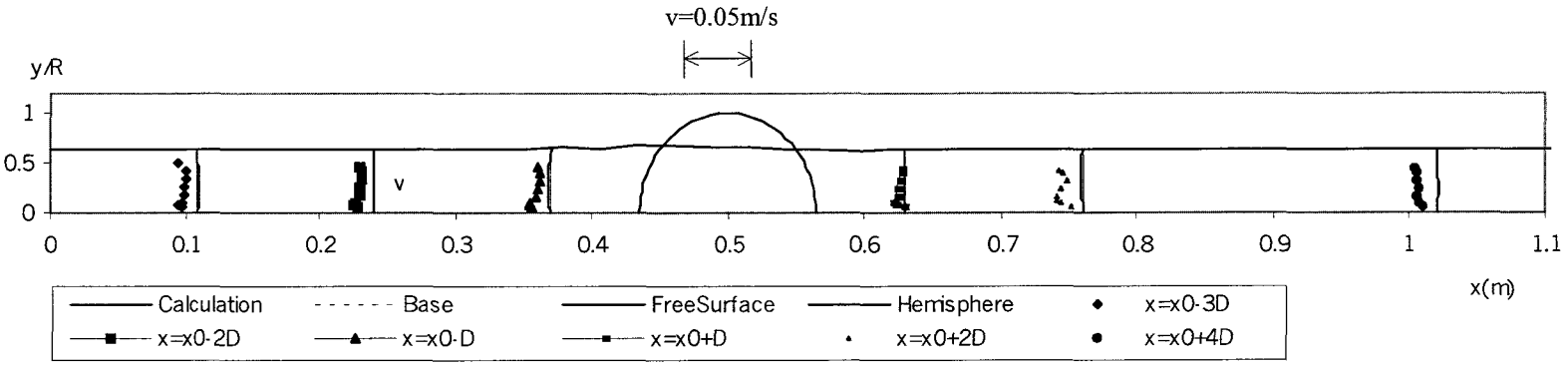

Figure 4.3.13 Vertical Velocity Distribution: H = 0.042 m

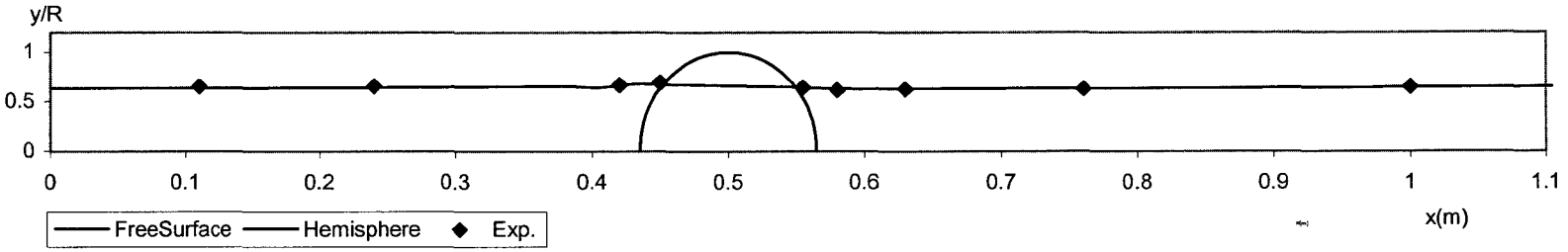

Figure 4.3.14 Free Surface: H = 0.042m

4.3.3 Flow Pattern around a Three Obstacle Cluster in an Open Channel

Similar to Shamloo's work, C. D. Albers presented a series experiments on open channel flow with an obstacle cluster on the channel bed (C. D. Albers, 1997). The experiments were done in a flume with three obstacles (hemispheres or natural rocks) glued to the bed. With a variation of the obstacle dimensions, the distance between obstacles and the water depths, the flow patterns were studied a graphically by analysis of videotape records or photographs.

A typical experimental result was chosen to test the current numerical model. In this experiment obstacles are three hemispheres with diameters of 10 cm. The water depth is 13.5 cm, and average flow velocity is 0.187 m/s. The obstacles are laid on the channel bed, as shown in Figure 4.3.15 with SD/D = 1.4 and S'D/D = 1.6. Figure 4.3.16 is a picture of the flow pattern in the experiment. One sees that there is a clear separation line between the main-stream and the local flow. The streamlines of the calculated flow are plotted in Figure 4.3.17. In the numerical solution the distances between obstacles are SD/D=1.61 and S'D/D=2.28. Figure 4.3.17 shows a flow pattern and separation line that are similar to that sees in Figure 4.3.16. Outside the separation line the flow pattern is much like potential flow around a blunt body of semi-infinite length. All circulation in the flow is inside this separation line.

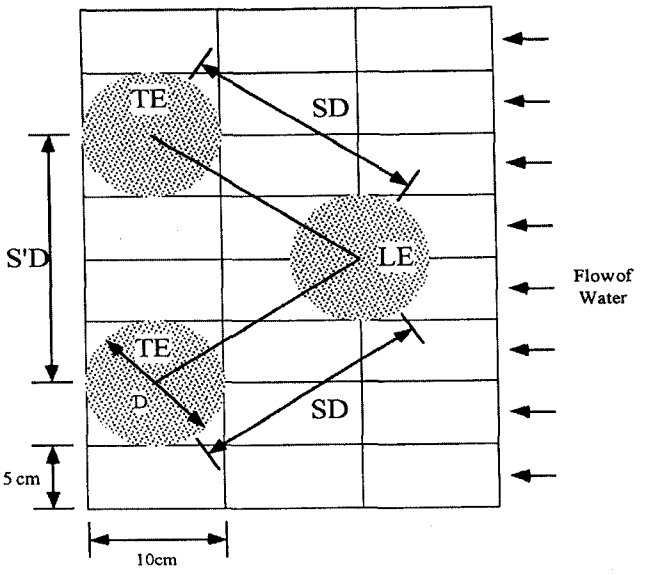

Figure 4.3.15 Layout of Obstacles (adapted from Albers, 1997)

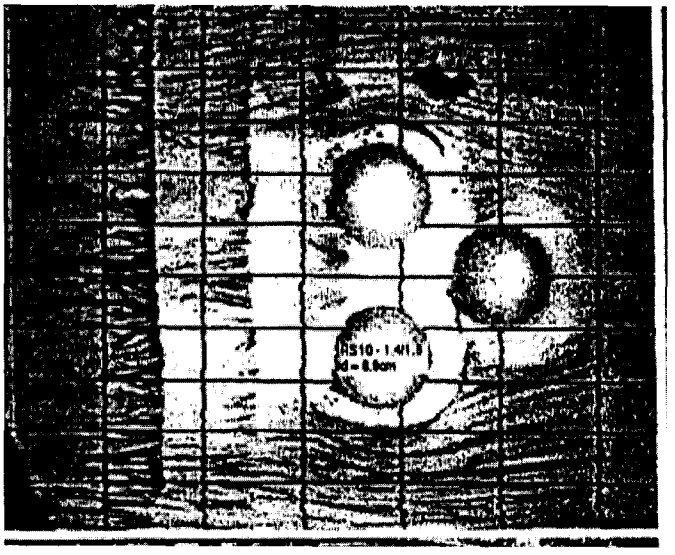

Figure 4.3.16 Picture of Flow Pattern around Obstacles (Adapted from Albers, 1997)

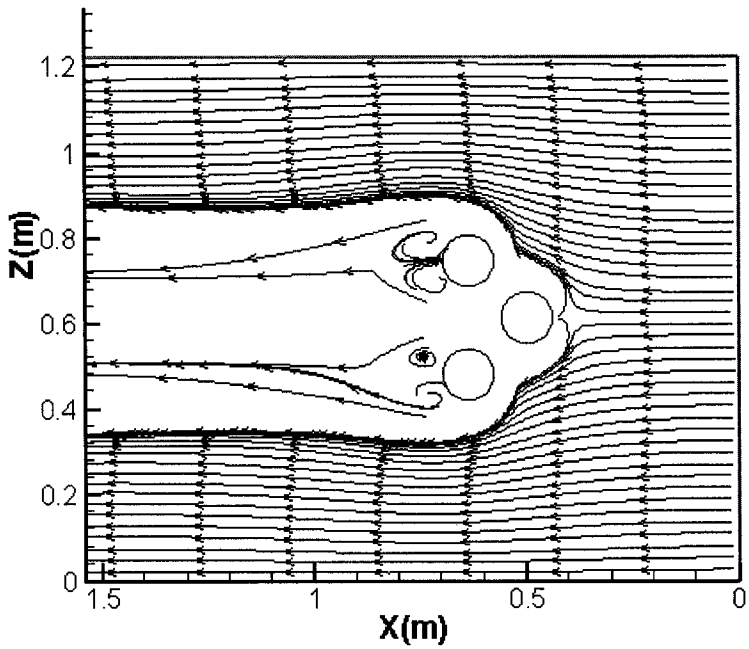

Figure 4.3.17 Streamlines from Numerical Model

4.4 Numerical Study of Flow around Obstacles in an Open Channel

4.41 Specifications of Numerical Tests

In this section a systematic numerical study of free surface flow around and over a hemisphere and clusters of up to three hemispheres is presented. These hemisphere structures are used to represent simple but common fish habitat structures, whether natural or artificial. The interaction between the hemispheres and the flow pattern at different water depths are investigated. The purpose of the numerical tests is to find the general flow properties and then to establish a guide for fish habitat structure design. In this section it will also be shown that numerical tests using the current numerical model can provide a useful alternative or supplement to experimental studies, due to the flexibility, efficiency and economy of the numerical model.

In this study seven test cases with different water depths or different hemisphere configurations were completed. These test cases can be divided into two groups. The first group uses the same channel configuration but different undisturbed water depths. Tests **A, B, C** and **G** belong to this group. In this group the channel configuration is the same as that mentioned in Section 4.3 with a single hemisphere attached to the bed. The ratio of water depth to the radius of the hemisphere varies from 0.646 to 3.077. From this group of tests the interaction between obstacle and free surface is studied.

In the second group of tests (cases **D, E, F**) the water depth is fixed with a ratio of water depth to obstacle radius of 1.846. The number and location of the obstacles change in different cases, but all of the obstacles are hemispheres of the same size as the one in Shamloo's experiments. From the calculated results, the interaction between obstacles can be found. For all tests the Reynolds numbers specified by the diameter of the hemisphere and average velocity is on the order of 10^4. The flow is fully developed turbulent flow. The Froude number, an indicator of the ratio between gravity and inertia, varies from 0.243 to 0.407. For these ranges of Reynolds and Froude numbers, both gravity and viscosity are important factors. The detailed flow specifications for the seven test cases are shown in Tables 4.4.1 and 4.4.2. The Froude number is defined by average main-stream velocity and water depth.

Table 4.4.1 Flow Characteristics

CASES	Water Depth H (m)	Depth to Obstacle Radius Ratio	Discharge $Q(m^3/s)$	Average Velocity $U_0(m/s)$	Froude No. Fr	Reynolds No. Re
A	0.120	1.846	0.054	0.369	0.340	$4.8*10^4$
B	0.072	1.108	0.030	0.342	0.407	$4.4*10^4$
C	0.042	0.646	0.008	0.156	0.243	$2.0*10^4$
D	0.120	1.846	0.054	0.369	0.340	$4.8*10^4$
E	0.120	1.846	0.054	0.369	0.340	$4.8*10^4$
F	0.120	1.846	0.054	0.369	0.340	$4.8*10^4$
G	0.200	3.077	0.090	0.369	0.263	$4.8*10^4$

Table 4.4.2 Calculation Conditions

CASES	Computation Domain x*y*z	Computation Grids L*M*N	Number of Hemispheres	Coordinates of Hemispheres (m)		
				(x_1, z_1)	(x_2, z_2)	(x_3, z_3)
A	1.54m*0.120m*1.22m	59*18*47	1	(0.500, 0.610)		
B	1.54m*0.072m*1.22m	59*18*47	1	(0.500, 0.610)		
C	1.54m*0.042m*1.22m	59*18*47	1	(0.500, 0.610)		
D	1.54m*0.120m*1.22m	59*18*47	3	(0.500, 0.610)	(0.770, 0.339)	(0.770,0.881)
E	1.54m*0.120m*1.22m	59*18*47	2		(0.770, 0.339)	(0.770,0.881)
F	1.54m*0.120m*1.22m	59*18*47	3	(0.500, 0.610)	(0.635, 0.474)	(0.635,0.746)
G	1.54m*0.200m*1.22m	59*28*47	1	(0.500, 0.610)		

4.4.2 Numerical Results

About 2-D Plots for 3-D Flows

To present a picture of the calculated flow, it is ideal to show 3-D streamlines. However, this is not an easy job. First it is not easy to obtain accurate coordinates of 3-D streamlines by integrating the discretized data of velocity components numerically. Moreover, the 3-D streamlines must be eventually plotted on a 2-D paper, so overlaps in a 2-D picture have to be properly addressed. In this section all calculated results are plotted in 2-D plane section by section. The 2-D streamlines in a plane in the plots are not real, but only indicators of the direction of two velocity components in that plane. However, in certain cases such as when one velocity component is absent or is very small in comparison with other two velocity components, the 2-D streamlines are very close to real streamlines.

Two methods were used to draw 2-D streamlines in this thesis. One is to draw contours of a 2-D stream function that was obtained by integrating two velocity components in the plane considered. The other method is to draw integrated curves of two velocity components in the plane considered.

Since 2-D streamlines are not real streamlines, a 2-D streamline may intersect another streamline or boundary in a plane view. The numerical errors from integration of velocity components may also lead to two 2-D streamlines intersecting.

The name of u-v, u-w and v-w streamlines are used in following drawings to distinguish them from real streamlines.

CASE A: Flow Pattern

All calculated results are plotted in Figure 4.4.A. Figures 4.4.A1 to A3 are u-v streamlines in the x-y plane. The u-v streamlines are curves integrated from the velocity components u, v in the x-y plane. Although they are not true streamlines, they are good indicators of the flow pattern. If the transverse velocity component is very small, there is little difference between a u-v streamline and a real streamline. The plot in Figure 4.4.A1 should be a sets of real streamlines because the velocity component w = 0 at the centerline plane of the channel. However, numerical errors in the integration of stream function may make the streamlines in the plot only an approximation of the real streamlines. This figure clearly shows the vortices formed in front of and behind the hemisphere. This result agrees with Shamloo's experimental observation. Figures 4.4.A2 and A3 show the decay process for these vortices from the centerline to the side of the hemisphere.

Figures 4.4.A4 to A7 show plots of the u, w components of velocity vectors and traced u-w streamlines. Like the u-v streamlines, the u-w streamlines are integrating values of the u, w components in the x-z plane. The data plotted in Figure 4.4.A4 is calculated in a plane close to the channel bed where the vertical velocity is very small, so the streamlines plotted are very nearly real streamlines. It clearly shows a separation line around the hemisphere and that matches the experimental results of Shamloo and Albers qualitatively. Behind the hemisphere, two vortex systems are formed in a pattern that was observed in many experiments on viscous flow around a cylindrical body. Looking at this figure together with Figure 4.4.A1, one can imagine the three-dimensional shape of the vortex system. The vortex behind the hemisphere looks like an arch attached to the channel bed. The height of this arch is about the same height as the hemisphere radius. It should be noticed that the flow is perfectly symmetric because it was treated as a steady flow. For a real flow, one might observe periodic changes of the vortex position.

Figures 4.4.A8 to 4.4.A11 are plots of v, w velocity components in the y-z plane. From Figure A9 it can be seen that water flows downward from the free surface caused by the low pressure on the top of the hemisphere due to fast flow and then flows outward just

before it meets hemisphere. At section A10 the water near the hemisphere flows inward behind the hemisphere to form the vortex as shown in Figure 4.4.A4. From streamlines in Figures 4.4.A10 one can see the separation line near the channel bed where transverse velocity component points away from the hemisphere. Figure 4.4.A11 shows a section about 3D (D = diameter of the hemisphere) down-stream from the hemisphere. At this section strong transverse flows toward the center of the channel were found.

The non-dimensional velocity components u, w are plotted at different water depths in Figures 4.4.A12 to 4.4.A20. These figures show that it takes a very long distance for the flow to recover in the wake of the obstacles. The calculated data show at a distance of twice the hemisphere diameter that only 60% recovery is reached. The wake width measured at a place where the velocity at centerline of the channel reaches 90% of the mean channel velocity is about twice the obstacle diameter.

Figures 4.4.A21 is the calculated free surface. Just before the obstacle, the highest water surface was observed. Above the top of the obstacle, there is a quick drop of the water surface. Then there is a gentle recovery process. A small secondary undulation can be seen in the recovery process.

CASES B, C and G: Effect of Water depth

The calculation conditions of the test **Case B** are the same as in the **Case A** except that the water depth, H = 0.072m, is about 60% less than that in the **Case A**. The purpose of this test is to find interactions between the free surface and the obstacle. The test results show that, if the water depth is just above the top of the obstacle, the highest surface disturbance will be created. Comparing Figure 4.4.B with Figure 4.4.A, it was found that the disturbance to the free surface caused by the obstacle increases significantly as the water depth decreases to the obstacle height. The wake is also longer and wider and the vortices are stronger. The overall flow pattern remains similar. Figure 4.4.B13 shows a very sharp wave in front of the obstacle. To examine the sharp peak in the Figure 4.4.B13, a 2-D plot, Figure 4.4.B14 was provided to show the surface height near the

center of the channel. It appears the grid used in the calculation for this case is not fine enough to produce a smooth free surface plotting.

Figure 4.4.B1 shows streamlines along the center of the channel. It is similar to the plot in Figure 4.4.A1 but with a higher peaked surface wave. In Figures B2 through B4 velocity components u, w and u-w streamlines are plotted. Comparing them with Figure A4 through A7, it is found that the region inside the separation line is much larger and the wake is also longer in test case B. That means that the disturbance from the obstacle increases when the water level is near the obstacle. Like the Figures in **Case A**, Figures B5 to B8 show the v-w velocity components. A pair of vortices is clearly shown in the wake. Figures B9 to B12 are non-dimensional velocity components u, w at different levels to the channel bed.

Test **Case C** is similar to test **Case B** but with an even shallower water depth. The water depth, H = 0.042m, is about half the height of the obstacle. When the obstacle penetrates the water surface, the flow pattern is notably different from **Case A** or **Case B**. In this case the flow is more like the flow around a cylinder. The surface disturbance is not as high as that in **Case A** or **B**. From Figures 4.4.C it was found that the effect of the obstacle was dramatically increased. As shown in Figures C2 through C4, a much larger wake was generated behind the obstacle, but the vortex region becomes smaller. Another notable phenomenon is that the vortex is not symmetric any more. The reason may be that, in reality, the flow will be unsteady and Karman vortices will be present. Although the current calculation is based on a steady state assumption, the numerical solution is iterative, and the residual of the iterations can not be exactly zero. Thus, the approximation in the numerical solution will act as the unsteady term and makes an unsymmetric vortex possible. From Figures C5 through C8, another observed difference is the presence of vortices generated beside the obstacle and shed downstream. In contrast, in **Cases A** and **B** this kind of vortex was not found, or it might be too weak to be detected.

In Figures C9 to C12, the downstream velocity profiles at different levels are plotted.

In test **Case G** the water depth was increased to 0.2m, more than three times the obstacle height. Calculated results for u-v streamlines at the channel center plane, velocity vectors and streamlines at the plane y = 0.004m and the plane x = 0.595m, and the calculated free surface are plotted in Figures 4.4.G1 to G4. Comparing these results with corresponding plots in test **Case A** shows that all flow properties are very similar in the two cases except the surface wave in **Case G** is not significant. Thus the effects of the free surface are negligible when the water depth is greater than twice the obstacle height (as in **Case A**). In **Case G** the fluctuation of the water surface above the obstacle is less than 2% of the water depth.

CASES D, E, F: Interaction between Obstacles

In test **Case D** three identical hemispheres labeled 1, 2, and 3 were laid on the channel bed to study interactions between these hemispheres. All other conditions remain the same as **Case A**. The layout of the hemispheres and the cross-sections where 2-D streamlines and velocity components are plotted are shown on Figure 4.4.D0. The non-dimensional distance from the center of the hemisphere 1 to the center of the hemisphere 2 or 3 is 3.22 and the non-dimensional distance between the centers of the hemispheres 2 and 3 is 4.56.

Figures 4.4.D1 through 4.4.D4 are plots of the u-v streamlines as in the previous cases. Comparing Figures 4.4.D1 and 4.4.D3, which are plots of the flow past hemispheres 1 and 3, one sees similar vortex structures, but the recirculation zone of hemisphere 1 is noticeably smaller than the recirculation zone of hemisphere 3. If one compares with test **Case A**, it can be found that Figure 4.4.D3 and Figure 4.4.A1 have a very similar recirculation zone and flow pattern. It seems the effect of hemisphere 1 is not significant determinant of the velocity distribution of hemisphere 3 in the primary flow direction.

The v-w velocity components are plotted in Figures 4.4.D5 to D12. In the wake of three hemispheres, the flow becomes very complex, especially in the far wake. Figure 4.4.D12 shows that the "2-D vortex structures" of the three hemispheres tangle together. The "2-D vortex structure" behind front hemisphere is noticeably different from that shown in Figure 4.4.A11.

Figures 4.4.D13 to D16 show the u-w velocity components and u-w streamlines. Figure D13 shows that the wake of hemisphere 1 was constricted by hemispheres 2 and 3. Between the wakes of the front and back hemispheres, there is a strip of intense flow where strong velocity gradients are found. More careful observation shows that the wakes behind the hemispheres 2 or 3 become unsymmetric relative to the centerline of each hemisphere. Both wakes are shifted toward the channel centerline, as shown in Figure 4.4.D13.

Figures 4.4.D17 through D22 show the u velocity distribution at different elevation. In Figures 4.4.D23 through D25, the w velocity distribution is plotted. From these figures interference of the velocity distributions for these three wakes can be observed.

Besides the flow patterns, the calculated free surface shows a more notable change due to the interactions between the hemispheres. The existence of the front hemisphere significantly reduces the water surface height above the downstream hemispheres as shown in Figure 4.4.D26. On the other hand, the back hemispheres also limit the size of the depression behind the front hemisphere.

To examine the pure effect of an upstream hemisphere on a downstream hemisphere, in test **Case E** the upstream hemisphere was removed. This change is the only difference between **Case D** and **Case E.** The calculated results for **Case E** are shown in Figures 4.4.E.

By comparing Figures 4.4.E1 and E2 with Figures 4.4.D2 and D3, for u-v streamlines, one sees great similarity in these two cases. Some differences are found in w-u and v-w

streamlines by comparing Figures 4.4.E3 through E6 with Figures 4.4.D13 through D16 and Figures 4.4.E7 through E11 with Figures 4.4.D8 through D12. First of all, the unsymmetric wakes are not found in Figures 4.4.E3 through E6, and the wakes behind the two hemispheres are almost identical. That indicates the unsymmetric wake is caused by the front hemisphere, and the interaction between the two back hemispheres is negligible. Only at distances far from the obstacles, do the two wakes tangle together to form complex vortices, as shown in Figure E11. In **Case D** where the downstream hemispheres are in the wake of the front hemisphere, the average water elevation above the downstream hemispheres is much lower than that in **Case E** (refer to Figures 4.4.E23 and 4.4.D26). Looking at the velocity profiles in Figures 4.4.E13 through E22, basically one can find no sign of interaction. The velocity distributions around two hemispheres are almost identical and are symmetric about the centerline of each hemisphere.

A further examination of interactions between the hemispheres was done by changing the distances between the hemispheres. Test **Case F** evolved from test **Case D**. The only difference between the two tests is the distance between hemispheres in **Case F** which is only half of that in **Case D**. In **Case F** the non-dimensional distances between the hemispheres are 1.61 and 2.29. Comparing Figure 4.4.F1 with 4.4.D1, it was found that the recirculation zone behind the front hemisphere is gone. Figures 4.4.F5 through F8 show that the three hemispheres act almost as one object and generate a large single wake. However, the cress-sectional area of this single wake is less than the total area of three wakes in **Case D**. The u and w velocity distributions are shown in Figures 4.4.F14 through F18 and F19 through F23. The wakes behind the three hemispheres mix together as can be seen from the velocity distribution.

As shown in Figure 4.4.F24, the three waves above the hemispheres merge together.

4.4.3 Wake Areas for Different Fish Habitat Structures

The efficiency of fish habitat structures may be measured by two major flow properties: the plan wake area and the velocity distribution. The examples in this chapter show that

the numerical model is an efficient method to determine these flow properties. In section 4.4.2, velocity distributions of flow around seven simplified fish habitat structures are discussed. In this section the wake areas and wave heights for different fish habitat structures are studied.

First the wake area is studied by using the calculated results from the early section in this chapter. In Figures 4.4.H 1 through H14, contours of velocity magnitude q at an elevation of half the hemisphere height above the channel bed are plotted for all test cases. For each case, two kinds of wakes, in which the velocity is less than 50% and less 75% of the average velocity U_0 are plotted. In these plots the white area inside the contours is the region where the velocity is below 0.03m/s (0.015m/s for **Case** C). On the outermost contour lines, the velocity is 50% or 75% of the average velocity.

The first finding is that the water depth has little effect on the extent of the wake areas if the water depth is greater than twice the obstacle height. No notable differences are found between the wakes of test **Case A** (H = 0.12m, Figure 4.4.H1) and test **Case G** (H = 0.20m, Figure 4.4.H5). If the obstacles penetrate the water surface, the wake areas will increase dramatically (refer to test **Cases A, B, C**). Thus in a fish habitat structure design it is more efficient to let the obstacles penetrate the water surface. Detailed data of wake areas when $q/U_0<0.5$ for different cases are given in Table 4.4.3. For the multiple hemisphere cases total wake area divided by the number of the obstacles is used. Exact wake areas for $q/U_0<0.75$ can not be found because the wakes will go far beyond the downstream computational boundary. However, Figures 4.4.H7 through H10 and H13, H14 can give a qualitative indication of wake areas when $q/U_0<0.75$ for different cases. Figure 4.4.3 shows the relationship between the wake areas and the blockage rate defined by the ratio of the maximum cross-section area of the obstacle to the cross-section area of the channel.

The next conclusion concerns the relationship between the maximum wave height and the water depth. Although the free surface wave has less effect on the flow pattern, it affects the pressure on the channel bed. From this series of tests, a curve was drawn to represent

changes of maximum wave height against water depth. Figures 4.4.1 to 4.4.2 and Table 4.4.4 show the relations between maximum wave height and the water depth. The most obvious finding is that the highest wave is created when the water depth just exceed the obstacle height. If the water depth is more than three times the height of the obstacles, the surface wave is negligible. On the other hand, if the water depth is below the top of the obstacles, the surface waves are also lower. The length scale X_L used in the plot to normalize the wave height is the total length of the computational domain. In Table 4.4.4, there are two measurements of the variations in wave heights for **Cases D** and **E**. Rows D1, F1 are for a wave before the front hemisphere, and rows D2, F2 are for the waves before the back hemispheres.

Table 4.4.3 Wake Areas ($q/U_0<0.5$) behind Hemispheres for Different Test Cases

Cases	A	B	C	D	E	F	G
Area (m^2)	0.07	0.34	0.60	0.05	0.07	0.07	0.06

Table 4.4.4 Relative Wave Heights for Different Test Cases

CASES	H(m)	R/H	$(H_1-H)/X_L$%	$(H_p-H_r)/H$%	$(H_p-H_r)/(H-R)$%
A	0.120	0.54	0.09	6.2	13.3
B	0.072	0.90	0.27	23.3	239.
C	0.042	1.55	0.08	12.6	-23.0
D_1	0.120	0.54	0.13	6.6	14.3
D_2	0.120	0.54	0.13	7.7	16.7
E	0.120	0.54	0.10	7.0	15.3
F_1	0.120	0.54	0.14	5.3	11.5
F_2	0.120	0.53	0.14	6.6	14.4
G	0.200	0.33	0.02	1.9	1.7

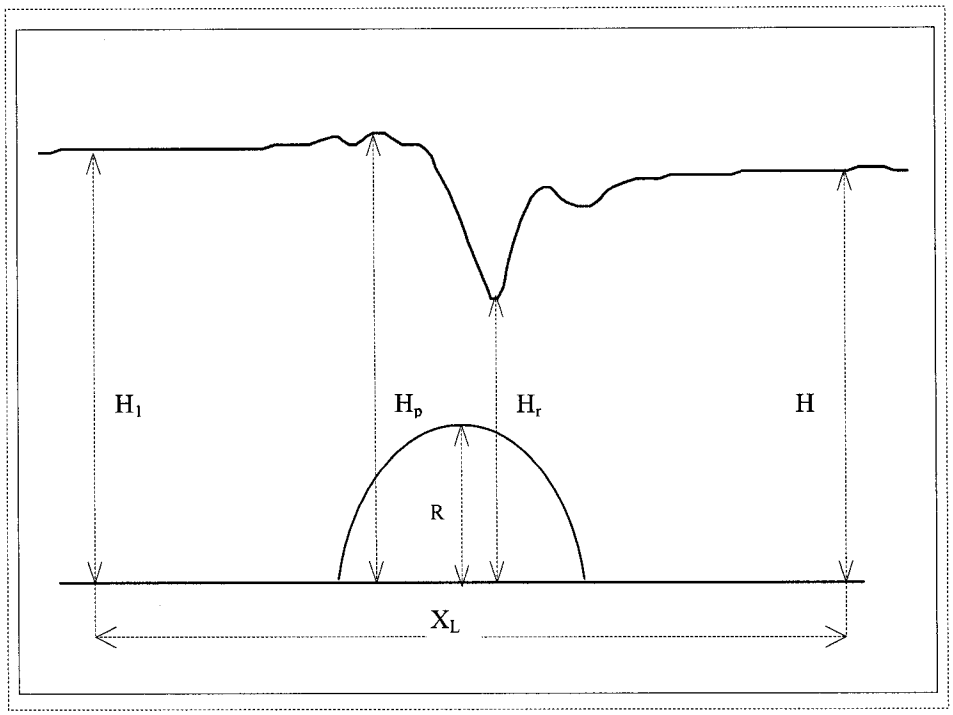

Figure 4.4.1 Relative Wave Height

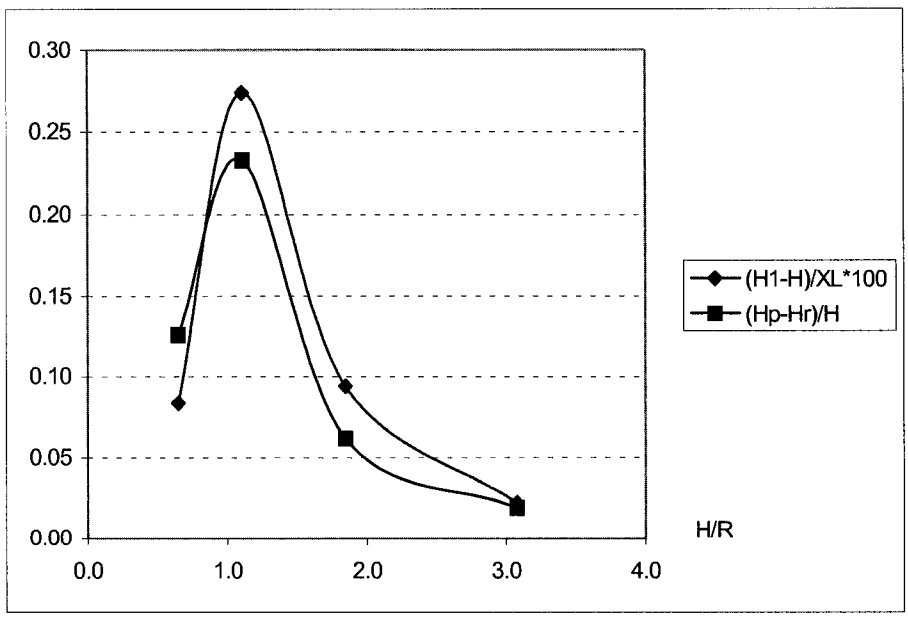

Figure 4.4.2 Relative Wave Height vs. H/R

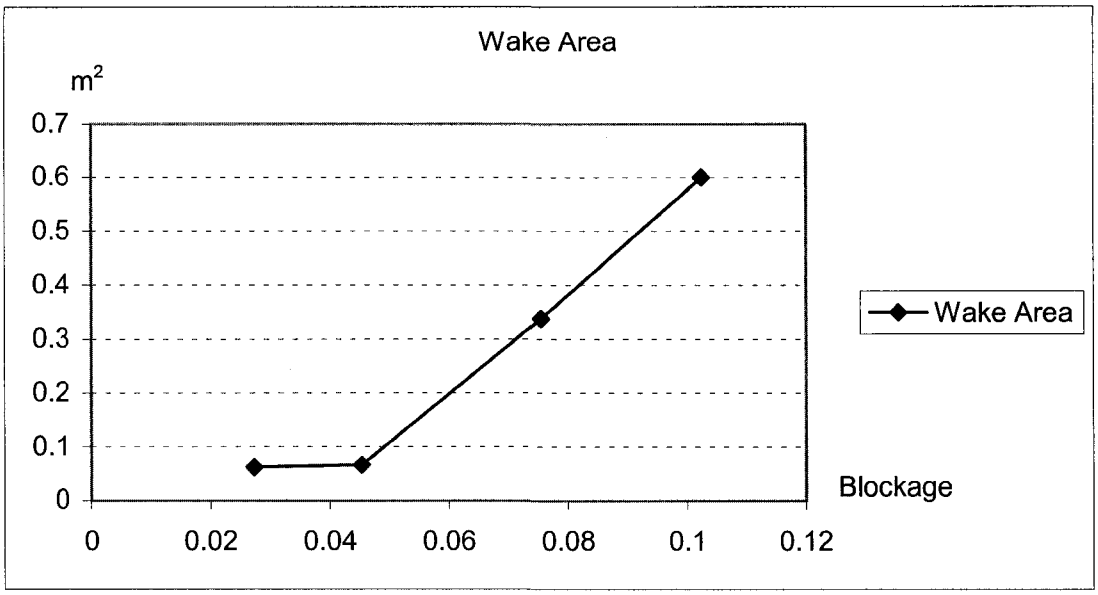

Figure 4.4.3 Wake Area vs. Blockage

4.5 Convergence Test and Grid Refinement Test

To verify the stability and reliability of this numerical model, the convergence and grid dependency of this numerical model were tested.

The residual R of the continuity equation as shown in equation (4.5.1) was used to judge the convergence of the solution.

$$R = (F_\xi \sqrt{g}\Delta\eta\Delta\zeta u)_e - (F_\xi \sqrt{g}\Delta\eta\Delta\zeta u)_w + (F_\eta \sqrt{g}\Delta\xi\Delta\zeta v)_n - (F_\eta \sqrt{g}\Delta\xi\Delta\zeta v)_s$$
$$(F_\varsigma \sqrt{g}\Delta\xi\Delta\eta w)_h - (F_\varsigma \sqrt{g}\Delta\xi\Delta\eta w)_l \qquad (4.5.1)$$

Two criteria SMAX and SSUM were employed in this model. The SMAX is the maximum of the absolute value of R in each cell over whole computational domain. The SSUM is the sum of R over the whole domain. It is obvious the value of these criteria depend on the scale of the problem interested and the requirement of a particular project.

The flow around a hemisphere in section 4.3 was used as test case, the convergence rate were plotted in Figure 4.5.1. It shows a very stable convergence. The results on 8000^{th} iteration are

$SMAX = 1.31 * 10^{-9}$

$SMUM = 1.87 * 10^{-8}$

For grid dependence test, the same test case was used. The results of grid sizes of 59*18*47 and 59*28*47 were compared. Only primary flow velocity u is plotted in Figure 4.5.2. The results show that the refinement of the grid only affects the velocity profile near the walls. The curves labeled Y-18 and Y-28 indicates the results of the calculations with a 59*18*47 grid and a 59*28*47 grid, respectively.

The grid used for this test case is plotted in Figures 4.5.3 and 4.5.4.

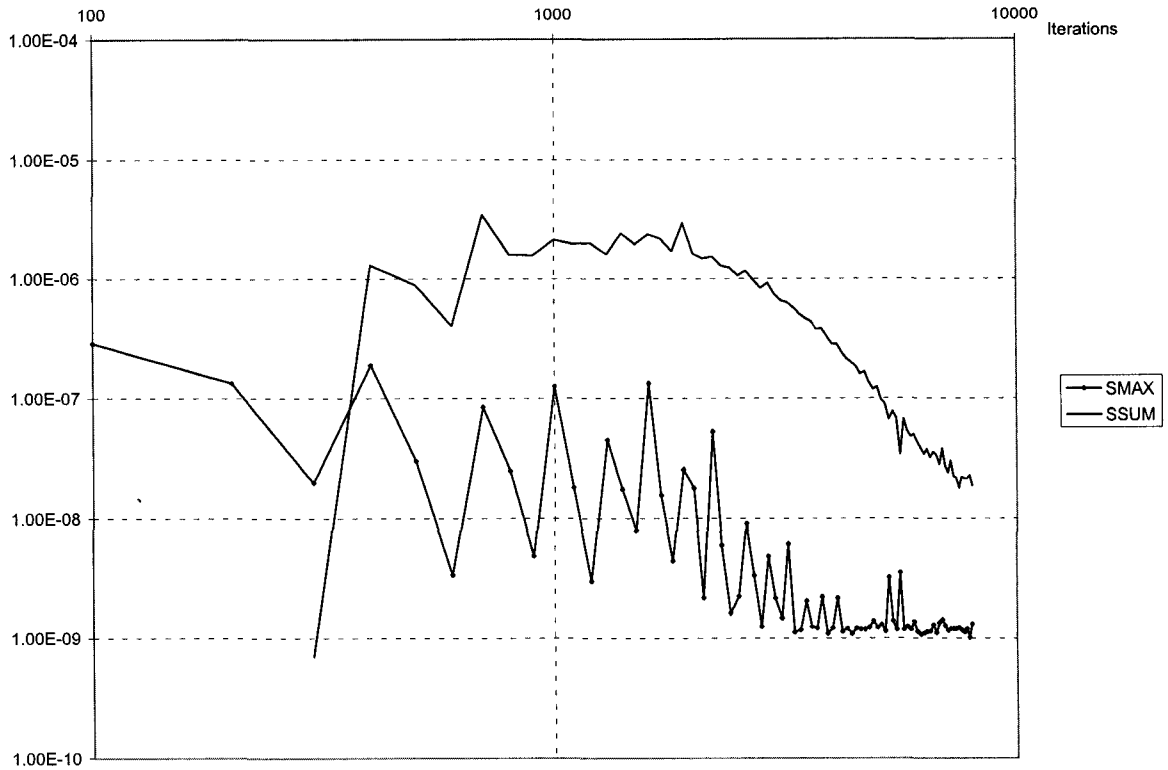

Figure 4.5.1 Convergence Test

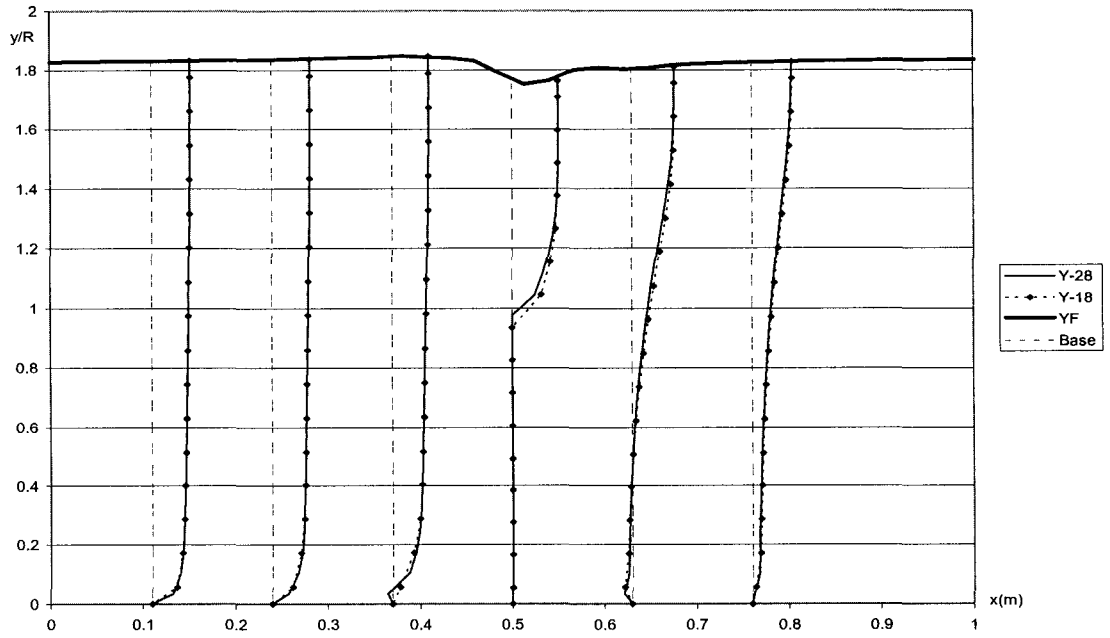

Figure 4.5.2 Grid Refinement Test

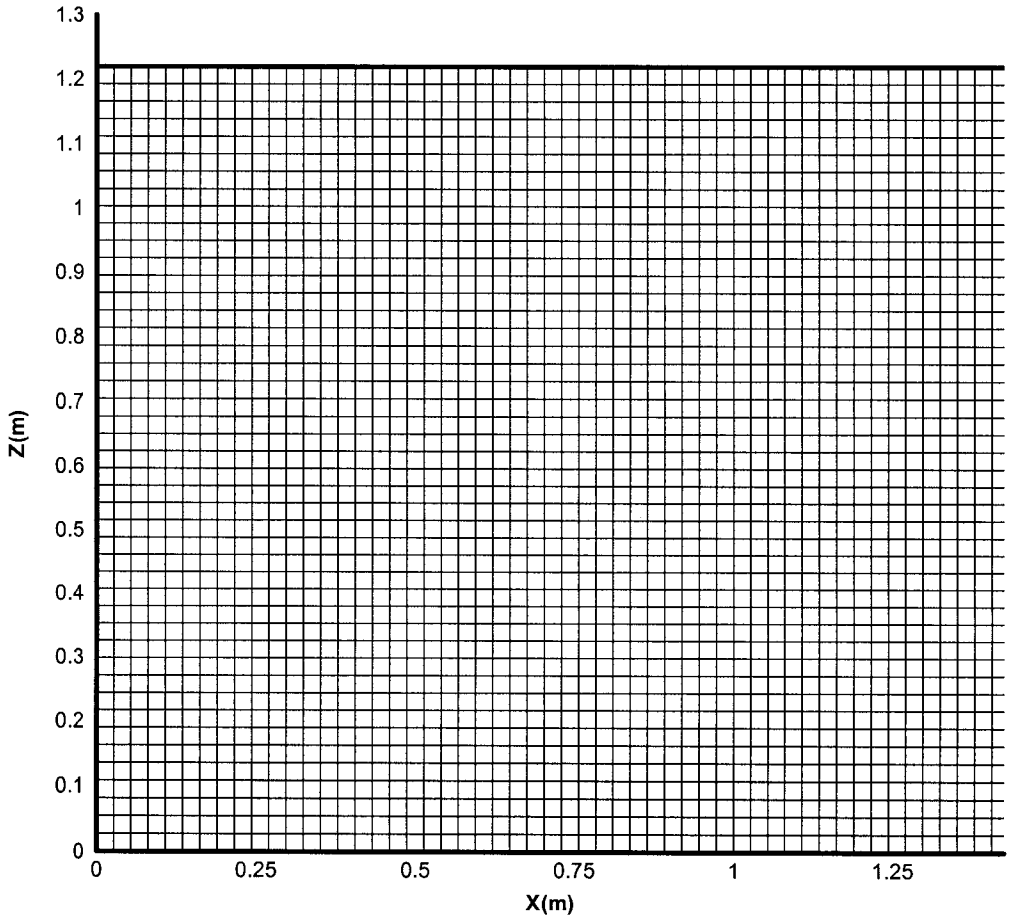

Figure 4.5.3 Grid in x-z Plane

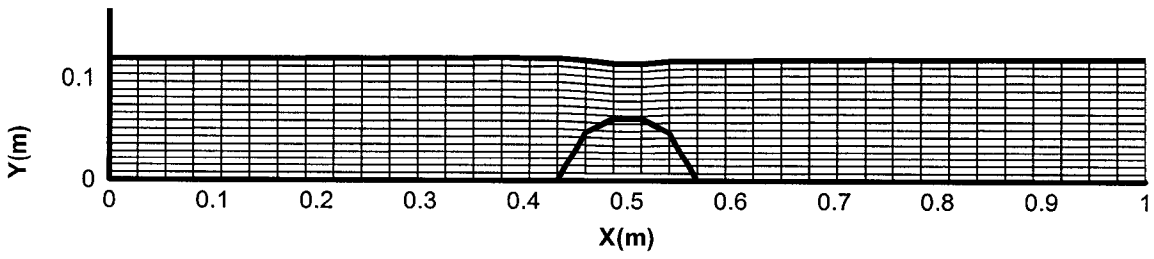

Figure 4.5.4 Grid in x-y Plane

Calculation Case A: Water Depth = 0.12 m, Single Obstacle

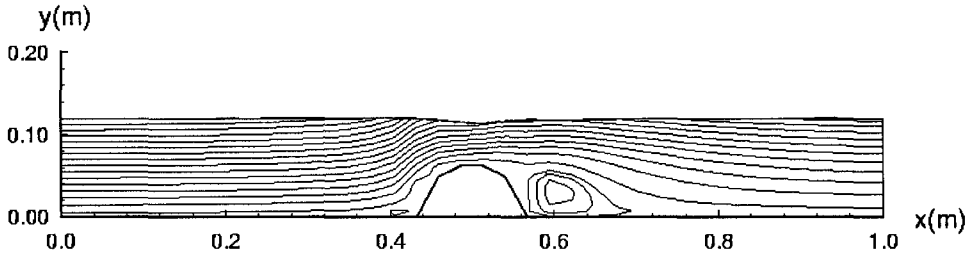

Figure 4.4.A1 u-v Streamlines in Plane z = 0.596 m

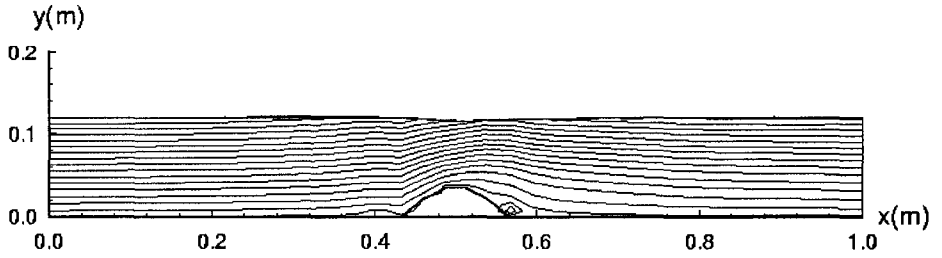

Figure 4.4.A2 u-v Streamlines in Plane z = 0.653 m

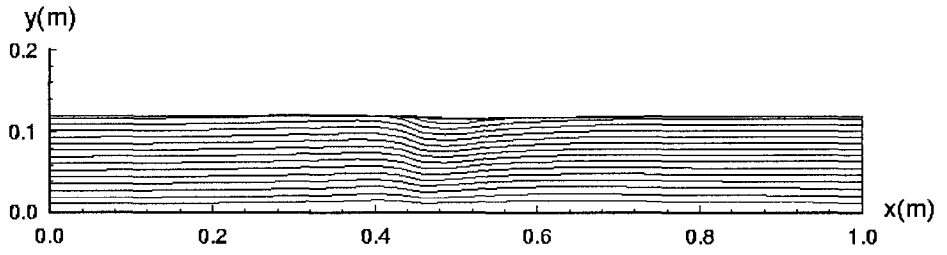

Figure 4.4.A3 u-v Streamlines in Plane z = 0.678 m

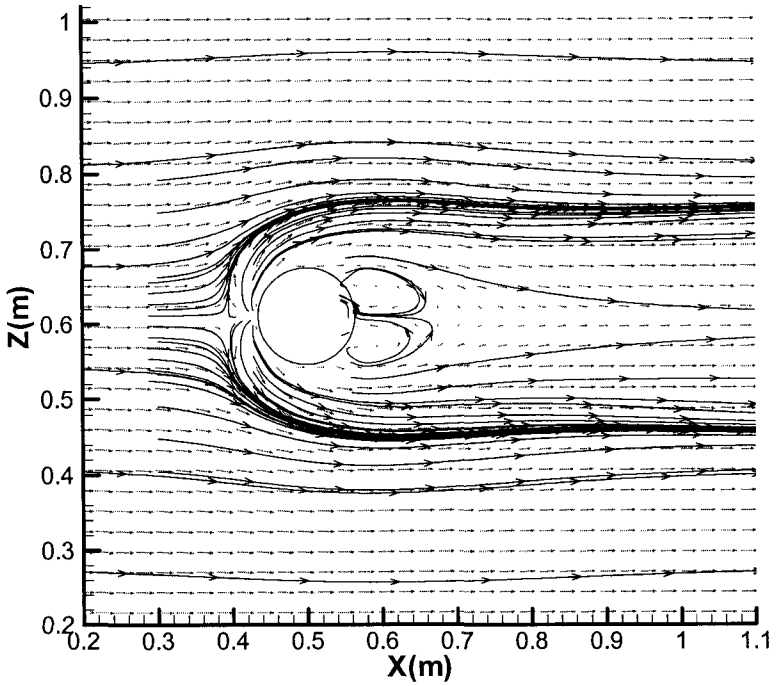

Figure 4.4.A4 u-w Streamlines and Velocity Vector in Plane y = 0.004 m

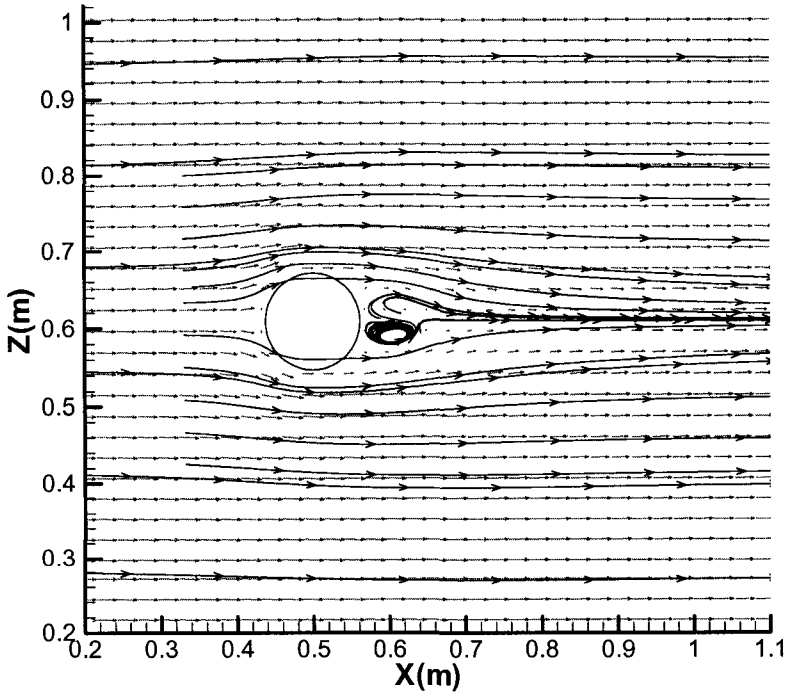

Figure 4.4.A5 u-w Streamlines and Velocity Vector in Plane y = 0.019 m

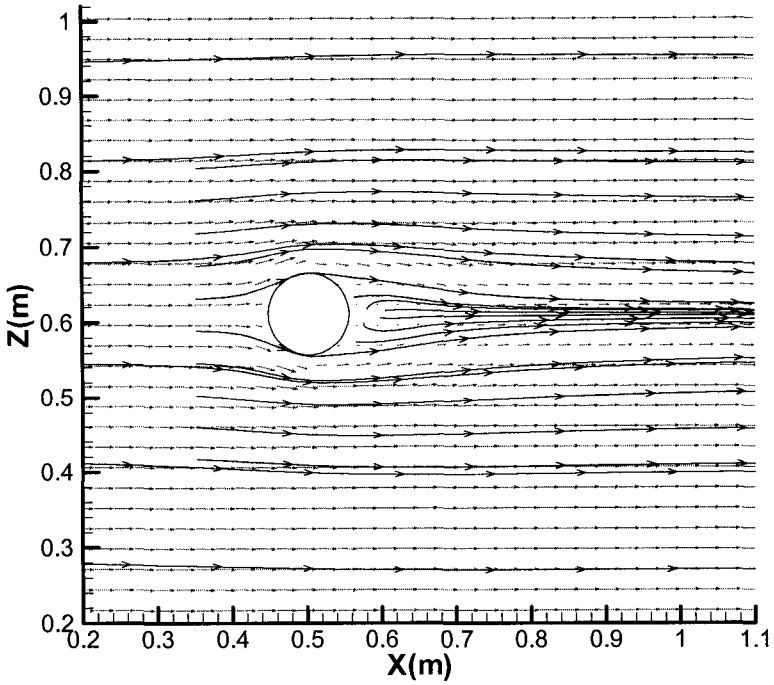

Figure 4.4.A6 u-w Streamlines and Velocity Vector in Plane y = 0.034 m

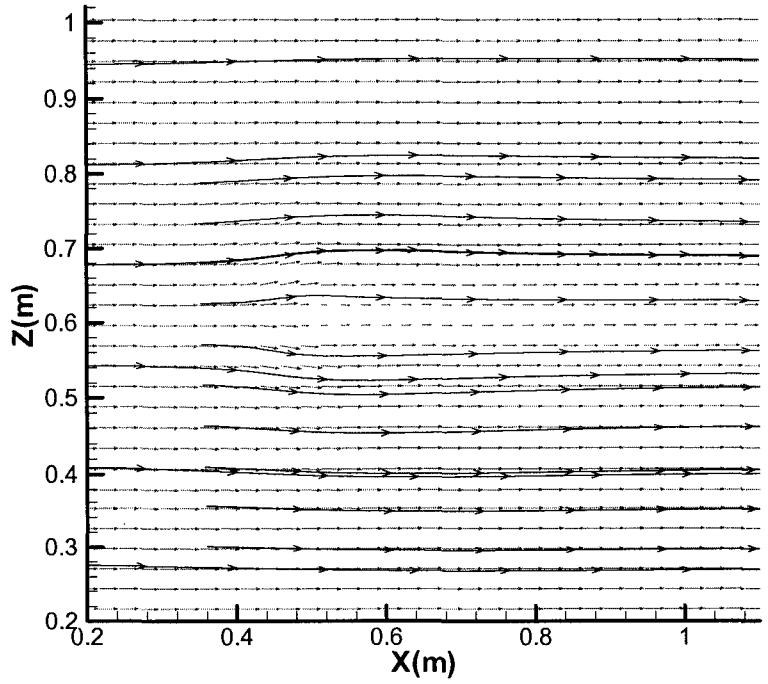

Figure 4.4.A7 u-w Streamlines and Velocity Vectors in Plane y = 0.064 m

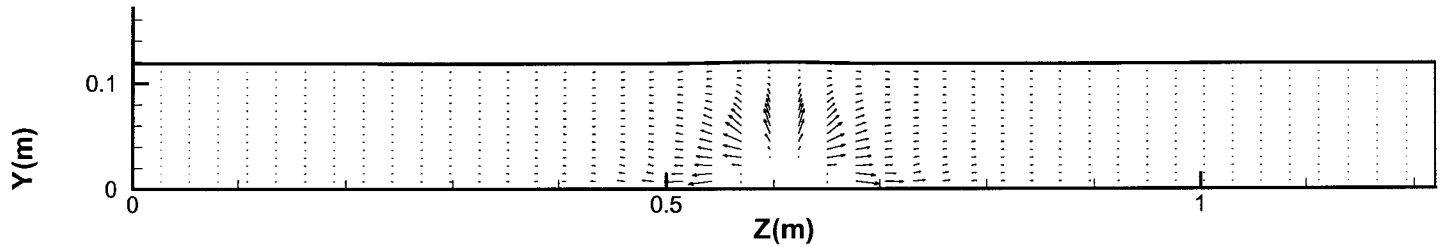

Figure 4.4.A8 v-w Velocity Vector in Plane x=0.432 m

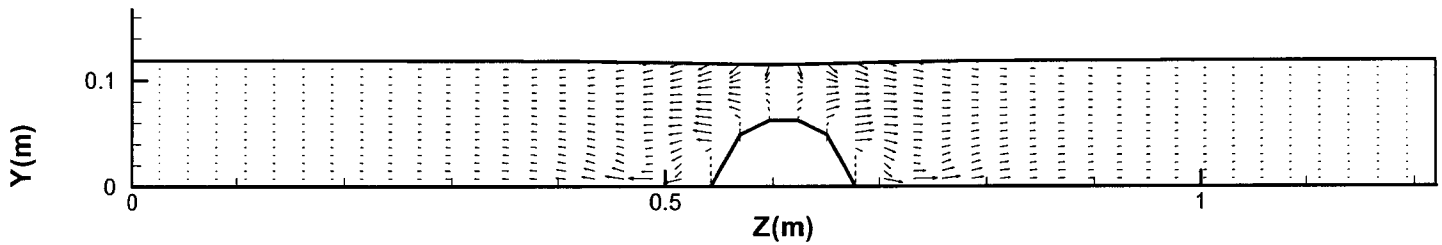

Figure 4.4.A9 v-w Velocity Vector in Plane x=0.486 m

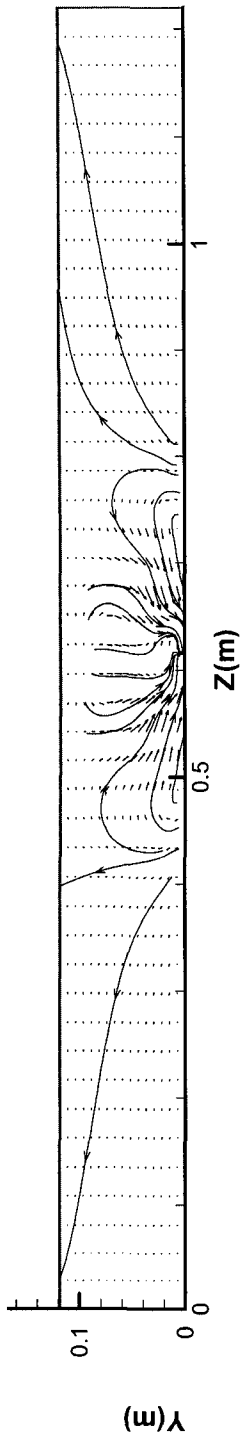

Figure 4.4.A10 v-w Velocity Vector in Plane x=0.595 m

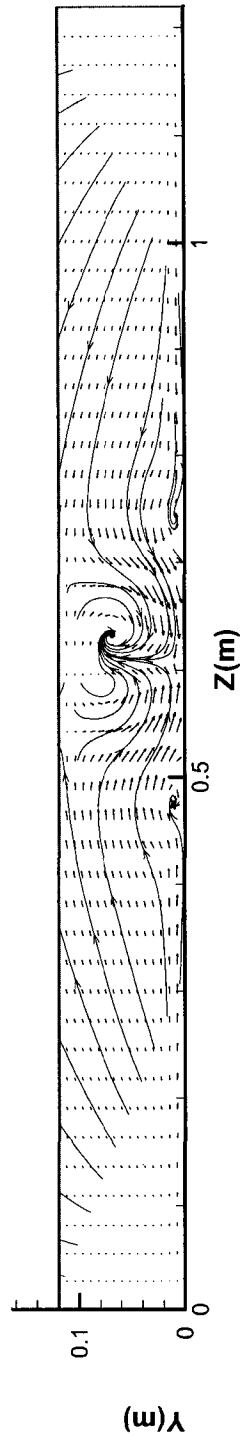

Figure 4.4.A11 v-w Streamlines in Plane x=0.919 m

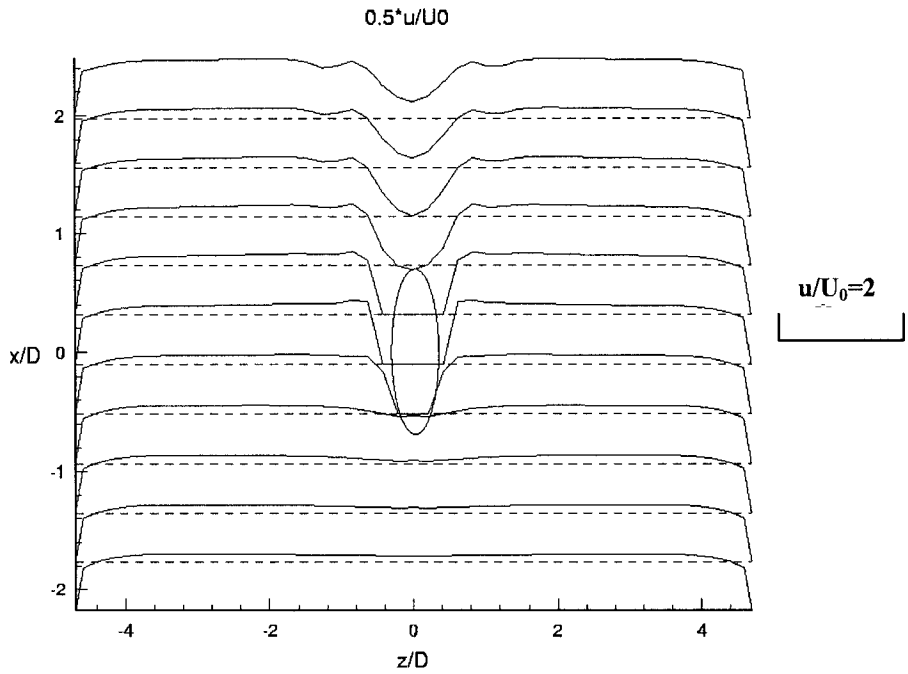

Figure 4.4.A12 Velocity Profile $0.5*u/U_0$ in Plane y=0.004 m

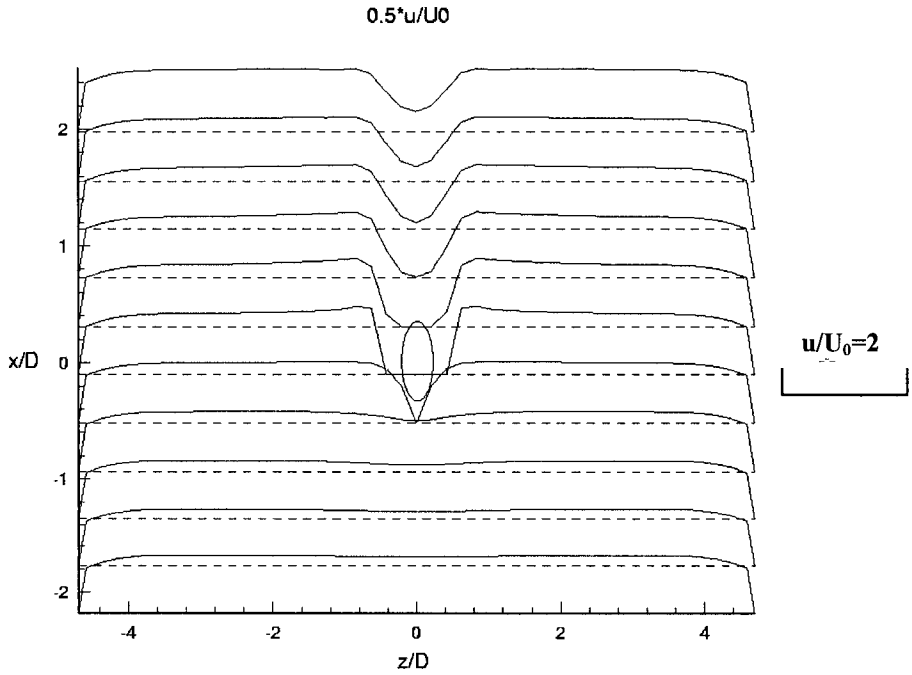

Figure 4.4.A13 Velocity Profile $0.5*u/U_0$ in Plane y=0.019 m

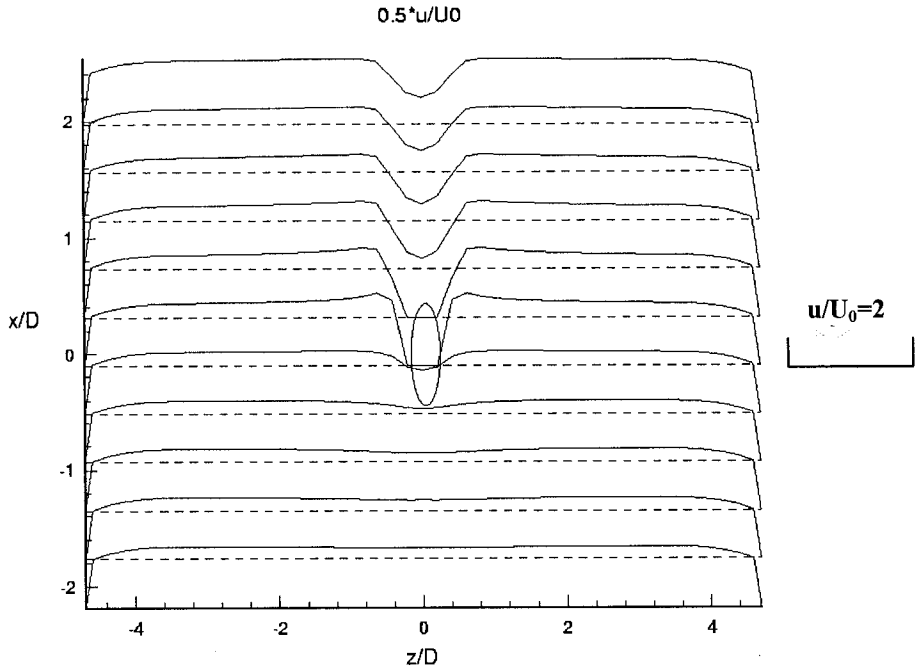

Figure 4.4.A14 Velocity Profile $0.5*u/U_0$ in Plane y=0.049 m

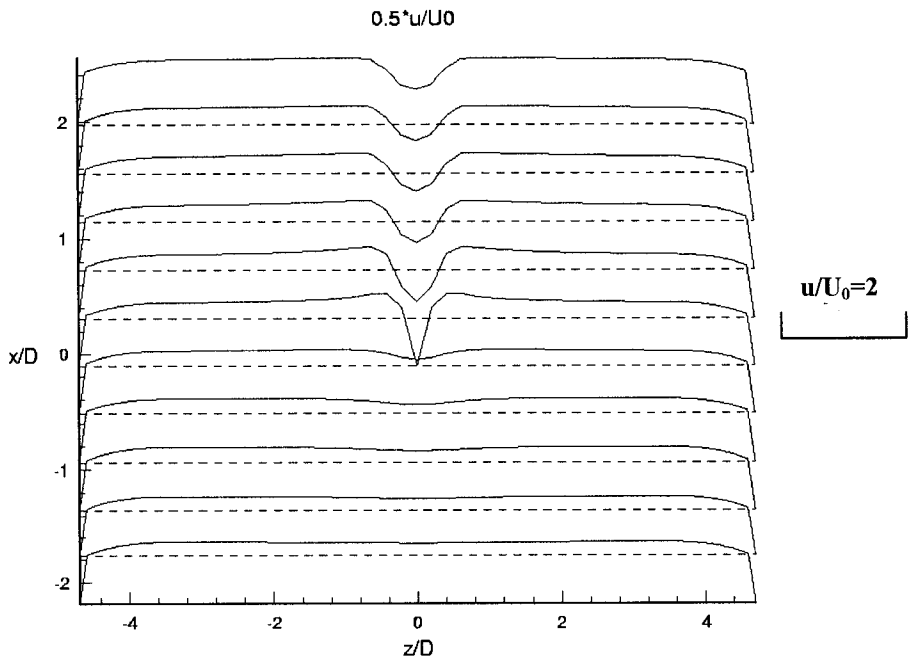

Figure 4.4.A15 Velocity Profile $0.5*u/U_0$ in Plane y=0.064 m

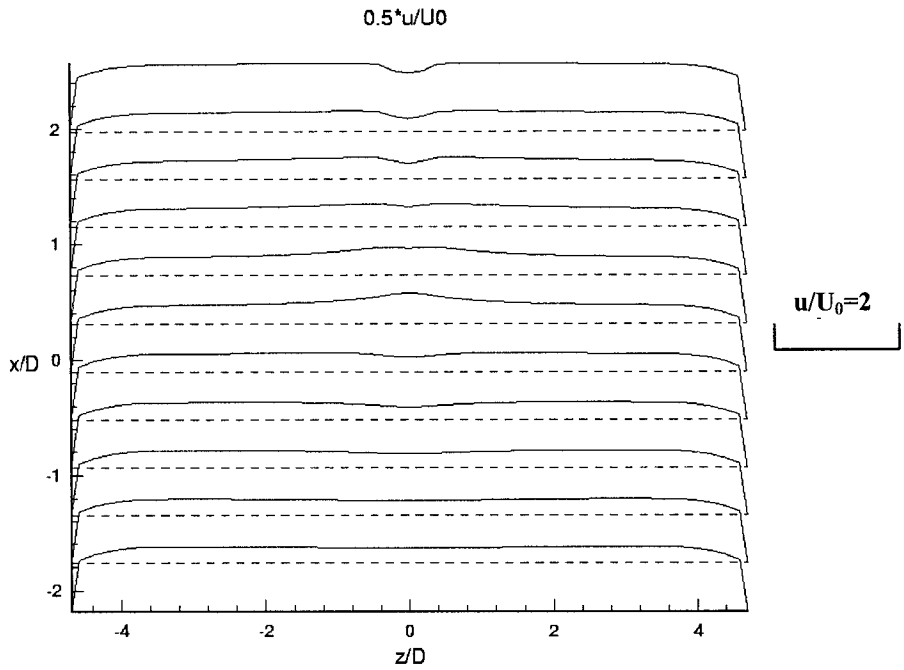

Figure 4.4.A16 Velocity Profile $0.5*u/U_0$ in Plane y=0.094 m

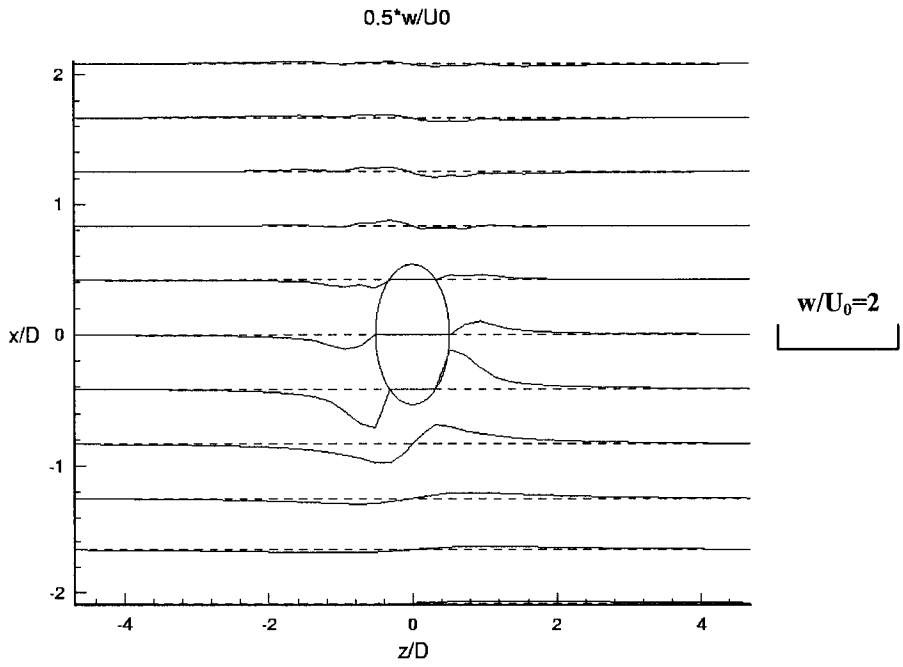

Figure 4.4.A17 Velocity Profile $0.5*w/U_0$ in Plane y=0.004 m

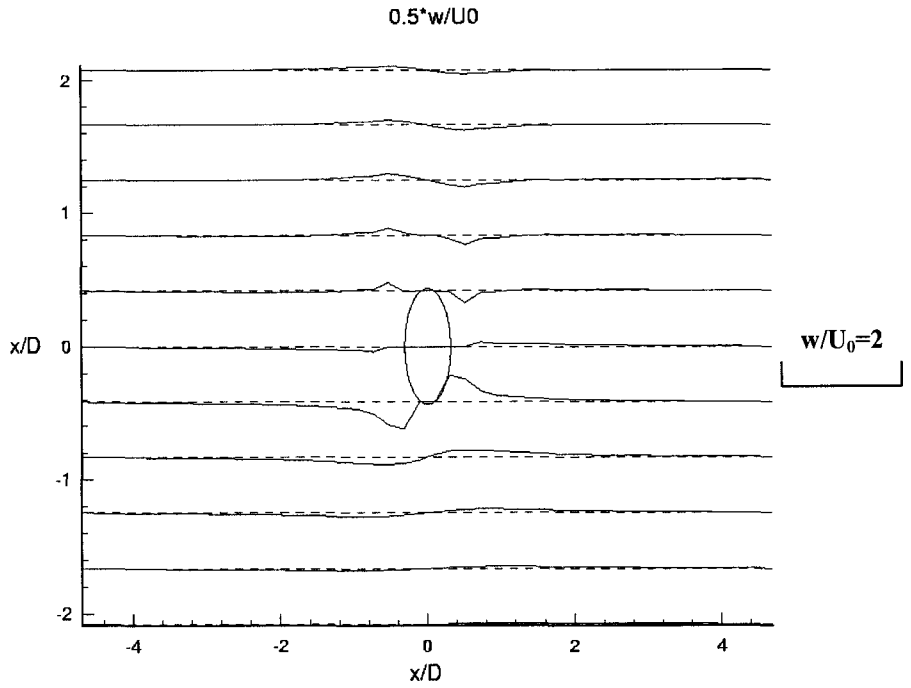

Figure 4.4.A18 Velocity Profile 0.5*w/U_0 in Plane y=0.034 m

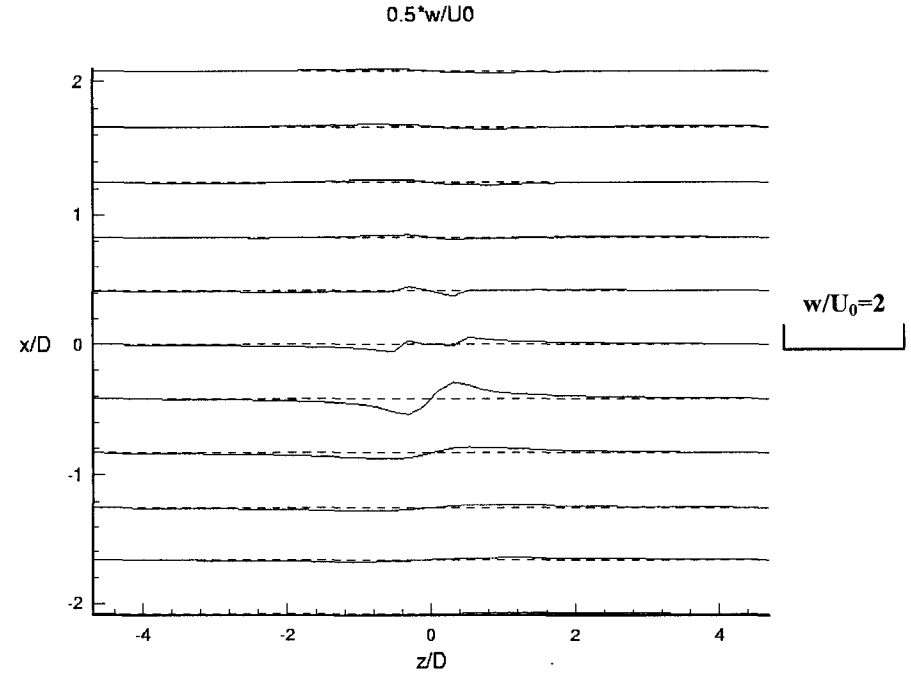

Figure 4.4.A19 Velocity Profile 0.5*w/U_0 in Plane y=0.064 m

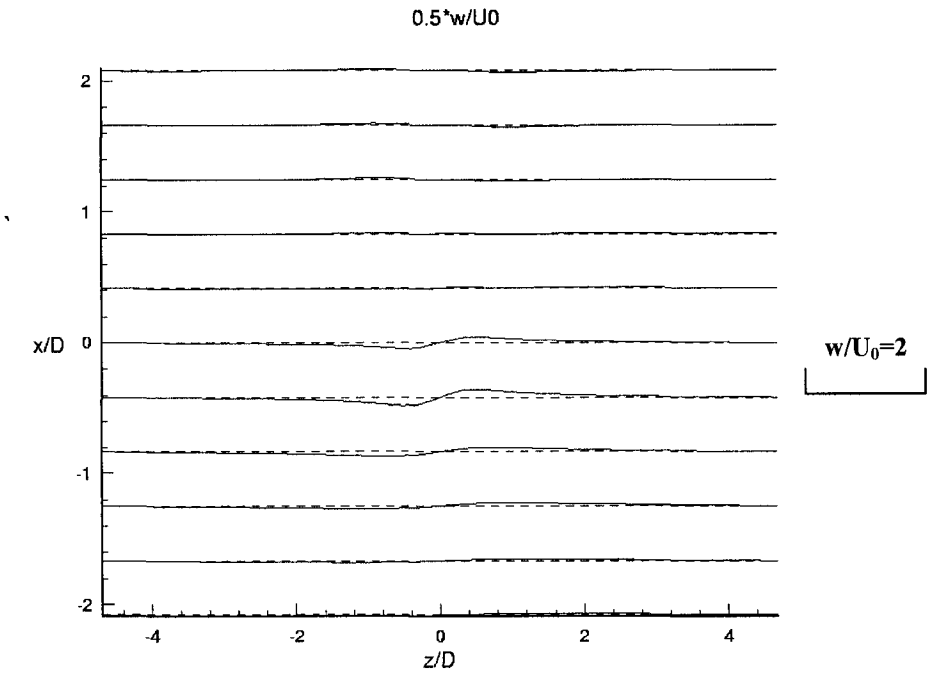

Figure 4.4.A20 Velocity Profile $0.5*w/U_0$ in Plane y=0.094 m

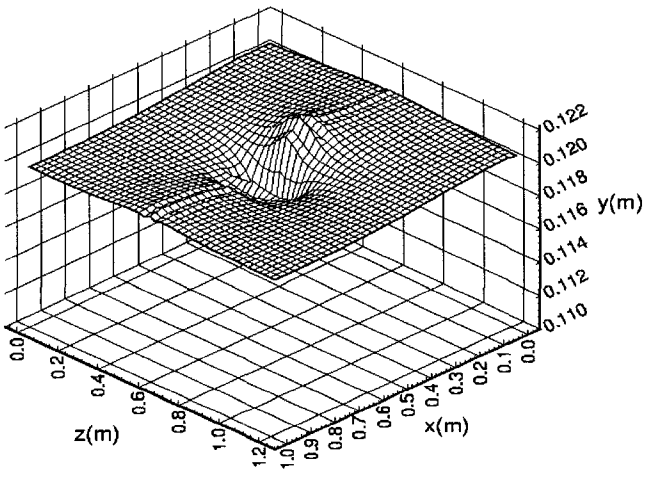

Figure 4.4.A21 Calculated Free Surface

Calculation Case B: Water Depth=0.072 m, Single Obstacle

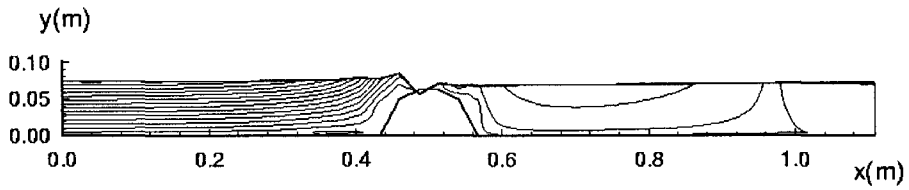

Figure 4.4.B1 u-v Streamlines in Plane z=0.596 m

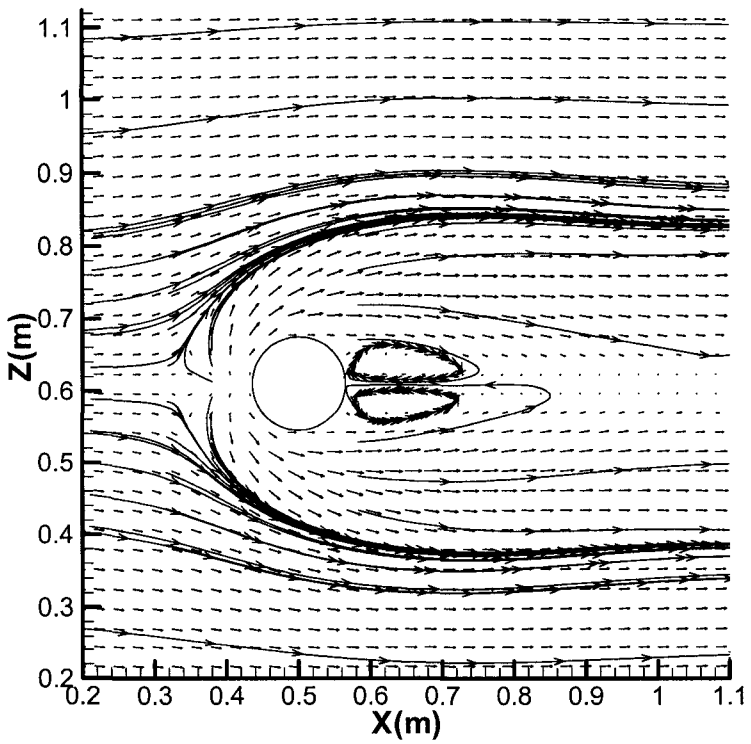

Figure 4.4.B2 u-w Streamlines and Velocity Vector in Plane y=0.0023 m

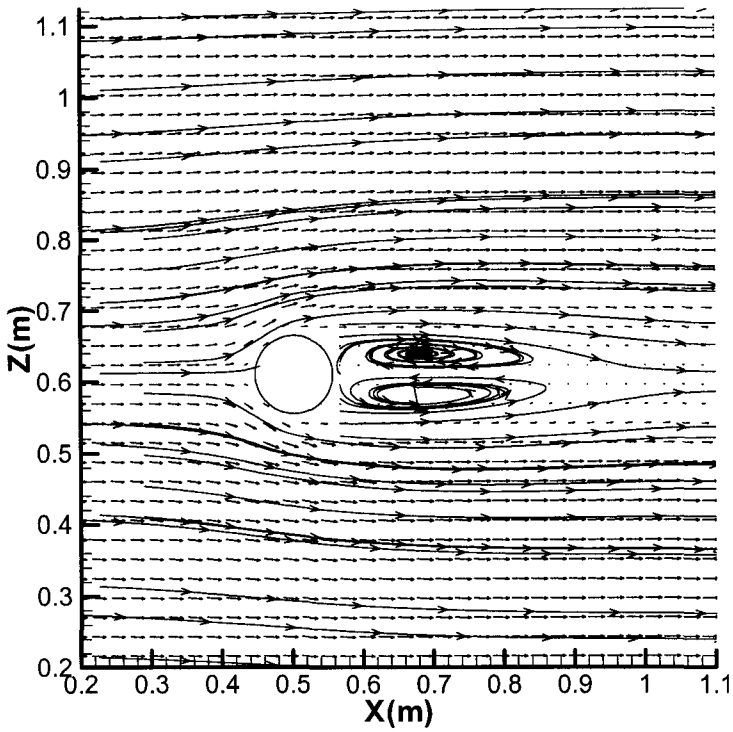

Figure 4.4.B3 u-w Velocity Vector in Plane y=0.0292 m

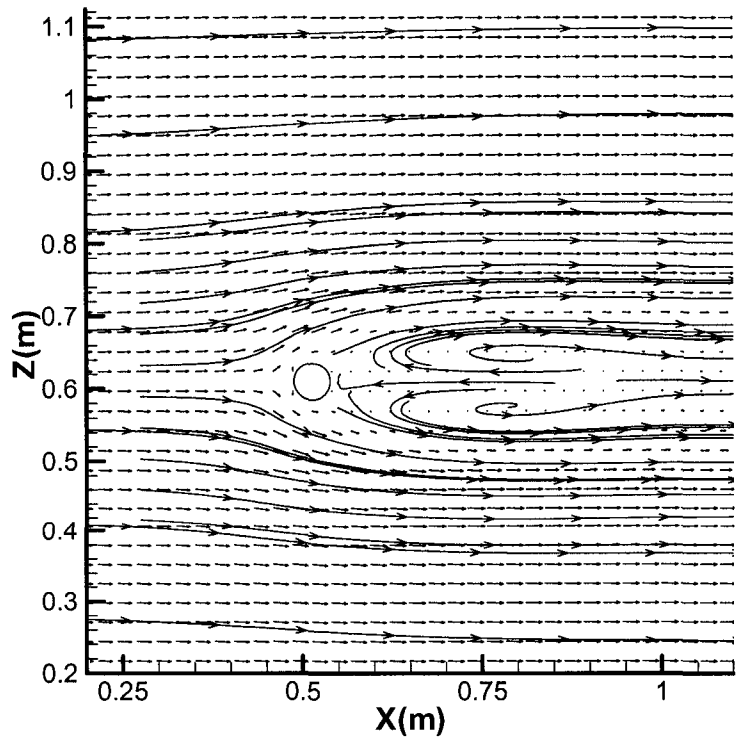

Figure 4.4.B4 u-w Velocity Vector in Plane y=0.0652 m

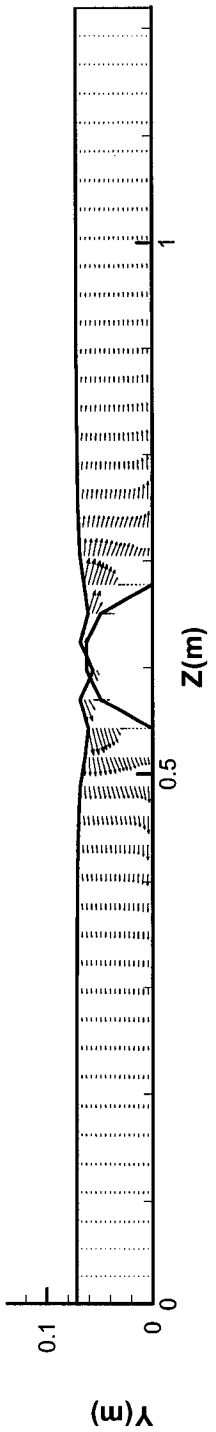

Figure 4.4.B5 v-w Velocity Vector in Plane x=0.486 m

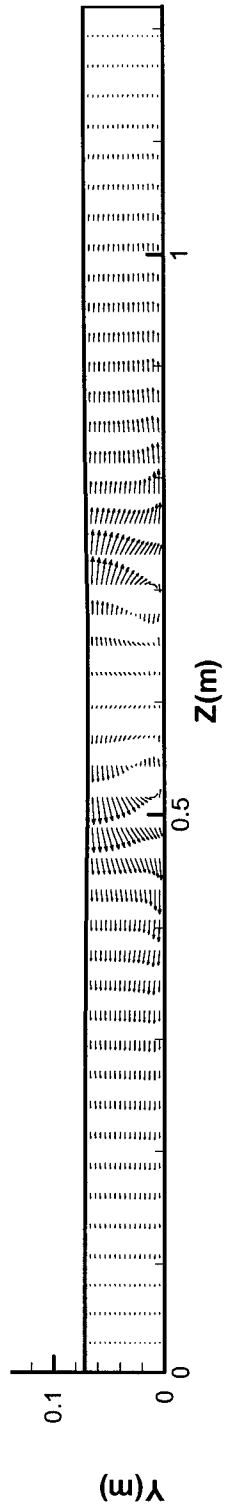

Figure 4.4.B6 v-w Velocity Vector in Plane x=0.595 m

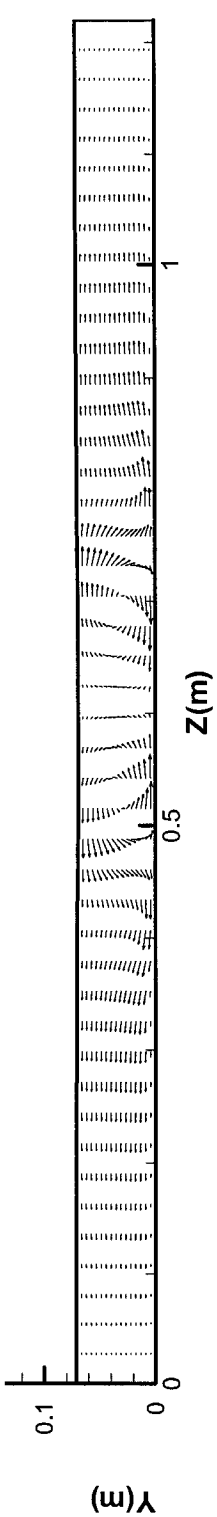

Figure 4.4.B7 v-w Velocity Vector in Plane x=0.703 m

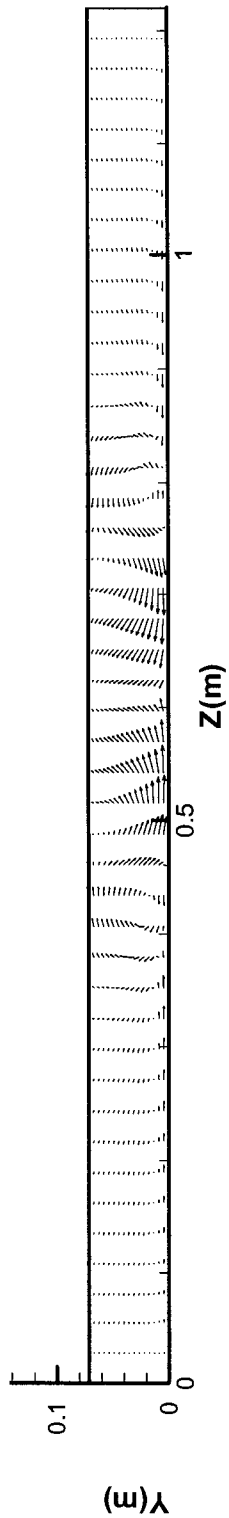

Figure 4.4.B8 v-w Velocity Vector in Plane x=1.027 m

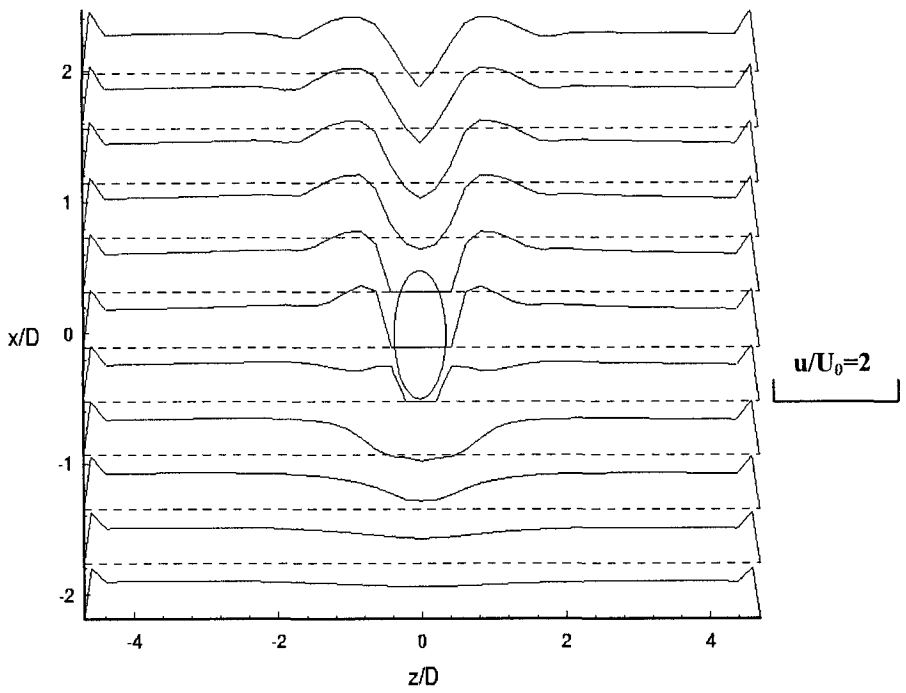

Figure 4.4.B9 Velocity Profile 0.5*u/U_0 in Plane y=0.0023 m

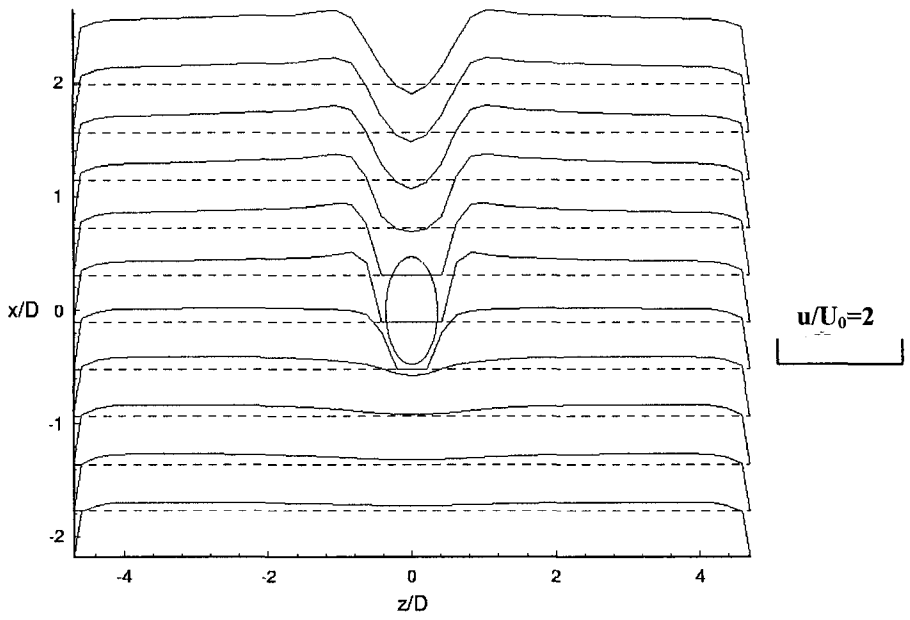

Figure 4.4.B10 Velocity Profile 0.5*u/U_0 in Plane y=0.0203 m

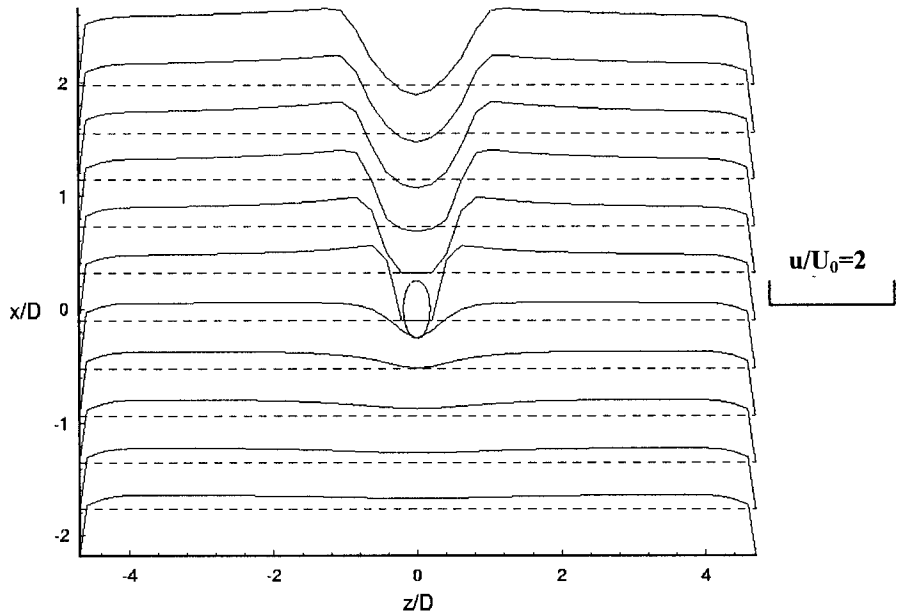

Figure 4.4.B11 Velocity Profile 0.5*u/U_0 in Plane y=0.0472 m

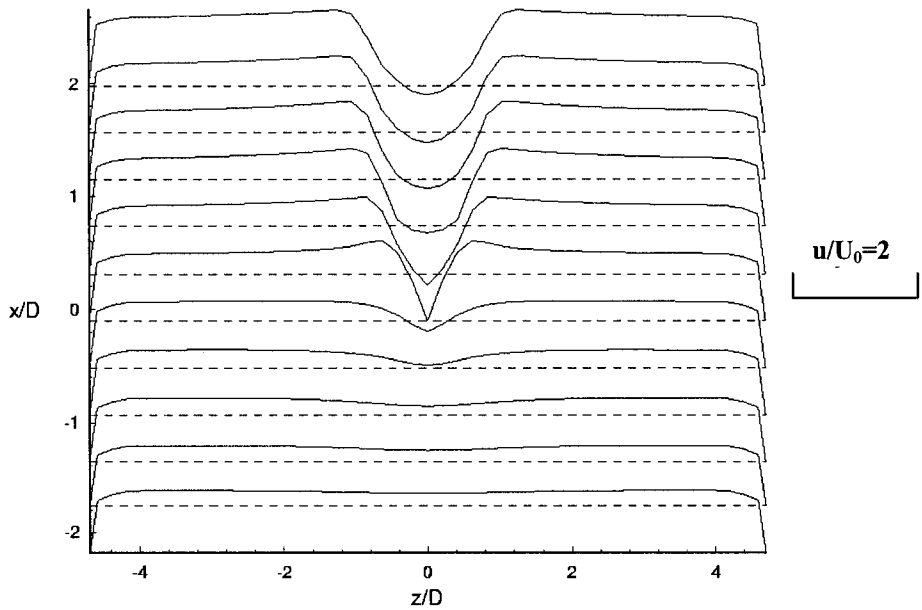

Figure 4.4.B12 Velocity Profile 0.5*u/U_0 in Plane y=0.0023 m

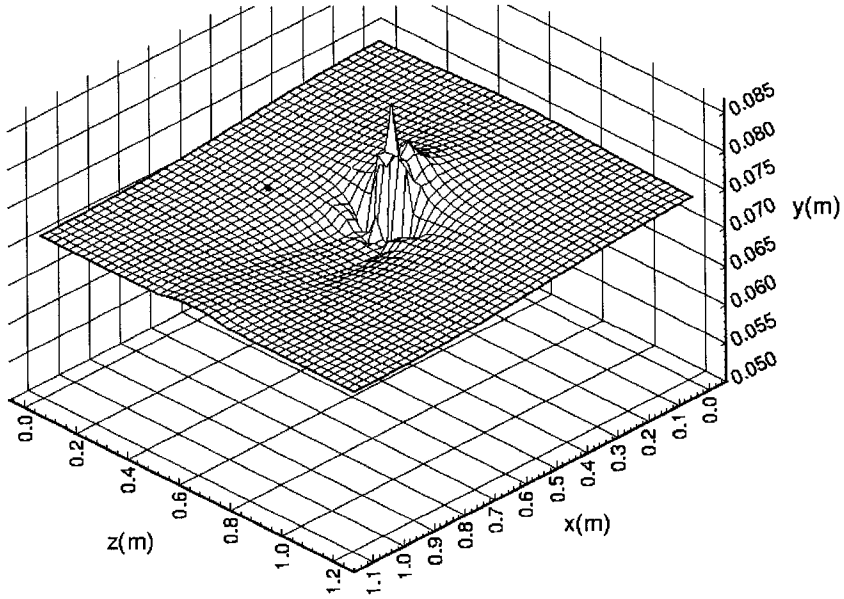

Figure 4.4.B13 Calculated Free Surface

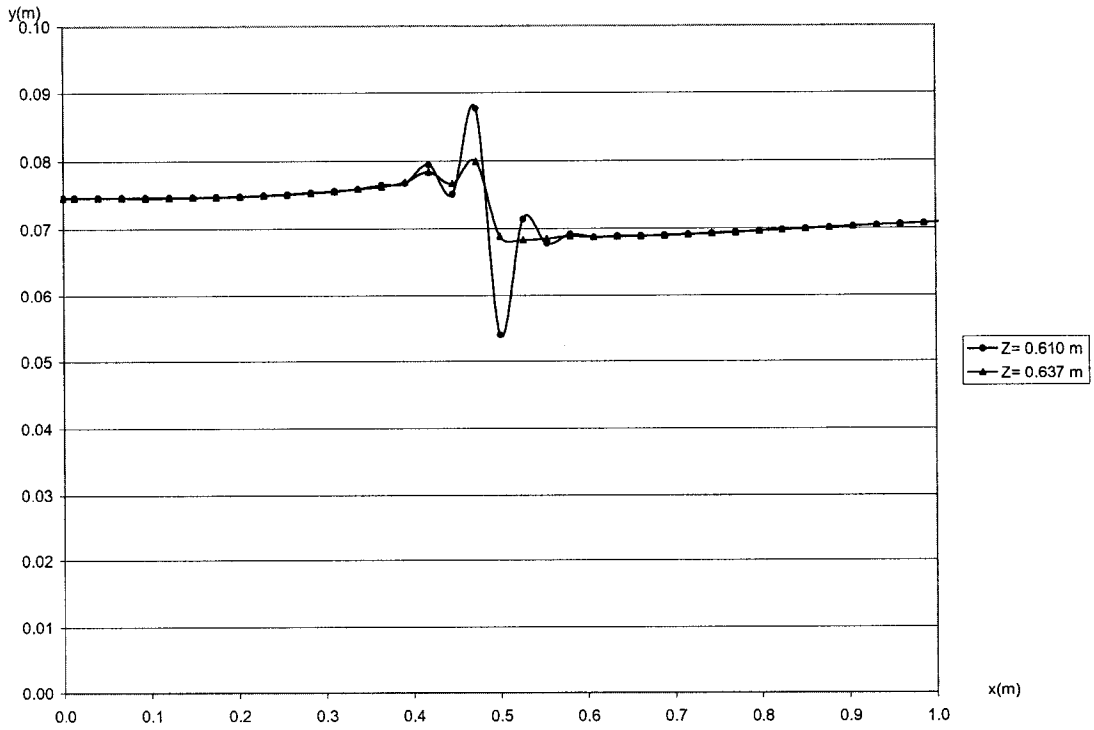

Figure 4.4.B14 Calculated Free Surface Profile near the Center of the Channel

Calculation Case C: Water Depth=0.042 m, Single Obstacle

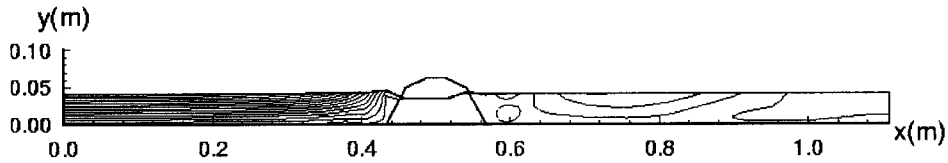

Figure 4.4.C1 u-v Streamlines in Plane z=0.596 m

\

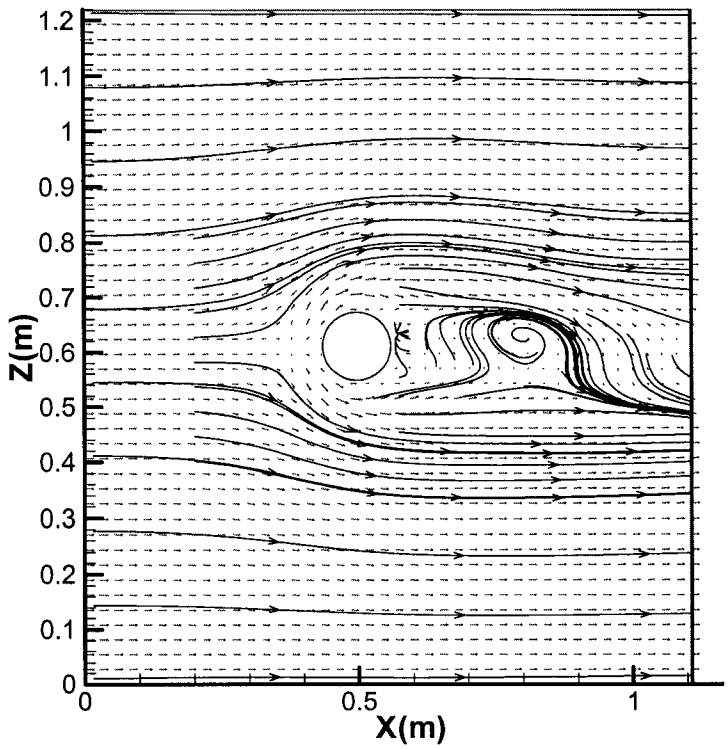

Figure 4.4.C2 u-w Streamlines and Velocity Vector in Plane y=0.0013 m

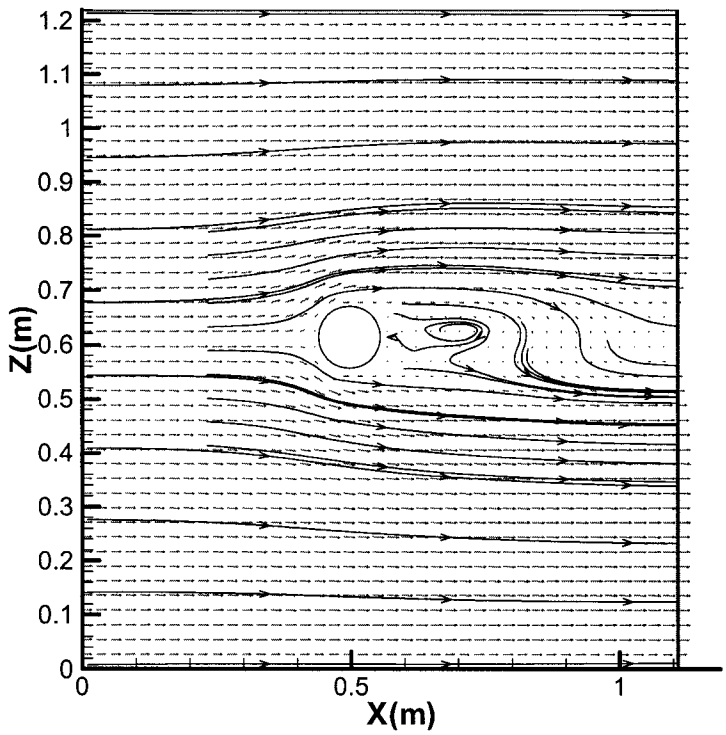

Figure 4.4.C3 u-w Streamlines and Velocity Vector in Plane y=0.0171 m

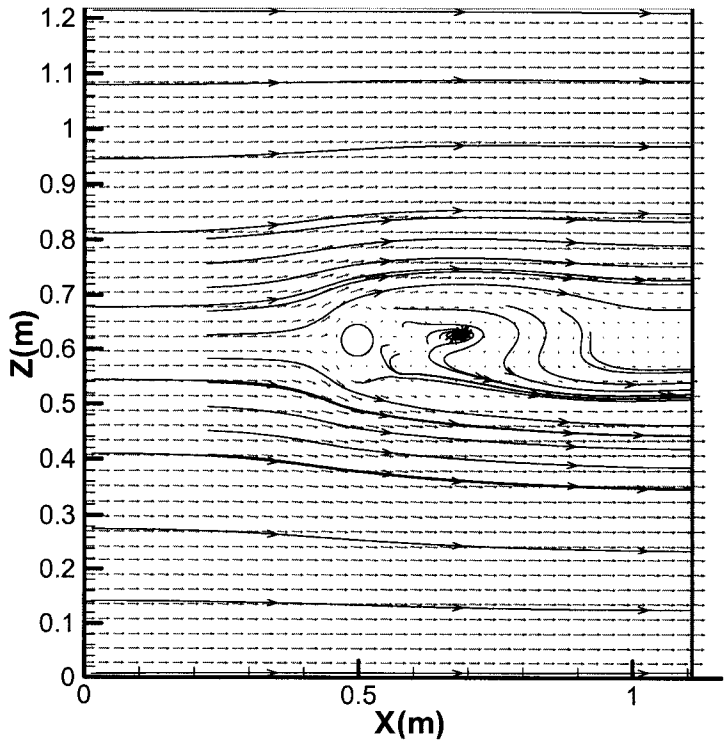

Figure 4.4.C4 u-w Streamlines and Velocity Vector in Plane y=0.0381 m

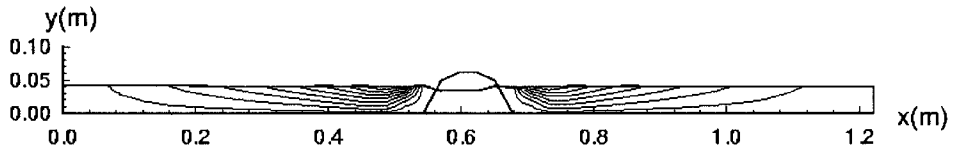

Figure 4.4.C5 v-w Streamlines in Plane x=0.486 m

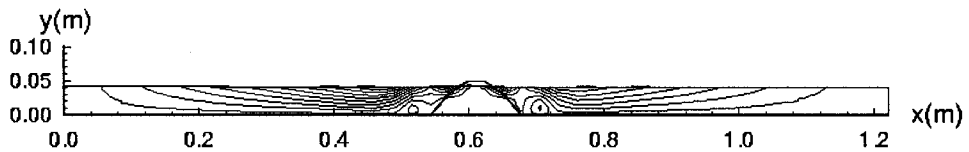

Figure 4.4.C6 v-w Streamlines in Plane x=0.541 m

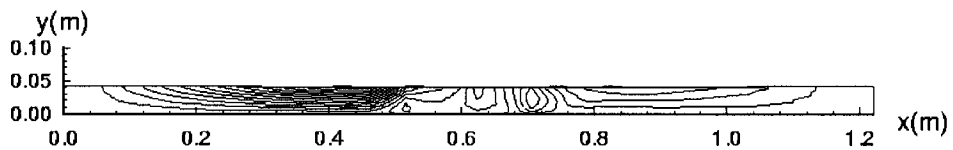

Figure 4.4.C7 v-w Streamlines in Plane x=0.649 m

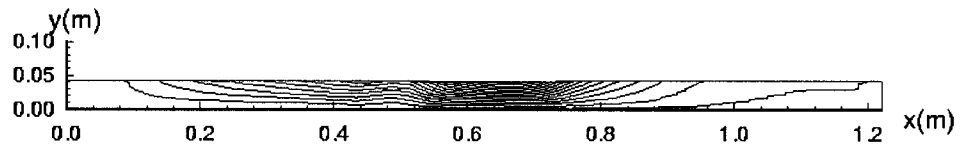

Figure 4.4.C8 v-w Streamlines in Plane x=0.757 m

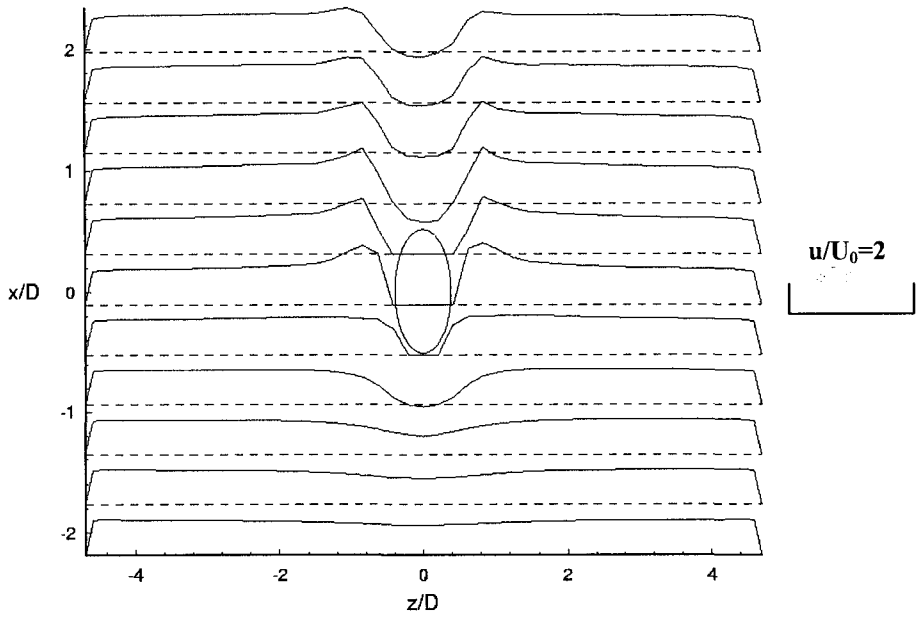

Figure 4.4.C9 Velocity Profile 0.5*u/U_0 in Plane y=0.0013 m

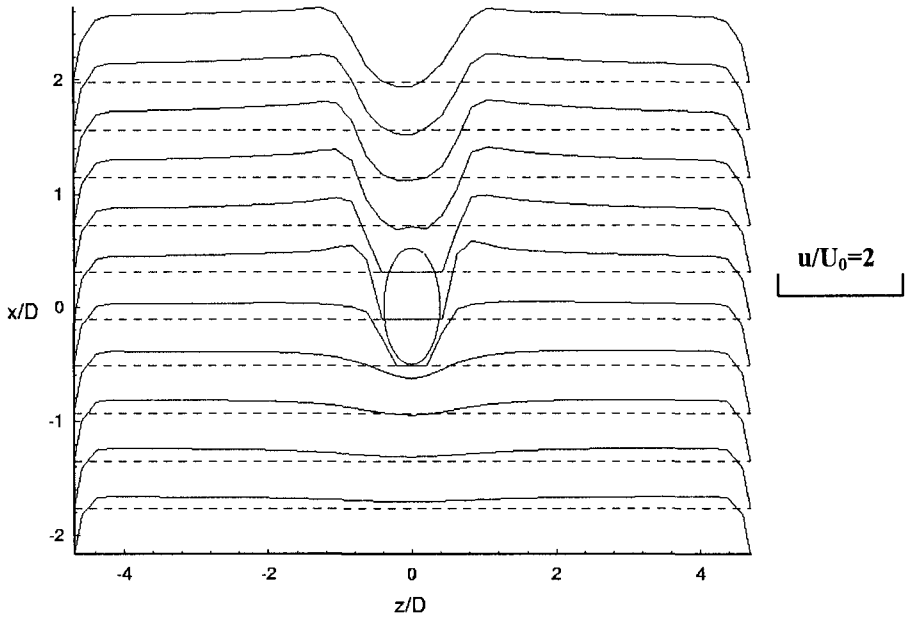

Figure 4.4.C10 Velocity Profile 0.5*u/U_0 in Plane y=0.0118 m

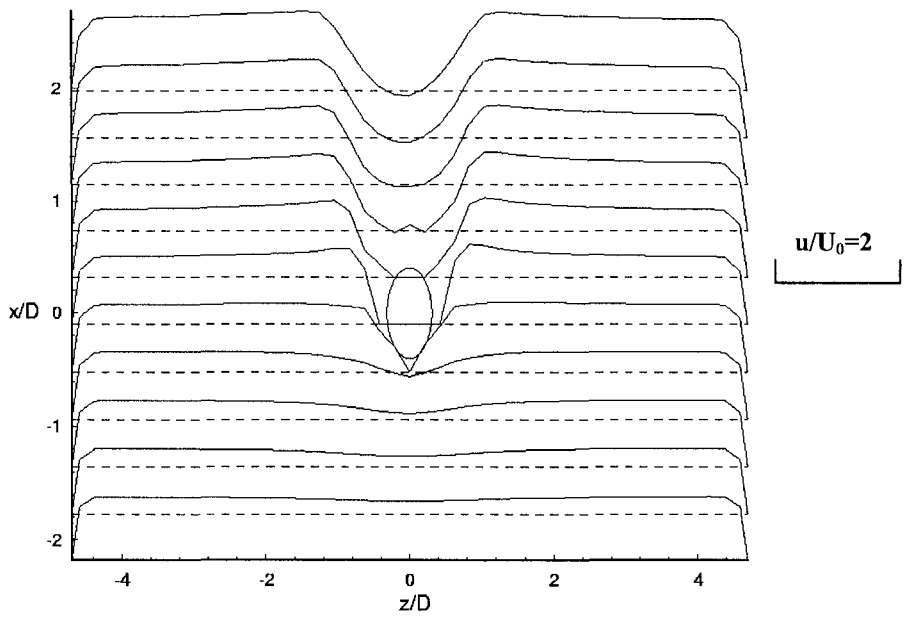

Figure 4.4.C11 Velocity Profile 0.5*u/U_0 in Plane y=0.0276 m

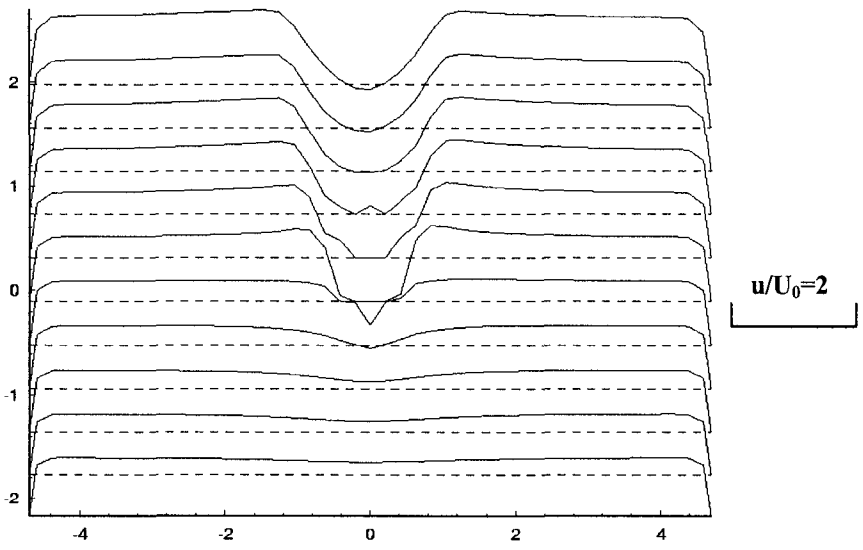

Figure 4.4.C12 Velocity Profile 0.5*u/U_0 in Plane y=0.0381 m

Calculation Case D: Water Depth=0.12 m, Three Obstacles

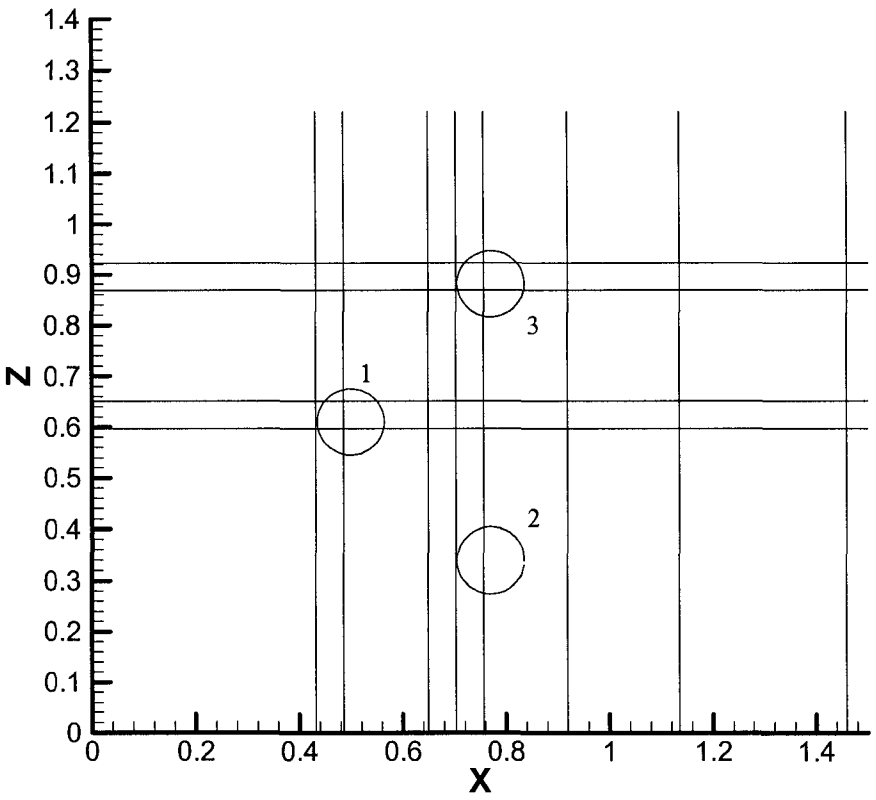

Figure 4.4.D0. Layout of Obstacles and Sections of Plotting

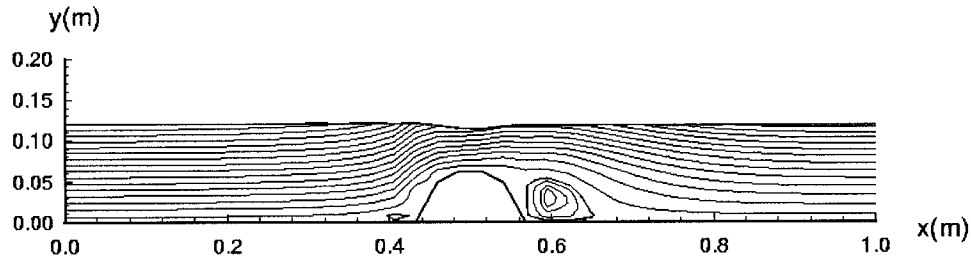

Figure 4.4.D1 u-v Streamlines in Plane z=0.596 m

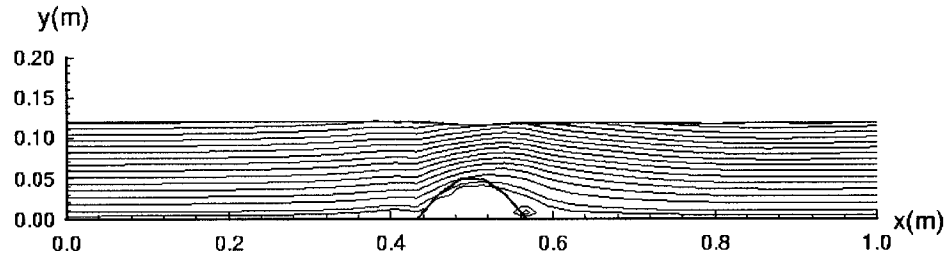

Figure 4.4.D2 u-v Streamlines in Plane z=0.651 m

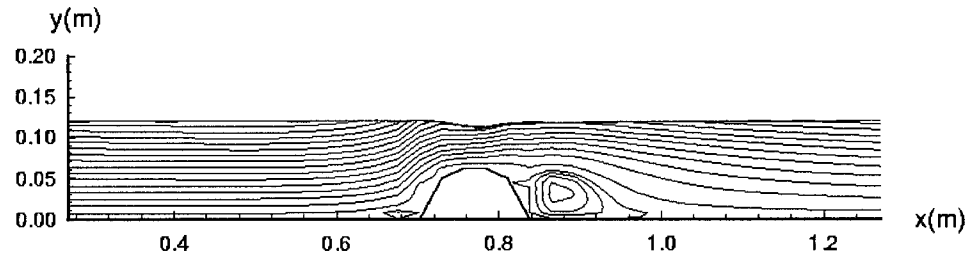

Figure 4.4.D3 u-v Streamlines in Plane z=0.868 m

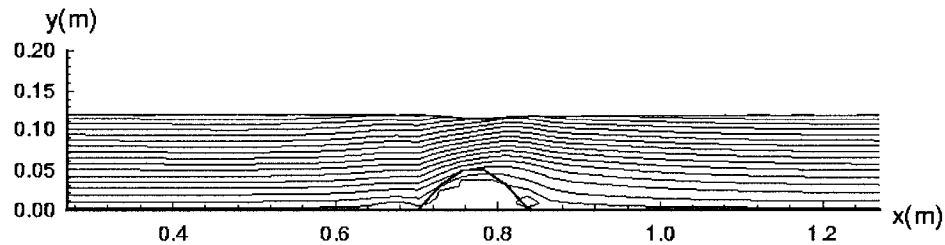

Figure 4.4.D4 u-v Streamlines in Plane z=0.922 m

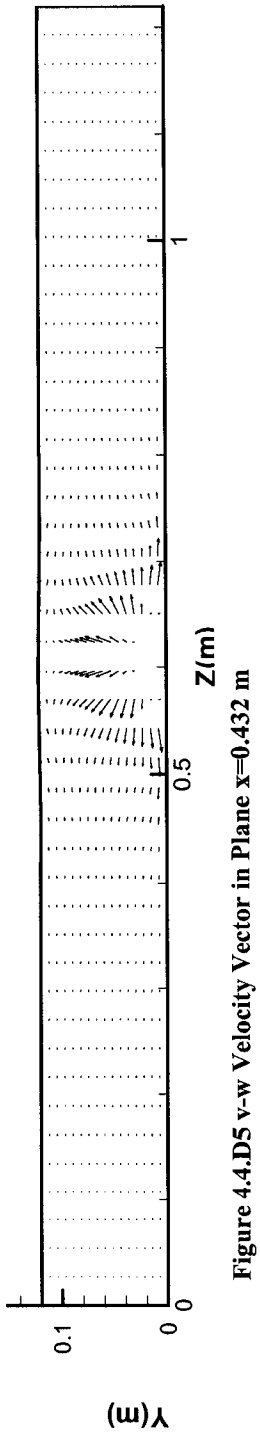

Figure 4.4.D5 v-w Velocity Vector in Plane x=0.432 m

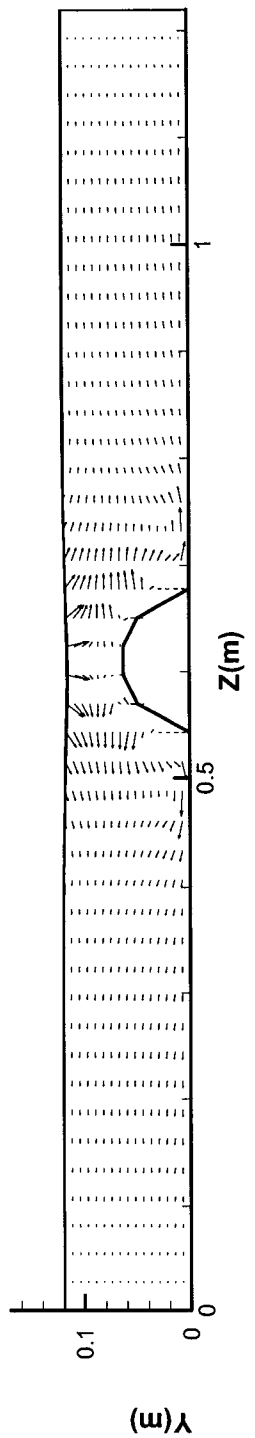

Figure 4.4.D6 v-w Velocity Vector in Plane x=0.486 m

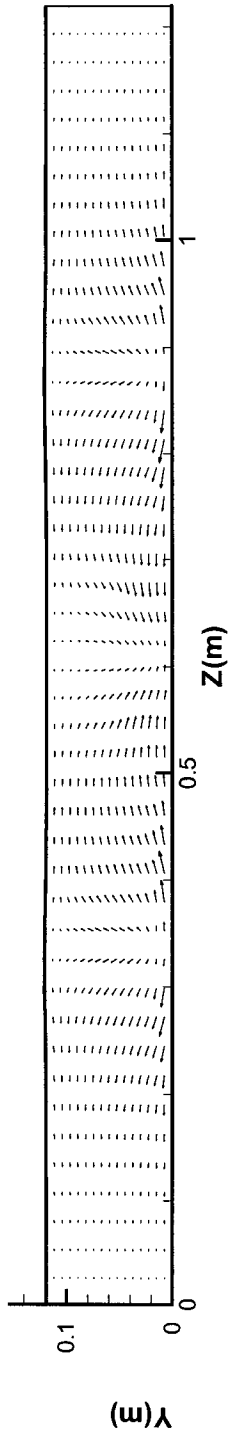

Figure 4.4.D7 v-w Velocity Vector in Plane x=0.649 m

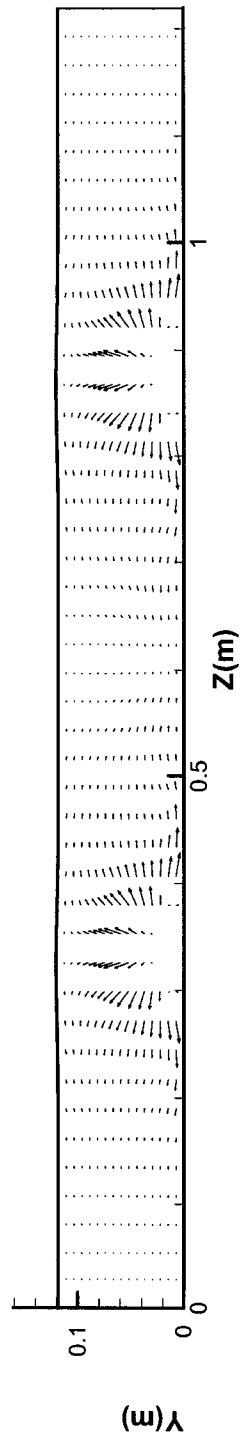

Figure 4.4.D8 v-w Velocity Vector in Plane x=0.703 m

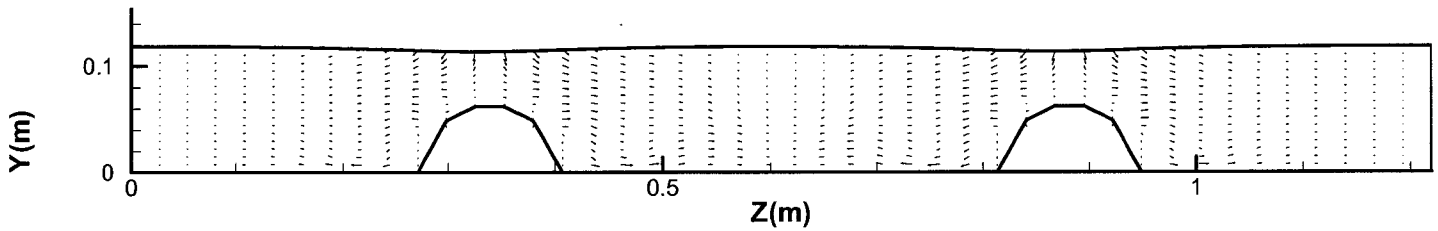

Figure 4.4.D9 v-w Velocity Vector in Plane x=0.757 m

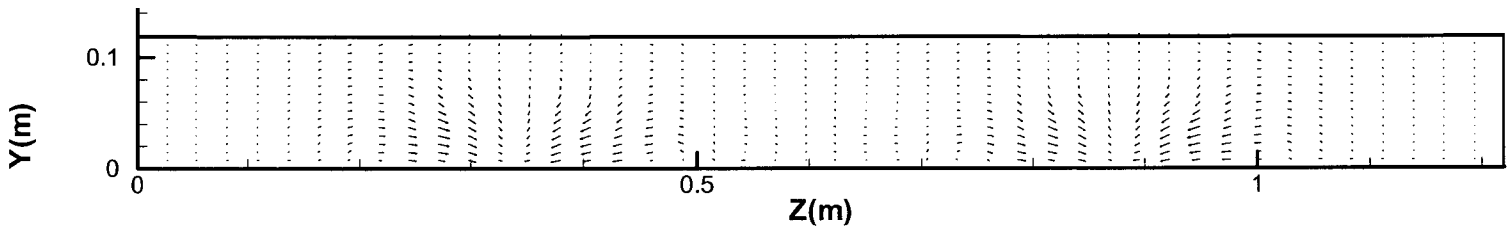

Figure 4.4.D10 v-w Velocity Vector in Plane x=0.919 m

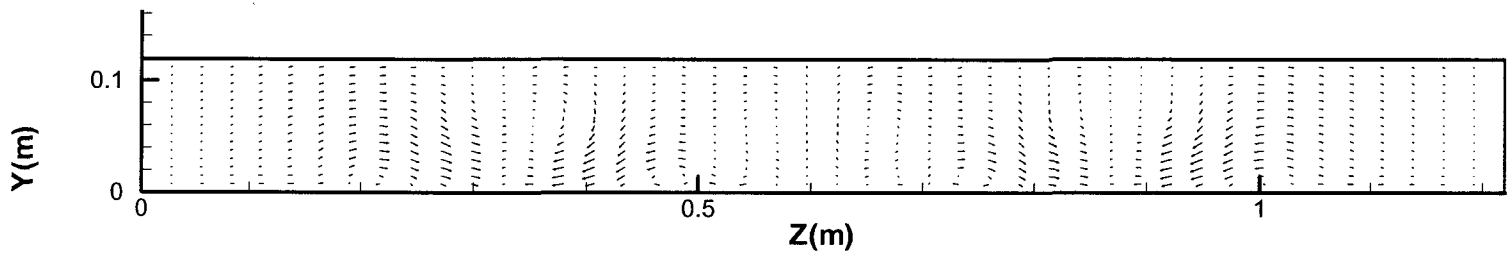

Figure 4.4.D11 v-w Velocity Vector in Plane x=1.135 m

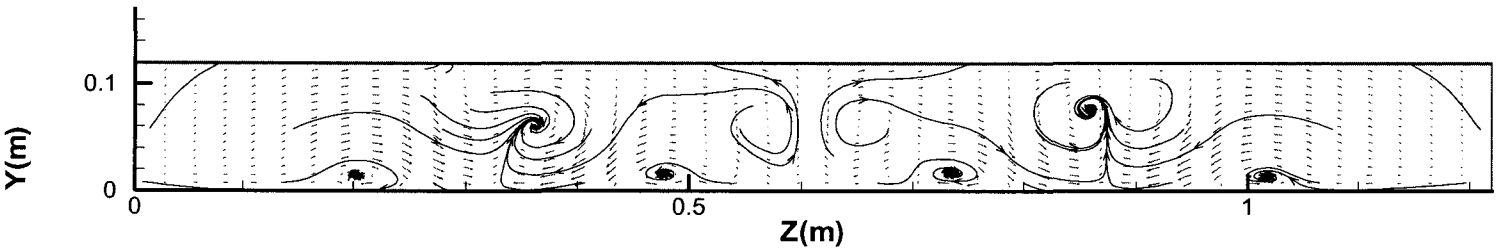

Figure 4.4.D12 v-w Velocity Vector and traced streamlines in Plane x=1.26 m

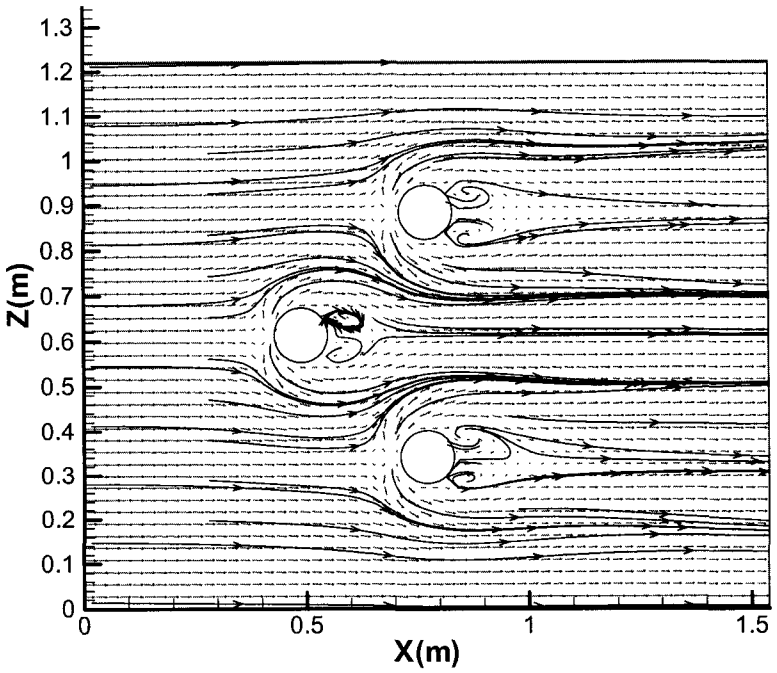

Figure 4.4.D13 u-w Streamlines and Velocity Vector in Plane y=0.0038 m

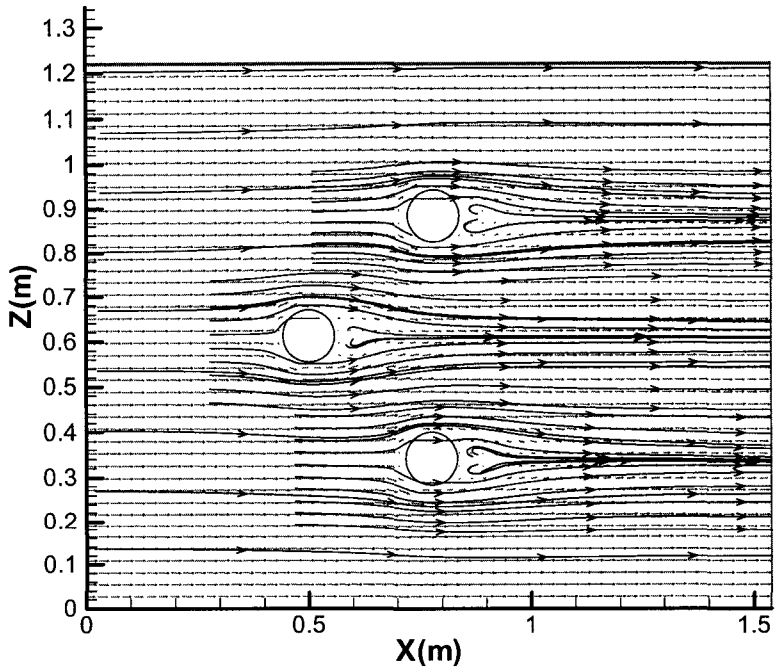

Figure 4.4.D14 u-w Streamlines and Velocity Vector in Plane y=0.0187 m

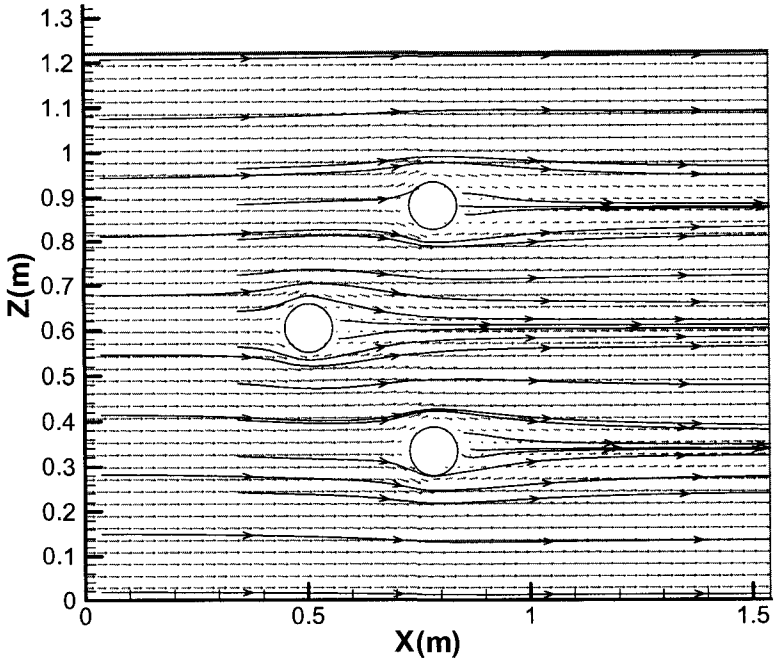

Figure 4.4.D15 u-w Streamlines and Velocity Vector in Plane y=0.0337 m

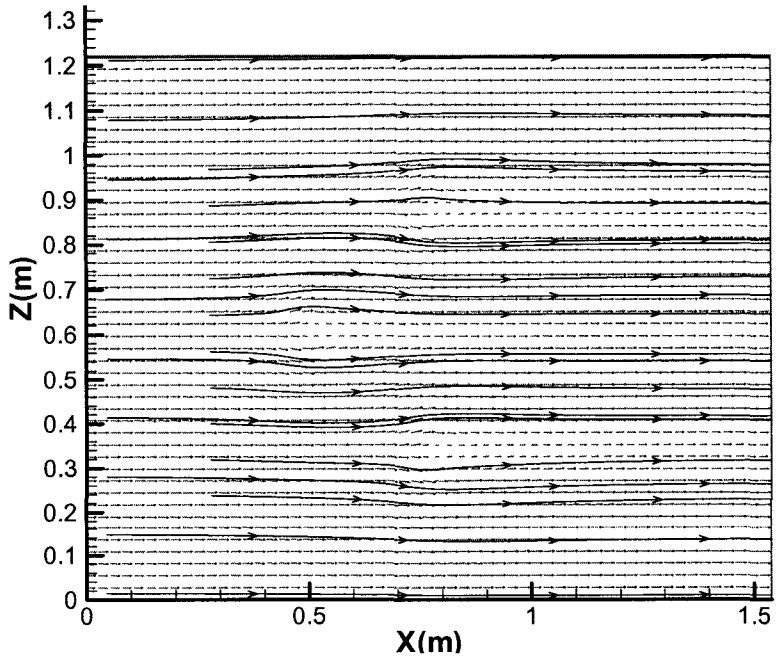

Figure 4.4.D16 u-w Streamlines and Velocity Vector in Plane y=0.0637 m

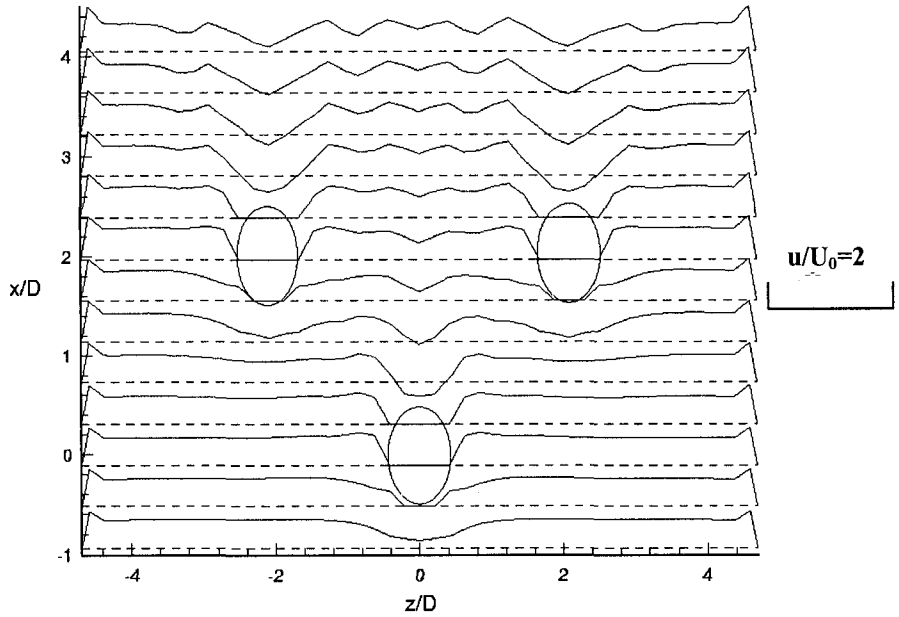

Figure 4.4.D17 Velocity Profile 0.5*u/U_0 in Plane y=0.0038 m

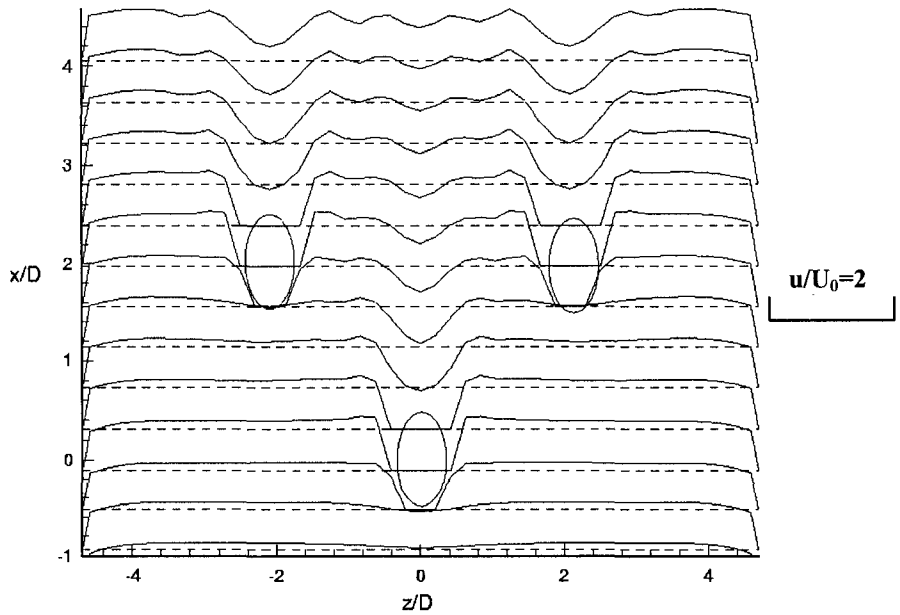

Figure 4.4.D18 Velocity Profile 0.5*u/U_0 in Plane y=0.0187 m

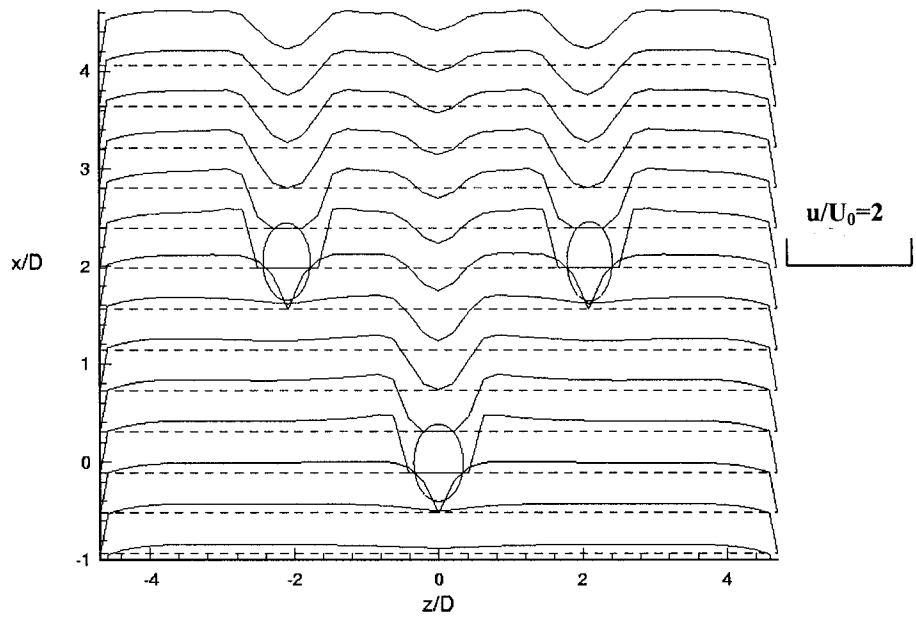

Figure 4.4.D19 Velocity Profile $0.5*u/U_0$ in Plane y=0.0337 m

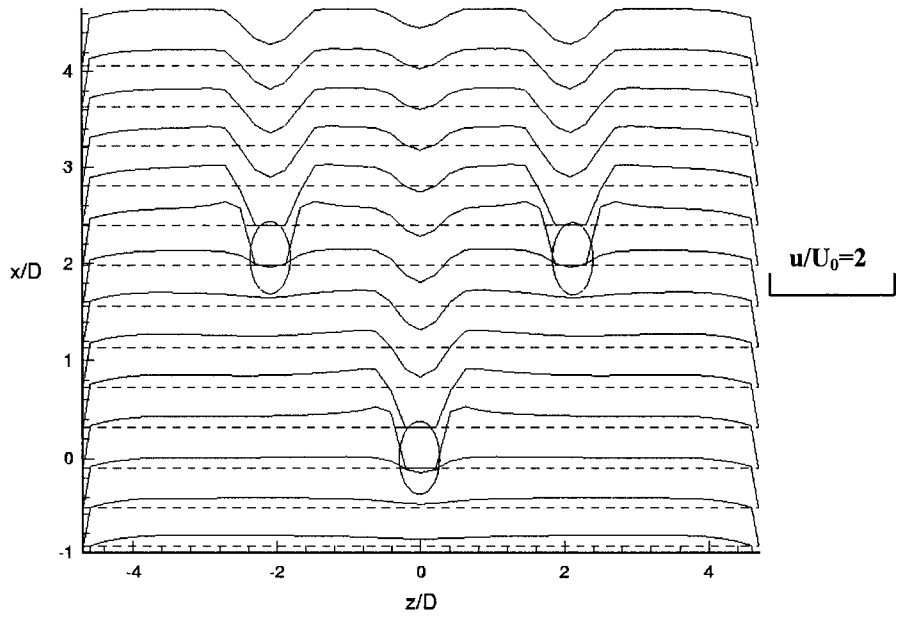

Figure 4.4.D20 Velocity Profile $0.5*u/U_0$ in Plane y=0.0487 m

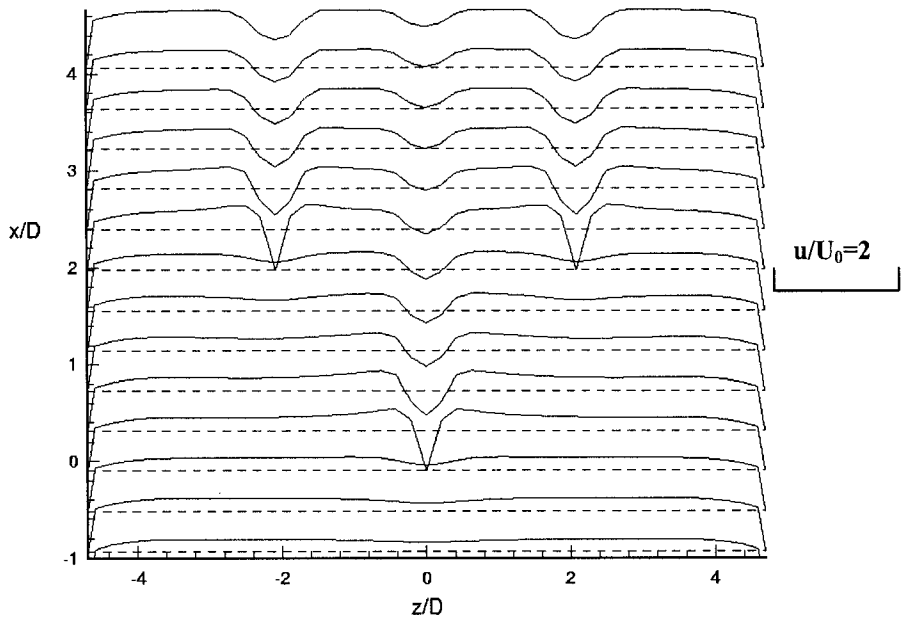

Figure 4.4.D21 Velocity Profile 0.5*u/U_0 in Plane y=0.0637 m

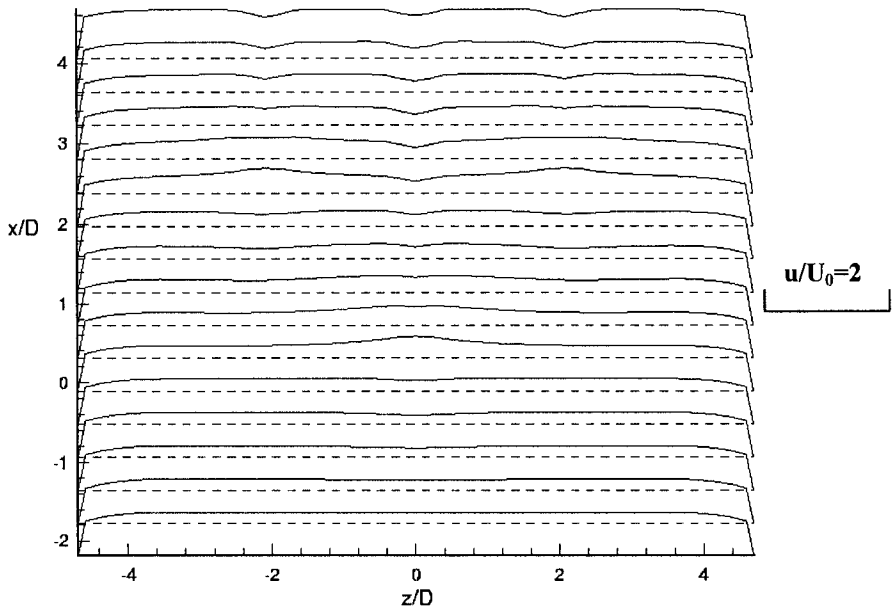

Figure 4.4.D22 Velocity Profile 0.5*u/U_0 in Plane y=0.0938m

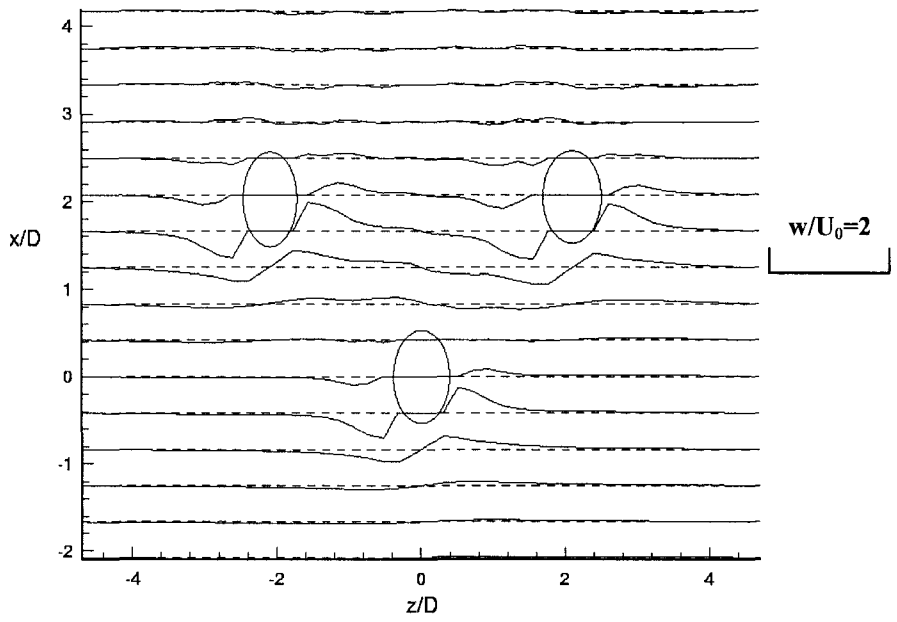

Figure 4.4.D23 Velocity Profile 0.5*w/U_0 in Plane y=0.0038 m

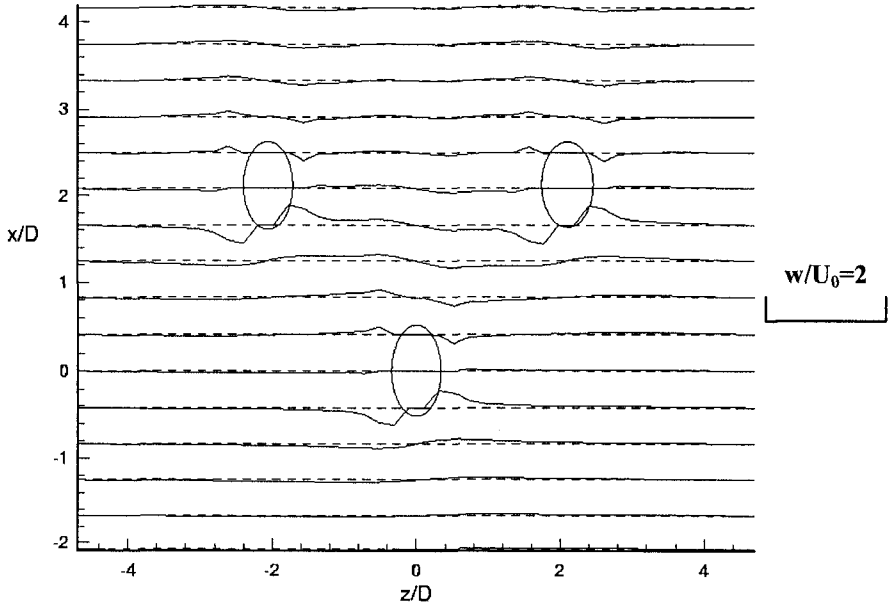

Figure 4.4.D24 Velocity Profile 0.5*w/U_0 in Plane y=0.0337 m

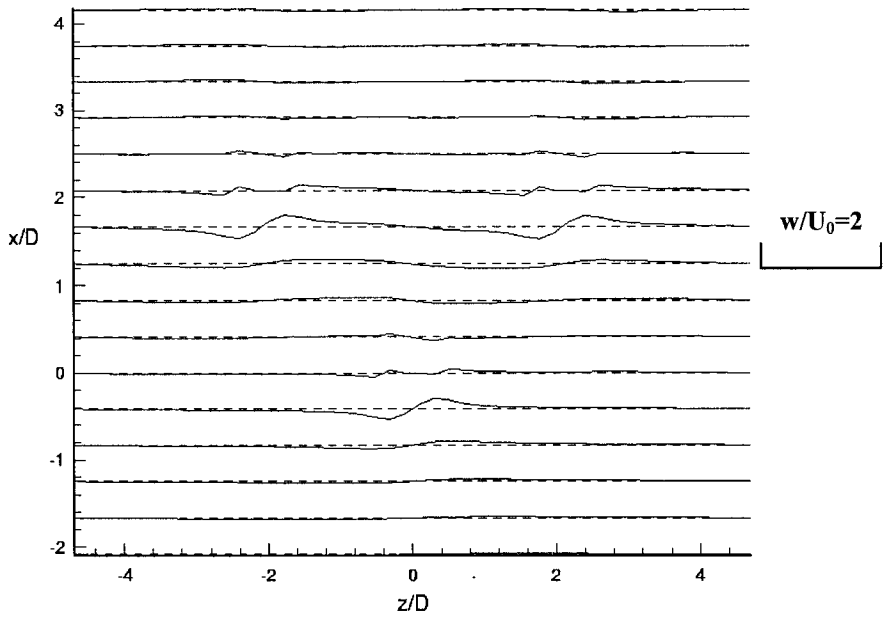

Figure 4.4.D25 Velocity Profile 0.5*w/U_0 in Plane y=0.0637 m

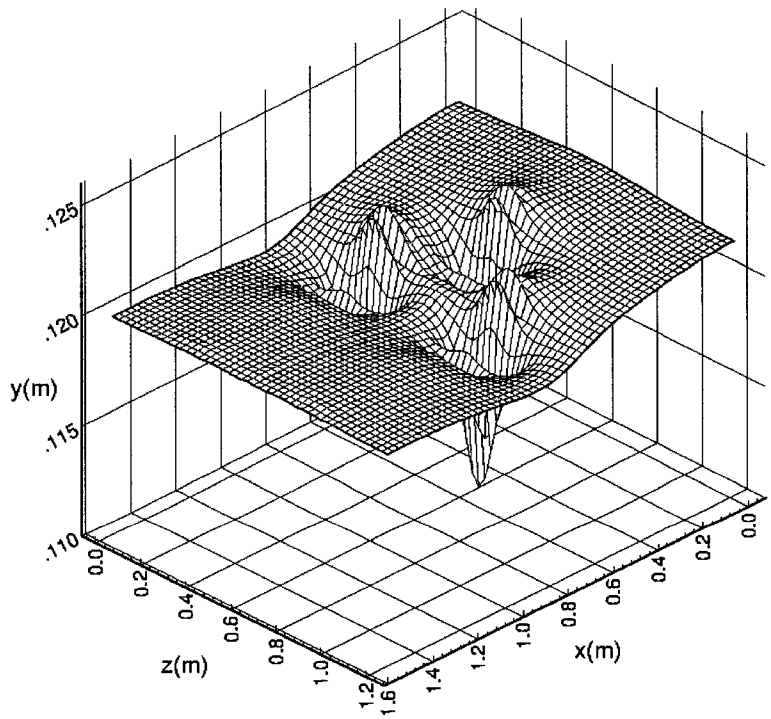

Figure 4.4.D26 Calculated Free Surface

Calculation Case E: Water Depth=0.12 m, Two Obstacles

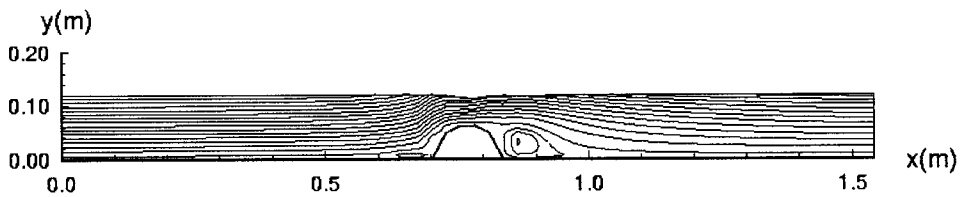

Figure 4.4.E1 u-v Streamlines in Plane z=0.868 m

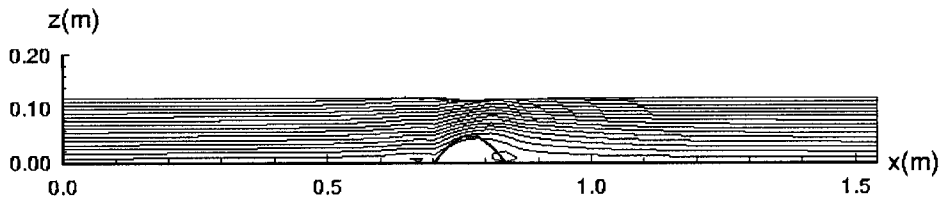

Figure 4.4.E2 u-v Streamlines in Plane z=0.922 m

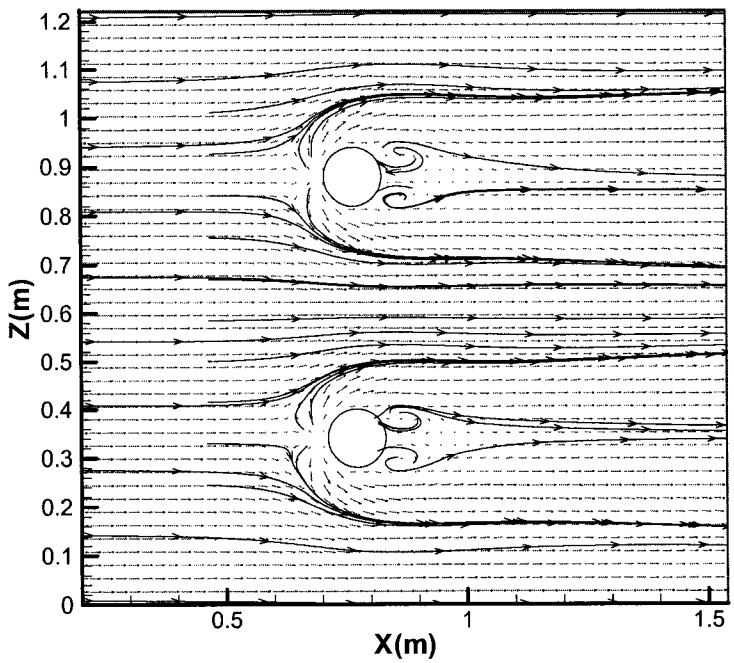

Figure 4.4.E3 u-w Streamlines and Velocity Vector in Plane y=0.0038m

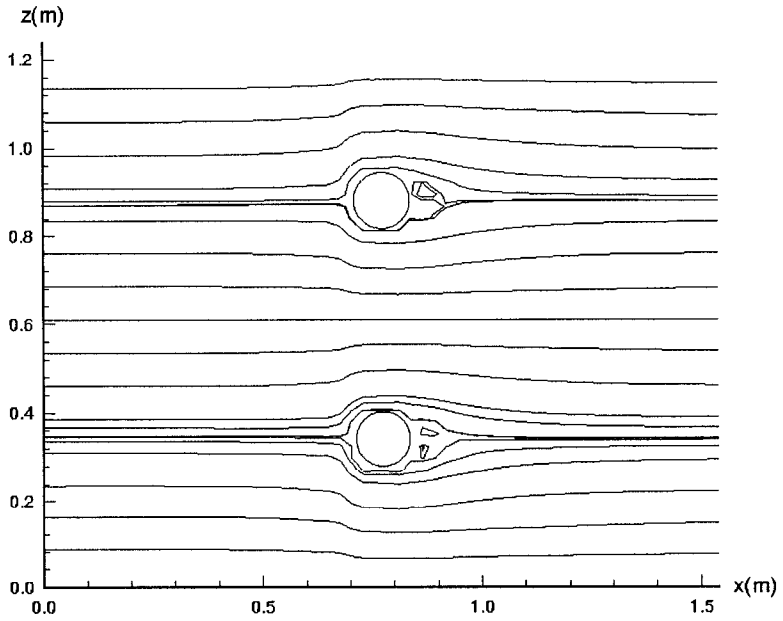

Figure 4.4.E4 u-w Streamlines in Plane y=0.0187 m

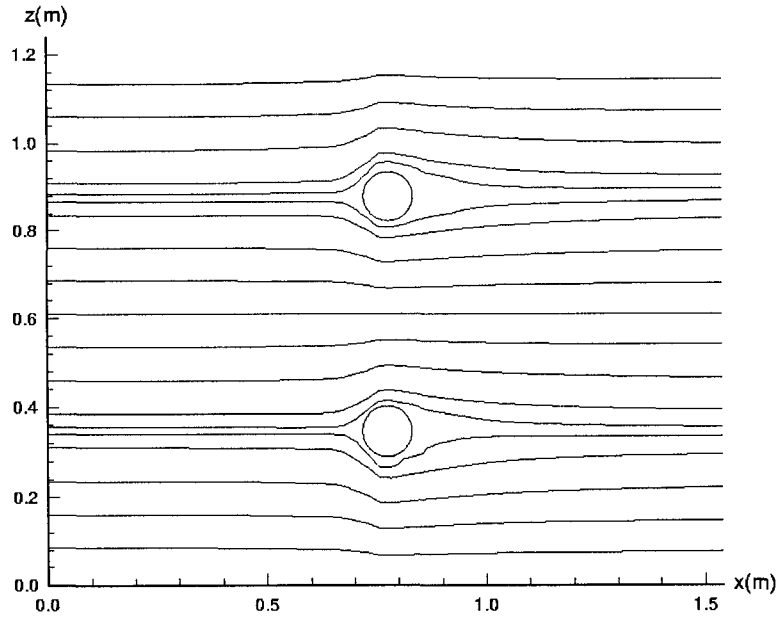

Figure 4.4.E5 u-w Streamlines in Plane y=0.0337m

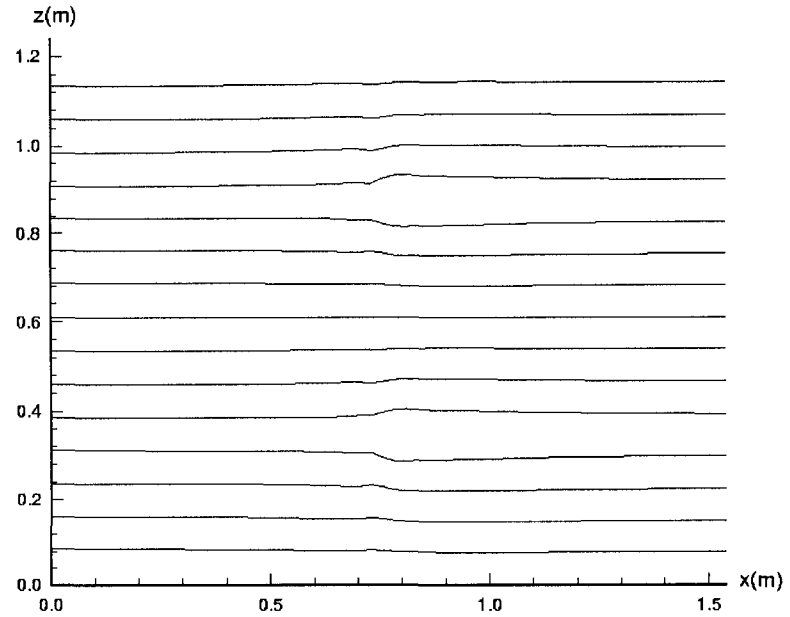

Figure 4.4.E6 u-w Streamlines in Plane y=0.0637m

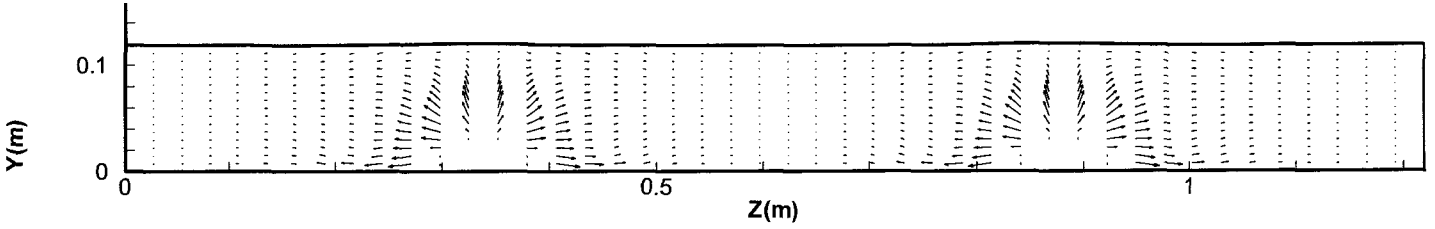

Figure 4.4.E7 v-w Streamlines and Velocity Vector in Plane x=0.703m

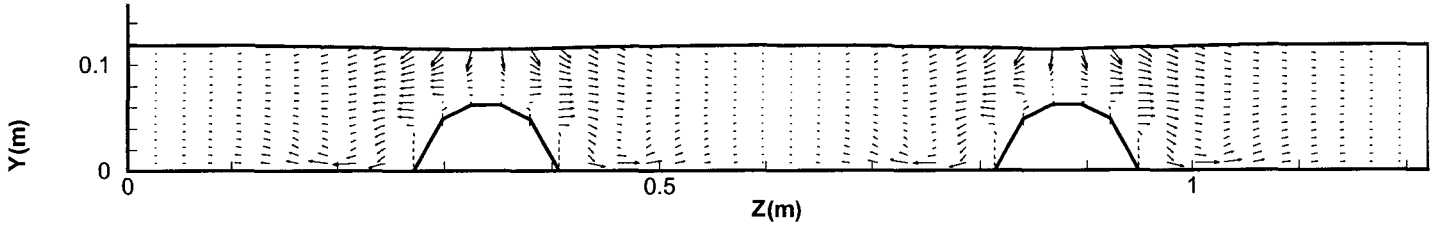

Figure 4.4.E8 v-w Streamlines and Velocity Vector in Plane x=0.757m

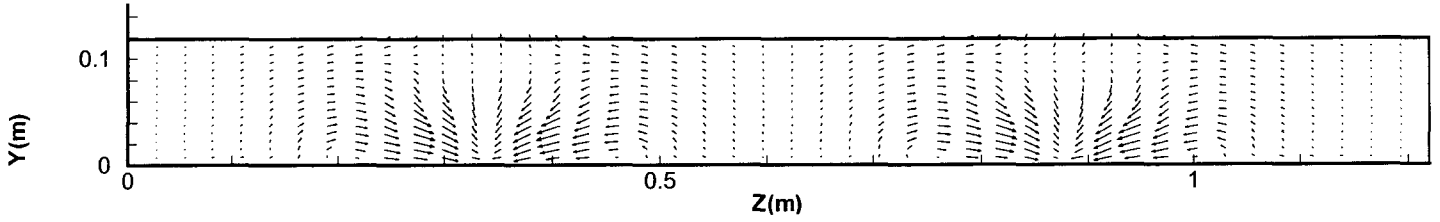

Figure 4.4.E9 v-w Streamlines and Velocity Vector in Plane x=0.919m

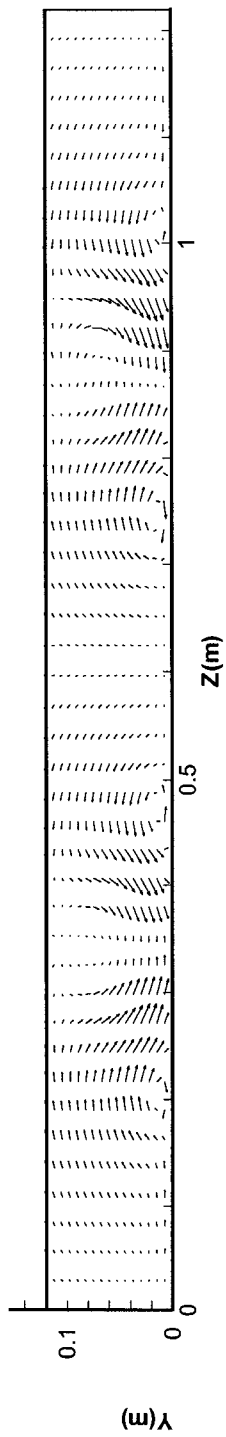

Figure 4.4.E10 v-w Streamlines and Velocity Vector in Plane x=1.135 m

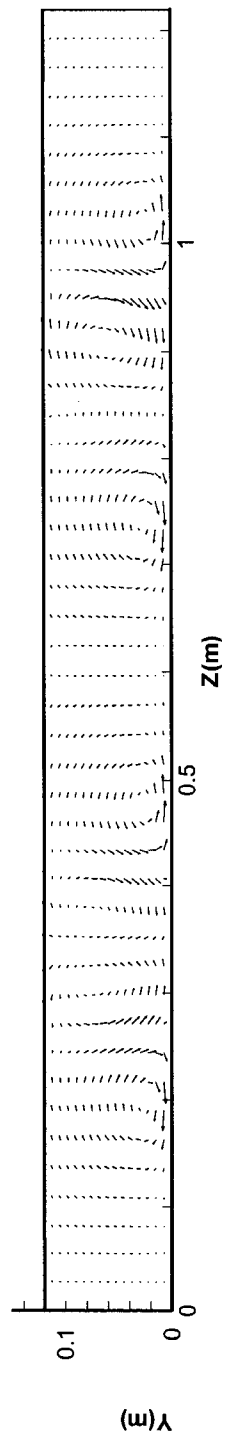

Figure 4.4.E11 v-w Streamlines and Velocity Vector in Plane x=1.459 m

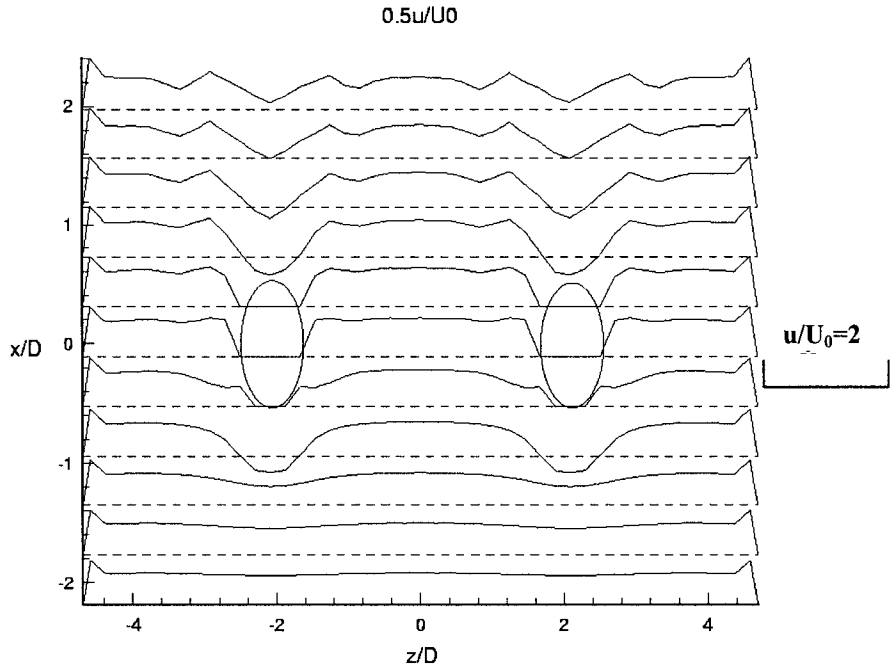

Figure 4.4.E12 Velocity Profile $0.5*u/U_0$ in y=0.0038 m

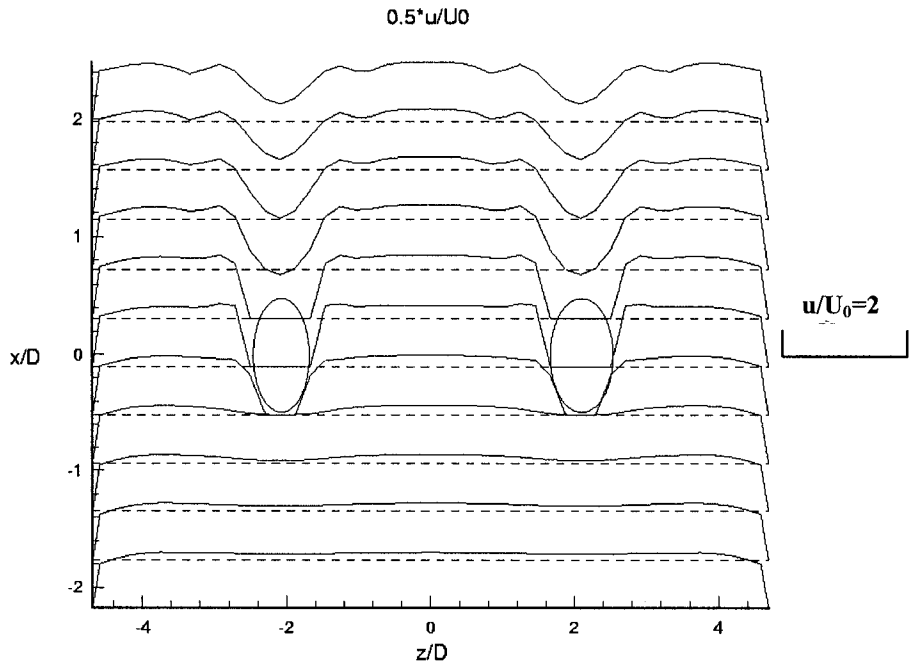

Figure 4.4.E13 Velocity Profile $0.5*u/U_0$ in y=0.0187 m

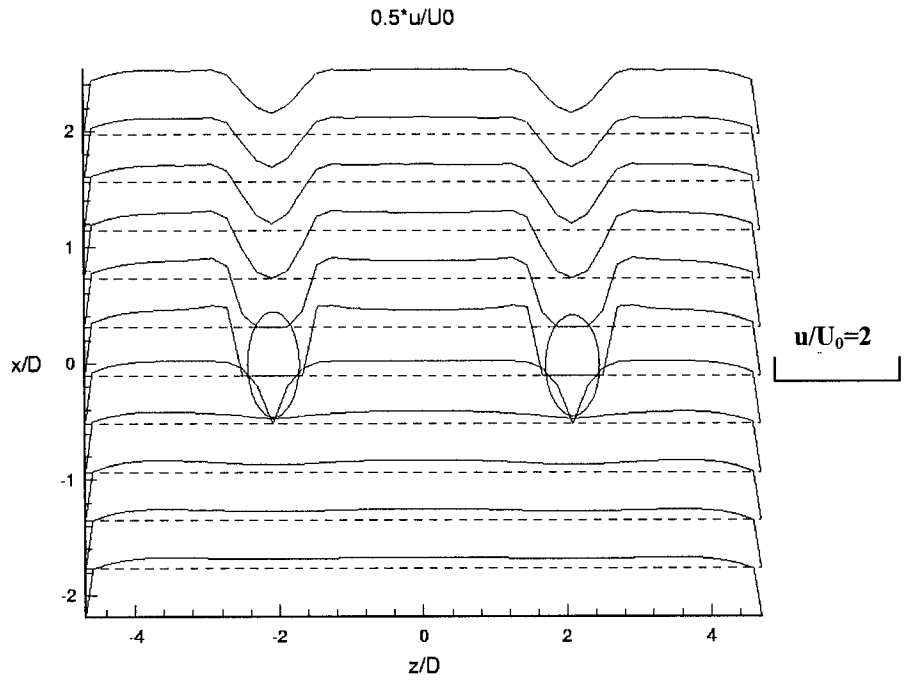

Figure 4.4.E14 Velocity Profile $0.5*u/U_0$ in y=0.0337 m

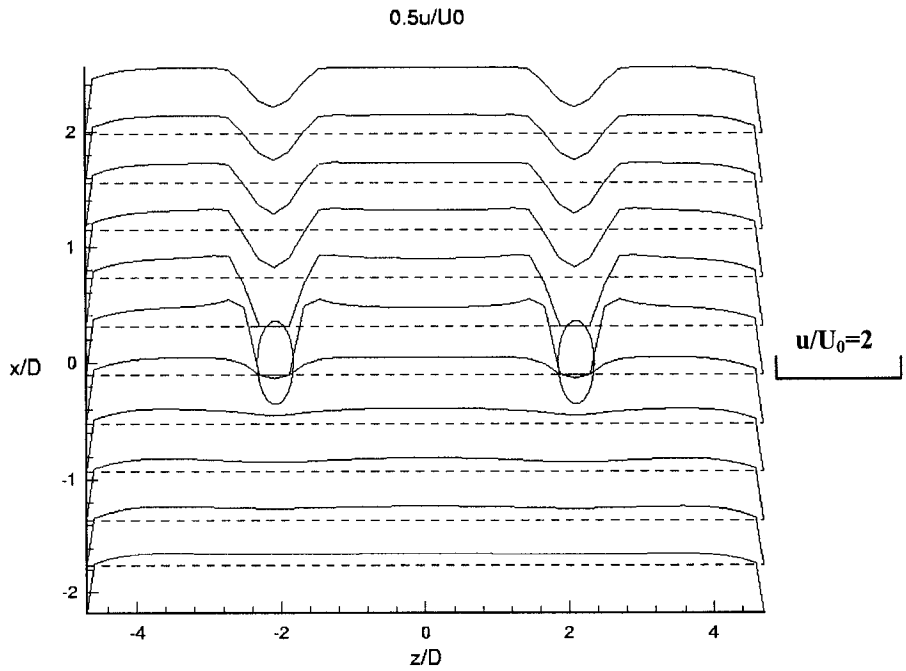

Figure 4.4.E15 Velocity Profile $0.5*u/U_0$ in y=0.0487 m

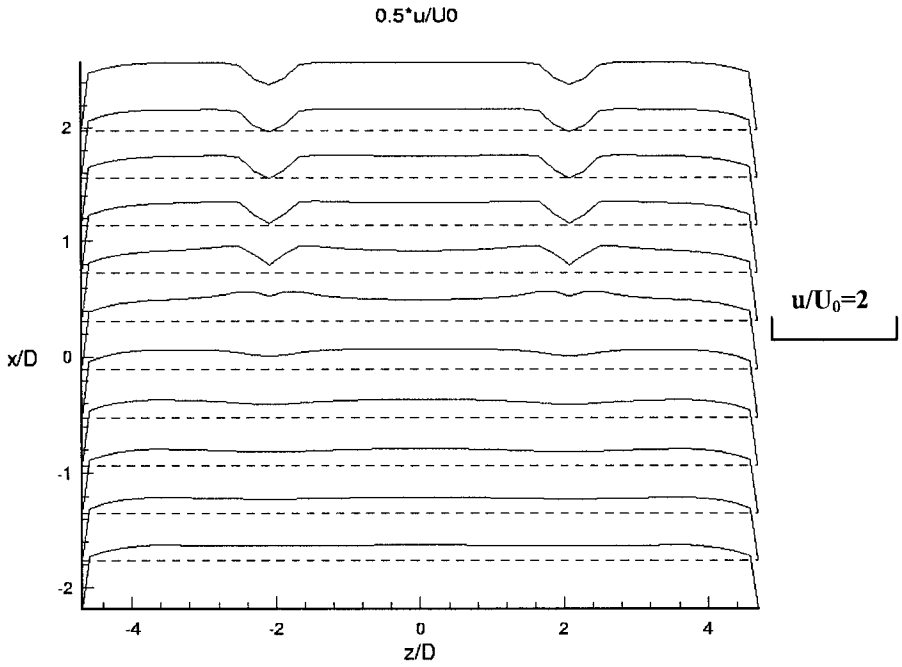

Figure 4.4.E16 Velocity Profile $0.5*u/U_0$ in y=0.0637 m

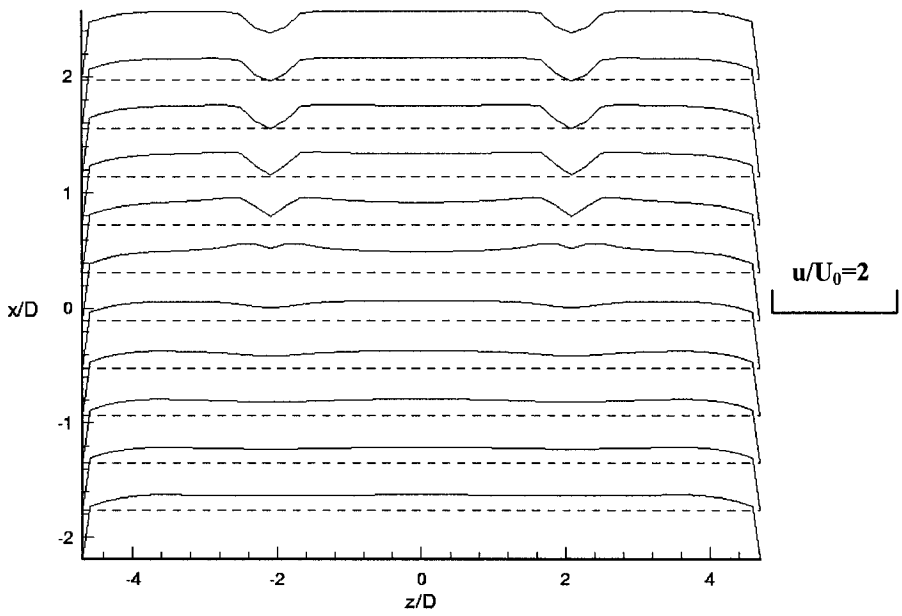

Figure 4.4.E17 Velocity Profile $0.5*u/U_0$ in y=0.0787 m

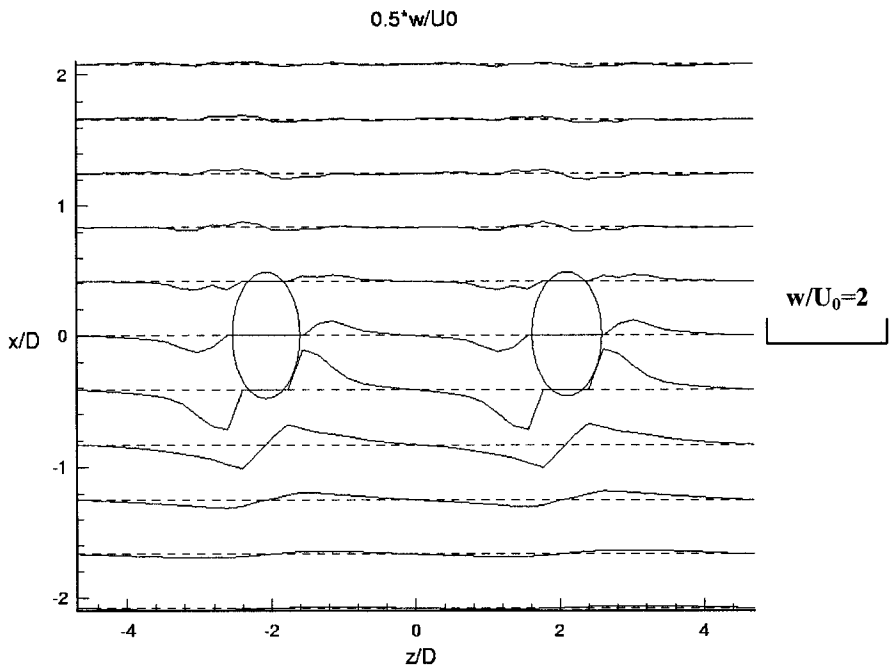

Figure 4.4.E18 Velocity Profile $0.5*w/U_0$ in y=0.0038 m

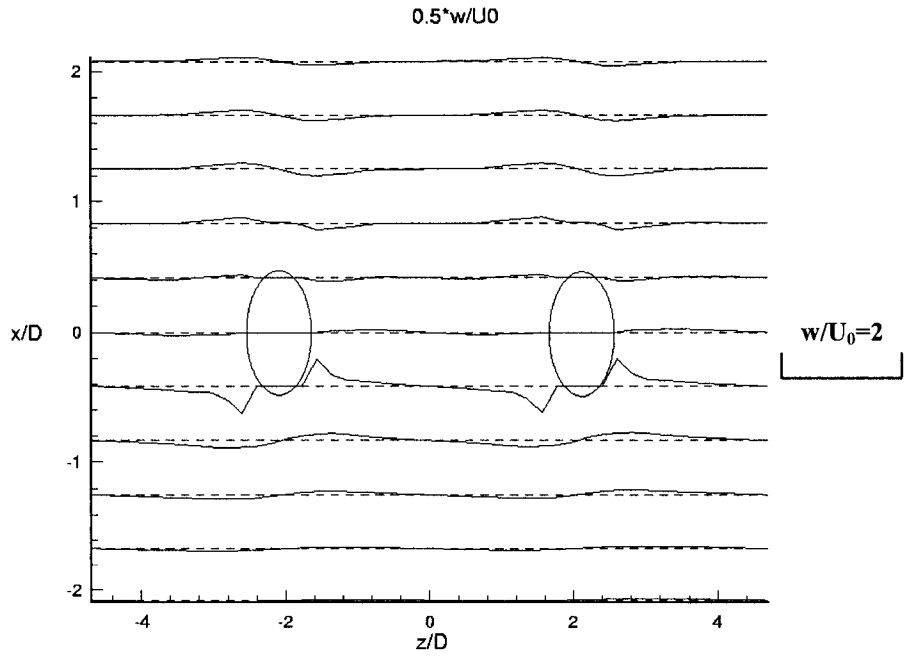

Figure 4.4.E19 Velocity Profile $0.5*w/U_0$ in y=0.0187 m

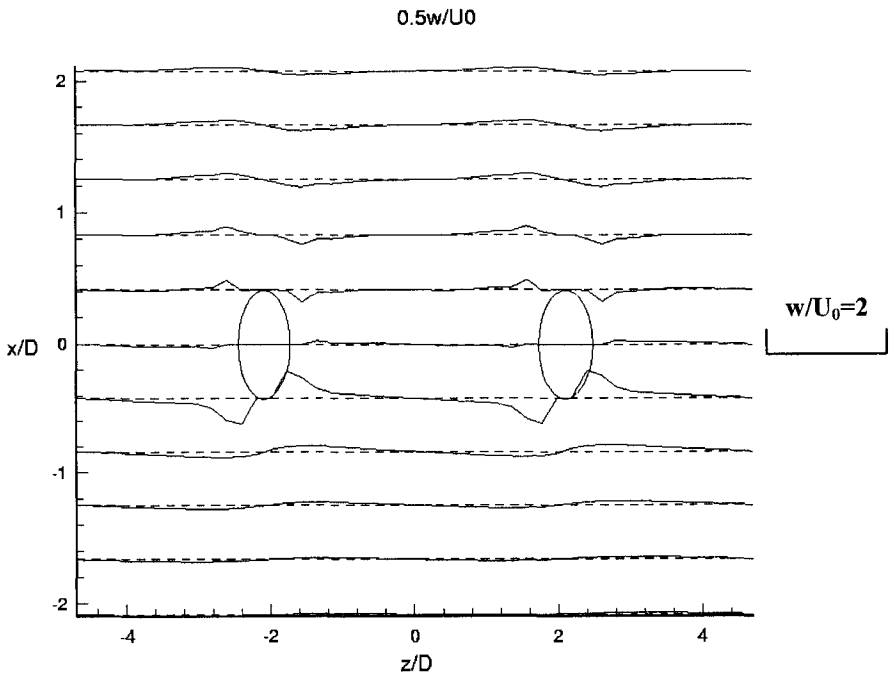

Figure 4.4.E20 Velocity Profile 0.5*w/U_0 in y=0.0337 m

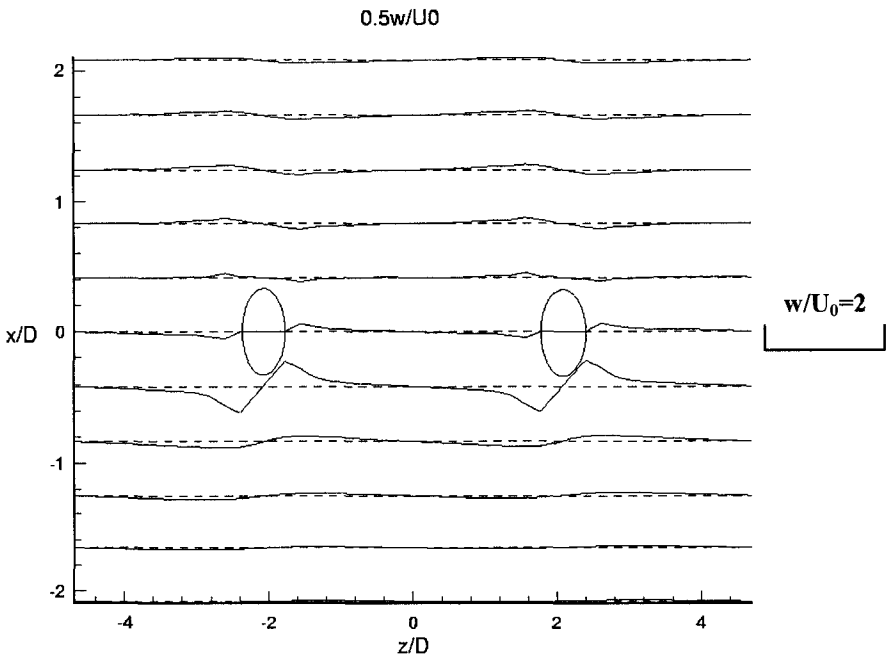

Figure 4.4.E21 Velocity Profile 0.5*w/U_0 in y=0.0487 m

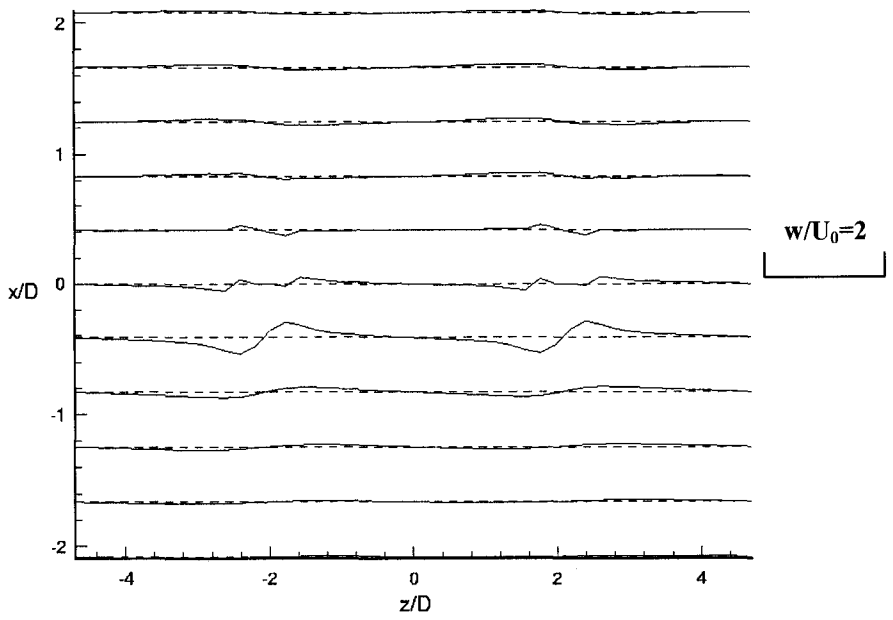

Figure 4.4.E22 Velocity w/U0 profile in y=0.0637 m

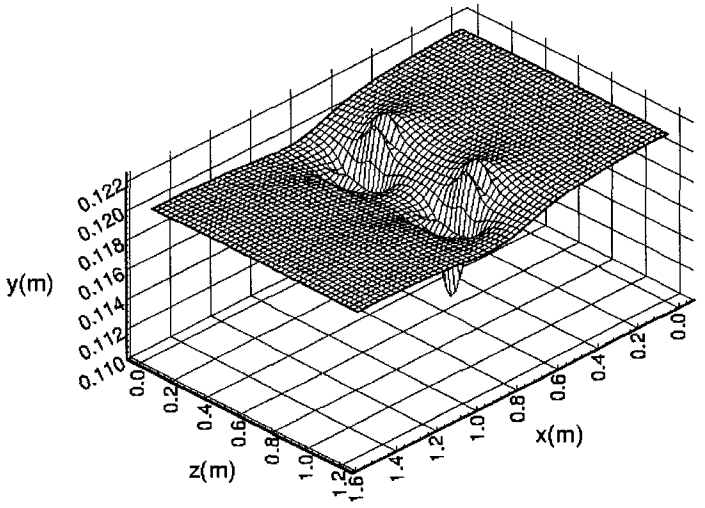

Figure 4.4.E23 Calculated Free Surface

Calculation Case F: Water Depth=0.12 m, Three Obstacles

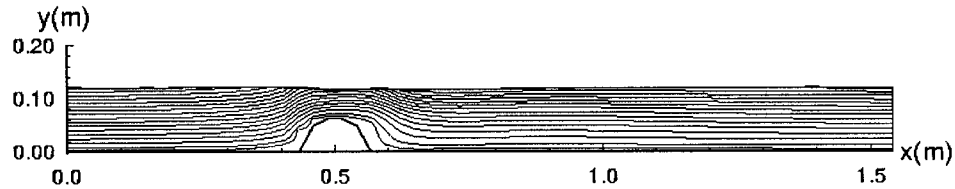

Figure 4.4.F1 u-v Streamlines in Plane z=0.596 m

Figure 4.4.F2 u-v Streamlines in Plane z=0.651 m

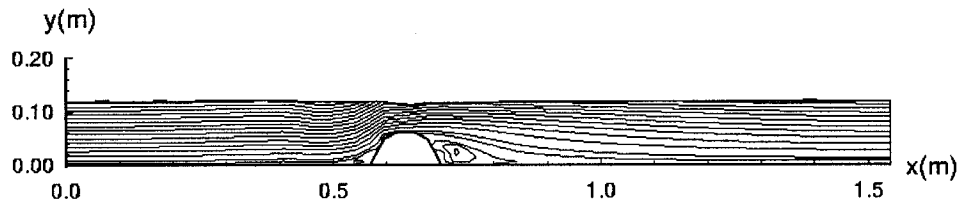

Figure 4.4.F3 u-v Streamlines in Plane z=0.705m

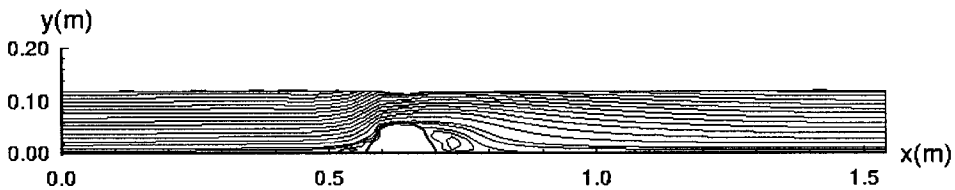

Figure 4.4.F4 u-v Streamlines in Plane z=0.759 m

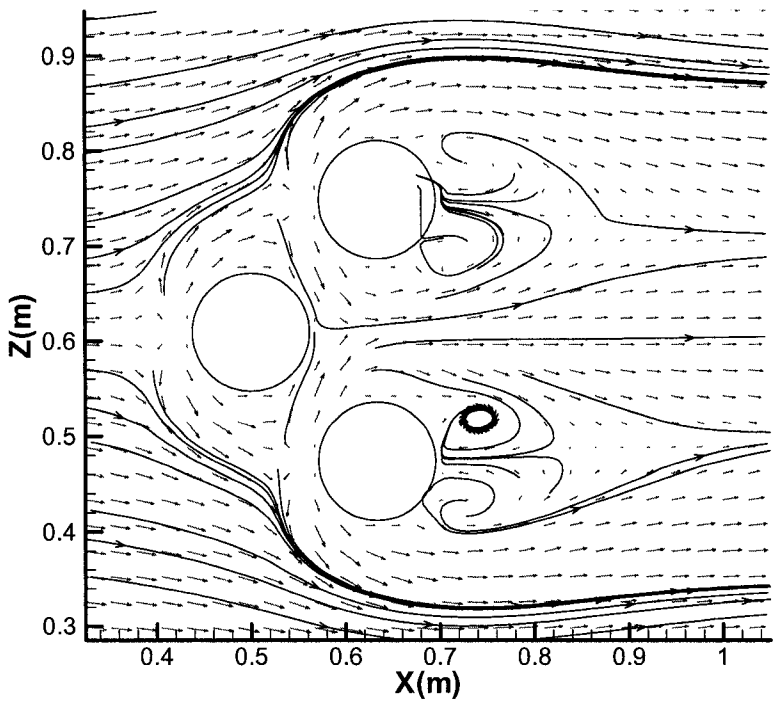

Figure 4.4.F5 u-w Streamlines and Velocity Vector in Plane y=0.004 m

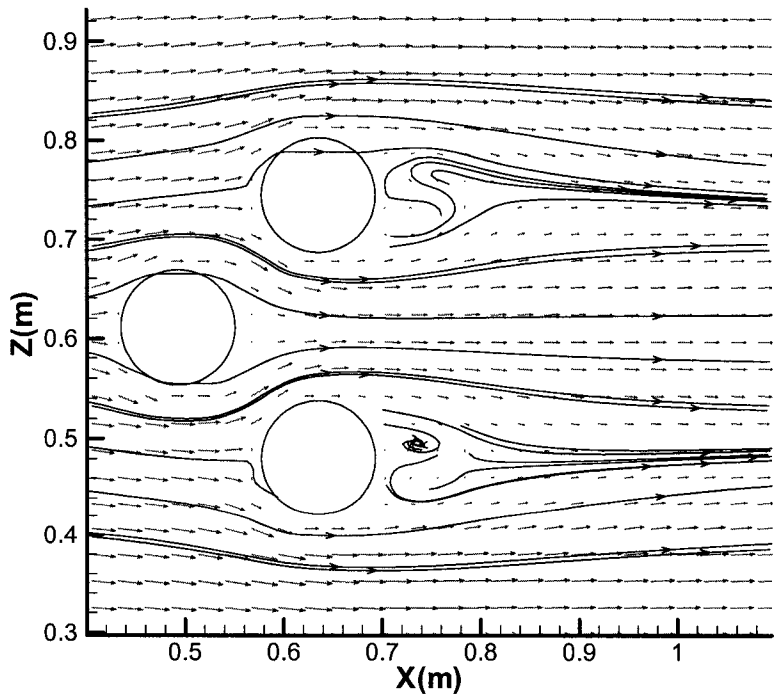

Figure 4.4.F6 u-w Streamlines and Velocity Vector in Plane y=0.019 m

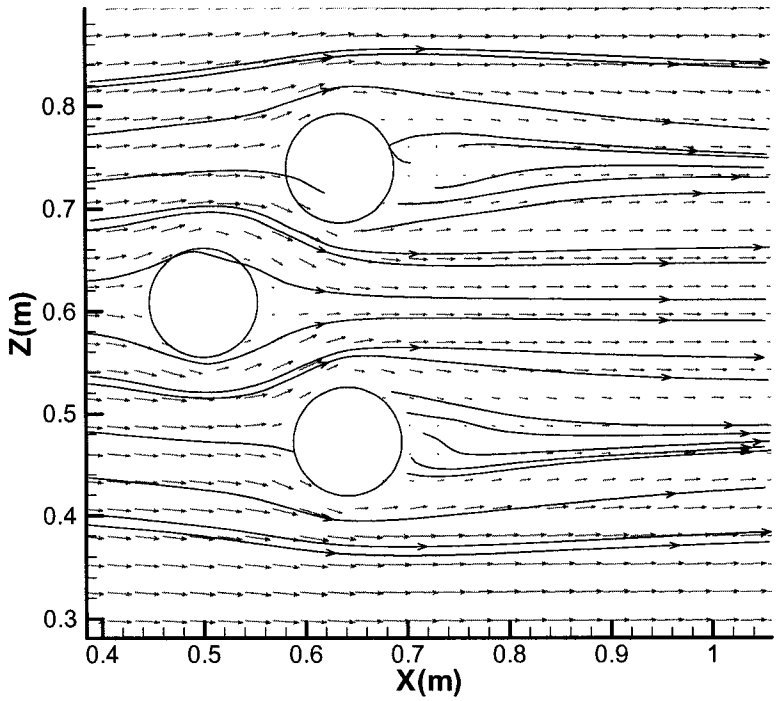

Figure 4.4.F7 u-w Streamlines and Velocity Vector in Plane y=0.034 m

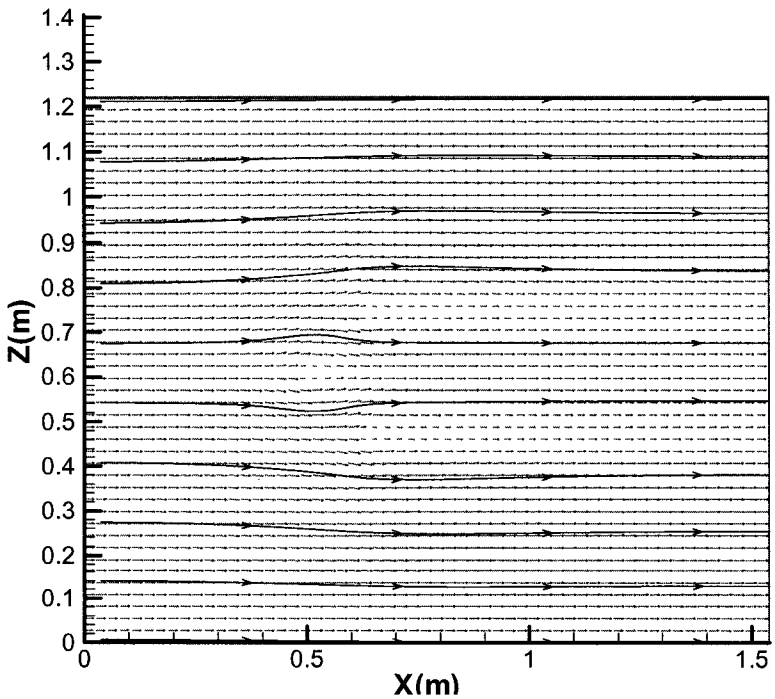

Figure 4.4.F8 u-w Streamlines and Velocity Vector in Plane y=0.064 m

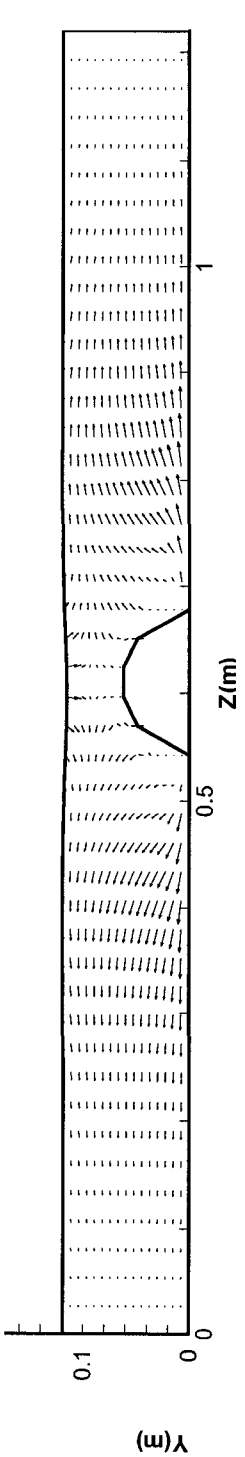

Figure 4.4.F9 v-w Velocity Vector in Plane x=0.486 m

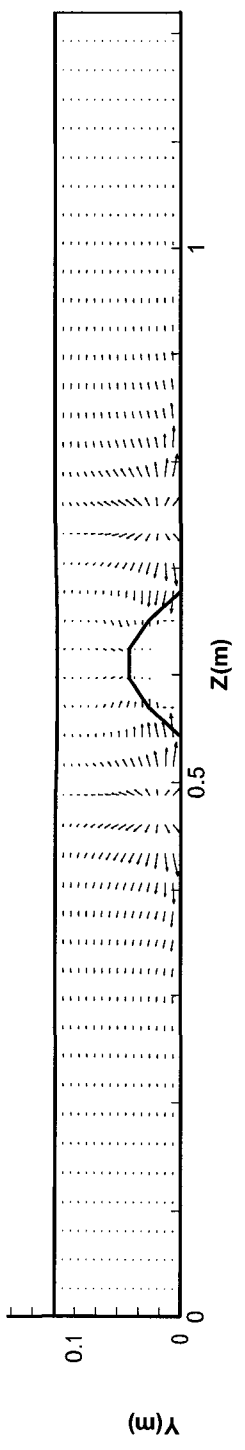

Figure 4.4.F10 v-w Velocity Vector in Plane x=0.541 m

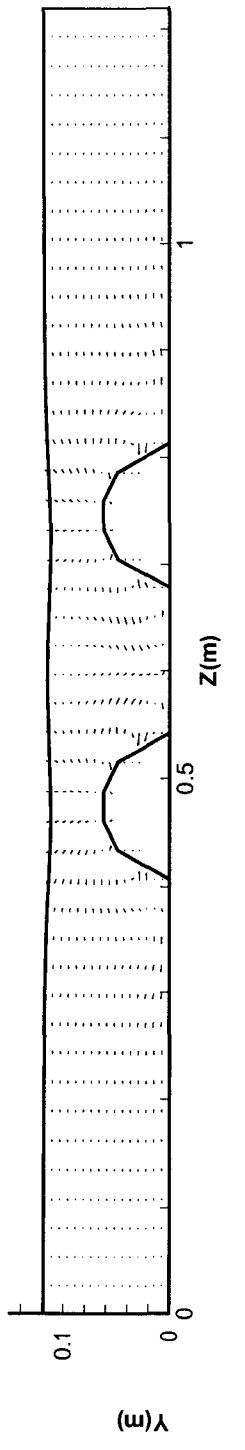

Figure 4.4.F11 v-w Velocity Vector in Plane x=0.649 m

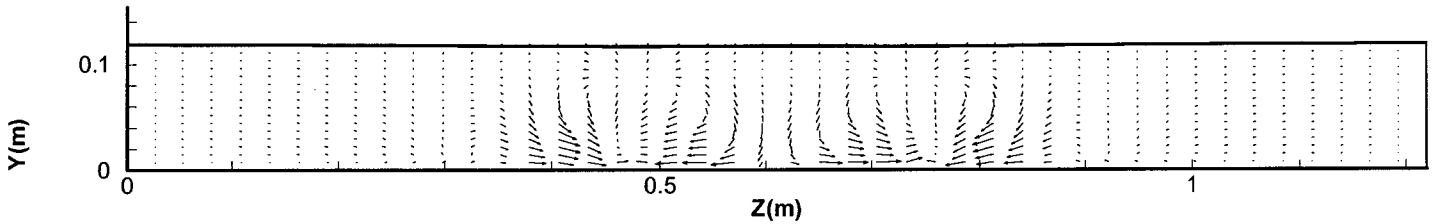

Figure 4.4.F12 v-w Velocity Vector in Plane x=0.757 m

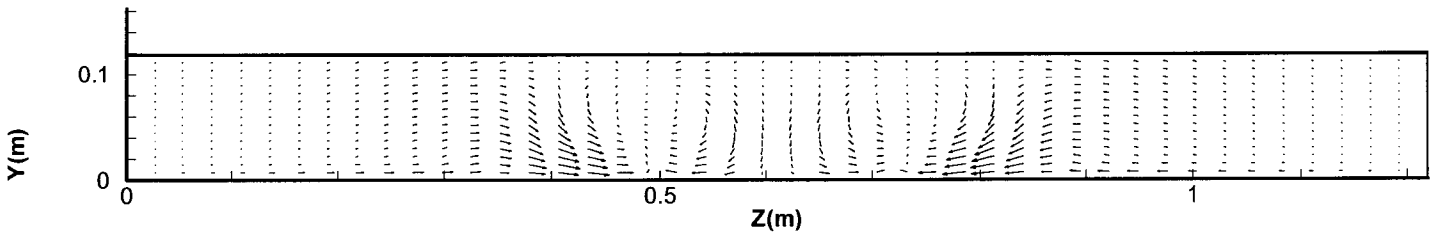

Figure 4.4.F13 v-w Velocity Vector in Plane x=1.243 m

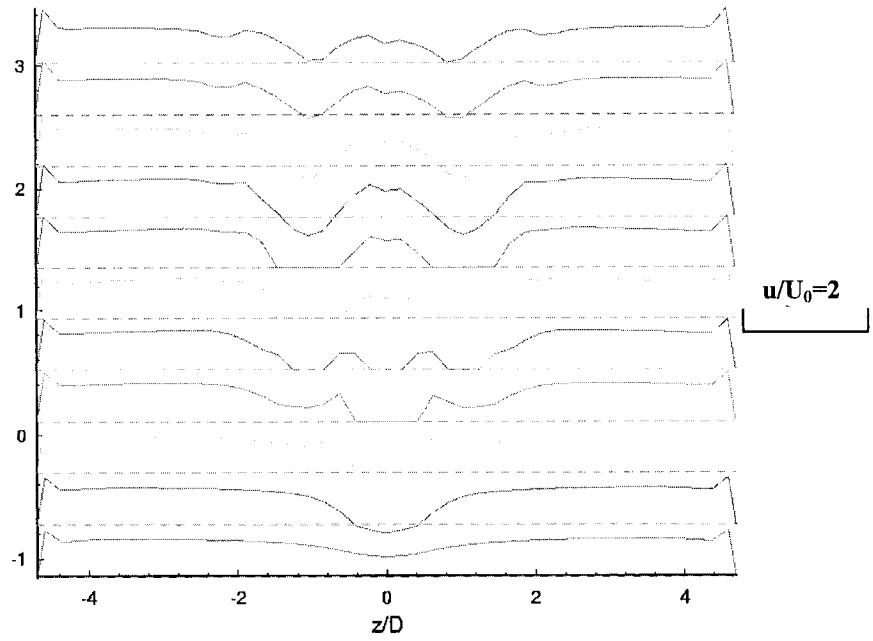

Figure 4.4.F14 Velocity Profile 0.5*u/U_0 in Plane y=0.004 m

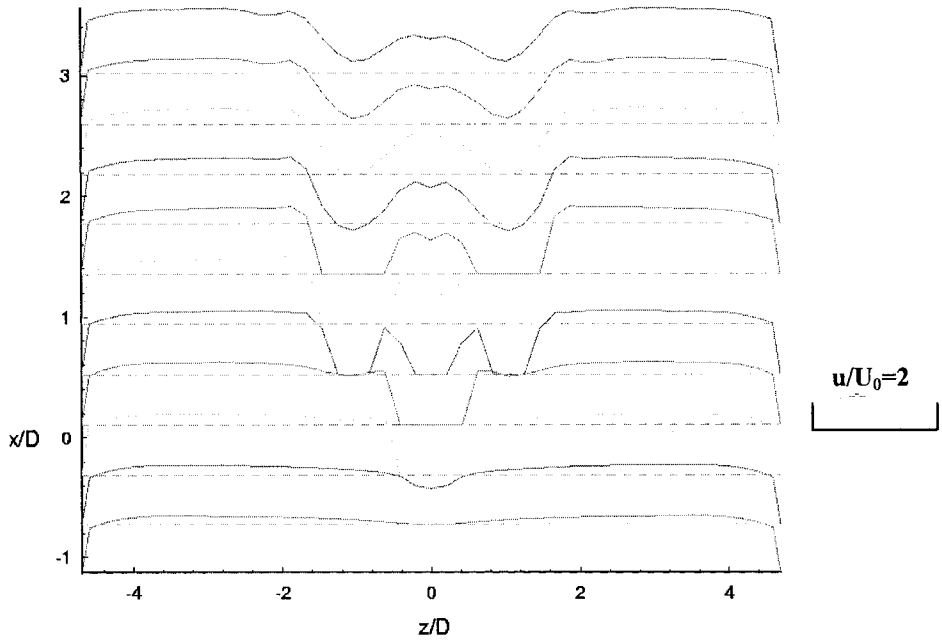

Figure 4.4.F15 Velocity Profile 0.5*u/U_0 in Plane y=0.019 m

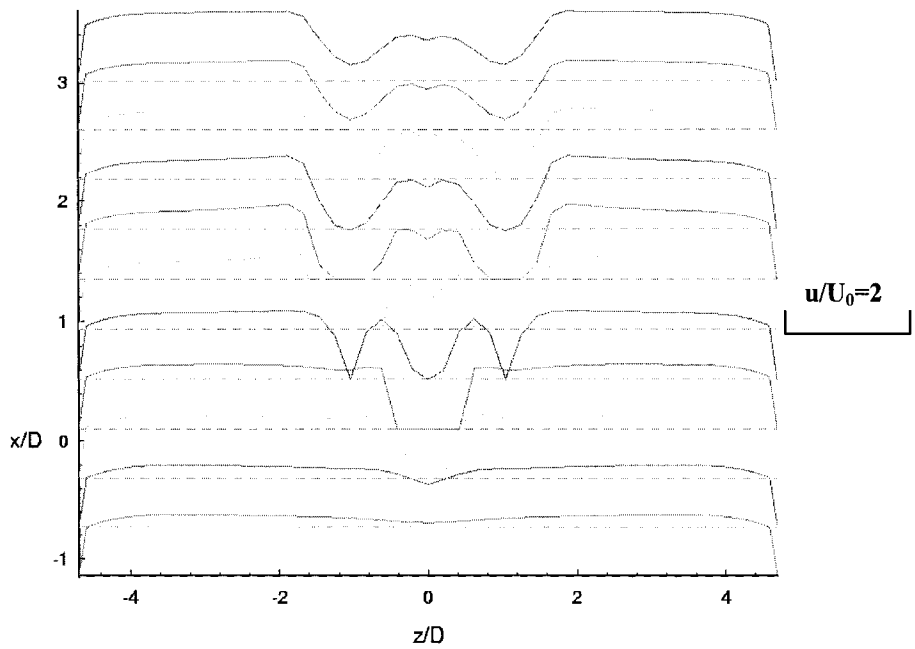

Figure 4.4.F16 Velocity Profile 0.5*u/U_0 in Plane y=0.034 m

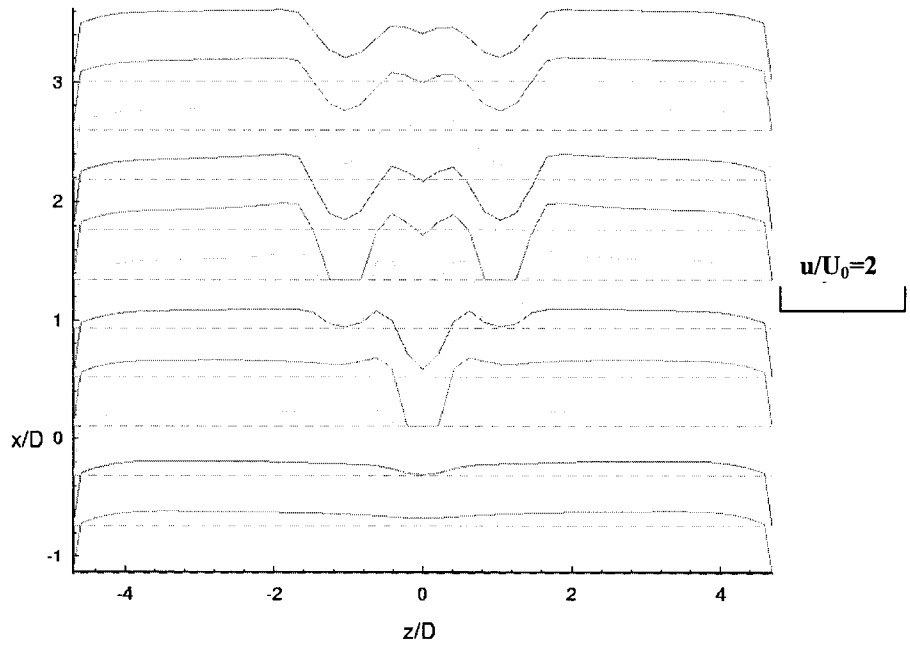

Figure 4.4.F17 Velocity Profile 0.5*u/U_0 in Plane y=0.049 m

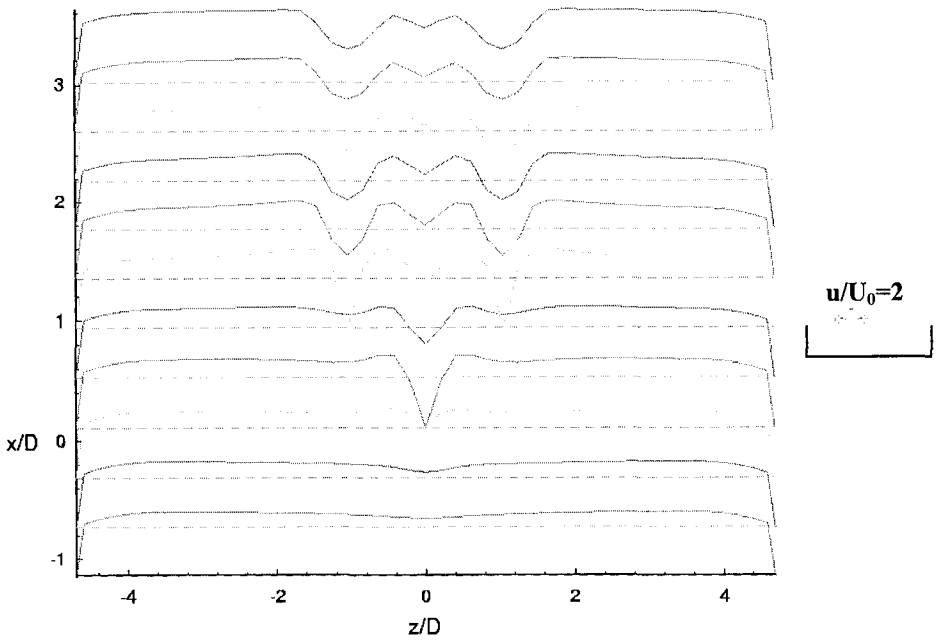

Figure 4.4.F18 Velocity Profile 0.5*u/U_0 in Plane y=0.064 m

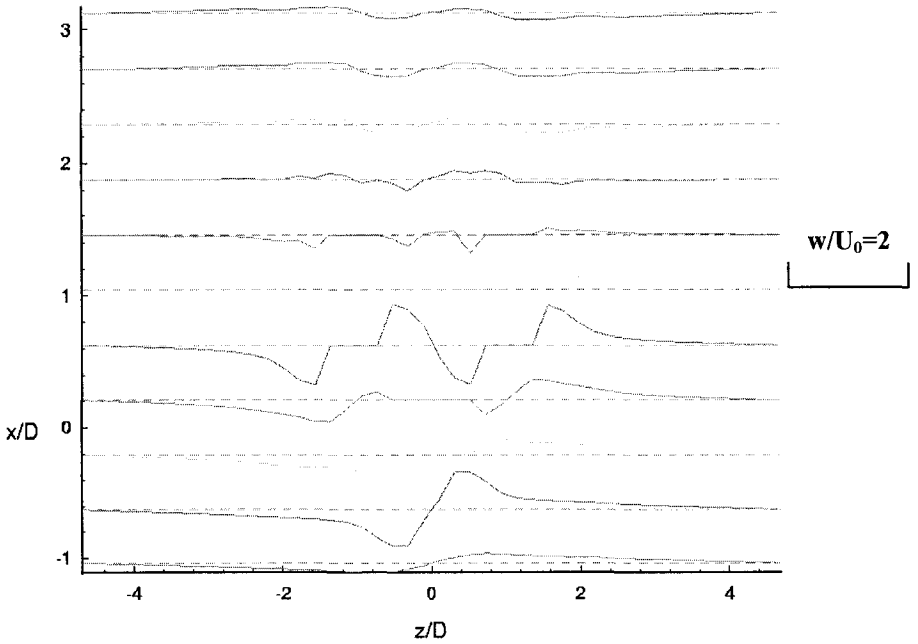

Figure 4.4.F19 Velocity Profile 0.5*w/U_0 in Plane y=0.004 m

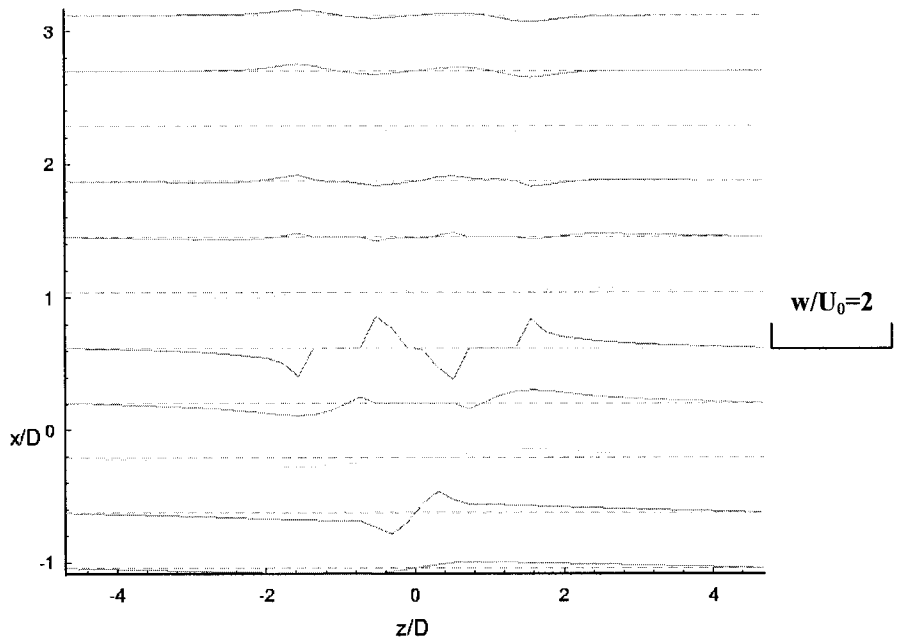

Figure 4.4.F20 Velocity Profile 0.5*w/U_0 in Plane y=0.019 m

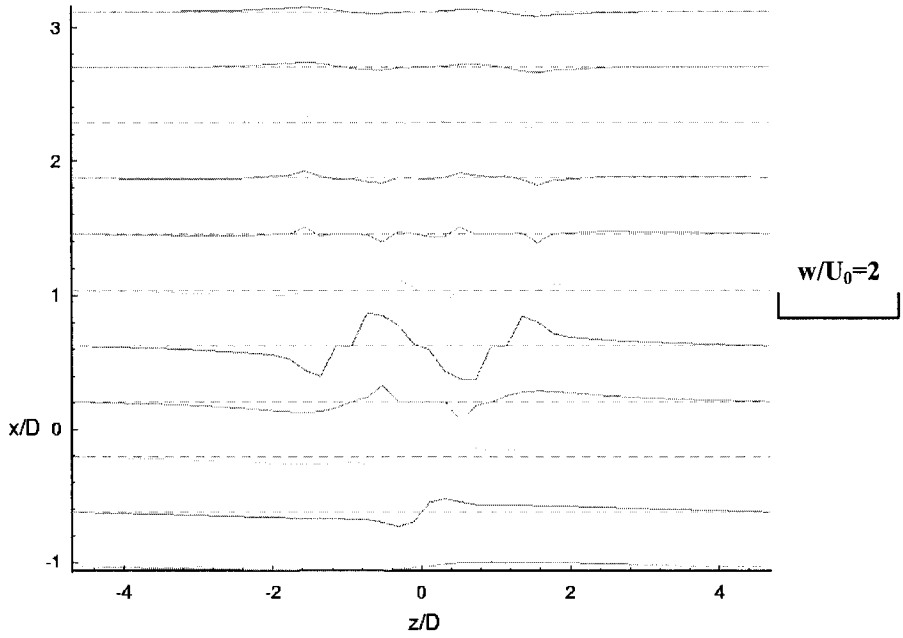

Figure 4.4.F21 Velocity Profile 0.5*w/U_0 in Plane y=0.034 m

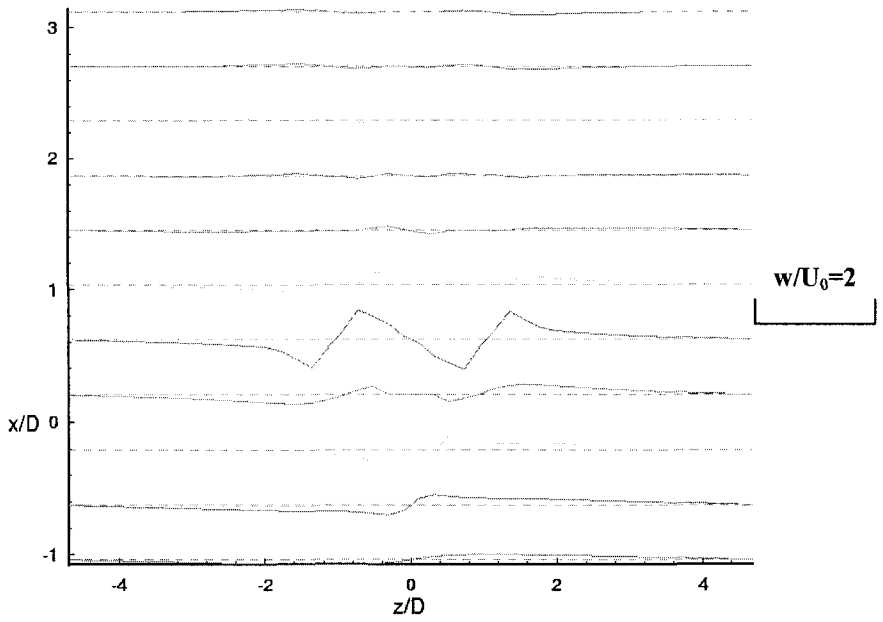

Figure 4.4.F22 Velocity Profile 0.5*w/U_0 in Plane y=0.049 m

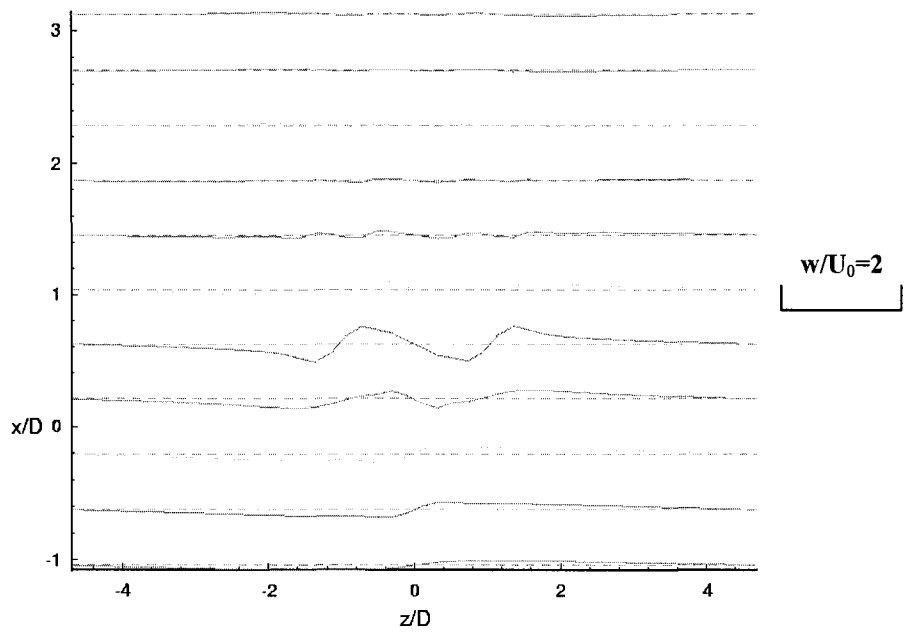

Figure 4.4.F23 Velocity Profile 0.5*w/U_0 in Plane y=0.064 m

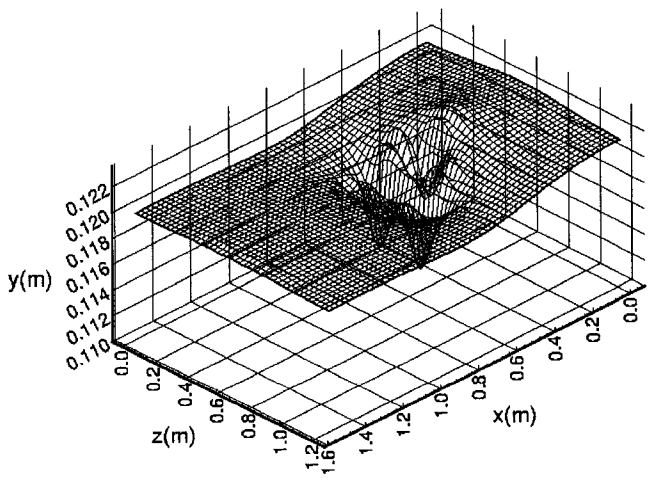

Figure 4.4.F24 Calculated Free Surface

Calculation Case G: Water Depth=0.2 m, Single Obstacle

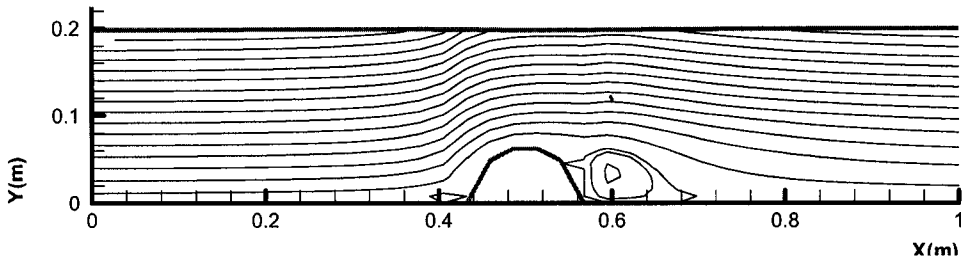

Figure 4.4.G1 u-v Streamlines in Plane z=0.596 m

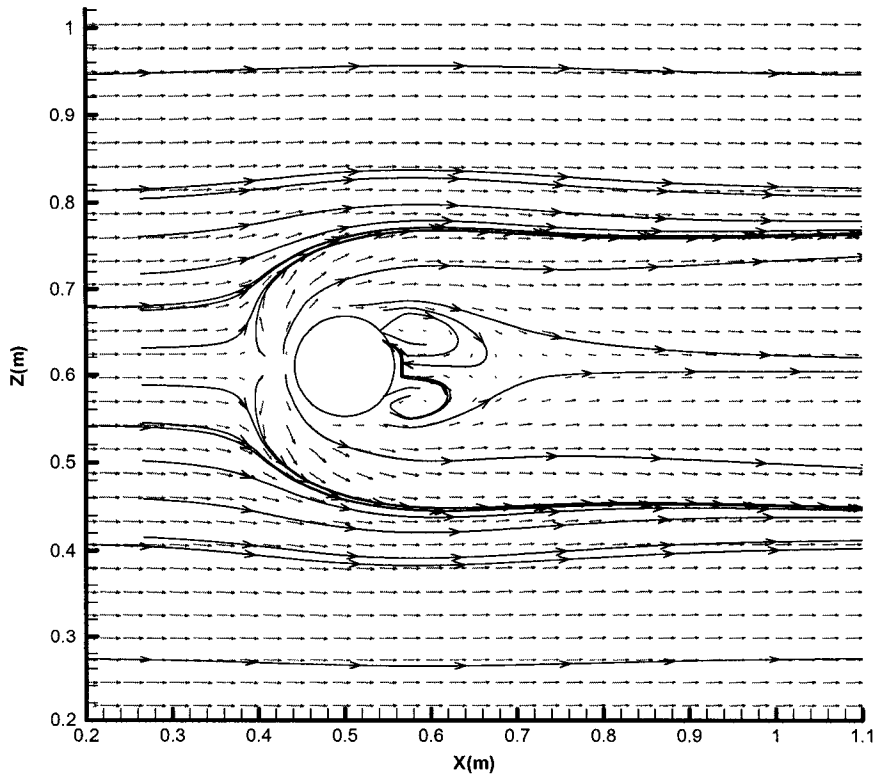

Figure 4.4.G2 u-w Streamlines and Velocity Vector in Plane y=0.004 m

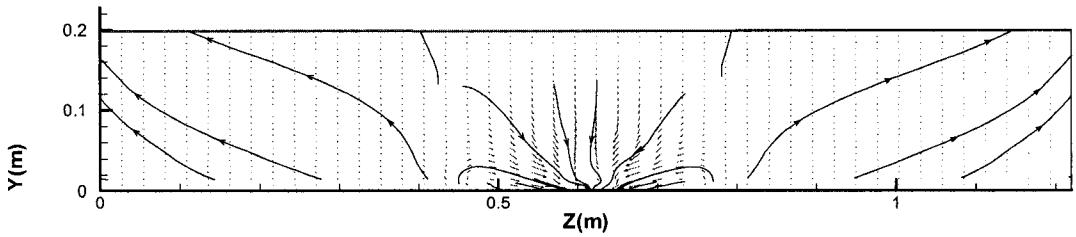

Figure 4.4.G3 v-w Velocity Vector in Plane x=0.595 m

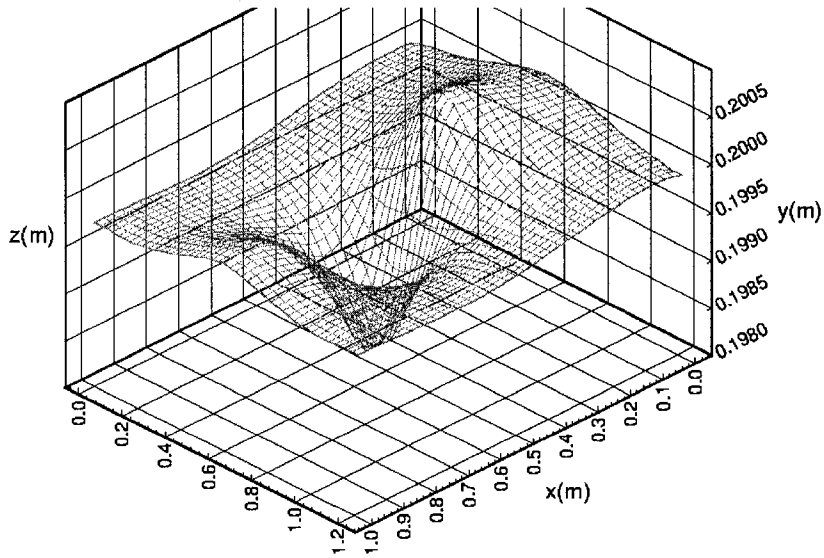

Figure 4.4.G4 Calculated Free Surface

Comparison of Wake Area for Different Cases

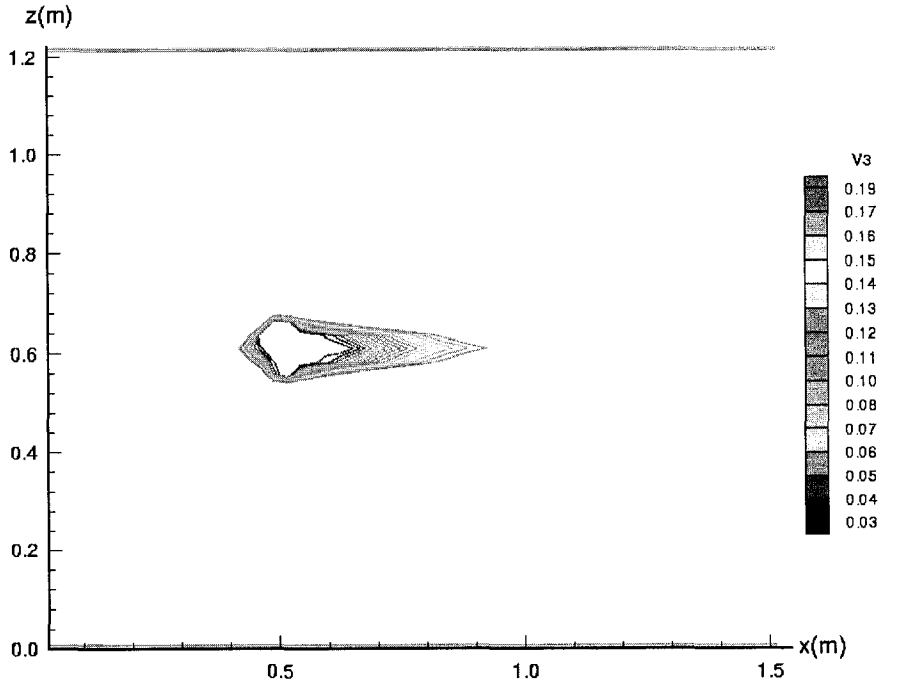

Figure 4.4.H1 Wake Area Where $q<U_0/2$: Case A

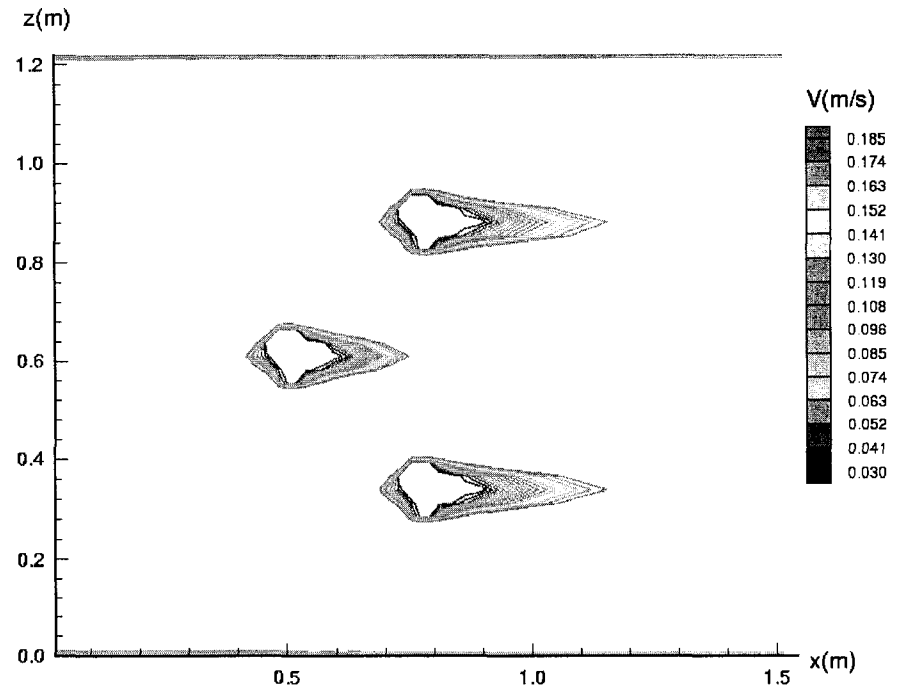

Figure 4.4.H2 Wake Area Where $q<U_0/2$: Case D

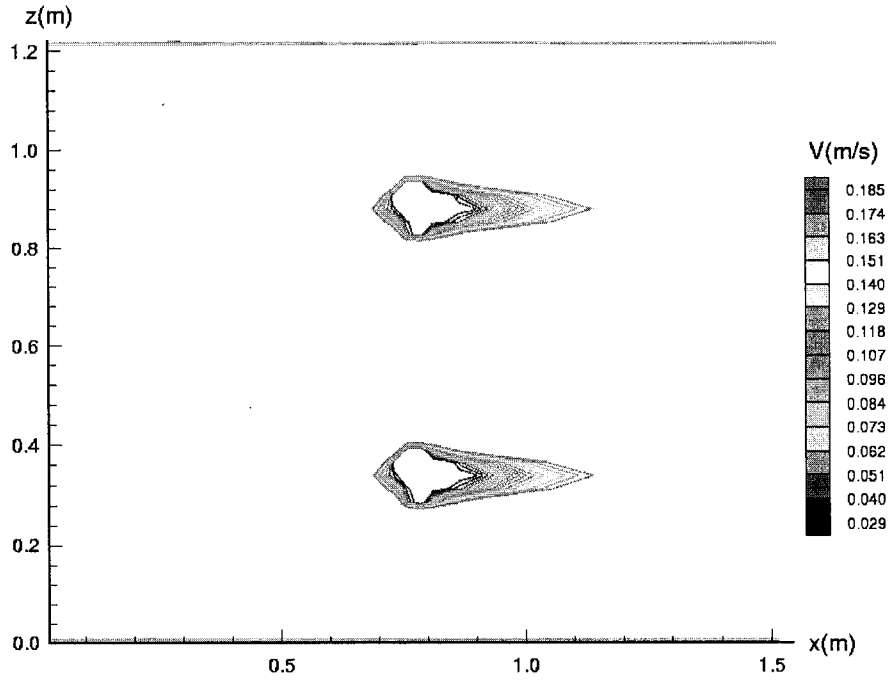

Figure 4.4.H3 Wake Area Where $q<U_0/2$: Case E

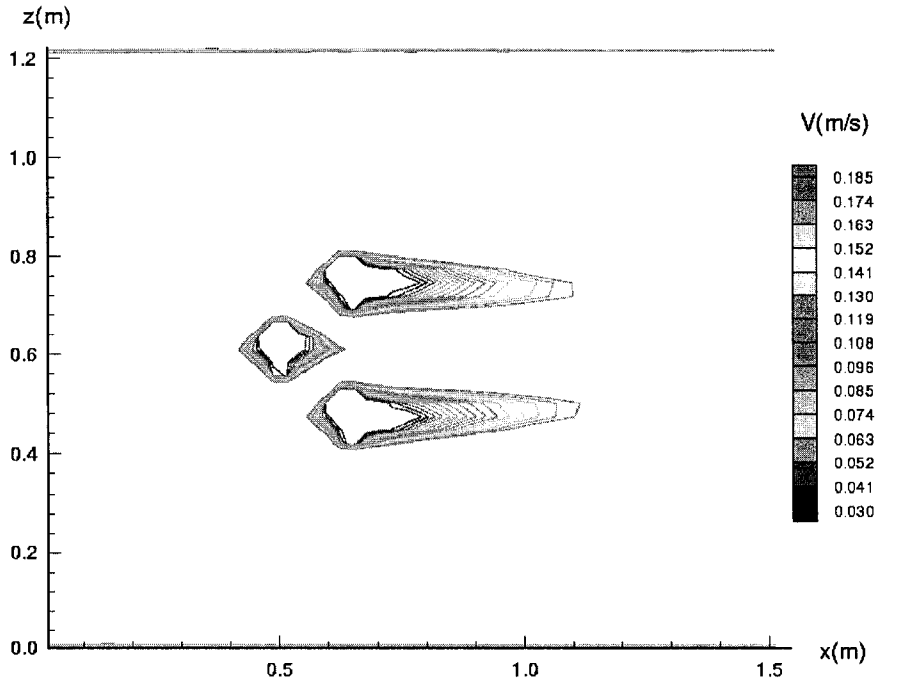

Figure 4.4.H4 Wake Area Where $q<U_0/2$: Case F

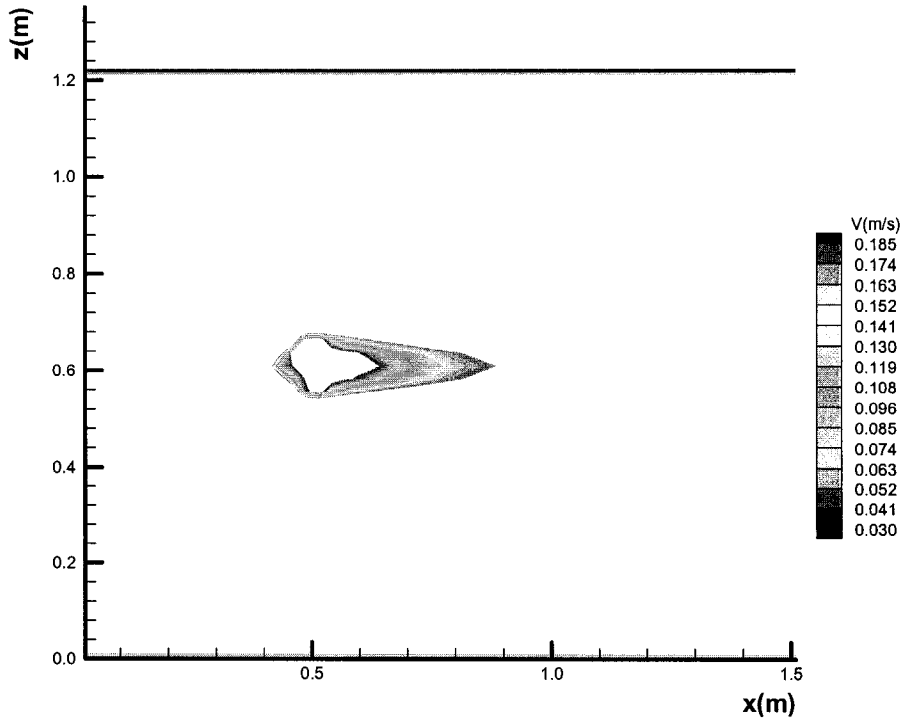

Figure 4.4.H5 Wake Area Where $q<U_0/2$: Case G

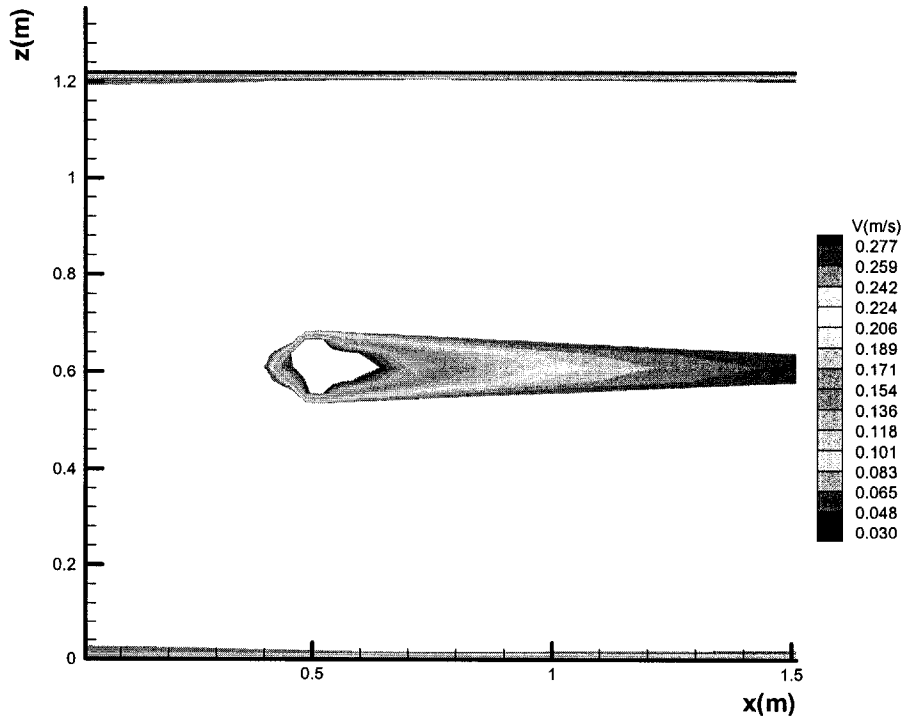

Figure 4.4.H6 Wake Area Where $q<3U_0/4$: Case G

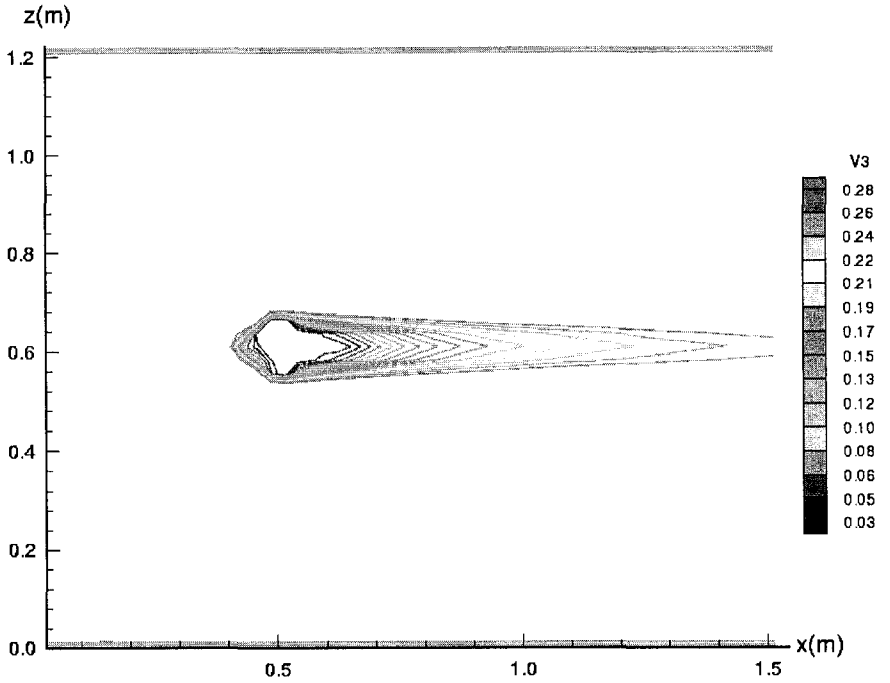

Figure 4.4.H7 Wake Area Where $q<3U_0/4$: Case A

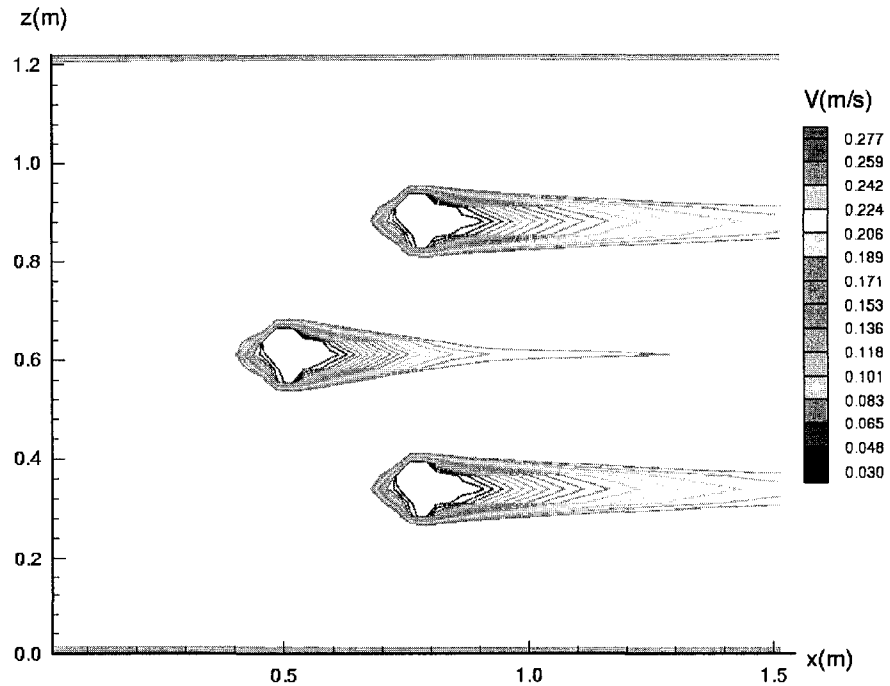

Figure 4.4.H8 Wake Area Where $q<3U_0/4$: Case D

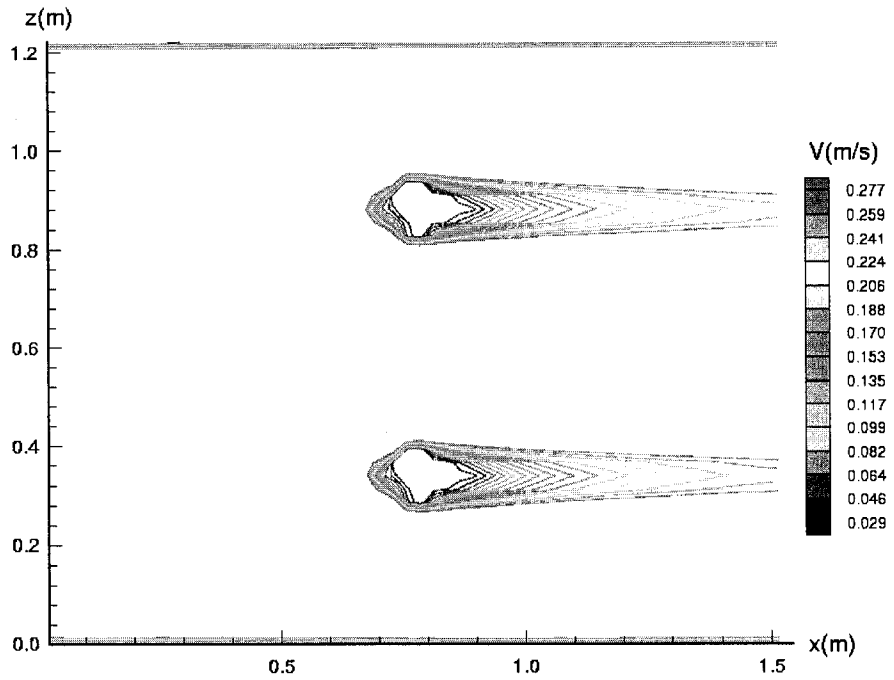

Figure 4.4.H9 Wake Area Where $q<3U_0/4$: Case E

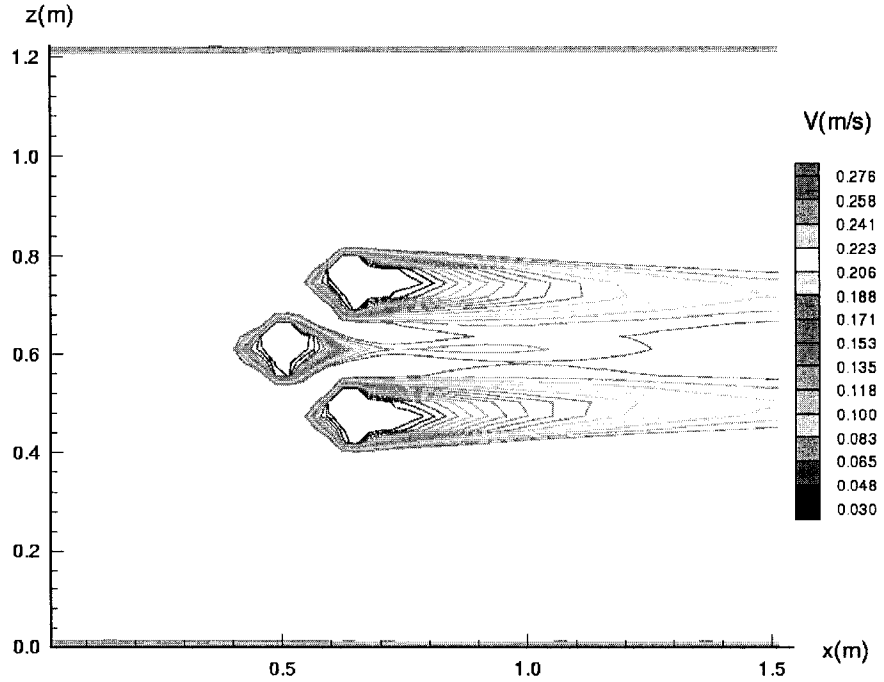

Figure 4.4.H10 Wake Area Where $q<3U_0/4$: Case F

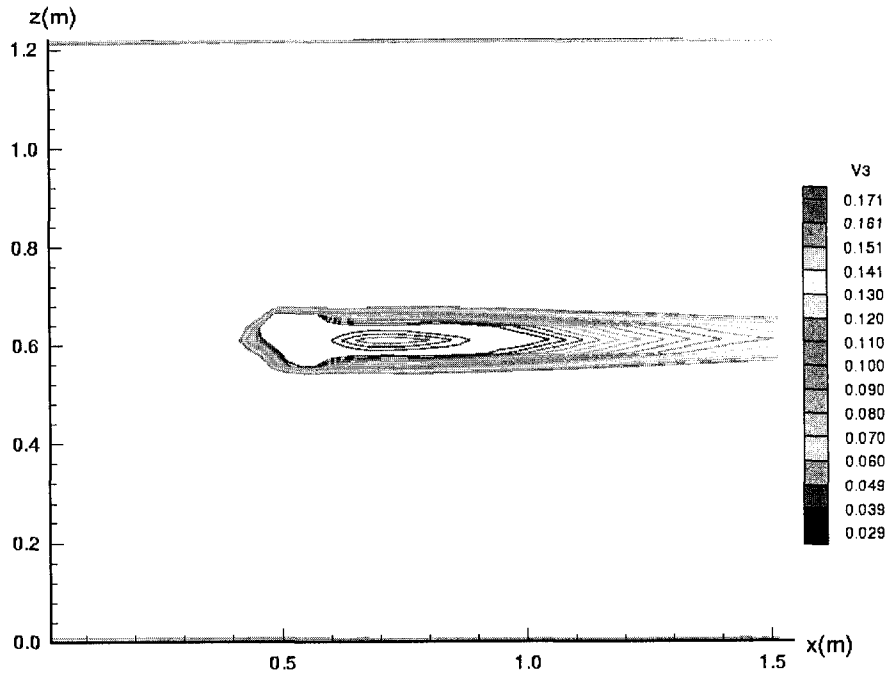

Figure 4.4.H11 Wake Area Where $q<U_0/2$: Case B

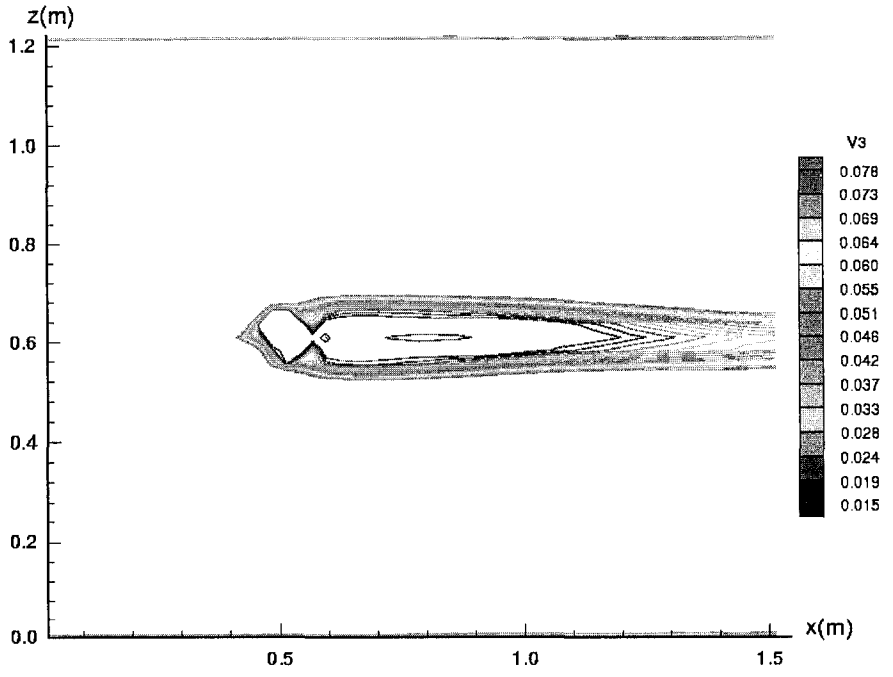

Figure 4.4.H12 Wake Area Where $q<U_0/2$: Case C

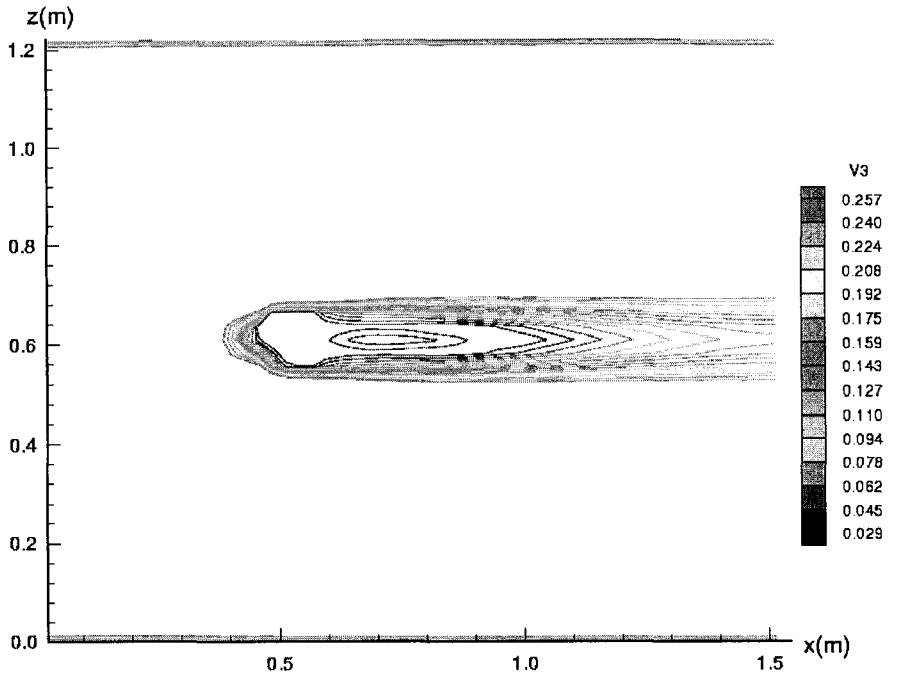

Figure 4.4.H13 Wake Area Where $q<3U_0/4$: Case B

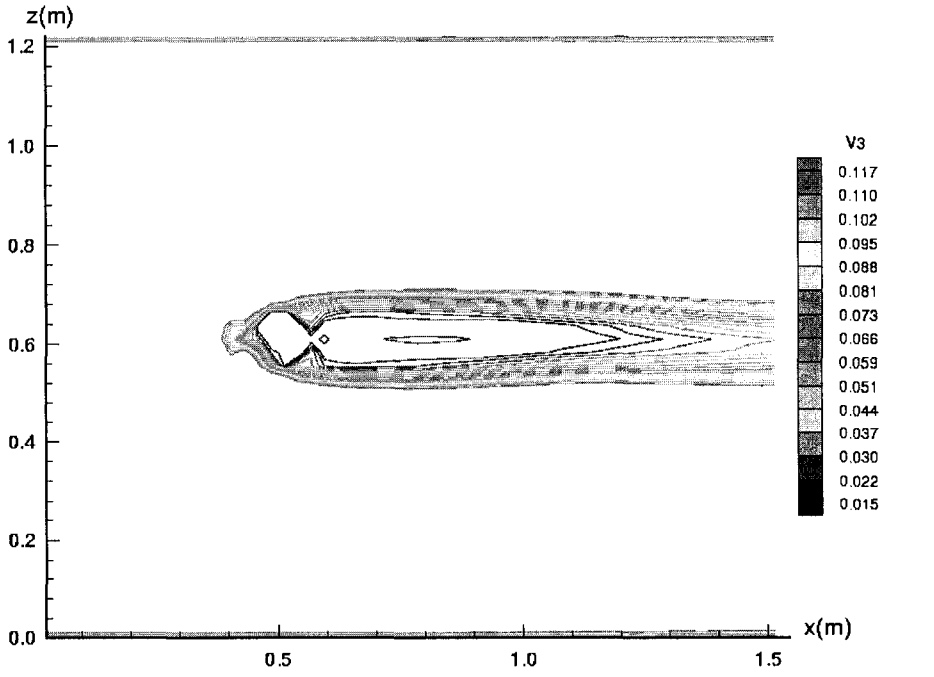

Figure 4.4.H14 Wake Area Where $q<3U_0/4$: Case C

Chapter 5

Conclusions

5.1 An Efficient Numerical Model and Its Applications

Three-dimensional turbulent flows around large obstacles of complex shape near a free surface are primarily studied by expensive experiments because numerical solution of these flows often requires too much computational effort. In this research an efficient numerical model was developed to simulate the three-dimensional turbulent flow around and/or over large, complex obstacles near a free surface. This numerical model was verified by the use of four groups of experimental data and proved to be capable of determining such flows with the use of a personal computer.

In the comparison with the experimental data for a submerged hydraulic jump (Long, et at.), the numerical results for velocities, the free surface profile and turbulence intensities compared well with the experimental results. In addition, the difference between a two-dimensional model and a three-dimensional model to simulate the flow in that submerged hydraulic jump was investigated using this numerical model. It was found that the two-dimensional model is applicable to the middle 50% of the flow.

The numerical model was further verified by use of the experimental data for a submerged hydraulic jump with a baffle wall (Wu and Rajaratnam, 1995). It showed the numerical model could produce a reasonably good simulation of the flow patterns and velocity of the submerged hydraulic jumps with two different baffle walls. The two possible states of the flow, a reattached wall jet and a deflected surface jet, were also detected by the numerical model. However, the bi-stable transition zone between the two states indicated in the experiments was not found in the numerical study. This

suggests that the transition zone is the result of disturbances or uncertainties in the real flow, which were filtered out by the numerical model.

By comparing numerical simulations with the flow visualization results for the flow past a three obstacle cluster in an open channel (Albers, 1997), it was found that this numerical model could clearly detect the separation line around the obstacles. In this study the size of the obstacles is of the same order as the water depth and the Reynolds number is $2.4*10^5$.

The numerical model was also used to calculate the flow around a simpler fish habitat structure, one hemisphere, in an open channel. The numerical results were verified by experimental data (Shamloo, 1996). The numerical simulation produced a flow pattern, vortex system and velocity distribution that were similar to the experiments. The calculated free surface profile also compared reasonably well with the measured data.

The success of this numerical model is due to following features. First, a unique design, which extended the FAVOR technique to a free-surface fitted-grid system, was developed to simulate free surface flows with obstacles. With a free-surface fitted-grid system accurate free surface boundary conditions can be applied because the free surface is also a coordinate surface. Moreover, with the free-surface fitted-grid system in this model, free surface locating can be achieved easily by adjusting the scale of the vertical coordinate. With the FAVOR technique the boundaries of the obstacles can be treated separately from the grid system. That means the shape of each obstacle can change freely without affecting the governing equations and that makes the numerical model capable of simulating the flow around arbitrary-shaped obstacles. Without considering the complex geometry of the obstacles, a simple grid system that only fits the free surface could be used. A simple grid system that can be generated easily is crucial for solving free surface flows because the grid system must be regenerated repeatedly during the free surface locating.

In contrast to other existing free surface locating methods, a free-surface locating method which integrates the momentum equation in the vertical direction was developed as part of this numerical model. After the integration, a simple algebraic equation was obtained for free surface locating. In comparison with other free surface locating methods such as Marker-and-Cell method or Volume-of-Fluid method that needs to solve a differential equation to find the local free surface elevation, this method can save significant computational time.

The evaluation of difference schemes in Chapter 3 confirmed that the QUICK difference scheme has higher accuracy in comparison with the popular but now relatively dated Power-Law difference scheme. The QUICK difference scheme with a UMIST limiter was used in this numerical model to achieve a more accurate and stable solution for turbulent flows. The validations by experimental data showed the QUICK difference scheme with the UMIST limiter worked well for three-dimensional turbulent flows.

The governing equations in this numerical model are the complete Reynolds-averaged Navier-Stokes equations and the k-ε turbulence model in a non-orthogonal curvilinear coordinate system. These general governing equations enable this numerical model to have wide applicability.

5.2 General Flow Structures of Turbulent Flows around Large Obstacles under a Free Surface

By performing systematic tests with the numerical model, some interesting properties of the flow around simple fish habitat structures were studied. First, the relationship between the maximum wave height and the relative water depth, defined by the ratio of water depth to the obstacle height, was investigated. It was found when the relative water depth was between 1 to 1.5 that the obstacles had a significant effect on the free surface profiles. This effect decreased when the relative water depth was less than 1. On the other hand, if the relative depth was greater than 3, the effect of the

obstacles on the free surface was negligible. In this case the maximum wave height was less than 2% of the water depth. This conclusion also agrees with Shamloo's experimental results (Shamloo, 1996). If the free surface waves can be ignored, the numerical solution can be significantly simplified. A chart was developed from a group of numerical tests to show the relationship between the maximum wave height and the relative water depth.

Secondly, the interaction between a group of hemispheres, serving as simple fish habitat structures, was studied with numerical simulations. From test cases A, D, E and F in Chapter 4 it was found that the interaction between two adjacent hemispheres was negligible when the distance between the two was greater than 4.5D, where D is the diameter of the hemispheres. In test case D it was shown that the upstream hemisphere had no significant effect on the local flow pattern near the downstream hemispheres but had an effect on free surface configuration above the downstream hemispheres. The wakes of the two downstream hemispheres were found to become unsymmetric as a consequence of the influence of the upstream hemisphere. When the distances between the hemispheres were less than 2.3D, as in test case F, notable interactions between the hemispheres were observed. In this case three hemispheres acted like one single larger obstacle. A single separate line was found to enclose the wake region behind the three hemispheres.

Wake areas behind fish habitat structures may be used to measure the efficiency of the fish habitat structures. In this research the wake areas behind a hemisphere were investigated as a function of water depth, where the wake areas were defined by $u/U_0<0.5$. It was found that the extent of the wake area was almost a constant when the water level was more than twice the hemisphere height. When the water level approached the top of the hemisphere, the wake area increased quickly. The wake area was found to be approximately proportional to the blockage rate, defined as the ratio of the maximum cross-section area of the hemisphere to the cross-section area of the channel, when the water level was near or below the top of the hemisphere. A chart showing the relationship between wake areas and blockage rate was provided.

5.3 Study on Governing Equations

Conventional fully transformed governing equations are often too complex to be practical in a three-dimensional non-orthogonal curvilinear coordinate system. In this research, the unique, concise fully transformed governing equations previously developed by the author in a general curvilinear coordinate system were further refined. In Chapter 2 it was shown that the newly developed governing equations were much simpler than the conventional fully transformed governing equations. Another advantage of the concise fully transformed governing equations is that there is only one pressure term in each momentum equation. Therefore, when the velocity field is known, the pressure can be obtained directly from any one of the momentum equations. The evaluation of these equations for a benchmark solution showed the concise governing equations had almost the same performance as the conventional governing equations.

The performance of the partially transformed governing equations was also examined with the benchmark solution in oblique Cartesian coordinate systems with 45 or 30 degree angles between the coordinate axes. In the 45-degree-angle coordinate system, it was found that the performance of the partially transformed governing equations was slightly inferior to the conventional or concise fully transformed governing equations on a relatively coarse grid but was as good as the fully transformed governing equations on a finer grid. However, the solution of the partially transformed governing equations failed to converge for the 30-degree-angle coordinate system.

5.4 Opportunities for Further Research

The coordinate system used in this numerical model suggests that this model is also applicable to flows in non-flat bed channels. If a boundary condition that governs the mobile bed profile is provided, there should be no difficulty in applying this model to the study of flows with a mobile bed.

Detailed evaluations of the governing equations and difference schemes were performed before this numerical model was built, but there was no evaluation of the k-ε turbulence model used. Although there are many successful examples of the application of k-ε turbulent models to turbulent flows, more evaluation of different turbulence models is recommended for three-dimensional turbulent free surface flows.

References

Aftosmis M. J., (1994) "Upwind Method for Simulation of Viscous Flow on Adaptively Refine Meshes", AIAA, Vol. 32, No 2, pp268-277

Albers, C. D. (1997), "Hydraulics of a Three Obstacle Cluster in Open Channels", Master Thesis, University of Alberta

Anderson V. K. and P. L. Bonhaus (1994), "An Implicit Upwind Algorithm for Computing Turbulent Flows on Unstructured Grid", Computers and Fluids, Vol. 23, No. 1, pp1-21

Aris R. (1962) "Vectors, Tensors, and the Basic Equations of Fluid Mechanics" Prentice Hall Inc., Cliffs, 1962

ASCE Task Committee on Turbulence Models in Hydraulic Computations, (1988), "Turbulence Modeling of Surface Water Flow and Transport", J. of Hydraulic Engineering, Vol. 114, No. 9, pp970-1073

Bai Xue-Song and Laszlo Fuchs (1994), "Modeling of Turbulent Reacting Flows past a Bluff Body: Assessment of Accuracy and Efficiency", Computers and Fluids, Vol. 23, No. 3

Bearman P. W. (1972), "An Investigation of Flow around Rectangular Cylinder", Journal of Aeronautical Quarterly, Vol. 23, Part 3, pp229-237

Bearman P. W and E. D. Obasaju (1982), "An Experiment Study of Pressure Fluctuations on Fixed and Oscillating Squire-Section Cylinder", Journal of Fluid Mechanics, Vol. 119, pp297-321

Chakravathy S. R. and S. Osher (1983), "High Resolution Applications of the Osher Upwind Scheme for the Euler Equations", AIAA Paper 83-1943

Chai R. and Y. Zhang (1988), "Applications of Ship Resistance Calculation Program to Bulbous Bows Design", Chinese Journal of Ship Science and Technology, No. 4, pp16-24

Dawson. C. W. (1977), "A Practical Computer Method for Solving Ship Wave Problems", Second International Conference on Numerical Ship Hydrodynamics, Berkeley, USA, pp30-38

Deardorff J. W. (1970), "A Numerical Study of Three-dimensional Turbulent Channel Flow at Large Reynolds Number", Journal of Fluid Mechanics, Vol. 41, pp453-480

Demirdzic I and M. Peric (1990), "Finite Volume Method for Prediction of Fluid Flow in Arbitrary Shaped Domains with Moving Boundaries", International Journal for Numerical Methods in Fluids, Vol. 10, pp771-790

Demirdzic I., Z. Lilek and M. Peric (1992), "Fluid Flow and Heat Transfer Test Problems for Non-Orthogonal Grids: Bench-Mark Solutions", International Journal for Numerical Methods in Fluids, Vol. 15, pp329-354

Farmer J. and L. Martinelli (1994), "Fast MultiGrid Method for Solving Incompressible Hydrodynamic Problem with Free Surface", AIAA, Vol. 32, No 6, pp1175-1182

Flow Science Inc., "FLOW-3D Applications", Flow Science, Inc., http://www.flow3d.com

Gaskell P. H. and A. K. C. Lau (1988), "Curvature Compensated Convective Transport: SMART, a New Boundedness Preserving Transport Algorithm", International Journal for Numerical Methods in Fluids, Vol. 8, pp1291

Gastro Z. P. and Robin A. G. (1977), "The Flow around a Surface Mounted Cube in Uniform and Turbulent Stream", Journal of Fluid Mechanics, Vol. 79, Part 2, pp307-335

Govinda R., and N. Rajaratnam (1989), "The Submerged Hydraulic Jump", Journal of Hydraulics Division, ASCE, 89 (1), pp136-162

Gowda B. H, L., Gerhardt H. and Kramer C. (1983), "Surface Flow Field around 3D Bluff Bodies" Journal of Wind Engineering and Industrial Aerodynamics, Vol.11, pp405-420

Hager W. H. (1992), "Energy Dissipaters and Hydraulic Jumps", Kluwer Academic Publishers, Dordrecht

Harlow, F. H. and J. E. Welch (1965), "Numerical Calculation of Time-Dependent Viscous Incompressible Flow", Physics of Fluids, Vol. 8, pp2182

Harten A. (1983), "High resolution Schemes for Hyperbolic Conservation Laws", Journal of Computational Physics, Vol. 49, pp357

He P. and M. Salcudean (1994), "A Numerical Method for 3-D Viscous Incompressible Flows Using Non-Orthogonal Girds", International Journal for Numerical Methods in Fluid, Vol. 18, pp449-469

Hess J. and A. M. O. Smith (1962), "Calculation on Non-Lifting Potential Flow about Three-Dimensional Bodies" Douglas Aircraft Company, Report E. S. 40622

Hirt, C. W. and B. D. Nichols (1981), "Volume of Fluid (VOF) Method for the Dynamics of Free Boundaries", Journal of Computation Physics, Vol. 39, pp201

Hirt, C. W., J. L. Cook and T. D. Butler (1970), "A Lagrangian Method for Calculating the Dynamics of an Incompressible Fluid with Free Surface", Journal of Computation Physics, Vol. 5, pp103

Hwang C. J. and S. J. Wu (1993), "Adaptive Finite Volume Upwind Approach on Mixed Quadrilateral-Triangular Meshes", AIAA, Vol. 31, No 1, pp61-67

Katopodis C. (1981), "Considerations in the Design of Fishways for Freshwater Species", Proceedings, 5th Canadian Hydrotechnical Conference, Fredericton, NB, Canada, pp857-878

Katopodis C. and N. Rajaratnam (1983), "A Review and Laboratory Study of the Hydraulics of Denil Fishways", Canadian Technical Report of Fisheries and Aquatic Sciences, No. 1145

Kim, J and P. Moin (1986), "The Structure of the Velocity Field in Turbulent Channel Flow", Journal of Fluid Mechanics, Vol. 162, pp339-363

Kline, S. J., W. C. Reynolds, F. A. Schraub and P. W. Runstadler (1967), "The Structure of Turbulent Boundary Layer", Journal of Fluid Mechanics, Vol. 30, pp741-773

Launder, B. E. and J. L. Spalding (1972), "Mathematical Models of Turbulent Flows", Academic Press, New York

Launder B. E., G. J. Reece, and W. Rodi (1975), "Progress in the Development of a Reynolds-Stress Turbulence Closure", Journal of Fluid Mechanics, Vol. 68, pp537-566

Lee B. E. (1975), "The Effect of Turbulence on The Surface Pressure Field of a Squire Prism", Journal of Fluid Mechanics, Vol. 69, pp263-282

Leer B. V. (1976), "Towards the Ultimate Conservative Difference Scheme. II. Monotonicity and Conservation Combined in a Second Order Scheme", Journal of Computational Physics, Vol. 16, pp85

Leonard B. P. (1979), "A Stable and Accurate Convective Modeling Procedure Based on Quadratic Upstream Interpolation", Computer Methods and Applied Mechanics in Engineering, Vol. 19, pp59

Leonard B. P. (1988), "Simple High Accuracy Resolution Program for Convection Modeling of Continuities", International Journal for Numerical Methods in Fluids, Vol. 8, pp1291

Leonard B. P. and S. Mokhtari (1990), "Beyond First Order Upwinding: The ULTRA-SHARP Alternative for Non-Oscillatory Steady State Simulation of Convection", International Journal for Numerical Methods in Engineering, Vol. 30, pp729-766

Leschziner, M. A. (1995), "Computation of Aerodynamic Flow with Turbulent-Transport Models based on Second-Order Closure", Computers and Fluids, Vol. 24, No 4, pp377-392.

Lien F. S. and M. A. Leschziner (1993), "Approximation of Turbulence Convection in Complex Flows with a TVD-MUSCL Scheme", Proceedings, 5th International IAHR Symposium on Refined Flow Modeling and Turbulence Measurement, Paris

Lien F. S. and M. A. Leschziner (1994a), "Upstream Monotonic Interpolation for Scalar Transport with Application to Complex Turbulent Flows", International Journal for Numerical Methods in Fluids, Vol. 19, pp527-548

Lien, F. S. and M. A. Leschziner (1994b), " Assessment of Turbulence Transport Models including Non-Linear and Eddy-Viscosity Formulation and Second-Moment Closure for Flow over a Backward-Facing Step", Computers and Fluids, Vol. 23, No 8, pp983-1004

Lien, F. S. and M. A. Leschziner (1996), " Second Moment Closure for Three-dimensional Turbulent Flow around and within Complex Geometries", Computers and Fluids, Vol. 25, No 3, pp237-262, 1996

Long D., P. M. Steffler and N. Rajaratnam (1990), "LDA Study of Flow Structure in Submerged Hydraulic Jumps", Journal of Hydraulic Research, Vol. 28, No. 4, pp437-460

Long D., P. M. Steffler and N. Rajaratnam (1991), "A Numerical Study of Submerged Hydraulic Jumps", Journal of Hydraulic Research, Vol. 29, No. 3, pp293-308

Ma D., A. H. Eraslan and G. Ahamid (1993), "A Computer Code for Analyzing Transient 3D Rapid Granular Flows in Complex Geometric", Computers and Fluids, Vol. 22, No 1, pp25-50

Mavriplis D. J. (1995), "3D MultiGrid RANS Solver for Unstructured Meshes", AIAA, Vol. 33, No3, 1995, pp445-453

Meller G, and P. Yamada (1982) "Development of a Turbulence-Closure Model for Geophysical Fluid Problem", Reviews of Geophysics and Space Physics, Vol. 20, No 2, pp851-875

Michelassi U., W. Rodi and J. Zhu (1993), "Testing a Low Reynolds Number k-ε Model based on Direct Simulation Data", AIAA, Vol. 31, No 9, pp1720-1723

Nakajima, K. and Y. Kallinderis (1994), "Comparison of FEM and FVM for Incompressible Viscous Flow", AIAA, Vol. 32, No 5, pp1090-1093

Ogava Y. and Oikava S. (1982), "An Field Investigation of Flow and Diffusion around a Model Cube", Atmosphere Environment, Vol. 16, No 2, pp207-222

Oosterlee C. W., P. Wesseling, A. Segal and E. Brakkee (1993), "Benchmark Solutions for the Incompressible Navier-Stokes Equations in General Coordinates on Staggered Grids", International Journal for Numerical Methods in Fluids, Vol. 17, pp301-321.

Pan D. and J. Cheng (1993), "Upwind Finite Volume N-S Computations on Unstructured Triangular Meshes", AIAA, Vol. 31, No 9, pp1618-1625

Patankar S. V. (1980), "Numerical Heat Transfer and Fluid Flow", Hemisphere Publishing Company

Quirk J. J. (1994), "An Alternative to Structured Grid for Computing Gas Dynamic Flow around Arbitrary Complex 2D Bodies", Computers and Fluids, Vol. 23, No 1, pp125-142

Rajaratnam N. (1964), "The Forced Hydraulic Jump", Water Power, Vol. 16

Rajaratnam N. and V. Murahari (1971), "A Contribution to Forced Hydraulic Jumps", Journal of Hydraulic Research, Vol. 9, No. 1, pp217-240

Rajaratnam N., (1976), "Turbulent Jets", Elsevier Scientific Publication Co.

Rajaratnam N. (1991), "Submerged Hydraulic Jump", Journal of Hydraulic Division, ASCE, 91(4), pp71-96

Ramshaw, J. D. (1991), "Numerical Viscosities of Difference Schemes", Journal of Numerical Methods in Engineering, Vol. 10, pp927-931

Rizzetta D. P. (1994), "Numerical Simulation of Turbulent Cylinder Juncture Flow Field", AIAA, Vol. 32, No 6, pp1113-1119

Rodi W. (1980), "Turbulence Models and Their Application in Hydraulics", International Association for Hydraulic Research, Delft, the Netherlands

Roe P. L. (1985), "Some Contributions to the Modeling of Discontinuous Flows", Lectures in Applied Mathematics, Vol. 22, Proceedings, 1983 AMS-SIAM Summer Seminar on Large Scale Computing in Fluid Mechanics, SIAM, Philadelphia, USA, pp163

Rogallo R. S. and P. Moin (1984), "Numerical Simulations of Turbulent Flows", Annual Review, Fluid Mechanics, Vol. 16, pp99-137

Schlichting H. (1979), "Boundary Layer Theory", McGraw-Hill, New York

Shamloo H. (1996), "Hydraulics of Simple Habitat Structures in Open Channels", Ph. D. Thesis, University of Alberta, Edmonton

Shamloo, H., N. Rajaratnam and C. Katopodis (2001), "Hydraulics of Simple habitat structures", Journal of Hydraulic Research, Vol. 39, No. 4, pp351-366

Shahyar Pirzadeh (1992), "Unstructured Viscous Grid Generation by Advancing-Layers Method", AIAA, Vol. 30, No 8, pp1735-1737

Shahyar Pirzaden (1993), "Structured Background Grids for Generation of Unstructured Grids by Advancing-Front Method", AIAA, Vol. 31, No 2, pp257-265

Sharif, M. A. R. and Y. K. E. Wong (1993), "Evaluation of the Performance of Three Turbulence Closure Models in the Prediction of Confined Swirling Flow", Computers and Fluids, Vol. 24, No 1, pp81-100

Shen Q., Zhang Y and Chai R. (1988), "Numerical Solution of Fully Elliptic N-S Equation for Ship Viscous Flow", Proceedings, The 2nd National Conference on Ship Resistance and Propulsion, Ningbo, China

Shen Q., Y. Zhang and R. Chai (1989), "Calculations of Ship Stern and Wake Flow by Solving the Complete Reynolds-Averaged Navier-Stokes Equations", Proceedings, International Symposium on Ship Resistance and Powering Performance, pp25-29, Shanghai, China

Shen Q., Y. Zhang and R. Chai (1991), "Calculations of Viscous Flow around Two HSVA Ship Models by Solving the Reynolds Averaged Navier-Stokes Equation", Ship Viscous Flow, Proceedings, The 1990 SSPA-CTH-IIHR Workshop, Goteborg, Sweden

Shin Tsan-Hsing, W. W. Liou, A. Shabbir, Z. Yang and J. Zhu (1995), "A New k-ε Model for High Reynolds Number Turbulent Flow", Computers and Fluids, Vol. 24, No 3, pp227-238

Sotiropoulos F., W. J. Kim and V. C. Patel (1994), "A Computational Comparison of Two Incompressible Navier-Stokes Solvers in Three-dimensional Laminar Flows", Computers and Fluids, Vol. 23, No. 4, pp627-646

Speziale C. G. and S. Sarkar (1987), "On Nonlinear k-ε Model of Turbulence", Journal of Fluid Mechanics, Vol. 178, pp459-475

Speziale, G. G. and T. B. Gatski (1994), "Assessment of Second-Order Closure Models in Turbulent Shear Flows", AIAA, Vol. 32, No 10, pp2113-2115

Steffler, P. M., N. Rajaratnam and A. W. Peterson (1985) "LDA measurements in open channel" , J. Hydraulic Engineering, Vol. 111, pp119-130

Sweby P. K. (1984), "High Resolution Schemes Using Flux Limiter for Hyperbolic Conservation Laws", SIAM, J. of Numerical Analysis, Vol. 21, pp995

Taffersall P. and J. McGuirk (1994), "Evaluation of Numerical Diffusion in Viscous Flow Calculation", Computers and Fluids, Vol. 23, No 1, pp177-201.

Thomas T. G. (1995), "Large Eddy Simulation of Turbulent Flow in an Asymmetric Compound Open Channel", Journal of Hydraulic Research, Vol. 33, No 1 pp27-42

Tropea C. and Gackstatter K. (1985), "The Flow over 2D Surface Mounted Obstacles at Low Reynolds Numbers", Journal of Fluid Engineering, Vol. 107, pp489-494

Tsan-Hsing-Shih and J. L. Lumley (1993), "Critical Comparison of Second-Order Closures with Direct Numerical Simulation of Homogeneous Turbulence", AIAA, Vol. 31, No 4, pp663-670

Tyagi, D. M., P. K. Pande and M. K. Mittal (1978), "Drag on Baffle Walls in Hydraulic Jump", Journal of Hydraulics Division, ASCE, 104(4), pp515-525

Vickery B. J. (1966), "Fluctuating Lift and Drag on a Long Cylinder of Squire Cross-section in a Smooth and in a Turbulent Stream", Journal of Fluid Mechanics, Vol. 125, pp481-494

Werner H. and Wengle H. (1989), "Large-Eddy Simulation of Turbulent Flow over a Square Rib in a Channel", 7th Symposium of Turbulent Shear Flows, Stanford University, Stanford, CA, Aug21-23

White F. M. (1974), "Viscous Fluid Flow", McGraw-Hill Book Company

Wu S. and N. Rajaratnam (1995), "Effects of Baffles on Submerged Flows", Journal of Hydraulic Engineering, September, pp644-652

Yang K. S. and J. H. Ferziger (1993), "Large-eddy Simulation of Turbulent Obstacle Flow Using a Dynamic SubGrid-Scale Method", AIAA, Vol. 31, No 8, pp1407-1413

Yang Z. and T. H. Shih (1993), "New Time Scale based k-ε Model for Near Wall Turbulence", AIAA, Vol. 31, No 7, pp1191-1198

Zhang Y. (1984), "Turbulent Flow in Thick Axisymmetric Boundary Layer", Master Thesis, Harbin Engineering University, Harbin

Zhang Y. (1987), "Calculation of Non-Lifting Potential Flow around Three-Dimensional Bodies by Submerged Sources", Chinese Journal of Ship Research and Design, No 2, pp11-15

Zhang Y (1988), "The Governing Equations of Turbulent Flow in General Curvilinear Coordinate System", The First East-China Conference of Fluid Mechanics, pp244-252, Wuxi, China

Zhang Y. and Q. Shen (1990), "Prediction of Ship Stern and Wake Viscous Flow", Proceedings, The Third National Conference on Hydrodynamics, Shanghai, China

Zijlema M., A. Segal and P. Wesselng (1995), "Invariant Discretization of k-ε Model in General Coordinates for Prediction of Turbulent Flow in Complicated Geometry", Computers and Fluids, Vol. 24, No 3, pp209-225

Appendix

Derivation of Concise Fully Transformed Momentum Equations in a General Curvilinear Coordinate System

The momentum equations in covariant components in the Cartesian coordinate system are

$$\frac{\partial(\rho u_i u^j)}{\partial x^j}+\frac{\partial p}{\partial x^i}+\gamma_i-\frac{\partial \tau_i^j}{\partial x^j}=0 \qquad (i=1,2,3) \qquad \text{A1}$$

To write equation (A1) in tensor form, one has

$$(\rho u_i u^j)\,|_j+p\,|_i+\gamma_i-\tau_i^j\,|_j=0 \qquad (i=1,2,3) \qquad \text{A2}$$

Since tensor equations are invariant with respect to any coordinate transformation, equation (A2) is valid in any coordinate system. The next step is to expand the tensor derivatives in equation (A2) in a general coordinate system (ξ^1,ξ^2,ξ^3).

By tensor analysis, the stress term can be written as

$$\tau_i^j\,|_j=\frac{\partial \tau_i^j}{\partial \xi^j}-\tau_k^j\Gamma_{ij}^k+\tau_i^j\Gamma_{kj}^k \qquad \text{A3}$$

The Christoffel symbols Γ_{ij}^k are defined as

$$\Gamma_{ij}^k=\vec{e}^{\,k}\frac{\partial \vec{e}_j}{\partial \xi^i} \qquad \text{A4}$$

From tensor analysis

$$\Gamma_{kj}^{k} = \frac{1}{\sqrt{g}} \frac{\partial \sqrt{g}}{\partial \xi^{j}} \tag{A5}$$

Then

$$\tau_{i}^{j}\,|_{j} = \frac{1}{\sqrt{g}} \frac{\partial (\sqrt{g}\tau_{i}^{j})}{\partial \xi^{j}} - \tau_{k}^{j}\Gamma_{ij}^{k} \tag{A6}$$

Switching the subscript/superscript k in last term results in

$$\tau_{k}^{j}\Gamma_{ij}^{k} = \tau^{jk}\Gamma_{ijk} \tag{A7}$$

Because τ^{ij} and Γ_{ijk} are symmetric about i, j, then

$$\begin{aligned} \tau^{jk}\Gamma_{ijk} &= \frac{1}{2}(\tau^{jk} + \tau^{kj})\Gamma_{ijk} \\ &= \frac{1}{2}(\tau^{jk}\Gamma_{ijk} + \tau^{jk}\Gamma_{ikj}) \\ &= \frac{1}{2}(\Gamma_{ijk} + \Gamma_{ikj})\tau^{jk} \\ &= \frac{1}{2}\frac{\partial g_{jk}}{\partial \xi^{i}}\tau^{jk} \end{aligned} \tag{A8}$$

Here the following relationships are used:

$$g_{jk} = \vec{e}_{j}\vec{e}_{k} \tag{A9}$$

$$\begin{aligned} \frac{\partial g_{jk}}{\partial \xi^{i}} &= \vec{e}_{j}\frac{\partial \vec{e}_{k}}{\partial \xi^{i}} + \vec{e}_{k}\frac{\partial \vec{e}_{j}}{\partial \xi^{i}} \\ &= \Gamma_{ikj} + \Gamma_{ijk} \end{aligned} \tag{A10}$$

To summarize the above procedures, one can write

$$\tau_i^j\,|_j = \frac{1}{\sqrt{g}}\frac{\partial(\sqrt{g}\tau_i^j)}{\partial\xi^j} - \frac{1}{2}\frac{\partial g_{jk}}{\partial\xi^i}\tau^{jk} \qquad \text{A11}$$

Similarly, for velocities,

$$(\rho u_i u^j)\,|_j = \frac{1}{\sqrt{g}}\frac{\partial(\sqrt{g}\rho u_i u^j)}{\partial\xi^j} - \frac{1}{2}\frac{\partial g_{jk}}{\partial\xi^i}\rho u^j u^k \qquad \text{A12}$$

The pressure term is straightforward:

$$p\,|_i = \frac{\partial p}{\partial\xi^i} \qquad \text{A13}$$

The final form for equation (A2) after transformation is

$$\frac{1}{\sqrt{g}}\frac{\partial}{\partial\xi^j}[\sqrt{g}(\rho u_i u^j - \tau_i^j)] - \frac{1}{2}\frac{\partial g_{jk}}{\partial\xi^i}(\rho u^j u^k - \tau^{jk}) + \frac{\partial p}{\partial\xi^i} - \gamma_i = 0 \qquad \text{A14}$$

Now look further at the expression for the shear stress. First two useful equations are derived.

Since

$$g^{im}g_{mj} = \delta_j^i \qquad \text{A15}$$

then

$$g^{im}\frac{\partial g_{mj}}{\partial\xi^k} + g_{mj}\frac{\partial g^{im}}{\partial\xi^k} = 0 \qquad \text{A16}$$

Multiplying this equation by g^{nj},

$$g^{nj}g^{im}\frac{\partial g_{mj}}{\partial \xi^k}+g^{nj}g_{mj}\frac{\partial g^{im}}{\partial \xi^k}=0 \qquad \text{A17}$$

and one obtains

$$g^{nj}g^{im}\frac{\partial g_{mj}}{\partial \xi^k}+\frac{\partial g^{in}}{\partial \xi^k}=0 \qquad \text{A18}$$

or

$$\begin{aligned}\frac{\partial g^{in}}{\partial \xi^k} &= -g^{nj}g^{im}\frac{\partial g_{mj}}{\partial \xi^k}\\ &= -g^{nj}g^{im}(\Gamma_{kjm}+\Gamma_{kmj})\\ &= -g^{nj}\Gamma^{i}_{kj}-g^{im}\Gamma^{n}_{km}\end{aligned} \qquad \text{A19}$$

The final result is

$$\frac{\partial g^{ij}}{\partial \xi^k} = -g^{im}\Gamma^{j}_{mk}-g^{jm}\Gamma^{i}_{mk} \qquad \text{A20}$$

Using the above expressions, the stress can be expanded as

$$\tau^{ij} = \mu_e \varepsilon^{ij} \qquad \text{A21}$$

$$\begin{aligned}\varepsilon^{ij} &= u^i\,|^j + u^j\,|^i\\ &= g^{jm}u^i\,|_m + g^{im}u^j\,|_m\\ &= g^{jm}\left(\frac{\partial u^i}{\partial \xi^m}+u^k\Gamma^{i}_{mk}\right)+g^{im}\left(\frac{\partial u^j}{\partial \xi^m}+u^k\Gamma^{j}_{mk}\right)\\ &= g^{jm}\frac{\partial u^i}{\partial \xi^m}+g^{im}\frac{\partial u^j}{\partial \xi^m}+u^k\left(g^{jm}\Gamma^{i}_{mk}+g^{im}\Gamma^{j}_{mk}\right)\\ &= g^{jm}\frac{\partial u^i}{\partial \xi^m}+g^{im}\frac{\partial u^j}{\partial \xi^m}-\frac{\partial g^{ij}}{\partial \xi^m}u^m\end{aligned} \qquad \text{A22}$$

Similarly, using equation (A10);

$$\tau_{ij} = \mu_e \varepsilon_{ij} \tag{A23}$$

$$\begin{aligned}
\varepsilon_{ij} &= u_i|_j + u_j|_i \\
&= g_{im} u^m|_j + g_{jm} u^m|_i \\
&= g_{im}\left(\frac{\partial u^m}{\partial \xi^j} + u^k \Gamma^m_{jk}\right) + g_{jm}\left(\frac{\partial u^m}{\partial \xi^i} + u^k \Gamma^m_{ik}\right) \\
&= g_{jm}\frac{\partial u^m}{\partial \xi^i} + g_{im}\frac{\partial u^m}{\partial \xi^j} + u^k(\Gamma_{jki} + \Gamma_{ikj}) \\
&= g_{jm}\frac{\partial u^m}{\partial \xi^i} + g_{im}\frac{\partial u^m}{\partial \xi^j} + \frac{\partial g_{ij}}{\partial \xi^m} u^m
\end{aligned} \tag{A24}$$

and

$$\tau^i_j = \mu_e \varepsilon^i_j \tag{A25}$$

$$\begin{aligned}
\varepsilon^i_j &= u^i|_j + u_j|^i \\
&= u^i|_j + g^{im} u_j|_m \\
&= \frac{\partial u^i}{\partial \xi^j} + u^m \Gamma^i_{jm} + g^{im}\left(\frac{\partial u_j}{\partial \xi^m} - u_n \Gamma^n_{jm}\right) \\
&= \frac{\partial u^i}{\partial \xi^j} + g^{im}\frac{\partial u_j}{\partial \xi^m} + u^m g^{ik}\left(\frac{\partial g_{jk}}{\partial \xi^m} - \frac{\partial g_{jm}}{\partial \xi^k}\right)
\end{aligned} \tag{A26}$$

To summarize the above derivations, one has now obtains

Momentum Equation:

$$\frac{1}{\sqrt{g}}\frac{\partial}{\partial \xi^j}[\sqrt{g}(\rho u_i u^j - \tau^j_i)] - \frac{1}{2}\frac{\partial g_{jk}}{\partial \xi^i}(\rho u^j u^k - \tau^{jk}) + \frac{\partial p}{\partial \xi^i} - \gamma_i = 0 \tag{A27}$$

where

$$\tau^{jk} = \mu_e (g^{km} \frac{\partial u^j}{\partial \xi^m} + g^{jm} \frac{\partial u^k}{\partial \xi^m} - \frac{\partial g^{jk}}{\partial \xi^m} u^m) \qquad \text{A28}$$

$$\tau_i^j = \mu_e [\frac{\partial u^j}{\partial \xi^i} + g^{jm} \frac{\partial u_i}{\partial \xi^m} + u^m g^{jk} (\frac{\partial g_{ik}}{\partial \xi^m} - \frac{\partial g_{im}}{\partial \xi^k})] \qquad \text{A29}$$